School of Civil and Mechanical Engineering

Using Inerter-based Damper for Offshore Semi-submersible Platform Vibration Control

Ruisheng Ma

This thesis is presented to the Degree of
Doctor of Philosophy
of
Curtin University

December 2020

Declaration

To the best of my knowledge and belief this thesis contains no material previously published by any other person except where due acknowledgement has been made.

This thesis contains no material which has been accepted for the award of any other degree or diploma in any university.

Signature: ……..

Date: ……...

ABSTRACT

Semi-submersible platforms (SSPs) are widely used in offshore industries for oil exploration and exploitation due to its many merits, e.g. large deck area and big payload capacity. However, SSP may be subject to excessive motions due to its shallow draft and large pontoons, which in turn influence the crew health, reduce the platform productivity, and even endanger the structural safety. It is therefore imperative to effectively suppress the excessive motions of SSP.

In the past decades, extensive research efforts have been dedicated to suppressing the excessive motions of offshore platforms, and various vibration control methods have been proposed. For SSP, the most commonly used method is installing a fixed heave plate (FHP) to increase the displacement of platforms or using a tuned heave plate (THP) to absorb energy based on the tuned mass damper (TMD) concept. It is found that with the same mass ratio, the control effectiveness of THP is normally higher than that of FHP. Additionally, a larger mass ratio between FHP/THP and SSP can lead to better control effectiveness. However, it should be noted that adding a large auxiliary mass to the primary structure not only increases the cost but also is not technically practical in some cases. It would be better if the same or better control effectiveness could be realized by using a small auxiliary mass.

Recently, a novel two-terminal mechanical element, dubbed inerter, sheds some light on reducing the auxiliary mass of the control system. As a real counterpart of a capacitor, inerter was proposed based on the analogy between mechanical and electrical networks. The fundamental property of inerter is that it can generate a force proportional to the relative acceleration across its two terminals, and the proportionality constant is normally called "inertance" with a unit of kilogram. This property endows the inerter with two attractive effects: the mass amplification and negative stiffness effects. Due to these appealing characteristics, many inerter-based vibration control systems have been proposed recently and used to control the vibrations of various engineering structures. It should be noted that, previous studies mainly focused on the onshore structures, the studies of using inerter damper to control the vibrations of offshore structures are relatively limited, and no open literature reports applying inerter-based device for SSP vibration control yet.

The primary objective of this study is to explore the feasibility of applying different inerter-based control systems for offshore SSP vibration control. Extensive analytical and experimental studies are carried out. Following the literature review on the research status of the related studies in Chapter 1, the remaining parts of the thesis are organized as follows:

A novel tuned heave plate inerter (THPI) is proposed in Chapter 2 for the heave motion mitigation of SSP. Analytical studies are performed to investigate the control effectiveness of

the proposed THPI system. For comparison, the control effectiveness of the conventional FHP and THP systems are also investigated. The analytical results demonstrate that the THPI is more effective to mitigate the heave motion of SSP compared to the conventional FHP and THP systems. However, it is also found that the THPI system can only further reduce the heave motion up to 19% compared to the THP system.

To further improve the control efficiency, another inerter-based vibration control system, namely a rotational inertia damper (RID), is proposed. Analytical studies are performed to investigate its effectiveness to mitigate the heave motion and the simultaneous heave and pitch motions of SSP in Chapters 3 and 4, respectively. Similar to Chapter 2, the responses of the SSP controlled by the FHP and THP systems are also calculated. The analytical results show that the proposed RID system can achieve similar control performances to the FHP and THP systems with a much smaller plate size/mass.

In Chapter 5, a RID prototype is manufactured and tested under harmonic excitations. A precise mechanical model considering inerter nonlinearities is proposed to predict the behaviors of the RID, and the corresponding parameters are identified by using a nonlinear least-squares method based on the experimental results. After the device tests in Chapter 5, large-scale wave flume tests are further performed in Chapter 6 to investigate the control effectiveness of the RID in reducing the motions of SSP. In particular, a 1:70 scaled SSP model is constructed, and regular and irregular wave tests are carried out. The test results verified the effectiveness of using the RID for SSP vibration control.

Besides the THPI and RID systems, this thesis also develops an inerter-based vibration isolation system (IVIS) for the heave motion mitigation of SSP subjected to sea waves, and the corresponding concept and results are reported in Chapter 7. In particular, an analytical model of a classical SSP equipped with IVIS is established and validated by comparing the heave response amplitude operator (RAO) with the experimental and numerical results reported by other researchers. The results also demonstrate the performance benefits of such a design concept.

Finally, some concluding remarks are made in Chapter 8, and some recommendations for future studies are also suggested in this chapter.

ACKNOWLEDGEMENTS

Foremost, I would like to express my sincere gratitude and respect to my supervisor Prof. Hong Hao and co-supervisor Dr. Kaiming Bi, who have been giving me insightful guidance and persistent encouragement during my PhD study at Curtin University. I would not have completed this challenging thesis without their supervision and continuous supports.

I would also like to thank the staff and postgraduate students in the School of Civil and Mechanical Engineering and Centre for Infrastructure Monitoring and Protection (CIMP) for their encouragement and kind help during my PhD study.

My sincere thanks also go to China Scholarship Council (CSC) and Curtin University for supporting me to pursue this study.

Finally, but definitely not least, I wish to express my deep gratitude to my family, for their unconditional support and love.

LIST OF PUBLISHED WORK AND/OR WORK PREPARED FOR PUBLICATION

This thesis contains published work and/or work prepared for publication, which has been co-authored. The bibliographical details of the work and where it appears in the thesis are outlined below.

Chapter 1

Ma R, Bi K, Hao H. Inerter-based vibration control systems: A state-of-the-art review. 2020. (Under review).

Chapter 2

Ma R, Bi K, Hao H. Mitigation of heave response of semi-submersible platform (SSP) using tuned heave plate inerter (THPI). Eng Struct. 2018;177:357-73.

Chapter 3

Ma R, Bi K, Hao H. A novel rotational inertia damper for heave motion suppression of semisubmersible platform in the shallow sea. Struct Control Health Monit. 2019;26:e2368.

Chapter 4

Ma R, Bi K, Hao H. Using inerter-based control device to mitigate heave and pitch motions of semi-submersible platform in the shallow sea. Eng Struct. 2020;207:110248.

Chapter 5

Ma R, Bi K, Hao H. A novel rotational inertia damper for amplifying fluid resistance: Experiment and mechanical model. Mech Syst Signal Process. 2021;149:107313.

Chapter 6

Ma R, Bi K, Hao H. Wave flume tests of a semi-submersible platform controlled by a novel rotational inertia damper. 2020. (Under review).

Chapter 7

Ma R, Bi K, Hao H. Heave motion mitigation of semi-submersible platform using inerter-based vibration isolation system (IVIS). Eng Struct. 2020;219:110833.

STATEMENT OF CONTRIBUTION OF OTHERS

The works presented in this thesis were primarily designed, executed, interpreted and written by the candidate and also the first author of the publications (Ruisheng Ma). Significant input to the works was also provided by co-authors. Contributions of the co-authors are described below. The signed contribution form is attached in the appendix.

Hong Hao and Kaiming Bi defined the overall scope and objectives of the works and suggested research methodologies and approaches. All the analytical and experimental studies were performed by Ruisheng Ma. The manuscripts were written by Ruisheng Ma with revisions and editions from Hong Hao and Kaiming Bi, both of whom also provided additional intellectual input in the discussions of the results.

LIST OF RELEVANT ADDITIONAL PUBLICATIONS

The additional publications relevant to the thesis with the bibliographical details are listed below.

1. Zuo H, Bi K, Hao H, **Ma R**. Influences of ground motion parameters and structural damping on the optimum design of inerter-based tuned mass dampers. Eng Struct. 2021;227:111422.
2. **Ma R**, Bi K, Hao H. Heave response control of semi-submersible platform using tuned heave plate inerter (THPI). 7th World Conference on Structural Control and Monitoring, 22-25 July, 2018, Qingdao, China.
3. Hao H, Bi K, Zuo H, Nikoo M, Zhou T, **Ma R**. Recent research on passive control of offshore structural vibrations in the Centre for Infrastructure Monitoring and Protection (CIMP) at Curtin University. 7th World Conference on Structural Control and Monitoring, 22-25 July, 2018, Qingdao, China.

TABLE OF CONTENTS

LIST OF FIGURES

LIST OF TABLES

CHAPTER 1 INTRODUCTION

Abstract[1]

Structural vibration control has received considerable research attentions in the past few decades, with special emphasis on developing effective, affordable and applicable control systems to protect the structures against natural or man-made hazards. In 2002, a two-terminal mechanical element, dubbed inerter, was proposed based on the force-current analogy, offering many potentials for upgrading conventional structural vibration control systems. In the past two decades especially in the recent five years, extensive research efforts have been made for the development of inerter-based vibration control systems. This paper aims to provide a state-of-the-art review on the research and development of inerter-based passive vibration control systems and their applications. It begins with the basic concept and existing issues of conventional passive control systems, which include energy dissipator, dynamic vibration absorber (DVA) and vibration isolator. The concept, physical realizations and mechanical models of inerter are then presented in detail. Subsequently, this paper reviews the applications of inerter in civil engineering and discusses its benefits comparing to the conventional vibration control systems. Finally, some discussions are made on the unresolved problems and the possible topics for future studies.

1.1 Introduction

Vibration is defined as the oscillating, reciprocating, or other periodic motion of a rigid or elastic body or medium forced from a position or state of equilibrium [1], which is widely encountered in mechanical, civil and aerospace engineering. For a civil engineering structure, undesirable or excessive vibrations could cause extreme loads/deformations, fatigue, human discomfort, and/or even collapse of the structure. For example, the collapse of the Tacoma Narrows bridge in 1940 was caused by resonance induced by wind loads. Various structural vibration control systems have been developed to improve the structural functionality and safety against natural or man-made vibration loads, which can be broadly classified into passive, semi-active, active and hybrid groups [2]. A passive control system consisting of a range of materials and devices (e.g. dashpot, spring and mass, etc.) can generate a control force in response to the structural motion and does not require external power supply. Active, semi-active, and hybrid control systems generally consist of controllable force devices, sensors, and controllers. They can produce control forces according to the real-time information by using external power sources to drive these devices. Among these control systems, the passive

[1] Ma R, Bi K, Hao H. Inerter-based vibration control systems: A state-of-the-art review. 2020. (Under review).

control system is more widely applied in civil structures due to its simplicity and independence on external energy. However, the passive control system is not flawless and it has some inherent limitations, e.g. it often requires a large additional mass for a tuned mass damper (TMD) to be effective and the conventional vibration isolator has limited effective frequency range as will be discussed in Section 1.2. To this end, extensive efforts have been devoted to upgrading these conventional passive control systems for higher performance or tackling some inherent issues.

A two-terminal mechanical element initially proposed by Smith [3] in 2002, dubbed inerter, has attracted a lot of attentions in civil engineering community recently. As the real counterpart of a capacitor, the inerter is proposed based on the analogy between the mechanical and electrical networks, which can be realized by various physical means, such as the ball screw assembly, rack-and-pinion, hydraulic, and fluid, etc. The fundamental property of inerter is that it can generate a force proportional to the relative acceleration across its two terminals, and the proportionality constant is normally called "inertance" with a unit of kilogram. This property endows the inerter with two attractive effects: the mass amplification and negative stiffness effects. The mass amplification effect refers to that the inerter can achieve the inertance several orders of magnitude larger than its physical mass; As for the negative stiffness effect, it means that the inerter can generate a force assisting rather than opposing the motion. Moreover, inerter can enrich the mechanical networks (i.e. the configurations) of conventional control systems since it is a two-terminal mass element and can be connected like the "ordinary" spring and damper elements. Due to these attractive characteristics, inerter opens many potential opportunities for upgrading conventional passive control systems. Various inerter-based vibration control systems have been developed in the past two decades especially in the recent five years.

In this paper, a state-of-the-art review is presented for inerter-based vibration control systems, with special emphasis laid upon the application of inerter in the passive structural vibration control. The remaining of this paper is organized as follows: in Section 1.2, the basic concept and existing inherent issues of conventional passive control systems are presented; Section 1.3 deals with the concept and various physical realizations of inerter; mechanical models of inerter are shown in Section 1.4; Section 1.5 reviews the applications of inerter in different vibration control systems; Some discussions on the existing challenges of these inerter-based vibration control are made in Section 1.6; finally, some conclusions are drawn in Section 1.7.

1.2 Passive Control Systems

As mentioned above, passive vibration control is a control strategy that does not require any external power and imparts a control force in response to the structural motions. It has been

under investigation for several decades. In this area, many excellent review papers concerning the passive structural vibration control have been published (e.g. Refs. [4-7]). By and large, the passive vibration control can be grouped into the following three categories: energy dissipator, dynamic vibration absorber (DVA), and vibration isolator. In this section, basic concepts and limitations of these three control systems are discussed.

1.2.1 Energy Dissipators

Energy dissipators are the vibration control devices with the basic principle of converting the kinetic energy into heat and thus reducing the structural vibrations. According to different dissipating ways, energy dissipators can be primarily subdivided into the following four types: metallic yield dampers, friction dampers, viscoelastic dampers, and viscous fluid damper. In particular, they dissipate the energy through (1) the inelastic deformation of metals; (2) the solid friction between two bodies sliding relatively; (3) the shear deformation of copolymers and glassy substances; and (4) the viscous fluid flowing through orifices, respectively. Notably, these energy dissipators have some obvious advantages such as simple construction, low cost and easy manufacturing, etc. Due to these benefits, the energy dissipators were extensively applied in the seismic- and wind-induced vibration protections of civil structures, such as in the Twin World Trade Center Towers in New York and St. Francis Shangri-La Place in Philippine.

Although these energy dissipators have been found to be effective for vibration control, there still exist some shortcomings. For example, conventional friction dampers have no self-reset capability and their performance may be influenced by the corrosion of friction surface [8]; the performance of viscoelastic dampers is temperature-dependent and their performances would be degraded at higher temperatures [9]. Moreover, the implementation of energy dissipators would sacrifice valuable space of buildings, and it would be better if the number and size of energy dissipators could be reduced as much as possible. Therefore, considerable attentions are still being paid to the research and development of more effective energy dissipators.

1.2.2 Dynamic Vibration Absorbers

Dynamic vibration absorbers (DVAs) work on the principle of transferring the vibration energy to auxiliary systems, which have two common forms: tuned mass damper (TMD) and tuned liquid damper (TLD). A TMD normally consists of a secondary mass connected by a spring and a dashpot, which can date back to the 1940s. In the past few decades, TMDs have been demonstrated to be effective in mitigating the vibrations induced by various loads, such as earthquake, wind, wave, vortex and human, etc. Moreover, researchers also proposed some

variants of TMD by changing configurations or adding new techniques, which include multiple tuned mass damper (MTMD) [10], pounding tuned mass damper (PTMD) [11], particle tuned mass damper (PTMD) [12], shape memory alloy-tuned mass damper (SMA-TMD) [13], nonlinear tuned mass damper (NTMD) [14], and nonlinear energy sink (NES) [15], etc. In practice, a number of TMDs have been installed in structures, e.g. in the Centerpoint Tower in Sydney, Taipei 101 tower and Shanghai Tower. The TLD is another common form of DVA, which absorbs the vibration energy through the viscous actions of fluid and wave breaking [16]. In other words, the TLD can be regarded as a special type of TMD where the mass is replaced by a liquid. In some cases, the TLD is more attractive than the TMD due to: (1) lower cost and simpler maintenance; (2) functional use of liquid containers, e.g. building water supply. In the past decades, TLDs were also applied in the vibration control of many high-rise buildings, such as the Cosima Hotel in Tokyo and the Comcast Center in Philadelphia.

It should be noted that the control effectiveness of DVA is highly dependent on the mass ratio, i.e. the ratio between the physical masses of secondary and primary structures. Generally speaking, a large secondary mass is required to achieve the desired control performance. Taking the TMD inside the Taipei 101 as an example, the mass of the TMD reaches 800 tonnes [17]. A large secondary mass not only increases the construction costs but also raises the complexity of the connecting system, which thus prevents the extensive application of TMD to some extent. Developing "light-weight" DVAs has therefore become a hot research topic in recent years.

1.2.3 Vibration Isolators

Vibration isolation is a control strategy with the premise that the structure can be uncoupled or isolated from harsh disturbances, thereby protecting the structures from hazards [18]. By introducing an isolator, the fundamental frequency of the isolated structure can be effectively shifted from the dominant frequency of external disturbance, and the transmitted vibrations and forces thus can be attenuated. In the field of civil structures, base isolation systems (BISs) are widely placed between the superstructure (i.e. the host structure) and base for reducing the seismic energy propagation to the structure. Excellent reviews about BISs are presented in Refs. [19, 20]. In the past decade, a lot of isolated buildings and bridges have been constructed, such as Kunming airport terminal and Hong Kong-Zhuhai-Macau bridge [21], etc.

Like other vibration control systems, conventional isolators also have some disadvantages: (1) the conventional isolators are effective only when the input frequencies are larger than $\sqrt{2}$ times of the fundamental natural frequency of the isolated structure. For the input frequencies below $\sqrt{2}$ times of the fundamental natural frequency, the responses of the isolated structure

would be aggravated rather than suppressed. In other words, the conventional isolators have a limited effective frequency range; (2) when a structure is isolated by BIS, most of the lateral displacement would be concentrated at the isolation level due to the high flexibility of BIS. Therefore, a large displacement demand is generally required for BISs to prevent possible collisions and instabilities.

1.3 Concept and Realizations of Inerter

This section introduces the concept of inerter and its various physical realizations including the ball-screw, rack-and-pinion, hydraulic, helical fluid, electromagnetic and living-hinge types. Meanwhile, corresponding formulas to calculate the inertance are given as well.

1.3.1 Concept of Inerter

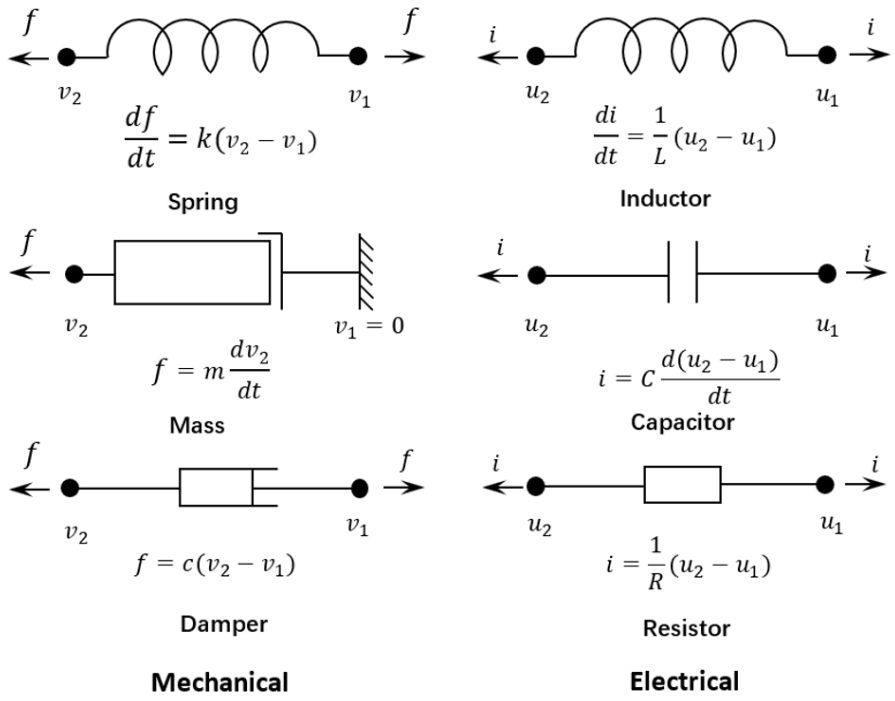

Figure 1-1 Force-current analogy (after [22])

The concept of inerter was proposed by Smith based on the force-current analogy between the electrical and mechanical networks. Figure 1-1 shows the correspondences in the force-current analogy. In the figure, f, v, k, m and c are the force, velocity, stiffness, mass and damping coefficient in the mechanical network, respectively; and i, u, L, C and R are the current, voltage, inductance, capacitance and resistance in the electrical network, respectively. As shown, the spring, mass and damper elements in the mechanical network correspond to the inductor, capacitor and resistor elements in the electrical network, respectively, and all the elements except the mass are two-terminal. In other words, the one-terminal mass element

cannot complete the analogy with the capacitor element. To fully realize the analogy between the mechanical and electrical elements, Smith [3] proposed the two-terminal inerter element which can generate a force proportional to the relative acceleration across its two terminals. Figure 1-2 shows the schematic drawing of one-terminal mass element and two-terminal inerter element, in which b is the inertance. Very recently, Smith also provided an excellent review on the inerter concept and devices in Ref. [22]. However, Smith [22] mainly focused on the inerter concept and devices, and inerter-based vibration control systems were not discussed in detail. In this paper, more attentions are paid to the applications of inerter-based vibration control systems especially in the field of civil engineering.

(a) (b)

Figure 1-2 One-terminal mass element and two-terminal inerter element

1.3.2 Physical Realizations of Inerter

In practice, many inerter prototypes have been constructed by using different mechanisms, primarily including the ball-screw, rack-and-pinion, hydraulic, helical fluid, electromagnetic, and living-hinge. In this subsection, these different inerter devices are summarized with a special emphasis on the working principles.

1.3.2.1 Ball-screw Inerter

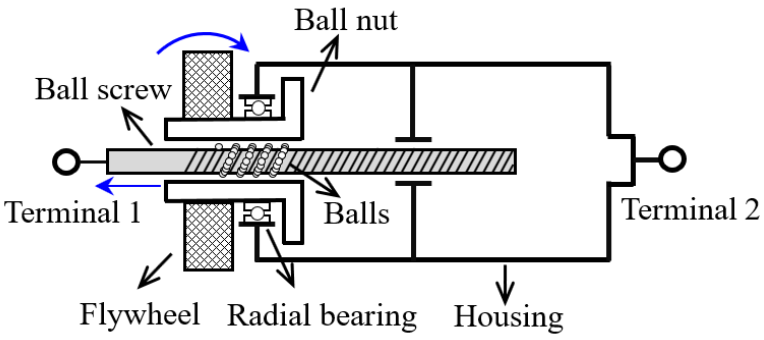

Figure 1-3 Schematic drawing of ball-screw inerter

Figure 1-3 shows the schematic drawing of a typical ball-screw inerter. It can be seen that this device consists of a ball screw, a ball nut, a radial bearing, a housing, and a flywheel connected to the ball nut. In the ball-screw inerter, the ball screw is the key component which can transform the linear motion between its two terminals into the rotation of the ball nut, and thus the rotation of the flywheel. By such a design, the physical mass of flywheel can be amplified,

and a significant apparent mass (namely inertance) can be realized. The ideal inertance of the ball-screw inerter can be calculated by the following equation:

$$b = (\frac{2\pi}{L})^2 \cdot I \tag{1.1}$$

in which I is the moment of inertia of the flywheel, L is the lead of the ball screw, i.e. the linear distance traveled for each complete turn of the screw. It can be seen that a larger inertance can be achieved by either increasing I or reducing l, and the optimal design can be selected based on the real situation in engineering practice. For example, if there is no space limit (e.g. in the ocean environment), a larger I might be a good option [23]. A number of ball-screw inerters have been developed (e.g. Refs. [24, 25]), and Figure 1-4 shows a typical ball-screw inerter developed by Papageorgiou et al. [24].

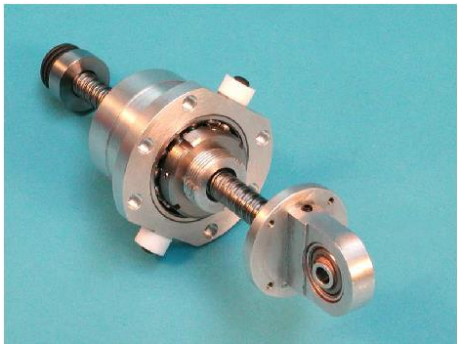

Figure 1-4 Ball-screw inerter developed by Papageorgiou et al. [24]

1.3.2.2 Rack-and-pinion Inerter

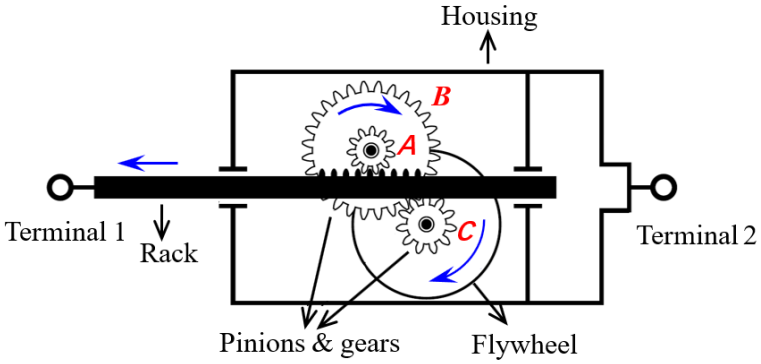

Figure 1-5 Schematic drawing of rack-and-pinion inerter (after [26])

Figure 1-5 shows the schematic drawing of a rack-and-pinion inerter, which consists of a rack, a flywheel, a housing, pinions and gears. As shown, the rack can slide in the housing and drive the rotation of flywheel through the pinions and gears. The ideal inertance of a rack-and-pinion inerter depends on the moment of inertia of flywheel (I) and gear ratio (η), which can be expressed as follows:

$$b = \eta^2 \cdot I \tag{1.2}$$

in which $\eta = \frac{r_2}{r_1 r_3}$, and r_1, r_2 and r_3 represent the radiuses of Gears A, B and C, respectively. Figure 1-6 shows the rack-and-pinion inerter prototype developed by Papageorgiou et al. [24].

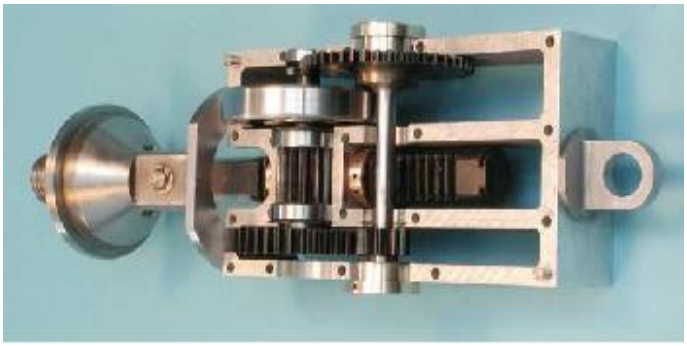

Figure 1-6 Rack-and-pinion inerter developed by Papageorgiou et al. [24]

1.3.2.3 Hydraulic Inerter

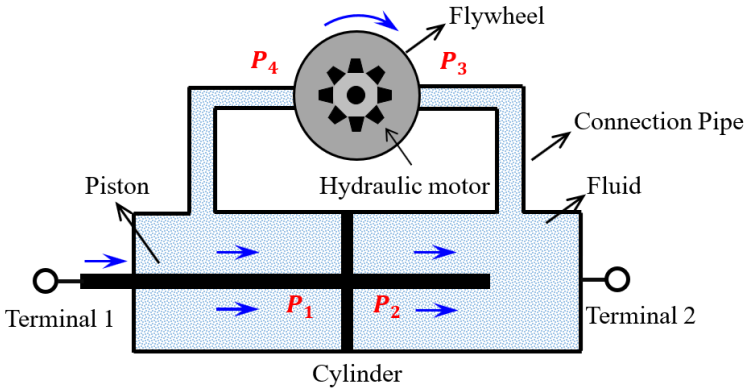

Figure 1-7 Schematic drawing of hydraulic inerter (after [27])

Figure 1-7 illustrates the schematic drawing of the hydraulic inerter, which utilizes a hydraulic mechanism to drive the flywheel. As illustrated, the hydraulic inerter consists of a hydraulic motor, a cylinder, a piston, a flywheel, and connection pipes. In particular, the moving piston can cause pressure difference at two sides of the hydraulic motor (i.e. P_3 and P_4), and the fluid will flow through the pipes. The flowing fluid could drive the rotation of the hydraulic motor, and thus the rotation of the flywheel. The ideal inertance of hydraulic inerter is

$$b = (\frac{A}{D})^2 \cdot I \tag{1.3}$$

where A is the working area of the hydraulic cylinder, D is the pitch of the hydraulic motor, and I is the moment of inertia of the flywheel again. Figure 1-8 shows the prototype of hydraulic inerter developed by Wang et al. [27].

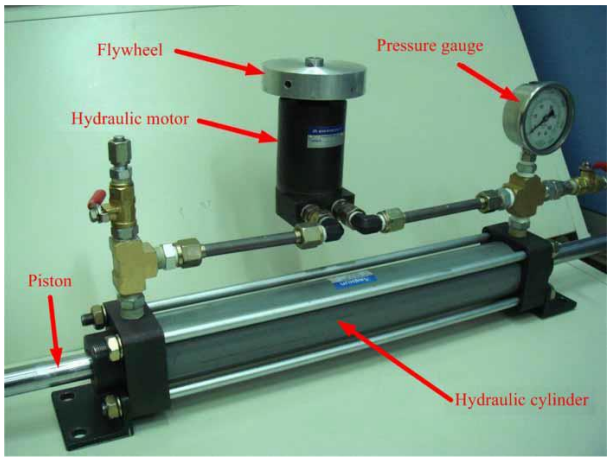

Figure 1-8 Hydraulic inerter developed by Wang et al. [27]

1.3.2.4 Helical Fluid Inerter

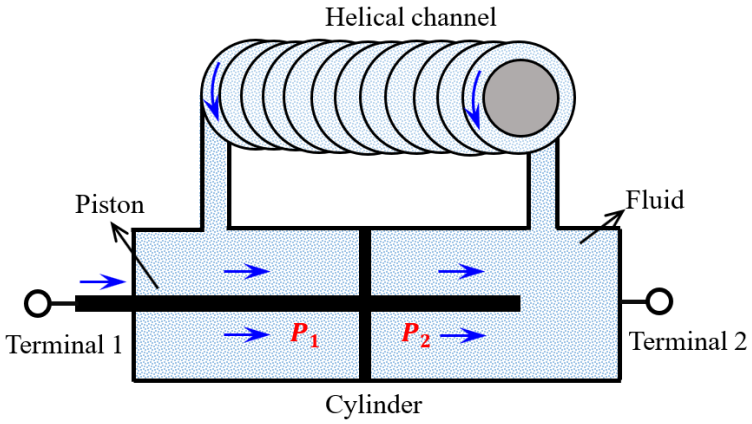

Figure 1-9 Schematic drawing of helical fluid inerter (after [28])

The helical fluid inerter utilizes the fluid flowing through an external channel to generate inertance, Figure 1-9 shows the schematic drawing of a helical fluid inerter. As shown, the helical fluid inerter primarily consists of a piston, a cylinder, and helical channel. When the piston moves relative to the cylinder, the fluid would flow through the external helical channel due to the pressure difference between the left and right chambers. Then, the fluid velocity in the helical channel can be scaled up by the ratio of cylinder area to helical channel area.

The ideal inertance of the helical fluid inerter can be calculated by

$$b = \rho l_h \frac{A_1^2}{A_2} \tag{1.4}$$

where ρ is the density of fluid, l_h is the length of helical channel, A_1 is the annular area of cylinder, and A_2 is the cross-sectional area of helical channel. Figure 1-10 shows the prototype of helical fluid inerter developed by Domenico et al. [29].

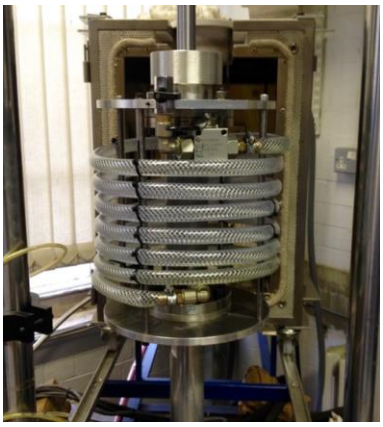

Figure 1-10 Helical fluid inerter developed by Domenico et al. [29]

For the helical fluid inerter, there also exists another simple physical realization, the internal-helix fluid inerter, as shown in Figure 1-11 [30, 31]. As shown, the internal-helix fluid inerter consists of a moving piston with a helical channel surrounding its outer surface and a cylinder filled with fluid. Obviously, no additional helical channels are required for this internal-helix fluid inerter, and the corresponding helical path is formed between the piston and the cylinder when the piston is moving in the cylinder. Similarly, an inertial force can be generated due to the moving fluid mass when the moving piston drives the fluid to flow through the helical path. It is worth mentioning that Equation (1.4) is still valid to calculate the inertance of internal-helix fluid inerter.

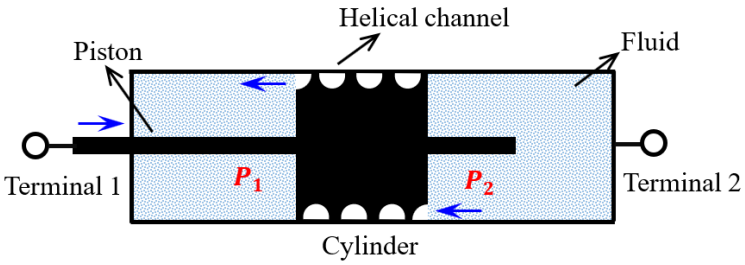

Figure 1-11 Schematic drawing of internal-helix fluid inerter (after [30])

1.3.2.5 Electromagnetic Inerter

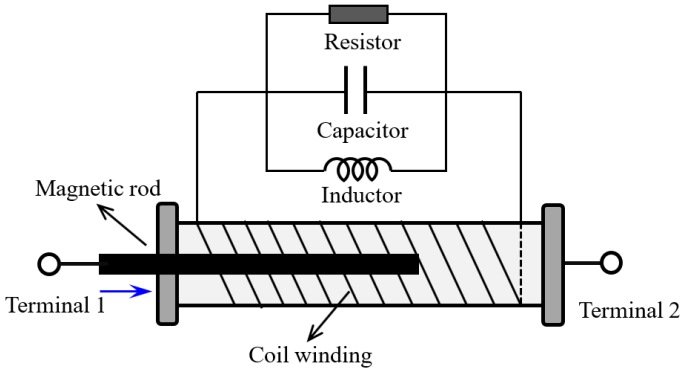

Figure 1-12 Schematic drawing of electromagnetic inerter (after [32])

Figure 1-12 shows the schematic drawing of an electromagnetic inerter, which consists of coil winding, magnet rod and capacitor. When the magnetic rod moves, a voltage is generated across the coil due to the change of magnetic flux. A resistant force will be generated due to the creation of an opposing magnetic field by the current flowing the coil. The total inertance of electromagnetic inerter can be calculated as follows:

$$b = (Bl)^2 C_a \tag{1.5}$$

where Bl is the coupling coefficient, and C_a is the capacitance. Figure 1-13 shows the prototype of the electromagnetic inerter developed by Gonzalez-Buelga et al. [32].

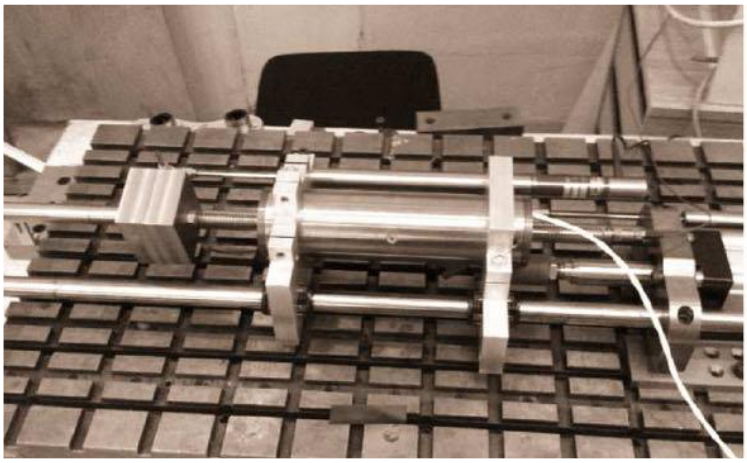

Figure 1-13 Electromagnetic inerter developed by Gonzalez-Buelga et al. [32]

1.3.2.6 Living-hinge Inerter

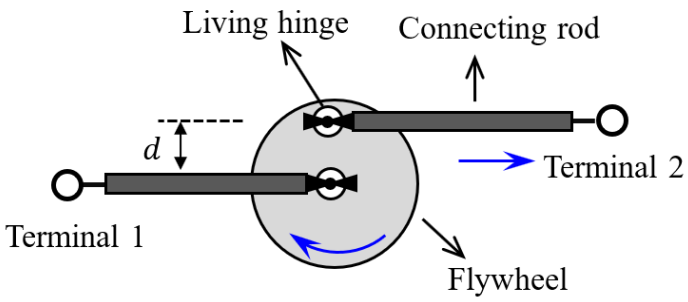

Figure 1-14 Schematic drawing of living-hinge inerter

Figure 1-14 shows the schematic drawing of a living-hinge inerter which consists of two connecting rods, two living hinges and one flywheel. It is worth mentioning that one living hinge is at the centre of the flywheel while another one is offset the centre with a distance of d. Due to such a design, the linear motion is transformed into the rotational motion of the flywheel, and the lever arm effect can be realized. The ideal inertance of living-hinge inerter can be calculated as follows:

$$b = \frac{1}{d^2} \cdot I \tag{1.6}$$

Obviously, the inertance of living-hinge inerter increase with the decrease of the distance between two living hinges. Figure 1-15 shows the prototype of a living-hinge inerter developed by John et al. [33].

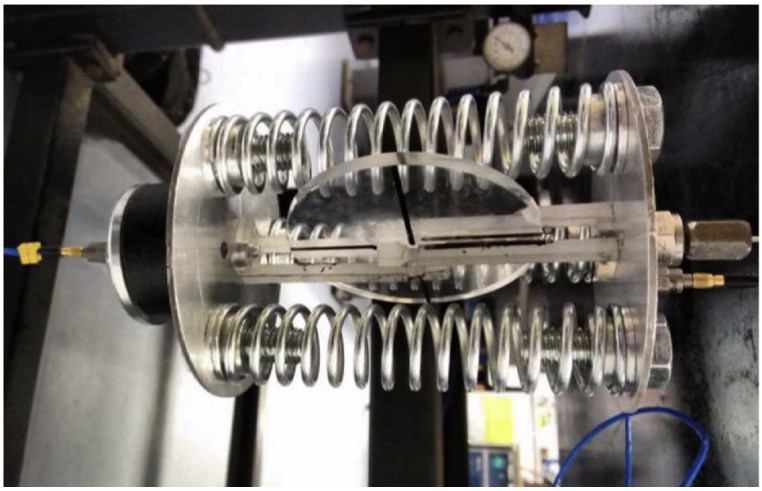

Figure 1-15 Living-hinge inerter developed by John et al. [33]

1.4 Mechanical Models of Inerters

1.4.1 Ideal Mechanical Model

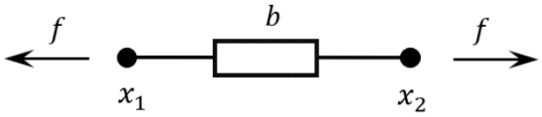

Figure 1-16 Ideal mechanical model of inerter

Figure 1-16 illustrates the ideal mechanical model of an inerter. As defined in Ref. [22], inerter is a two-terminal mechanical element with the property that the applied force is proportional to the relative acceleration across its two terminals, and its ideal mechanical behavior can thus be expressed by the following equation:

$$f(t) = b\left(\ddot{x}_2(t) - \ddot{x}_1(t)\right) \tag{1.7}$$

where t is the time; $b > 0$ is the inertance with a unit of kilogram; $\ddot{x}_1$ and $\ddot{x}_2$ are the accelerations at two terminals.

Assuming x_1 and x_2 are harmonic excitations with a vibration frequency ω, Equation (1.7) can be rewritten in the frequency domain as follows:

$$Fe^{i\omega t} = -b\omega^2(X_2 - X_1)e^{i\omega t} \tag{1.8}$$

in which F is the force amplitude, X_1 and X_2 are the displacement amplitudes. Obviously, F is negatively correlated with the relative displacement amplitude (i.e. $X_2 - X_1$), with a negative stiffness of $-b\omega^2$. In addition, the negative stiffness produced by inerter is proportional to the square of vibration frequency (i.e. ω^2), and it thus increases rapidly with the increment of vibration frequencies. This is different from the traditional negative-stiffness devices, which possess constant negative stiffness under different vibration frequencies, and it may cause some problems in applications as will be discussed in Section 1.6.

1.4.2 Mechanical Models Considering Nonideal Parameters

As shown in Equation (1.7), the ideal mechanical model of inerter is simple and straightforward. However, an ideal inerter element is unavailable in practice since there always exist several nonideal factors influencing its performance. In this subsection, the mechanical models considering nonideal factors are presented for two classical inerters: i.e. the ball-screw and helical fluid inerters.

1.4.2.1 Ball-screw Inerter

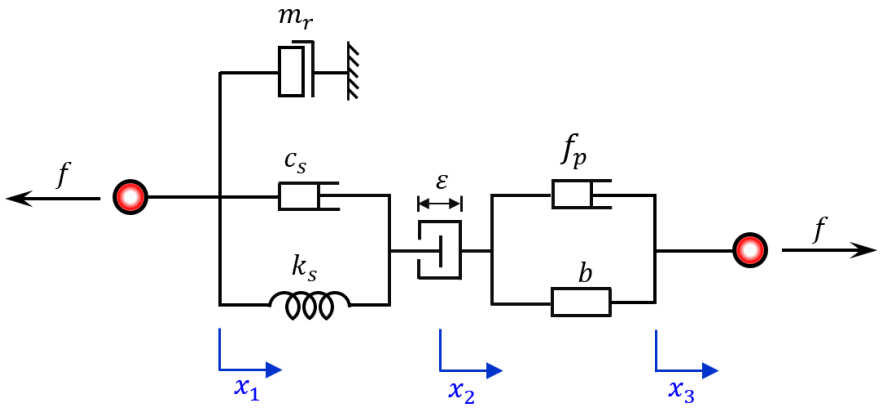

Figure 1-17 Mechanical model of the ball-screw inerter considering nonlinearities (after [25])

For the ball-screw inerter, the nonideal factors generally include the structural mass, parasitic damping, backlash (play) and elastic effect. It should be noted that these nonideal factors are also called "nonlinearities" in some studies (e.g. Ref. [34]). Figure 1-17 shows the mechanical model of the ball-screw inerter considering nonlinearities. In this mechanical model, the elastic deformation of ball screw, backlash displacement and linear displacement between two terminals are defined as $x_1 - x_2$, $x_2 - x_3$ and $x_1 - x_3$, respectively. An overdot and two overdots represent the first- and second-order derivative with respect to time, respectively.

The first nonideal factor is the structural mass m_r, which refers to the mass of some components moved linearly (e.g. the rack in Figure 1-5). According to Ref. [25], m_r can be

considered as a mass element with a grounded virtual terminal, and the corresponding inertial force can therefore be written as follows:

$$f_r = m_r \ddot{x}_1 \tag{1.9}$$

As for the parasitic damping (i.e. f_p in Figure 1-17), it corresponds to the various mechanical losses, e.g. the friction of contact surfaces. Generally, the parasitic damping consists of two components: Coulomb and viscous frictions, and it can thus be expressed as follows:

$$Fe^{i\omega t} = -b\omega^2(X_2 - X_1)e^{i\omega t} \tag{1.10}$$

where f_c is the Coulomb friction force, c_m is the viscous friction coefficient, and sgn is the signum function.

Another nonideal factor is the elastic effect, e.g. the elastic deformation of the ball screw under loads. It should be noted that an internal damping effect would also appear when an object deforms. Therefore, the elastic effect is generally modeled by using a spring k_s in parallel with a dashpot c_s as shown in Figure 1-17.

The backlash (play) ε exists widely in mechanical devices and is caused by the clearances between mating components, e.g. the clearance between balls and ball nut as shown in Figure 1-3. A number of static and dynamic models have been developed to capture the backlash effect (e.g. Ref. [35]). These models are not presented in detail in this paper, interested readers can refer to Ref. [35] for more details.

Furthermore, torque ripples of ball screw drive are also observed in previous experimental studies (e.g. Ref. [36]), which has dominant harmonics at integer multiples of the excitation frequency [37]. However, torque ripples are generally neglected in the mechanical model of ball screw inerter since they are obvious only at low-speed rotations.

1.4.2.2 Helical Fluid Inerter

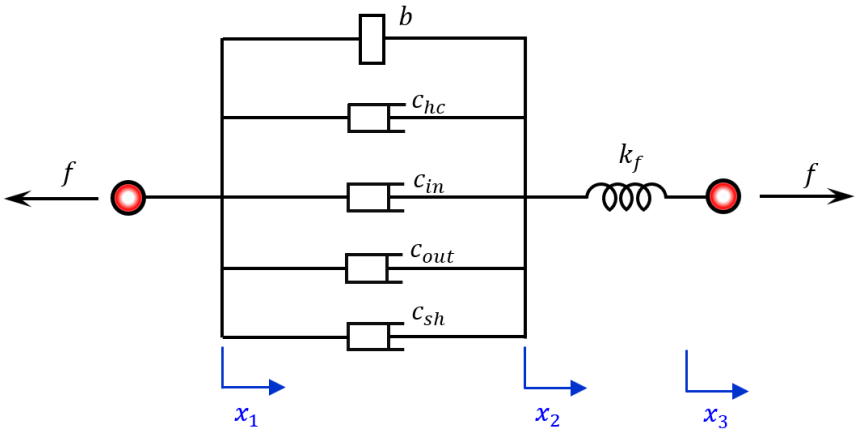

Figure 1-18 Mechanical model of the helical fluid inerter considering nonideal parameters

Since the birth of the helical fluid inerter, several mechanical models have been proposed to accurately capture its mechanical behaviors (e.g. Refs. [28, 31, 38]). In this review, only the mechanical model of the helical fluid inerter developed by Swift et al. [38] is briefly introduced, and it is shown in Figure 1-18. As shown, besides the ideal inertance b, there exist several nonideal factors which include the pressure drop of the helical channel c_{hc}, the pressure drop across the inlet/outlet of the helical channel c_{in}/c_{out}, the viscous shear friction between the piston and cylinder c_{sh} and the fluid spring coefficient k_f (refer to Figure 1-18). The calculation of each nonideal factor was presented in Ref. [38], interested readers can refer to Ref. [38] for more details. As for the other models (e.g. those reported in Refs. [28] and [31]), please refer to the corresponding references as well.

1.5 Applications of Inerter-based Vibration Control Systems

The concept, physical realizations and mechanical models of inerter are respectively reviewed in the prior sections, and three potential benefits of inerter can be found: (1) Two-terminal mass element. The "ordinary" mechanical networks (i.e. configurations) consisting of only springs and dampers have been under investigation for many decades and their potential to further improve the performance of the vibration control systems is almost exhausted. As a two-terminal mass element, the inerter can constitute more effective mechanical networks for the vibration control systems by combining with springs and dampers. (2) Negative stiffness effect. As mentioned above, the negative stiffness effect indicates that the inerter can generate a force to assist the motion instead of opposing the motion in the conventional positive stiffness system. Due to this property, inerter can be utilized to reduce the natural frequency of a vibration system. In addition, inerter does not respond to the static loads, thus it can avoid the aggravated static responses and structural instability issues in the system with conventional negative stiffness devices. (3) Mass amplification effect. The inerter has a significant mass amplification effect especially when its one terminal is connected to the ground. This endows the inerter with high application potential for reducing the auxiliary mass of conventional vibrations control systems.

To clearly illustrate the effect of applying an inerter-based control device to a structure, consider a structure modeled by a n degree-of-freedom (n DOFs) lumped mass-spring-damper system. The equation of motion of the system can be written in the following form [39]:

$$\boldsymbol{M}\ddot{\boldsymbol{x}}(\boldsymbol{t}) + \boldsymbol{C}\dot{\boldsymbol{x}}(\boldsymbol{t}) + \boldsymbol{K}\boldsymbol{x}(\boldsymbol{t}) = \boldsymbol{D}\boldsymbol{f}_{\boldsymbol{c}}(\boldsymbol{t}) + \boldsymbol{E}\boldsymbol{f}_{\boldsymbol{e}}(\boldsymbol{t}) \tag{1.11}$$

where $\boldsymbol{M}$, $\boldsymbol{C}$ and $\boldsymbol{K}$ are the mass, damping and stiffness matrices, respectively; $\boldsymbol{x}(\boldsymbol{t})$, $\dot{\boldsymbol{x}}(\boldsymbol{t})$, and $\ddot{\boldsymbol{x}}(\boldsymbol{t})$ are the displacement, velocity and acceleration vectors, respectively; $\boldsymbol{f}_{\boldsymbol{c}}(\boldsymbol{t})$ is the control

force vector; $\boldsymbol{f_e(t)}$ denotes the external excitations, e.g. earthquake, wind and wave, etc.; $\boldsymbol{D}$ and $\boldsymbol{E}$ are the location matrices of the applied force and external excitation, respectively.

The control force $\boldsymbol{f_c(t)}$ is assumed to be a linear function of the displacement $\boldsymbol{x(t)}$, velocity $\boldsymbol{\dot{x}(t)}$, acceleration $\boldsymbol{\ddot{x}(t)}$ and excitation $\boldsymbol{f_e(t)}$, which can be approximately written as

$$\boldsymbol{f_c(t) = b_1\ddot{x}(t) + C_1\dot{x}(t) + K_1x(t) + E_1f_e(t)} \tag{1.12}$$

in which $\boldsymbol{b_1}$, $\boldsymbol{C_1}$, and $\boldsymbol{K_1}$ are the inertance, damping and stiffness matrices of the inerter-based control device, respectively; $\boldsymbol{E_1}$ is the gain matrices of the external excitation acting on the control system.

Substituting Equation (1.12) into Equation (1.11), one yields:

$$\boldsymbol{(M - Db_1)\ddot{x}(t) + (C - DC_1)\dot{x}(t) + (K - DK_1)x(t) = (E + DE_1)f_e(t)} \tag{1.13}$$

Similarly, the control force $\boldsymbol{f_c(t)}$ of conventional control systems can be written in the following form:

$$\boldsymbol{f_c(t) = C_1\dot{x}(t) + K_1x(t) + E_1f_e(t)} \tag{1.14}$$

Substituting Equation (1.14) into Equation (1.11), the equation of motion of the system equipped with conventional control systems is given by

$$\boldsymbol{M\ddot{x}(t) + (C - DC_1)\dot{x}(t) + (K - DK_1)x(t) = (E + DE_1)f_e(t)} \tag{1.15}$$

Comparing Equations (1.13) and (1.15), it is seen that the conventional control systems reduce the structural vibrations by modifying the damping and stiffness terms only, while inerter-based vibration control systems could suppress the structural vibrations by adjusting the inertial term as well. In other words, inerter provides another method for structural vibration control, i.e. by adjusting the mass matrix of the system, which completes the vibration control theory by adjusting all the possible properties of the structure (namely mass, stiffness and damping) to control the structural vibrations.

Due to this appealing characteristic, the inerter has been extensively applied in the vibration control systems and many inerter-based vibration control systems have been proposed and developed in the past two decades. In this section, the inerter-based vibration control systems will be reviewed in detail. Similar to the classification method in Section 1.2, the inerter-based vibration control systems are categorized into the following groups: inerter-based energy dissipator, inerter-based dynamic vibration absorber and inerter-based vibration isolator. It should be noted that the applications of inerter in automotive engineering will also be briefly presented for facilitating readers to comprehensively understand the development and evolution of the inerter devices when necessary.

1.5.1 Inerter-based Energy Dissipators

Previous studies have revealed that an energy dissipator with a negative stiffness component can have a larger motion and thus dissipate more vibration energy [40, 41]. In view of this, the inerter has been widely applied to upgrade the conventional energy dissipators due to its negative stiffness effect, and many inertial mass dampers (IMDs) were newly proposed and developed. Figure 1-19 shows a typical model of IMD, in which the inerter b is in parallel with a dashpot c.

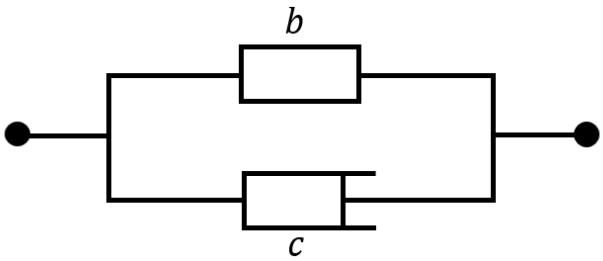

Figure 1-19 Typical model of IMD

In this aspect, Pradono et al. [42] proposed an angular-mass damper for the passive control of a base-isolated building. The essential component of this IMD was a wheel with the mass concentrated on its outer perimeter. By such a design, a large moment of inertia and thus considerable inertance could be generated when the wheel rotates. Their results demonstrated that the angular-mass damper was effective in reducing the seismic responses of buildings and its hysteretic loop showed a negative slope due to the influence of the negative stiffness effect. Similarly, Saitoh [43] also developed an IMD, namely the "gyro-mass" damper (GMD), to mitigate the lateral displacement of base isolators. The GMD consisted of a rotating disk and a rod that was connected to the disk with strong friction and gears. It was found that the GMD in parallel with a damper was more effective in reducing the lateral displacement of the system subjected to long-period ground motions. The GMD was also examined through a series of tests and its potential to enhance the seismic performance of structures was further demonstrated [44]. Hwang et al. [45] proposed an IMD, dubbed rotational inertia viscous damper (RIVD), in which a ball screw was utilized to transform the inter-storey drift into the rotation of a flywheel immersed in the viscous fluid. Numerical results demonstrated that the proposed RIVD was an effective control device and its efficiency highly depended on the lead of ball screw. Lu et al. [46] developed a viscous inertial mass damper (VIMD) for vibration control, in which the ball screw was applied as well. It was found that the VIMD had properties similar to negative-stiffness dampers and could achieve the modal damping ratio nearly an order of magnitude larger than that of the conventional linear viscous damper. Similar conclusions were also drawn in Ref. [47], in which the dynamic characteristics of stay cables with IMDs were investigated. Ikago et al. [48, 49] developed a tuned viscous mass damper

(TVMD) by using a spring to connect an IMD to a structure, and performed shaking table tests to verify its control effectiveness. Different from conventional IMDs, the proposed TVMD should be tuned close to the fundamental period of the primary structure. It was observed that the developed TVMD outperformed the conventional viscous damper and IMD with the same damping coefficient. Notably, the TVMD has been commercially incorporated into a building in Japan [50], and on-site photos are shown in Figure 1-20.

(a) (b)

Figure 1-20 On-site photos of TVMD in Ref. [51]

By combining the TVMD and electromagnetic transducer, Asai et al. [52] proposed a tuned inertial mass electromagnetic transducer (TIMET) for both the vibration control and energy harvesting, and verified its control performance through experiments and numerical simulations. The results demonstrated that the TIMET could not only effectively reduce seismic-induced responses but also efficiently harvest the vibration energy [53-55]. Later on, Nakamura et al. [56] integrated the IMD and electromagnetic damper together for developing an electromagnetic inertial mass damper (EIMD), and a mechanical model was proposed to predict the behaviors of the EIMD. Analytical and experimental results indicated that the developed EIMD was capable of generating a large inertial force by rotating the flywheel and a controllable damping force by the electric generator. Zhu et al. [57] extended the work of Nakamura et al. [56] by adding an energy harvesting circuit (EHC) into the EIMD for vibration control and energy harvesting simultaneously, derived a more accurate mechanical model to capture its nonlinear behavior, and then performed dynamic tests to validate the proposed model. Due to the performance benefits, EIMDs were also utilized to reduce the vibrations of cables and good control performances were observed [58-60]. Furthermore, Makris and Kampas [61] proposed a clutching inerter damper (CID) consisting of an IMD and a clutch, to avoid the energy stored by the inerter transferring back to the superstructure. By doing so, the moving rack in the CID can drive the pinion-gearwheel, but not vice versa. Due to this unique characteristic, the CID has been utilized in the seismic protection of SDOF structure [62], multi-storey steel structure [63] as well as rocking structures [64], and good control effectiveness was demonstrated. For controlling the seismic responses of adjacent buildings,

Basili et al. [65] proposed a spring-dashpot-inerter system (SDIS) consisting of an IMD in parallel with a spring. Control effectiveness of the proposed connection in reducing the seismic responses of adjacent buildings was investigated, and corresponding analytical solutions were derived [66, 67]. The results demonstrated that the proposed spring-dashpot-inerter connection was beneficial for the seismic control of adjacent buildings by properly selecting the connection parameters. However, the soil-structure interaction (SSI) effect was not considered in Refs [65-67]. To this end, Zhao et al. [68] extended the work in Ref. [65] by considering the SSI effect in the theoretical analysis of the adjacent buildings equipped with SDIS. It was found that the SSI effect should be carefully considered for inerter-based adjacent buildings, especially in soft soil conditions.

Besides the IMDs for onshore structures, Ma et al. [69] also developed an inerter-based energy dissipating device under the name of rotational inertia damper (RID) for offshore structures, which primarily consists of a ball screw assembly and a set of turning plates as shown in Figure 1-21. The turning plates of RID immersed in the water could churn the water surrounding the device, which in turn led to a very large damping force due to the fluid resistance. The analytical and experimental results demonstrated that the RID had a superior capacity of dissipating the vibration energy. Recently, the proposed RID was applied to a semi-submersible platform in the shallow sea and demonstrated to be effective in reducing both the heave and pitch motions of the platform [70].

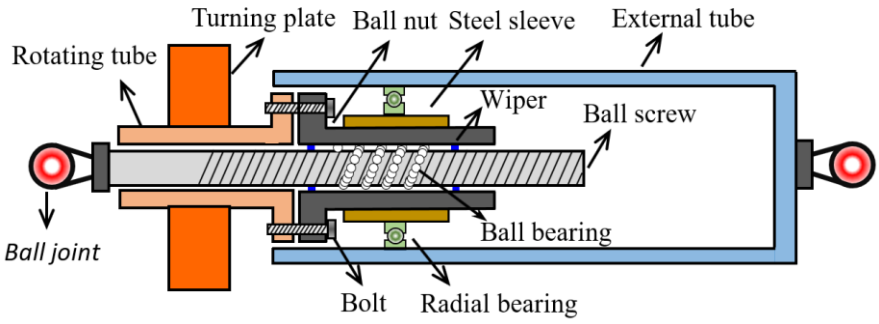

Figure 1-21 Schematic drawing of rotational inertia damper [69]

In order to facilitate the reader's understanding, the name, corresponding reference and model of some representative inerter-based energy dissipators are summarized in Table 1-1. In this table, the symbol "↗" denotes this term is nonlinear, k and k_0 represent the spring, c_e is the electromechanical coupling coefficient of TIMET, and other parameters have the same meanings as those used above.

Table 1-1 Summary of inerter-based energy dissipators

Name	Abbreviation	Reference	Model
Angular-mass damper	--	Pradono et al. [42]	
Gyro-mass damper	GMD	Saitoh [43]	
Rotational inertia viscous damper	RIVD	Hwang et al. [45]	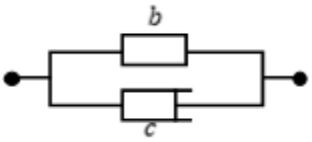
Viscous inertial mass damper	VIMD	Lu et al. [46]	
Electromagnetic inertial mass damper	EIMD	Nakamura et al. [56]	
Rotational inertia damper	RID	Ma et al. [69]	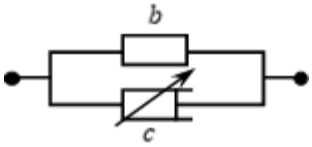
Clutching inerter damper	CID	Makris and Kampas [61]	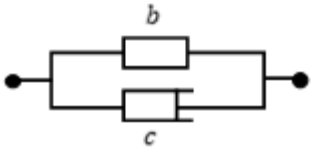
Tuned viscous mass damper	TVMD	Ikago et al. [48, 49]	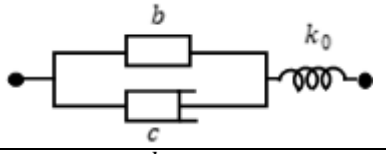
Tuned inertial mass electromagnetic transducer	TIMET	Asai et al. [52]	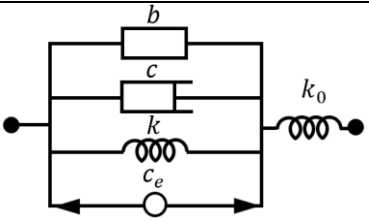
Spring-dashpot-inerter system	SDIS	Basili et al. [65]	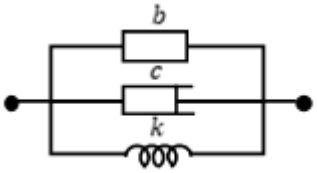

1.5.2 Inerter-based Dynamic Vibration Absorbers

As indicated in Section 1.2.2, the control effectiveness of conventional DVA highly depends on the mass ratio between the physical masses of the secondary and host structures, and a large secondary mass is generally required for realizing the desired control performance. However, a large secondary mass prevents the practical applications of DVA since it can sacrifice the valuable space and increase the construction cost. The inerter is a two-terminal mechanical element with the negative stiffness and mass amplification effects, which offers possibilities to either improve the control effectiveness or reduce the secondary mass of DVAs.

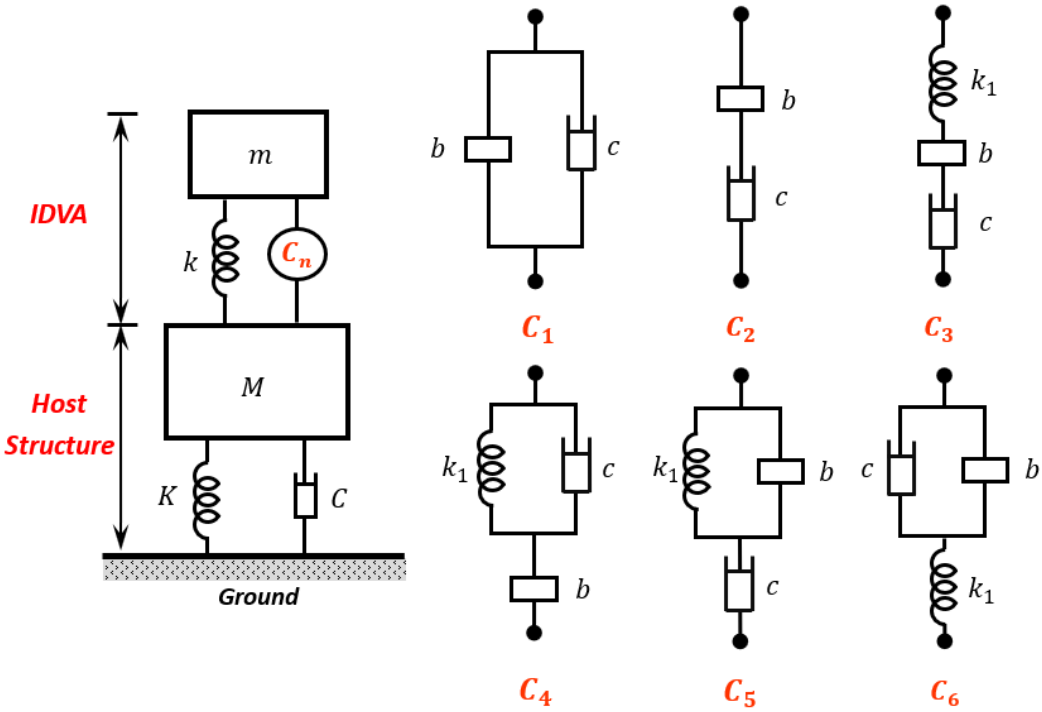

Figure 1-22 Six configuration of IDVA investigated in Ref. [71]

In this regard, the inerter was firstly utilized to upgrade the conventional configuration of DVA only consisting of a spring and a dashpot. As shown in Figure 1-22, Hu and Chen [71] proposed six configurations for inerter-based dynamic vibration absorbers (IDVAs) based on different arrangements between spring, damper and inerter, and investigated their H_2 and H_∞ performances. In this figure, C_n denotes the different configurations, and M, K and C are respectively the mass, stiffness and damping coefficient of the host structure while m, k, k_1, c and b are the tuned mass, primary stiffness, secondary stiffness, damping coefficient and inertance of IDVA, respectively. It was observed that the IDVAs with the configurations C3, C4, C5 and C6 performed better than the traditional DVA. However, the IDVAs with the configurations C1 and C2 provided no improvement for the H_∞ performance and negligible improvement for the H_2 performance. After identifying the beneficial configurations, Hu et al. [72] investigated the control effectiveness of IDVA in reducing the vibration of a floating

offshore wind turbine (FOWT) under the combination of wind and wave loadings. Numerical results demonstrated that the IDVA could enhance the overall performance of FOWT but tended to require more working space than the traditional DVA. Ma et al. [23] proposed a tuned heave plate inerter (THPI) for the heave motion mitigation of a semi-submersible plate (SSP) subjected to wave loading, in which the most effective configuration C6 in Figure 1-22 was adopted. It was found that the proposed THPI was more effective in reducing the heave motion of SSP as compared to the conventional control methods, i.e. fixed heave plate (FHP) and tuned heave plate (THP). Xu et al. [73] applied the IDVA to control the vortex-induced vibration of a long-span bridge and compared the control effectiveness of four configurations (i.e. C1, C2, C3 and C4 in Figure 1-22). Their results demonstrated that the configurations C3 and C4 were more efficient than the traditional TMD, and the configuration C1 could significantly reduce the static deformation of spring and stroke of the tuned mass although it increased the reaction force. Brzeski et al. [74, 75] developed a novel IDVA with changeable inertance and examined its control effectiveness through both the numerical and experimental studies. It was found that the developed IDVA could provide considerable damping efficiency over a wide range of exciting frequencies. Besides exploring beneficial configurations, Pan et al. [76, 77] developed a simple method for designing the IDVAs with different configurations and demonstrated its effectiveness based on case studies.

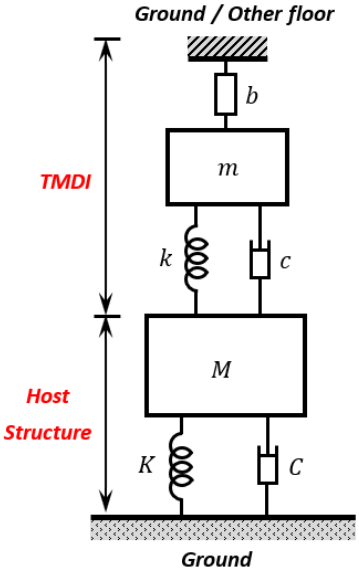

Figure 1-23 Host structure coupled with a TMDI

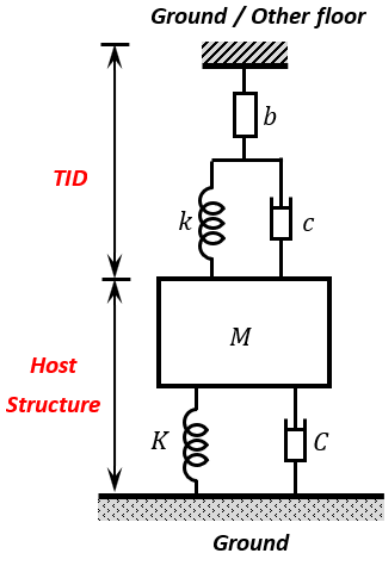

Figure 1-24 Host structure coupled with a TID

The inerter also shows high potential in reducing the secondary mass of DVAs. In this aspect, the concept of tuned mass damper inerter (TMDI) initially proposed by Marian and Giaralis [78] has attracted a lot of attentions. Figure 1-23 shows the schematic drawing of a single-degree-of-freedom (SDOF) structure incorporating a TMDI. As shown, the TMDI is achieved by connecting the tuned mass m via the inerter b to either the ground or a position different

from the one the TMD is already attached. It should be noted that this configuration is quite different from those in Figure 1-22, where the inerter is deployed between the TMD mass and the host structure. In Ref. [78], the TMDI was utilized to mitigate the oscillatory motion of chain-like systems under stochastic ground motions. It was observed that the TMDI could either reduce the secondary mass or improve the performance of the TMD for a given tuned mass. A lot of research efforts were then devoted to the optimal design of TMDI, in which the TMDI was optimized based on different criteria, such as the risk [79], reliability [80], energy [81] and multiple objectives [82, 83].

Besides the applications in the seismic protection, the TMDI was also utilized to mitigate the wind-induced vibrations of structures. The control effectiveness of the TMDI with different topologies to suppress the excessive wind-induced vibrations of a 74-storey building was investigated in Refs. [84, 85]. It was found that the TMDI performed better than the TMD with the same mass ratio in reducing the peak top-floor acceleration, and could be more effective by satisfying two conditions: (1) smaller attached mass; (2) the inerter spans more stories in connecting the attached mass to the host structure. Xu et al. [86] and Dai et al. [87, 88] investigated the control effectiveness of TMDI in reducing the vortex-induced vibration of bridges. They found that the TMDI could not only effectively suppress the VIV of bridges but also reduce the static stretching and stroke of the tuned mass in the system. Recently, the application of TMDI was extended to offshore structures, e.g. using the TMDI for the passive vibration control of FOWTs [89] and wind turbine blades [90]. Considering the limited working space in wind turbine towers or blades, the TMDI was believed to be more effective than the conventional TMD since it could significantly reduce the stroke of the tuned mass and thus decrease the requirements on the working space.

Moreover, a TMDI-like IDVA termed as tuned inerter damper (TID) was also proposed by Lazar et al. [91] to reduce the seismic responses of a multi-storey building. Figure 1-24 shows the schematic drawing of TID. As shown, the TID has a similar configuration with the TMDI in Figure 1-23, which can be retrieved as the special case of TMDI for a zero-value tuned mass. In Ref. [91], the authors investigated the possibility of using a TID to replace a conventional TMD system. It was concluded that the TID's performance highly depends on the installation location, and a grounded TID is more efficient and can realize almost the identical performance as the TMD system. However, the TID was more attractive due to its small mass and overall size. Recognizing the performance benefits, the TID was then used to reduce the vibrations of various structures including the beam [92], cables [26, 93], and multi-storey buildings [94, 95], as well as improve the power generation performance of wave energy converters (WECs) [96].

Furthermore, an electromagnetic tuned inerter damper (E-TID) was also developed by introducing an electromagnetic transducer into the TID [32, 97] such that the functions of

vibration control and energy harvesting could be realized simultaneously. To more effectively control vibrations, multiple TMDIs/TIDs were also proposed as an extension of the multiple tuned mass damper (MTMD) which has been proven to be an effective and robust strategy for multi-mode vibration control [98-100]. By using two or more TMDIs/TIDs, two obvious merits can be obtained: (1) multiple TMDIs/TIDs would be more practical since the additional mass of each TMDI/TID is much smaller than that of single TMDI/TID; (2) multiple TMDIs/TIDs would be more effective and robust than single TMDI/TID. This is because multiple TMDIs/TIDs could control higher vibration modes while single TMDI/TID can only control the fundamental vibration mode of structure. The results demonstrated that MTMDI/MTID was more effective than single TMDI/TID in reducing the structural vibrations, and could provide a high damping effect to multiple vibration modes [101-106].

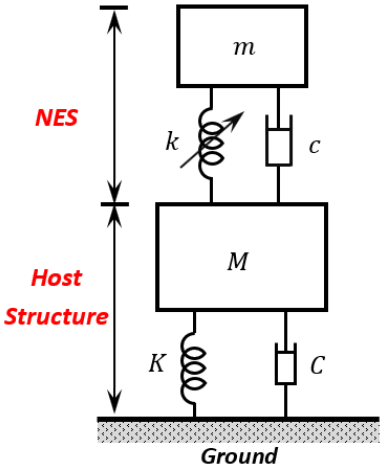

Figure 1-25 Host structure coupled with a conventional NES

Besides the applications to the linear DVAs (e.g. the TMDI and TID), the inerter was also applied to improve the performance of nonlinear energy sink (NES), which consists of an additional mass m attached to the host structure via a linear dashpot c and a nonlinear spring with cubic stiffness k (see Figure 1-25). Due to the inclusion of the nonlinear spring, the NES has two attractive advantages over linear DVAs: (1) the energy transferred from the structure to the NES is one-way and irreversible; (2) the NES has a wider effective frequency range [107-109]. However, the practical applications of NES are also penalized by the need to add a large additional mass [110]. To this end, Javidialesaadi and Wierschem [111] proposed a nonlinear energy sink-inerter (NESI) for the passive vibration control by introducing an inerter into the traditional NES. As shown in Figure 1-26, the inerter element is deployed between the fixed point and additional mass. In Ref. [111], the vibration suppression performance of NESI was evaluated. It was demonstrated that the NESI could provide more effective vibration control performance without increasing its additional mass. Moreover, Zhang et al. [112] also proposed an inertial NES for vibration suppression. The inertial NES is similar to the NESI

proposed in Ref. [111], and the only difference is that the inertial NES does not have an additional mass as shown in Figure 1-26. In other words, the inertial NES can be considered as the special case of the NESI for a zero-value of the additional mass. The results showed that inertial NES has higher vibration control performance and much smaller additional mass than the "ordinary" NES. Recently, the inertial NES was also adopted to eliminate the multimode resonances of a composite plate, and good control performances were found for both the low-order and high-order resonances by using a tiny additional mass [113]. Furthermore, Zhang et al. [114] developed another NES-inerter, in which the inerter is deployed between the additional mass and host structure as shown in Figure 1-27. It was demonstrated that the NES-inerter could mitigate vibration more effectively than a traditional NES in terms of both the energy absorption and amplitude-frequency responses.

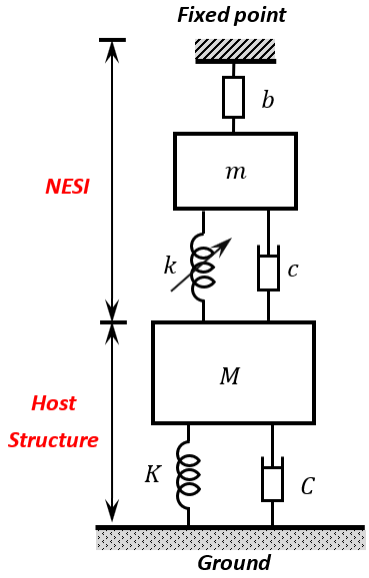

Figure 1-26 Host structure coupled with NESI proposed in Ref. [111]

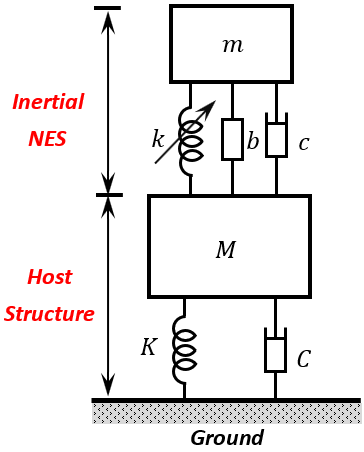

Figure 1-27 Host structure coupled with NES-inerter proposed in Ref. [114]

Very recently, the inerter was also introduced into another classical DVA, i.e. TLD. Zhao et al. [115] proposed a tuned liquid inerter system (TLIS) as shown in Figure 1-28 and performed stochastic analyses to investigate its control performance. Their results demonstrated that the TLIS was more effective in mitigating the structural responses (including the acceleration and displacement) as compared to the traditional TLD with the same liquid mass. Besides the TLD, the inerter was also applied to tuned liquid column damper (TLCD), which is a special variant of TLD consisting of a U-shaped container partially filled with liquid. In this aspect, a tuned liquid column damper-inerter (TLCDI) was developed by connecting the liquid column to the ground via an inerter in Ref. [116]. Similar to the TLIS proposed in Ref. [115], the TLCDI also outperformed the conventional TLCDI in reducing the seismic-induced responses of structures. The performance benefits acquired in Refs. [115, 116] are attributed to that the grounded inerter can significantly increase the effective mass ratio of TLD or TLCD, and thus

enhance the control effectiveness. Notably, this configuration (the TLD/TLCD with a grounded inerter) may be impractical for high-rise buildings due to its complexity and cost. To this end, Wang et al. [117] proposed a new configuration of TLCDI for the seismic response control of adjacent high-rise buildings. Specifically speaking, the TLCDI was integrated into the corridor between two adjacent high-rise buildings. Significant reduction ratios were achieved for the peak acceleration responses of both the buildings. However, the authors also pointed out that the TLCDI failed to effectively control the inter-storey drift ratios of buildings.

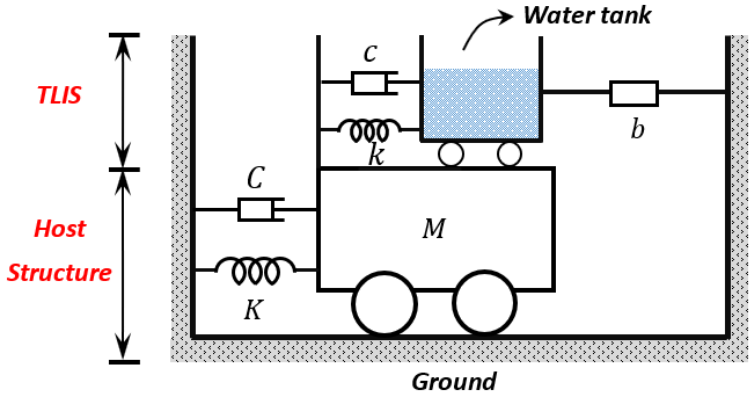

Figure 1-28 Schematic drawing of tuned liquid inerter system (TLIS) proposed in Ref. [115]

All the above theoretical studies rely largely on the assumption that the inerter behaves as an ideal linear mechanical element. However, this assumption might not be realistic since it has been demonstrated in Section 1.4 that the inerter has various inevitable nonlinearities, including the viscous damping, dry friction and backlash (play), etc. For this reason, Gonzalez-Beluga et al. [118] performed experimental and numerical studies to investigate the impact of the nonlinearities on the performance of TID. In Ref. [118], an off-shelf ball screw inerter was tested through harmonic excitations, and it was found that a simple nonlinear model only considering the dry friction can reasonably capture the behavior of inerter. Finally, they concluded that the nonlinearities could affect the behavior of TID, but this effect is not dramatic. Similar results were also observed in Ref. [119], in which three nonlinearities, i.e. the viscous damping, dry friction and play, were considered. The results showed that the effects introduced by the viscous damping and dry friction are quantitatively comparable while the play does not have a macroscopic influence on the dynamics of system. Table 1-2 summarizes the name, corresponding reference and model of different inerter-based vibration absorbers.

Table 1-2 Summary of inerter-based dynamic vibration absorbers

Name	Abbreviation	Reference	Model
Inerter-based dynamic vibration absorber	IDVA	Hu and Chen [71]	Refer to Figure 1-22
Tuned mass damper inerter	TMDI	Marian and Giaralis [78]	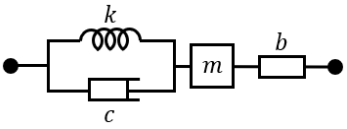
Tuned inerter damper	TID	Lazar et al. [91]	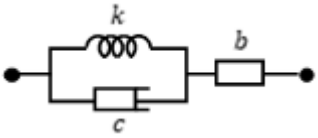
Rotational inertia double tuned mass damper	RIDTMD	Garrido et al. [120]	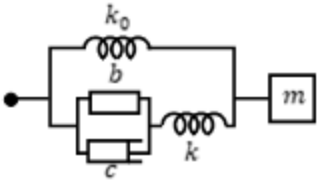
Tuned heave plate inerter	THPI	Ma et al. [23]	
Nonlinear energy sink inerter	NESI	Javidialesaadi and Wierschem [111]	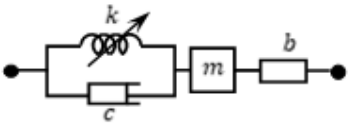
		Zhang et al. [114]	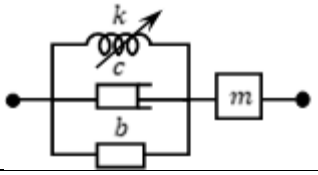
Tuned liquid inerter system	TLIS	Zhao et al. [115]	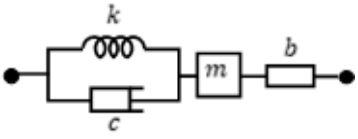
Tuned liquid column damper-inerter	TLCDI	Wang et al. [116]	

1.5.3 Inerter-based Vibration Isolators

In the past two decades, the inerter was also extensively applied in the field of vibration isolation, and many inerter-based vibration isolators were proposed and developed. In this subsection, these inerter-based vibration isolators will be reviewed in detail. It should be noted

that the applications of inerter in automotive engineering will also be presented in this subsection due to the following considerations: (1) the working mechanisms of automotive suspension and vibration isolators are almost the same, i.e. reducing the transmission of undesired vibration energy; (2) the inerter origins from the automotive engineering and has been commercially applied in automotive suspensions (e.g. the inerter shock developed by Penske). A review of the applications in automotive engineering would be beneficial for readers to comprehensively understand the evolution of inerter although this paper focuses on the structural vibration control in civil engineering.

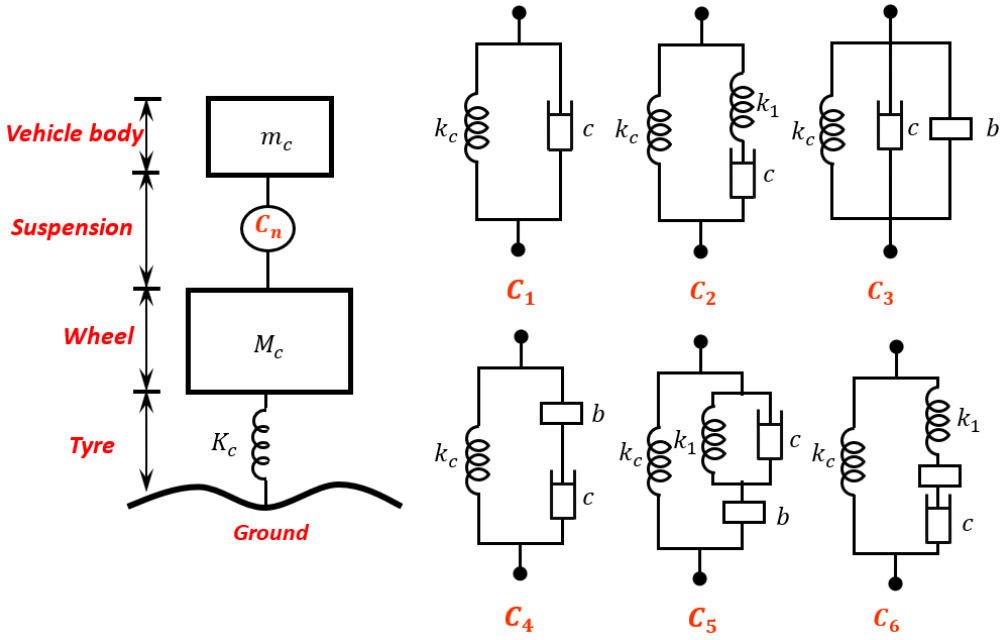

Figure 1-29 Quarter-car model and inerter-based suspension struts investigated in Ref. [121]

After the birth of inerter in 2002, the application potential of inerter in automotive suspensions was firstly noticed by researchers. In the past two decades, a variety of inerter-based suspension struts employing inerters as well as springs and dampers have been designed and evaluated in terms of multiple performance measures including the ride comfort, tire grip and suspension deflection, etc. [122-124] Figure 1-29 shows the quarter-car model and inerter-based suspension struts investigated in Ref. [121], in which six suspension configurations are considered, and C1 and C2 are the traditional suspension struts without inerter. In this figure, M_c, m_c and K_c respectively represent the wheel mass, vehicle mass and stiffness of tyre, and k_c is the suspension stiffness. Corresponding analytical solutions for the optimal performances of these inerter-based passive suspensions in Figure 1-29 were derived in Refs. [121, 125]. The results in these studies demonstrated that the suspensions with inerter (i.e. C3, C4, C5 and C6 in Figure 1-29) could improve the mixed performance of ride comfort and tyre grip but reduce the suspension deflection performance simultaneously. In the above analytical studies, the inerter was considered as an ideal mechanical element without considering the influence

of nonlinearities as mentioned in Section 1.4.2. For a comprehensive performance evaluation, the impact of nonlinearities on the performance of inerter-based suspensions was further investigated in Refs. [34, 126]. It was concluded that the overall performance of the suspension system employing inerter still outperformed the traditional ones although the performance benefits could be slightly degraded by inerter nonlinearities. Due to its performance benefits, the inerter has been commercially applied in the suspension strut of Formula One racing cars in 2005 [127], and extended to other aspects in automotive engineering, such as the motor steering systems [128, 129], train suspensions [130-132] as well as vehicle seat suspensions [133, 134].

In automotive engineering, most studies focus on searching for beneficial inerter-based configurations to further improve the suspension performances. This idea is also well developed in civil engineering, and many inerter-based configurations were proposed for vibration isolators. In Ref. [135], Hu et al. proposed five inerter-based isolation configurations and derived corresponding analytical solutions. Their results demonstrated that these inerter-based isolators outperformed the traditional isolator in terms of both the H_2 and H_∞ performances when the same inertance-to-mass (or mass) ratio was adopted. Among these configurations, the parallel-inerter isolator shown in Figure 1-30 was more attractive since it could widen the effective frequency band and improve the isolation performance at a specific frequency range. It should be noted that K_i and C_i are the spring stiffness and damping coefficient of vibration isolator, respectively. The same conclusion was also drawn in Refs. [136, 137] when a parallel-inerter isolator was applied. These performance benefits can be attributed to the fact that the inerter in this configuration can reduce the natural frequency of the receiving body due to its negative stiffness effect. Recognizing the benefits, Ma et al. [138] applied a parallel-inerter isolator (called inerter-based vibration isolation system, IVIS) to a semi-submersible platform (SSP) with the aim of reducing the wave-induced vibration of deck and vibration-sensitivity apparatuses. It was found that, compared to the traditional isolator, the proposed IVIS was more effective in reducing the heave motion of the receiving body and had a wider effective frequency band. More importantly, the practicality of IVIS was more attractive since it was capable of achieving the best isolating performance by adjusting the inertance rather than changing the spring stiffness and damping coefficient under different wave conditions. It should be noted that the inerter with changeable inertance is technologically feasible, and has been developed in the previous studies [139, 140]. Moreover, the parallel-inerter isolator was also used to reduce the sloshing of cylindrical tanks subjected to ground motions and the analytical solution for its optimal design was also derived [141, 142]. It was demonstrated that the parallel-inerter isolator not only effectively reduced the sloshing height response but also suppressed the base shear force and isolation displacement.

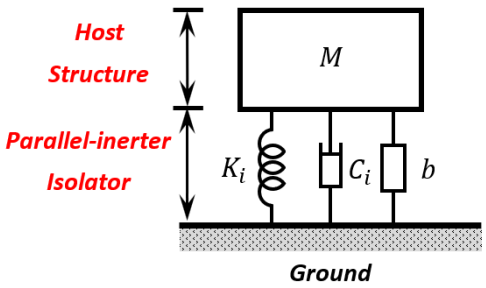

Figure 1-30 Parallel-inerter vibration isolator

As mentioned in Section 1.2.3, the BIS is a conventional vibration isolator in civil engineering, which has been increasingly adopted to suppress the excessive responses of structures subjected to ground motions. However, the lateral displacement demand of BIS may be large due to the following facts: (1) the BIS could lengthen the period of the host structure, which might in turn significantly increase the lateral displacement of BIS due to the resonance effects [143]; (2) BIS is more flexible than the above host structure, and most of seismic-induced displacement demand would thus be absorbed by BIS. A large lateral displacement demand would result in more difficulties for the design and application of BIS. It is therefore imperative to effectively reduce the lateral displacement responses of BIS. To this end, some inerter-based BISs were developed as shown in Figure 1-31 by combining the traditional BIS with IMDs, such as the "angular-mass" inertial damper [42] and GMD [43] mentioned in Section 1.5.1. By such incorporation, the seismic-induced lateral displacement response of BIS could be effectively suppressed.

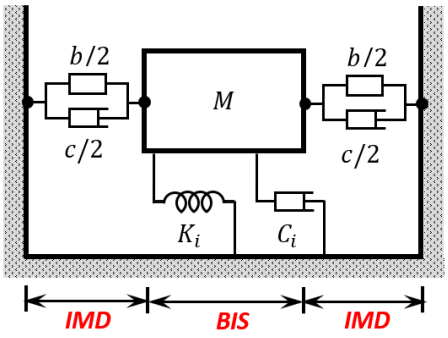

Figure 1-31 Schematic drawing of BIS with IMDs

Another approach for reducing the lateral displacement is introducing a DVA (e.g. TMD) into BIS, i.e. constituting a BIS-TMD system. The control effectiveness of BIS-TMD system in reducing the lateral displacement responses has been well demonstrated in the previous studies [144-146]. However, the inherent drawbacks of BIS-TMD are also evident: (1) as mentioned above, the performance of TMD is highly dependent on its tuned mass. Generally speaking, a larger tuned mass is required for more superior control effectiveness; (2) the displacement of tuned mass in BIS-TMD can be as large as 2 to 4 times of that of the isolation layer [147]. A large clearance is inevitably required to avoid possible collisions between the tuned mass and

foundation or structures. To address the above concerns, some researchers [148-152] proposed a novel BIS employed with TMDI as shown in Figure 1-32, in which the inerter is placed between the tuned mass block and ground. By such a design, the inerter can significantly enhance the effective inertial property of TMD because of its mass amplification effect. Numerical and experimental results showed that the optimized BIS-TMDI system could result in obvious performance improvements in terms not only of the lateral displacement of BIS but also of seismic responses of the isolated host structures by adding a limited physical mass. Moreover, as the special case of the TMDI for a zero-value of tuned mass, the TID was also introduced into the BIS (i.e. forming the BIS-TID system) and significant performance improvements were observed as well [153, 154]. It should be noted that the aforementioned studies were performed based on the assumption of a fixed base, i.e. ignoring the influence of soil-structure interaction (SSI) effect. However, this assumption is valid only when structures are built on rocks or firm soil with high stiffness. For this reason, the influence of soil conditions on the performance of inerter-based BIS was comprehensively evaluated in Refs. [155-158]. It was found that the SSI effect should be carefully considered for the structure equipped with inerter-based BIS, especially on flexible soil. Besides the applications in civil engineering, the inerter-based vibration isolator was also found to have application potentials in preserving cultural heritage structures in recent years. For example, Siami et al. [159] updated the isolation system of the famous statue of Michelangelo Buonarroti Pietà Rondanini by introducing the TMDI. The numerical results proved a significant reduction in the transmitted vibration to the statue due to the presence of the optimal TMDI, without imposing a large amount of mass or modification to the isolator.

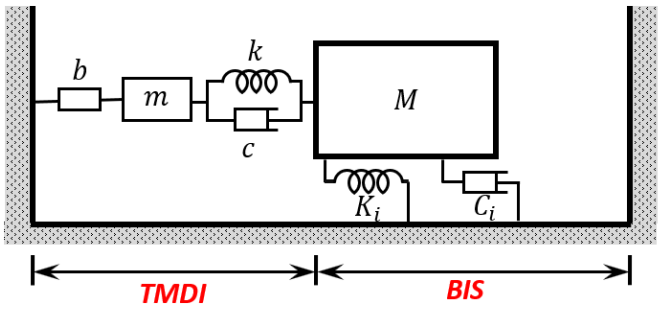

Figure 1-32 Schematic drawing of BIS with TMDI

Notably, all the above inerter-based vibration isolators adopted linear configurations of inerter, and some nonlinear vibration isolators were also proposed by either using geometrically nonlinear inerter (e.g. Refs. [160-162]) or incorporating a linear inerter into a quasi-zero stiffness (QZS) vibration isolator (e.g. Refs. [163, 164]). Figure 1-33 shows the schematic drawing of a typical nonlinear inerter-based isolator with geometrically nonlinear inerters. As shown, the key component of this geometric configuration is two hinged inerter elements, and the mass block M can thus move in a two-dimension (2D) plane. The results demonstrated that

vibration isolators with geometrically nonlinear inerter have performance benefits at higher frequencies as compared to conventional isolators. Figure 1-34 shows the schematic drawing of an inerter-based quasi-zero stiffness (IQZS) vibration isolator developed based on a diamond-shaped structure [164]. In this figure, k_v and k_h are the stiffnesses of the vertical and horizontal springs, respectively. The IQZS vibration isolator was found to possess several performance improvements over the traditional QZS vibration isolator, i.e. smaller displacement amplitude and force transmissibility peaks, wider isolation frequency band, and faster high-frequency force transmissibility attenuation rate. Very recently, the inerter was also applied for meta-structures, e.g., the meta-barriers for redirecting surface waves back into the ground, and the meta-foundations for counteracting the effects of seismic waves [165]. In this aspect, Cacciola et al. [166] incorporated a grounded inerter into a vibrating barrier (ViBa) as a mass/inertial amplifier to enhance the efficiency and applicability of conventional ViBas. It was found that a higher inertance in conjunction with sufficiently rigid inerter-to-ground connection could produce a higher weight reduction. Moreover, Sun et al. [167] proposed a novel configuration of a locally resonant periodic foundation (LRPF) by introducing the aforementioned TID into the meta-foundation of fuel storage tanks, as shown in Figure 1-35. The numerical results demonstrated that the optimal TID-equipped LRPF was more effective and robust in reducing the seismic responses of fuel storage tanks as compared to the conventional LRPF. Similarly, Table 1-3 summarizes the name, corresponding reference and model of different inerter-based vibration isolators.

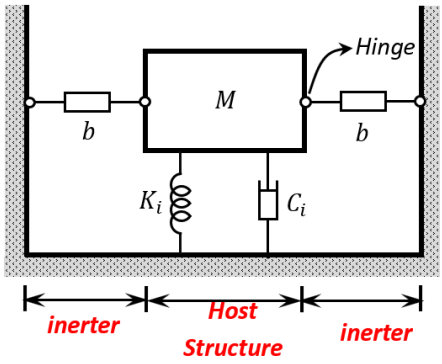

Figure 1-33 Schematic drawing of nonlinear inerter-based isolator with geometrically nonlinear inerters (after [160])

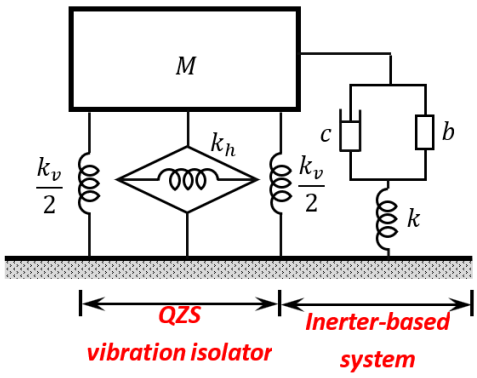

Figure 1-34 Schematic drawing of inerter-based quasi-zero stiffness (IQZS) (after [164])

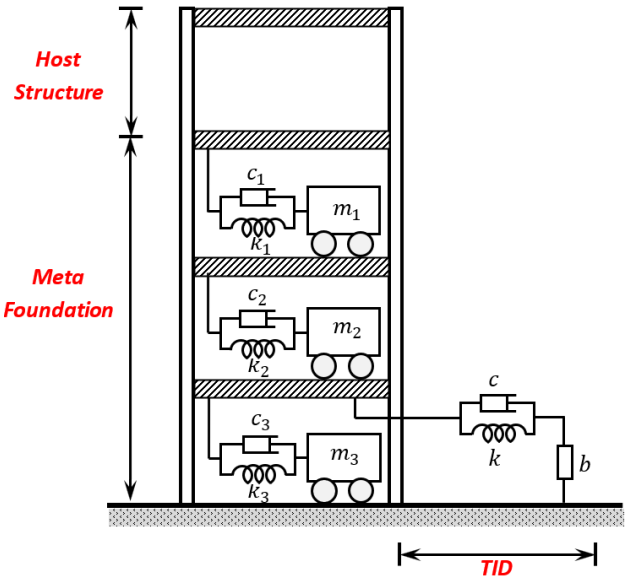

Figure 1-35 Schematic drawing of TID-equipped LRPFs (after [167])

Table 1-3 Summary of inerter-based vibration isolators

Name	Abbreviation	Reference	Model
Inerter-based isolators	--	Hu et al. [135]	Refer to Figure 1-29
Inerter-based vibration isolation system	IVIS	Ma et al. [138]	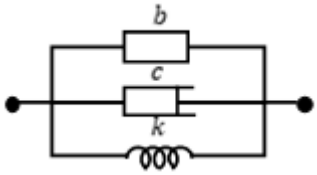
Friction pendulum inerter system	FPIS	Zhao et al. [154]	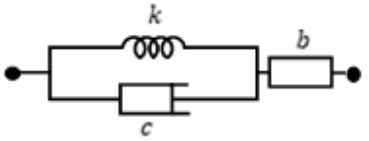 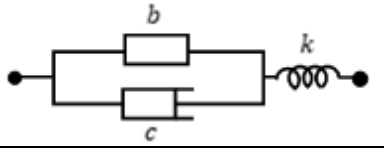
Base isolation system-inertial mass damper	BIS-IMD	Saitoh [43]	Refer to Figure 1-31
Base isolation system-tuned mass damper inerter	BIS-TMDI	Domenico et al. [148]	Refer to Figure 1-32

Inerter-equipped vibrating barrier	IViba	Cacciola et al. [166]	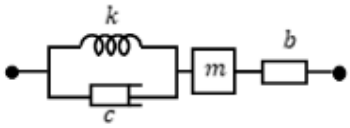
Inerter-based nonlinear vibration isolators	--	Moraes et al. [160]	Refer to Figure 1-33
		Wang et al. [164]	Refer to Figure 1-34
Locally resonant periodic foundation-tuned inerter damper	LRPF-TID	Sun et al. [167]	Refer to Figure 1-35

1.6 Discussions

In this paper, an attempt has been made to introduce and summarize the extensive applications of inerter-based devices in the passive structural vibration control. Evidently, significant strides were made in the past two decades especially in the recent five years, and many inerter-based energy dissipators, DVAs, and vibration isolators have been proposed with multifarious names. However, previous studies also indicated some problems of these devices, which deserve further investigations:

(1) In some previous studies (e.g. Refs. [23, 71-73]), different types of IDVAs were proposed by replacing the damper element in the conventional DVA with different inerter-based configurations consisting of different combinations of spring, damper and inerter. Some configurations were demonstrated to be effective in improving both the H_∞ and H_2 performances of conventional DVAs. However, the performance improvements of these IDVAs are not significant compared to the conventional DVAs, and the H_2 performance improvement is only about 10% in some cases (e.g. Ref. [71]). On the other hand, the introduction of inerter obviously increases the complexity and cost of the control system. The IDVAs therefore may not be regarded to fully outperform conventional DVAs in terms of control effectiveness against construction costs.

(2) Some previous studies (e.g. Refs. [86-90]) demonstrated that the TMDI/TID had better control performance and stroke reduction than conventional TMD especially when the end of inerter is connected to the ground. However, it should be noted that, it might be difficult and infeasible to implement a grounded inerter for some structures, e.g.

high-rise buildings and bridges. To address this concern, some researchers proposed connecting the inerter-based device to a position different from the one where the TMD is attached, e.g. other floors in high-rise buildings (e.g. Refs. [84, 85]). This scheme has been demonstrated to be effective, however, it also raises some concerns about its feasibility since it requires a very strong connecting system to connect different floors. From this perspective, the TMDI/TID system seems to be more suitable for low-rise structures (e.g. BIS), and its applications in high-rise structures and bridges deserve further discussions.

(3) Some IMDs have been developed by utilizing the negative stiffness effect of inerter. However, the negative stiffness produced by an inerter is not a constant, but proportional to the square of excitation frequency ω^2 (e.g. Ref. [168]). Consequently, the control force of IMD would increase rapidly with the increment of excitation frequency ω. This large control force, on the other hand, may cause local damage to the structure or connecting components. Because of this fact, some previous studies (e.g. Ref. [168]) clearly indicated that the inertial force of IMD is dominant at high frequencies and could amplify the high-frequency responses of the system. Therefore, the optimal design of IMD should consider multiple performance indices, e.g. low-frequency responses, high-frequency responses, and control force, etc.

(4) Previous studies on inerter-based vibration control systems mainly focused on the analytical part, the experimental studies are however relatively limited. For an in-depth understandings on the performances of inerters, more laboratory tests are necessary. Additionally, practical applications of inerter-based control systems are rarely reported. Developing effective, affordable and applicable inerter-based control systems is another significant yet challenging task.

(5) Most previous studies took the inerter as an ideal mechanical element, the studies on its nonlinearities are relatively less. Moreover, the developed inerter-based vibration control systems normally did not consider the capacity and fatigue issues of inerter itself (e.g. the ball-screw inerter). Integrating the design of inerter devices into the overall design of control systems thus deserves additional attentions.

1.7 Conclusions

In the last two decades, many inerter-based control systems were developed and applied in structural vibration control. This paper presents a comprehensive overview in this area. In particular, the concept, physical realizations and mechanical models, as well as the

applications in the passive structural vibration control are reviewed. The following conclusions can be drawn:

(1) Inerter is a two-terminal mass element with the mass amplification and negative stiffness effects. Due to these attractive properties, inerter was excessively applied in different vibration control systems, such as energy dissipator, dynamic vibration absorber and vibration isolator.

(2) Inerter could significantly improve the energy dissipation capacity of conventional energy dissipators because of its negative stiffness effect. However, the negative stiffness of inerter increases significantly with the increase of excitation frequencies and is thus possible to cause an excessive damping force at high frequencies. More attentions should be paid to the control performance of IMDs at high frequencies.

(3) Inerter-based dynamic vibration absorbers were developed from two perspectives: (a) inerter was placed between the tuned mass and the host structure to enrich the configuration of traditional DVA. However, the performance enhancement is normally not very evident in this scenario; (b) inerter was also deployed between the tuned mass and ground. This configuration could either reduce the secondary mass or improve the performance of traditional DVA for a given tuned mass. However, it might not be easy to implement a grounded inerter for high-rise structures and bridges. Practical applications deserve more investigations.

(4) In the field of vibration isolation, inerter especially parallel-connected inerter was found to be effective in enhancing the isolation performance of automotive suspensions and vibration isolators. The lateral displacement demand of BIS could be effectively reduced by introducing inerter-based energy dissipators (e.g. IMD) or inerter-based dynamic vibration absorbers (e.g. TMDI/TID). Moreover, inerter was also beneficial for the performance of nonlinear isolators and meta-structures.

1.8 Research Objectives and Outlines

This thesis is compiled by combining the technical papers prepared by the candidate during his PhD study. To make the thesis structure clearer, this subsection introduces the research objectives and outlines of the thesis. It should be noted that this subsection was not included in the journal paper.

The above critical literature review reveals that extensive research efforts have been devoted to developing inerter-based control systems for passive vibration control. However, no previous study explores the feasibility of utilizing inerter-based control systems for offshore SSP vibration control. This thesis carries out comprehensive analytical and experimental

studies to investigate the effectiveness of three inerter-based control systems for offshore SSP vibration control. The research objectives of this thesis include: (1) To propose novel inerter-based dynamic vibration absorber (tuned heave plate inerter, THPI), energy dissipator (rotational inertia damper, RID) and vibration isolator (inerter-based vibration isolation system, IVIS) for offshore SSP vibration control, and to perform analytical studies to investigate the control effectiveness of the proposed methods; (2) To experimentally investigate the mechanical behaviors of the proposed RID system and perform large-scale wave flume tests to further examine the performance of the proposed RID system for offshore SSP vibration control.

To achieve the above research objectives, eight chapters are formed in the thesis. The contents of the seven chapters following this introductory chapter are:

Chapter 2 proposes using a tuned heave plate inerter (THPI) for heave motion mitigation of SSP and analytical studies are performed to investigate its control effectiveness. For comparison, the control effectiveness of the conventional FHP and THP systems are also studied. In addition, parametric studies are performed to investigate the influences of different plate sizes and depths on the control performance.

To further improve the control efficiency of THPI, another inerter-based vibration control system, namely the rotational inertia damper (RID), is proposed in Chapter 3 to control the heave motion. The analytical model of the SSP controlled by the proposed RID system is established, and the equations of motion of the RID controlled system are derived. The control effectiveness is investigated in both frequency and time domains.

As an extension of the study presented in Chapter 3, two RIDs are utilized to simultaneously control the heave and pitch motions of SSP in Chapter 4. Analytical and Simulink models are established to investigate the control effectiveness in the frequency and time domains, respectively. Similarly, the control effectiveness of using two conventional FHPs and THPs to mitigate the simultaneous heave and pitch motions are also studied for comparison.

Chapter 5 performs experimental studies to examine the mechanical behaviors of the proposed RID system. Specifically, a RID prototype was manufactured and systematically tested under a series of harmonic excitations. The influences of different excitation frequencies and amplitudes on the performance of RID are discussed. A precise mechanical model considering inerter nonlinearities is established, with its parameters identified based on the experimental results. Theoretical results predicted by the proposed mechanical model are then compared with the experimental results.

In Chapter 6, large-scale wave flume tests were conducted to further investigate the feasibility and effectiveness of using the RID system in reducing the heave motion of SSP. In particular,

a 1:70 scaled SSP model was manufactured, and the vibration characteristics of the platform were determined firstly through free vibration tests. After that, the bare SSP and the SSP equipped with RID were tested under regular and irregular waves. For comparison, the SSP equipped with the FHP was also tested.

Besides the THPI and RID systems, Chapter 7 develops an inerter-based vibration isolation system (IVIS) for the heave motion mitigation of SSP. The analytical model of a classical SSP equipped with IVIS is established and validated by the experimental results from other researchers. A case study is then carried out to demonstrate the control performance of IVIS in both the frequency and time domains.

Chapter 8 summarizes the conclusions of the thesis, and some recommendations for future research are also suggested in this chapter.

Since this thesis is compiled by combining the technical papers, Chapters 1 to 7 can be read independently, and some repeated contents may exist in different chapters for completeness.

1.9 References

[1] House R. Webster's new universal unabridged dictionary. Barnes & Noble; 1986.

[2] Zuo H, Bi K, Hao H. A state-of-the-art review on the vibration mitigation of wind turbines. Renew Sust Energ Rev. 2020;121:109710.

[3] Smith MC. Synthesis of mechanical networks: the inerter. IEEE Trans Automat Contr. 2002;47:1648-62.

[4] Housner G, Bergman LA, Caughey TK, Chassiakos AG, Claus RO, Masri SF et al. Structural control: past, present, and future. J Eng Mech. 1997;123:897-971.

[5] Soong T, Spencer Jr B. Supplemental energy dissipation: state-of-the-art and state-of-the-practice. Eng Struct. 2002;24:243-59.

[6] Parulekar Y, Reddy G. Passive response control systems for seismic response reduction: A state-of-the-art review. Int J Struct Stab Dyn. 2009;9:151-77.

[7] Lu Z, Wang Z, Zhou Y, Lu X. Nonlinear dissipative devices in structural vibration control: A review. J Sound Vib. 2018;423:18-49.

[8] Xu Z, Guo Y, Zhu J, Xu F. Intelligent Vibration Control in Civil Engineering Structures: Zhejiang University Press; 2016.

[9] Constantinou MC, Symans M. Experimental and analytical investigation of seismic response of structures with supplemental fluid viscous dampers. National Center for earthquake engineering research; 1992.

[10] Yamaguchi H, Harnpornchai N. Fundamental characteristics of multiple tuned mass dampers for suppressing harmonically forced oscillations. Earthq Eng Struct Dyn. 1993;22:51-62.

[11] Li H, Zhang P, Song G, Patil D, Mo Y. Robustness study of the pounding tuned mass damper for vibration control of subsea jumpers. Smart Mater Struct. 2015;24:095001.

[12] Lu Z, Chen X, Zhou Y. An equivalent method for optimization of particle tuned mass damper based on experimental parametric study. J Sound Vib. 2018;419:571-84.

[13] Tian L, Liu J, Qiu C, Rong K. Temperature effect on seismic behavior of transmission tower-line system equipped with SMA-TMD. Smart Struct Syst. 2019;24:1-14.

[14] Gerges RR, Vickery BJ. Wind tunnel study of the across-wind response of a slender tower with a nonlinear tuned mass damper. J Wind Eng Ind Aerodyn. 2003;91:1069-92.

[15] Starosvetsky Y, Gendelman O. Vibration absorption in systems with a nonlinear energy sink: nonlinear damping. J Sound Vib. 2009;324:916-39.

[16] Fujino Y, Sun L, Pacheco BM, Chaiseri P. Tuned liquid damper (TLD) for suppressing horizontal motion of structures. J Eng Mech. 1992;118:2017-30.

[17] Cimellaro GP, Marasco S. Introduction to Dynamics of Structures and Earthquake Engineering: Springer; 2018.

[18] Ibrahim RA. Recent advances in nonlinear passive vibration isolators. J Sound Vib. 2008;314:371-452.

[19] Harvey Jr PS, Kelly KC. A review of rolling-type seismic isolation: Historical development and future directions. Eng Struct. 2016;125:521-31.

[20] Naeim F, Kelly JM. Design of seismic isolated structures: from theory to practice: John Wiley & Sons; 1999.

[21] Zhou F, Tan P. Recent progress and application on seismic isolation energy dissipation and control for structures in China. Earthq Eng Eng Vib. 2018;17:19-27.

[22] Smith MC. The Inerter: A Retrospective. Annu Rev Control Robot Auton Syst. 2020;3:361-91.

[23] Ma R, Bi K, Hao H. Mitigation of heave response of semi-submersible platform (SSP) using tuned heave plate inerter (THPI). Eng Struct. 2018;177:357-73.

[24] Papageorgiou C, Houghton NE, Smith MC. Experimental testing and analysis of inerter devices. J Dyn Syst Meas Contr. 2009;131:011001.

[25] Li C, Liang M, Wang Y, Dong Y. Vibration suppression using two-terminal flywheel. Part I: Modeling and characterization. J Vib Control. 2012;18:1096-105.

[26] Sun L, Hong D, Chen L. Cables interconnected with tuned inerter damper for vibration mitigation. Eng Struct. 2017;151:57-67.

[27] Wang FC, Hong MF, Lin TC. Designing and testing a hydraulic inerter. J Mech Eng Sci. 2010;225:66-72.

[28] Liu X, Jiang JZ, Titurus B, Harrison A. Model identification methodology for fluid-based inerters. Mech Syst Signal Process. 2018;106:479-94.

[29] De Domenico D, Deastra P, Ricciardi G, Sims ND, Wagg DJ. Novel fluid inerter based tuned mass dampers for optimised structural control of base-isolated buildings. J Franklin Inst. 2019;356:7626-49.

[30] Zhang XL, Gao Q, Nie J. The mem-inerter: A new mechanical element with memory. Adv Mech Eng. 2018;10:168781401877842.

[31] Zhang X, Geng C, Nie J, Gao Q. The missing mem-inerter and extended mem-dashpot found. Nonlinear Dyn. 2020;101:835-56.

[32] Gonzalez-Buelga A, Clare LR, Neild SA, Burrow SG, Inman DJ. An electromagnetic vibration absorber with harvesting and tuning capabilities. Struct Control Health Monit. 2015;22:1359-72.

[33] John EDA, Wagg DJ. Design and testing of a frictionless mechanical inerter device using living-hinges. J Franklin Inst. 2019;356:7650-68.

[34] Wang FC, Su WJ. Impact of inerter nonlinearities on vehicle suspension control. Veh Syst Dyn. 2008;46:575-95.

[35] Nordin M, Galic' J, Gutman PO. New models for backlash and gear play. Int J Adapt Control Signal Process. 1997;11:49-63.

[36] Ma R, Bi K, Hao H. A novel rotational inertia damper for amplifying fluid resistance: Experiment and mechanical model. Mech Syst Signal Process. 2021;149:107313.

[37] Kamalzadeh A, Erkorkmaz K. Accurate tracking controller design for high-speed drives. Int J Mach Tool Manu. 2007;47:1393-400.

[38] Swift SJ, Smith MC, Glover AR, Papageorgiou C, Gartner B, Houghton NE. Design and modelling of a fluid inerter. Int J Control. 2013;86:2035-51.

[39] Soong T. State-of-the-art review: active structural control in civil engineering. Eng Struct. 1988;10:74-84.

[40] Li H, Liu M, Ou J. Negative stiffness characteristics of active and semi-active control systems for stay cables. Struct Control Health Monit. 2008;15:120-42.

[41] Ou J, Li H. Analysis of capability for semi-active or passive damping systems to achieve the performance of active control systems. Struct Control Health Monit. 2010;17:778-94.

[42] Pradono MH, Iemura H, Igarashi A, Kalantari A. Application of angular-mass dampers to base-isolated benchmark building. Struct Control Health Monit. 2008;15:737-45.

[43] Saitoh M. On the performance of gyro-mass devices for displacement mitigation in base isolation systems. Struct Control Health Monit. 2012;19:246-59.

[44] Mirza Hessabi R, Mercan O. Investigations of the application of gyro-mass dampers with various types of supplemental dampers for vibration control of building structures. Eng Struct. 2016;126:174-86.

[45] Hwang J, Kim J, Kim Y. Rotational inertia dampers with toggle bracing for vibration control of a building structure. Eng Struct. 2007;29:1201-8.

[46] Lu L, Duan YF, Spencer BF, Lu X, Zhou Y. Inertial mass damper for mitigating cable vibration. Struct Control Health Monit. 2017;24:e1986.

[47] Shi X, Zhu S. Dynamic characteristics of stay cables with inerter dampers. J Sound Vib. 2018;423:287-305.

[48] Ikago K, Saito K, Inoue N. Seismic control of single-degree-of-freedom structure using tuned viscous mass damper. Earthq Eng Struct Dyn. 2012;41:453-74.

[49] Ikago K, Sugimura Y, Saito K, Inoue N. Modal Response Characteristics of a Multiple-Degree-Of-Freedom Structure Incorporated with Tuned Viscous Mass Dampers. J Asian Archit Build Eng. 2018;11:375-82.

[50] Sugimura Y, Goto W, Tanizawa H, Saito K, Nimomiya T. Response control effect of steel building structure using tuned viscous mass damper. Proceedings of the 15th world conference on earthquake engineering2012. p. 24-8.

[51] R. Zhang, Y Cao, C Pan, Inerter system and its state-of-the-art, Eng. Mech., 36 (2019) 8-27. (In Chinese)

[52] Asai T, Araki Y, Ikago K. Energy harvesting potential of tuned inertial mass electromagnetic transducers. Mech Syst Signal Process. 2017;84:659-72.

[53] Asai T, Watanabe Y. Outrigger tuned inertial mass electromagnetic transducers for high-rise buildings subject to long period earthquakes. Eng Struct. 2017;153:404-10.

[54] Asai T, Araki Y, Ikago K. Structural control with tuned inertial mass electromagnetic transducers. Struct Control Health Monit. 2018;25:e2059.

[55] Sugiura K, Watanabe Y, Asai T, Araki Y, Ikago K. Experimental characterization and performance improvement evaluation of an electromagnetic transducer utilizing a tuned inerter. J Vib Control. 2019;26:56-72.

[56] Nakamura Y, Fukukita A, Tamura K, Yamazaki I, Matsuoka T, Hiramoto K et al. Seismic response control using electromagnetic inertial mass dampers. Earthq Eng Struct Dyn. 2014;43:507-27.

[57] Zhu H, Li Y, Shen W, Zhu S. Mechanical and energy-harvesting model for electromagnetic inertial mass dampers. Mech Syst Signal Process. 2019;120:203-20.

[58] Li Y, Shen W, Zhu H. Vibration mitigation of stay cables using electromagnetic inertial mass dampers: Full-scale experiment and analysis. Eng Struct. 2019;200:109693.

[59] Wang Z, Gao H, Xu Y, Chen Z, Wang H. Impact of cable sag on the efficiency of an inertial mass damper in controlling stay cable vibrations. Smart Struct Syst. 2019;24:83-94.

[60] Wang Z, Xu Y, Gao H, Chen Z, Xu K, Zhao S. Vibration control of a stay cable with a rotary electromagnetic inertial mass damper. Smart Struct Syst. 2019;23:627-39.

[61] Makris N, Kampas G. Seismic Protection of Structures with Supplemental Rotational Inertia. J Eng Mech. 2016;142:04016089.

[62] Wang M, Sun F. Displacement reduction effect and simplified evaluation method for SDOF systems using a clutching inerter damper. Earthq Eng Struct Dyn. 2018;47:1651-72.

[63] Málaga-Chuquitaype C, Menendez-Vicente C, Thiers-Moggia R. Experimental and numerical assessment of the seismic response of steel structures with clutched inerters. Soil Dyn Earthq Eng. 2019;121:200-11.

[64] Thiers-Moggia R, Málaga-Chuquitaype C. Seismic protection of rocking structures with inerters. Earthq Eng Struct Dyn. 2019;48:528-47.

[65] Basili M, De Angelis M, Pietrosanti D. Dynamic response of a viscously damped two adjacent degree of freedom system linked by inerter subjected to base harmonic excitation. Procedia Eng. 2017;199:1586-91.

[66] Basili M, De Angelis M, Pietrosanti D. Modal analysis and dynamic response of two adjacent single-degree-of-freedom systems linked by spring-dashpot-inerter elements. Eng Struct. 2018;174:736-52.

[67] Basili M, De Angelis M, Pietrosanti D. Defective two adjacent single degree of freedom systems linked by spring-dashpot-inerter for vibration control. Eng Struct. 2019;188:480-92.

[68] Zhao Z, Chen Q, Zhang R, Jiang Y, Xia Y. Interaction of Two Adjacent Structures Coupled by Inerter-based System considering Soil Conditions. J Earthq Eng. 2020:1-21.

[69] Ma R, Bi K, Hao H. A novel rotational inertia damper for heave motion suppression of semisubmersible platform in the shallow sea. Struct Control Health Monit. 2019;26:e2368.

[70] Ma R, Bi K, Hao H. Using inerter-based control device to mitigate heave and pitch motions of semi-submersible platform in the shallow sea. Eng Struct. 2020;207:110248.

[71] Hu Y, Chen MZQ. Performance evaluation for inerter-based dynamic vibration absorbers. Int J Mech Sci. 2015;99:297-307.

[72] Hu Y, Wang J, Chen MZQ, Li Z, Sun Y. Load mitigation for a barge-type floating offshore wind turbine via inerter-based passive structural control. Eng Struct. 2018;177:198-209.

[73] Xu K, Bi K, Ge Y, Zhao L, Han Q, Du X. Performance evaluation of inerter-based dampers for vortex-induced vibration control of long-span bridges: A comparative study. Struct Control Health Monit. 2020;27:e2529.

[74] Brzeski P, Lazarek M, Perlikowski P. Experimental study of the novel tuned mass damper with inerter which enables changes of inertance. J Sound Vib. 2017;404:47-57.

[75] Lazarek M, Brzeski P, Perlikowski P. Design and identification of parameters of tuned mass damper with inerter which enables changes of inertance. Mech Mach Theory. 2018;119:161-73.

[76] Pan C, Zhang R. Design of structure with inerter system based on stochastic response mitigation ratio. Struct Control Health Monit. 2018;25:e2169.

[77] Pan C, Zhang R, Luo H, Li C, Shen H. Demand-based optimal design of oscillator with parallel-layout viscous inerter damper. Struct Control Health Monit. 2018;25:e2051.

[78] Marian L, Giaralis A. Optimal design of a novel tuned mass-damper–inerter (TMDI) passive vibration control configuration for stochastically support-excited structural systems. Probabilistic Eng Mech. 2014;38:156-64.

[79] Ruiz R, Taflanidis AA, Giaralis A, Lopez-Garcia D. Risk-informed optimization of the tuned mass-damper-inerter (TMDI) for the seismic protection of multi-storey building structures. Eng Struct. 2018;177:836-50.

[80] Giaralis A, Taflanidis AA. Optimal tuned mass-damper-inerter (TMDI) design for seismically excited MDOF structures with model uncertainties based on reliability criteria. Struct Control Health Monit. 2018;25:e2082.

[81] Pietrosanti D, De Angelis M, Basili M. A generalized 2-DOF model for optimal design of MDOF structures controlled by Tuned Mass Damper Inerter (TMDI). Int J Mech Sci. 2020;185:105849.

[82] Taflanidis AA, Giaralis A, Patsialis D. Multi-objective optimal design of inerter-based vibration absorbers for earthquake protection of multi-storey building structures. J Franklin Inst. 2019;356:7754-84.

[83] Kaveh A, Fahimi Farzam M, Hojat Jalali H. Statistical seismic performance assessment of tuned mass damper inerter. Struct Control Health Monit. 2020;27:e2602.

[84] Giaralis A, Petrini F. Wind-Induced Vibration Mitigation in Tall Buildings Using the Tuned Mass-Damper-Inerter. J Struct Eng. 2017;143:04017127.

[85] Petrini F, Giaralis A, Wang Z. Optimal tuned mass-damper-inerter (TMDI) design in wind-excited tall buildings for occupants' comfort serviceability performance and energy harvesting. Eng Struct. 2020;204:109904.

[86] Xu K, Bi K, Han Q, Li X, Du X. Using tuned mass damper inerter to mitigate vortex-induced vibration of long-span bridges: Analytical study. Eng Struct. 2019;182:101-11.

[87] Dai J, Xu ZD, Gai PP. Tuned mass-damper-inerter control of wind-induced vibration of flexible structures based on inerter location. Eng Struct. 2019;199:109585.

[88] Dai J, Xu Z, Gai P, Hu Z. Optimal design of tuned mass damper inerter with a Maxwell element for mitigating the vortex-induced vibration in bridges. Mech Syst Signal Process. 2021;148:107180.

[89] Sarkar S, Fitzgerald B. Vibration control of spar-type floating offshore wind turbine towers using a tuned mass-damper-inerter. Struct Control Health Monit. 2019;27:e2471.

[90] Zhang Z, Fitzgerald B. Tuned mass-damper-inerter (TMDI) for suppressing edgewise vibrations of wind turbine blades. Eng Struct. 2020;221:110928.

[91] Lazar IF, Neild SA, Wagg DJ. Using an inerter-based device for structural vibration suppression. Earthq Eng Struct Dyn. 2014;43:1129-47.

[92] Jin X, Chen MZQ, Huang Z. Suppressing Random Response of a Regular Structure by an Inerter-Based Dynamic Vibration Absorber. J Vib Acoust. 2019;141:041004.

[93] Lazar IF, Neild SA, Wagg DJ. Vibration suppression of cables using tuned inerter dampers. Eng Struct. 2016;122:62-71.

[94] Shen W, Niyitangamahoro A, Feng Z, Zhu H. Tuned inerter dampers for civil structures subjected to earthquake ground motions: optimum design and seismic performance. Eng Struct. 2019;198:109470.

[95] Krenk S. Resonant inerter based vibration absorbers on flexible structures. J Franklin Inst. 2019;356:7704-30.

[96] Sugiura K, Sawada R, Nemoto Y, Haraguchi R, Asai T. Wave flume testing of an oscillating-body wave energy converter with a tuned inerter. Appl Ocean Res. 2020;98:102127.

[97] Gonzalez-Buelga A, Clare L, Neild S, Jiang J, Inman D. An electromagnetic inerter-based vibration suppression device. Smart Mater Struct. 2015;24:055015.

[98] Igusa T, Xu K. Vibration control using multiple tuned mass dampers. J Sound Vib. 1994;175:491-503.

[99] Zuo H, Bi K, Hao H. Using multiple tuned mass dampers to control offshore wind turbine vibrations under multiple hazards. Eng Struct. 2017;141:303-15.

[100] Hussan M, Rahman MS, Sharmin F, Kim D, Do J. Multiple tuned mass damper for multi-mode vibration reduction of offshore wind turbine under seismic excitation. Ocean Eng. 2018;160:449-60.

[101] Zhang SY, Neild S, Jiang JZ. Optimal design of a pair of vibration suppression devices for a multi-storey building. Struct Control Health Monit. 2020;27:e2498.

[102] Wen Y, Chen Z, Hua X. Design and Evaluation of Tuned Inerter-Based Dampers for the Seismic Control of MDOF Structures. J Struct Eng. 2017;143:04016207.

[103] Cao L, Li C. Tuned tandem mass dampers-inerters with broadband high effectiveness for structures under white noise base excitations. Struct Control Health Monit. 2019;26:e2319.

[104] Palacios-Quiñonero F, Rubió-Massegú J, Rossell JM, Karimi HR. Design of inerter-based multi-actuator systems for vibration control of adjacent structures. J Franklin Inst. 2019;356:7785-809.

[105] De Domenico D, Qiao H, Wang Q, Zhu Z, Marano G. Optimal design and seismic performance of Multi-Tuned Mass Damper Inerter (MTMDI) applied to adjacent high-rise buildings. Struct Des Tall Spec Build. 2020;29:e1781.

[106] Cao L, Li C, Chen X. Performance of multiple tuned mass dampers-inerters for structures under harmonic ground acceleration. Smart Struct Syst. 2020;26:49-61.

[107] Vakakis AF. Inducing passive nonlinear energy sinks in vibrating systems. J Vib Acoust. 2001;123:324-32.

[108] Vakakis AF, Gendelman O. Energy pumping in nonlinear mechanical oscillators: part II—resonance capture. J Appl Mech. 2001;68:42-8.

[109] Gendelman O, Manevitch L, Vakakis AF, M'closkey R. Energy pumping in nonlinear mechanical oscillators: Part I—Dynamics of the underlying Hamiltonian systems. J Appl Mech. 2001;68:34-41.

[110] Zang J, Yuan T, Lu Z, Zhang Y, Ding H, Chen L. A lever-type nonlinear energy sink. J Sound Vib. 2018;437:119-34.

[111] Javidialesaadi A, Wierschem NE. An inerter-enhanced nonlinear energy sink. Mech Syst Signal Process. 2019;129:449-54.

[112] Zhang Z, Lu Z, Ding H, Chen L. An inertial nonlinear energy sink. J Sound Vib. 2019;450:199-213.

[113] Chen HY, Mao XY, Ding H, Chen LQ. Elimination of multimode resonances of composite plate by inertial nonlinear energy sinks. Mech Syst Signal Process. 2020;135:106383.

[114] Zhang Y, Lu Y, Zhang W, Teng Y, Yang H, Yang T et al. Nonlinear energy sink with inerter. Mech Syst Signal Process. 2019;125:52-64.

[115] Zhao Z, Zhang R, Jiang Y, Pan C. A tuned liquid inerter system for vibration control. Int J Mech Sci. 2019;164:105171.

[116] Wang Q, Tiwari ND, Qiao H, Wang Q. Inerter-based tuned liquid column damper for seismic vibration control of a single-degree-of-freedom structure. Int J Mech Sci. 2020;184.

[117] Wang Q, Qiao H, De Domenico D, Zhu Z, Tang Y. Seismic response control of adjacent high-rise buildings linked by the Tuned Liquid Column Damper-Inerter (TLCDI). Eng Struct. 2020;223:111169.

[118] Gonzalez-Buelga A, Lazar IF, Jiang JZ, Neild SA, Inman DJ. Assessing the effect of nonlinearities on the performance of a tuned inerter damper. Structural Control and Health Monitoring. 2017;24.

[119] Brzeski P, Perlikowski P. Effects of play and inerter nonlinearities on the performance of tuned mass damper. Nonlinear Dyn. 2017;88:1027-41.

[120] Garrido H, Curadelli O, Ambrosini D. Improvement of tuned mass damper by using rotational inertia through tuned viscous mass damper. Eng Struct. 2013;56:2149-53.

[121] Smith MC, Wang FC. Performance Benefits in Passive Vehicle Suspensions Employing Inerters. Veh Syst Dyn. 2004;42:235-57.

[122] Wang FC, Chan HA. Vehicle suspensions with a mechatronic network strut. Veh Syst Dyn. 2010;49:811-30.

[123] Hu Y, Chen MZQ, Sun Y. Comfort-oriented vehicle suspension design with skyhook inerter configuration. J Sound Vib. 2017;405:34-47.

[124] Hu Y, Chen MZQ, Shu Z. Passive vehicle suspensions employing inerters with multiple performance requirements. J Sound Vib. 2014;333:2212-25.

[125] Scheibe F, Smith MC. Analytical solutions for optimal ride comfort and tyre grip for passive vehicle suspensions. Veh Syst Dyn. 2009;47:1229-52.

[126] Sun X, Chen L, Wang S, Zhang X, Yang X. Performance investigation of vehicle suspension system with nonlinear ball-screw inerter. Int J Automot Technol. 2016;17:399-408.

[127] Chen MZQ, Papageorgiou C, Scheibe F, Wang FC, Smith M. The missing mechanical circuit element. IEEE Circuits Syst Mag. 2009;9:10-26.

[128] Evangelou S, Limebeer DJ, Sharp RS, Smith MC. Control of motorcycle steering instabilities. IEEE Control Systems Magazine. 2006;26:78-88.

[129] Evangelou S, Limebeer DJ, Sharp RS, Smith MC. Mechanical steering compensators for high-performance motorcycles. J Appl Mech. 2007;74:332-46.

[130] Wang FC, Liao MK, Liao BH, Su WJ, Chan HA. The performance improvements of train suspension systems with mechanical networks employing inerters. Veh Syst Dyn. 2009;47:805-30.

[131] Jiang JZ, Matamoros-Sanchez AZ, Goodall RM, Smith MC. Passive suspensions incorporating inerters for railway vehicles. Veh Syst Dyn. 2012;50:263-76.

[132] Wang FC, Hsieh MR, Chen H-J. Stability and performance analysis of a full-train system with inerters. Veh Syst Dyn. 2012;50:545-71.

[133] Ning D, Sun S, Du H, Li W, Zhang N, Zheng M et al. An electromagnetic variable inertance device for seat suspension vibration control. Mech Syst Signal Process. 2019;133.

[134] Ning D, Sun S, Yu J, Zheng M, Du H, Zhang N et al. A rotary variable admittance device and its application in vehicle seat suspension vibration control. J Franklin Inst. 2019;356:7873-95.

[135] Hu Y, Chen MZQ, Shu Z, Huang L. Analysis and optimisation for inerter-based isolators via fixed-point theory and algebraic solution. J Sound Vib. 2015;346:17-36.

[136] Zilletti M. Feedback control unit with an inerter proof-mass electrodynamic actuator. J Sound Vib. 2016;369:16-28.

[137] Alujević N, Čakmak D, Wolf H, Jokić M. Passive and active vibration isolation systems using inerter. J Sound Vib. 2018;418:163-83.

[138] Ma R, Bi K, Hao H. Heave motion mitigation of semi-submersible platform using inerter-based vibration isolation system (IVIS). Eng Struct. 2020;219:110833.

[139] Brzeski P, Kapitaniak T, Perlikowski P. Novel type of tuned mass damper with inerter which enables changes of inertance. J Sound Vib. 2015;349:56-66.

[140] Xu T, Liang M, Li C, Yang S. Design and analysis of a shock absorber with variable moment of inertia for passive vehicle suspensions. J Sound Vib. 2015;355:66-85.

[141] Luo H, Zhang R, Weng D. Mitigation of liquid sloshing in storage tanks by using a hybrid control method. Soil Dyn Earthq Eng. 2016;90:183-95.

[142] Jiang Y, Zhao Z, Zhang R, De Domenico D, Pan C. Optimal design based on analytical solution for storage tank with inerter isolation system. Soil Dyn Earthq Eng. 2020;129:105924.

[143] Heaton TH, Hall JF, Wald DJ, Halling MW. Response of high-rise and base-isolated buildings to a hypothetical Mw 7.0 blind thrust earthquake. Science. 1995;267:206-11.

[144] Tsai HC. The effect of tuned-mass dampers on the seismic response of base-isolated structures. Int J Solids Struct. 1995;32:1195-210.

[145] Taniguchi T, Der Kiureghian A, Melkumyan M. Effect of tuned mass damper on displacement demand of base-isolated structures. Eng Struct. 2008;30:3478-88.

[146] Xiang P, Nishitani A. Optimum design for more effective tuned mass damper system and its application to base-isolated buildings. Struct Control Health Monit. 2014;21:98-114.

[147] Hoang N, Fujino Y, Warnitchai P. Optimal tuned mass damper for seismic applications and practical design formulas. Eng Struct. 2008;30:707-15.

[148] De Domenico D, Ricciardi G. An enhanced base isolation system equipped with optimal tuned mass damper inerter (TMDI). Earthq Eng Struct Dyn. 2018;47:1169-92.

[149] De Domenico D, Ricciardi G. Improving the dynamic performance of base-isolated structures via tuned mass damper and inerter devices: A comparative study. Struct Control Health Monit. 2018;25:e2234.

[150] Michael F, De Domenico D, Ricciardi G. Optimal design and seismic performance of tuned mass damper inerter (TMDI) for structures with nonlinear base isolation systems. Earthq Eng Struct Dyn. 2018;47:2359-560.

[151] De Angelis M, Giaralis A, Petrini F, Pietrosanti D. Optimal tuning and assessment of inertial dampers with grounded inerter for vibration control of seismically excited base-isolated systems. Eng Struct. 2019;196:109250.

[152] Pietrosanti D, De Angelis M, Giaralis A. Experimental study and numerical modeling of nonlinear dynamic response of SDOF system equipped with tuned mass damper inerter (TMDI) tested on shaking table under harmonic excitation. Int J Mech Sci. 2020;184:105762.

[153] Sun H, Zuo L, Wang X, Peng J, Wang W. Exact H_2 optimal solutions to inerter-based isolation systems for building structures. Struct Control Health Monit. 2019;26:e2357.

[154] Zhao Z, Zhang R, Jiang Y, Pan C. Seismic response mitigation of structures with a friction pendulum inerter system. Eng Struct. 2019;193:110-20.

[155] De Domenico D, Impollonia N, Ricciardi G. Soil-dependent optimum design of a new passive vibration control system combining seismic base isolation with tuned inerter damper. Soil Dyn Earthq Eng. 2018;105:37-53.

[156] Chen Q, Zhao Z, Zhang R, Pan C. Impact of soil–structure interaction on structures with inerter system. J Sound Vib. 2018;433:1-15.

[157] Zhao Z, Chen Q, Zhang R, Pan C, Jiang Y. Optimal design of an inerter isolation system considering the soil condition. Eng Struct. 2019;196:109324.

[158] De Domenico D, Ricciardi G, Zhang R. Optimal design and seismic performance of tuned fluid inerter applied to structures with friction pendulum isolators. Soil Dyn Earthq Eng. 2020;132:106099.

[159] Siami A, Karimi H, Cigada A, Zappa E, Sabbioni E. Parameter optimization of an inerter-based isolator for passive vibration control of Michelangelo's Rondanini Pietà. Mech Syst Signal Process. 2018;98:667-83.

[160] De Haro Moraes F, Silveira M, Gonçalves PJP. On the dynamics of a vibration isolator with geometrically nonlinear inerter. Nonlinear Dyn. 2018;93:1325-40.

[161] Yang J, Jiang JZ, Neild SA. Dynamic analysis and performance evaluation of nonlinear inerter-based vibration isolators. Nonlinear Dyn. 2019;99:1823-39.

[162] Wang Y, Wang R, Meng H, Zhang B. An investigation of the dynamic performance of lateral inerter-based vibration isolator with geometrical nonlinearity. Arch Appl Mech. 2019;89:1953-72.

[163] Wang Y, Li H, Cheng C, Ding H, Chen L. A nonlinear stiffness and nonlinear inertial vibration isolator. J Vib Control. 2020.

[164] Wang Y, Li H, Cheng C, Ding H, Chen L. Dynamic performance analysis of a mixed-connected inerter-based quasi-zero stiffness vibration isolator. Struct Control Health Monit. 2020:e2604.

[165] Xiao L, Sun F, Bursi OS. Vibration Attenuation and Amplification of One-Dimensional Uncoupled and Coupled Systems with Optimal Metafoundations. J Eng Mech. 2020;146:04020058.

[166] Cacciola P, Tombari A, Giaralis A. An inerter-equipped vibrating barrier for noninvasive motion control of seismically excited structures. Struct Control Health Monit. 2019;27:e2474.

[167] Sun F, Xiao L, Bursi OS. Optimal design and novel configuration of a locally resonant periodic foundation (LRPF) for seismic protection of fuel storage tanks. Eng Struct. 2019;189:147-56.

[168] Shi X, Zhu S. A comparative study of vibration isolation performance using negative stiffness and inerter dampers. J Franklin Inst. 2019;356:7922-46.

CHAPTER 2 USING TUNED HEAVE PLATE INERTER (THPI) FOR HEAVE MOTION MITIGATION

Abstract[2]

The undesirable motions resulting from wave loading can lead to long-term fatigue damage or even catastrophic sinking of offshore semi-submersible platforms (SSP). It is therefore by all means necessary to suppress the excessive vibrations of SSP. Many methods have been proposed to mitigate the heave motion of offshore platforms, such as using a fixed heave plate (FHP) to increase the draft and damping of the system, or adopting a tuned heave plate (THP) to form a tuned mass damper (TMD) system. In this paper, a novel inerter-based control system, namely a tuned heave plate inerter (THPI), is proposed for control of SSP heave vibrations. In this system, an inerter device, which can transform the linear motion into the high-speed rotational motion and thus significantly amplifies the physical mass of the system, is added to the THP to further improve the performance of conventional THP. Analytical studies are performed to investigate the effectiveness of the proposed method. The mean square heave motions of SSP without control device and with FHP, THP and THPI are stochastically formulated, and the optimal design parameters for THP and THPI are derived. Parametric studies are conducted to investigate the influences of the size and original depth of heave plate on the optimal performances of FHP, THP and THPI. Finally, a novel waterwheel inerter is developed to realize the suggested device. The analytical results show that THPI is more effective to mitigate the heave motion of SSP compared to the conventional methods, and the novel waterwheel inerter is capable of generating a large apparent mass by using a small waterwheel.

2.1 Introduction

Due to the remarkable growth of fossil energy consumption, the oil and gas industry has moved into deep and ultra-deep waters to explore and exploit new hydrocarbon sources. Various types of floating platforms, such as tension leg platform (TLP), spar type platform and semi-submersible platform (SSP), have been developed for energy exploiting. Compared to the TLP and spar type platform, SSP is most widely used in the offshore oil and gas industry owing to its wider range of applicable water depth, larger deck area, and bigger payload capacity. However, SSP may be subject to large heave motion due to its shallow draft and large pontoons, which in turn not only affects the workplace health and safety, but also reduces platform

[2] This chapter was published in *Engineering Structures* with the full bibliographic citation as follows:
Ma R, Bi K, Hao H. Mitigation of heave response of semi-submersible platform (SSP) using tuned heave plate inerter (THPI). Eng Struct. 2018;177:357-73. https://doi.org/10.1016/j.engstruct.2018.09.085.

productivity, affects serviceability and endangers structural safety. It is therefore a key issue to suppress the undesired heave motion of offshore SSP.

In the past decades, extensive research works have been carried out to control the adverse vibrations of offshore platforms, and many vibration control methods have been proposed. These methods can be broadly classified as passive methods, active methods, semi-active methods and hybrid methods [1]. For SSP, previous studies mainly focused on increasing the draft and damping of the platform by mounting a large ballast or fixed heave plate (FHP) to SSP. The effectiveness of this method has been verified by the numerical and experimental studies [2-7]. Instead of using a fixed heave plate, tuned heave plate (THP) was proposed to suppress the heave response of SSP based on the concept of tuned mass damper (TMD), a method that has been widely applied in engineering practices to mitigate the wind-, earthquake- and wave-induced vibrations [8-12]. Zhu et al. [13] firstly proposed the conceptual design of a moveable heave plate (MHP) to reduce the heave motion of SSP and carried out analytical studies to investigate the control performance. Analytical results clearly demonstrated the effectiveness of the proposed control method. Liu and Ou [14] further developed this concept by adding a power take-off system to MHP. The developed tuned heave plate energy-harvesting system (THPEH) could not only mitigate the heave motion of SSP but also convert wave energy to electricity. A wave tank test was also reported in Ref. [14] and the experimental results showed that with properly designed heave plate size and connecting spring and dashpot, this method could suppress platform heave motion up to about 40%. These two studies [13, 14] proposed using a single heave plate installed at the middle of the platform to suppress the heave motion. Instead of using one single heave plate, Zhu et al. [15] proposed using multiple THPs to suppress the pitch motion of SSP induced by sea wave. Numerical results illustrated that the pitch motion of SSP could be remarkably reduced by the designed suspensions. Liu et al. [16] adopted the same concept in Ref. [15] and performed both experimental and numerical studies to examine the effect of THP on the SSP vibration control. The results showed that the THP could effectively control both the heave and pitch motions of SSP.

It is well known that the effectiveness of using TMD system for structural vibration control highly depends on the percentage of auxiliary mass. Larger auxiliary mass could lead to more evident control effectiveness. However, adding a large mass to the primary structure not only significantly increases the cost but also is not technically practical in some cases. It would be ideal if the same level of control effectiveness can be achieved by using smaller auxiliary mass. This paper proposes using a recently developed two-terminal mechanical device, dubbed inerter by Smith [17], in conjunction with the conventional TMD, to further improve the performance of TMD for SSP vibration control. Inerter is a device that can produce an apparent

mass that is much larger than its physical mass through the amplifying mechanism by transforming the linear motion into high-speed rotational motion. Therefore, the same level of vibration suppression can be achieved by using a much smaller (physical) mass in the inerter-based device.

Inerter was initially employed in the suspension system of high-performance vehicles such as Formula 1 racing cars under the name of J damper [18, 19]. Very recently, the inerter-based devices have been introduced to control the vibrations of civil engineering structures. Hwang et al. [20] developed a rotational inertia viscous damper (RIVD) for structural vibration control, in which a ball screw was utilized to transform the linear motion into high-speed rotational motion of an internal tube immersed in the viscous fluid which provided a significant damping force to the system. Based on the concept of RIVD, Ikago et al. [21] further proposed a tuned viscous mass damper (TVMD) to mitigate seismic induced vibrations of buildings, and they derived the closed-form solution of an optimum design for the TVMD incorporated into a single-degree-of-freedom (SDOF) structure. Some researchers introduced inerter into the conventional TMD system to increase its inertial property without evidently increasing its physical mass. Marian and Giaralis [22] proposed a tuned mass-damper-inerter (TMDI) by utilizing the mass amplification effect of the inerter, and they analytically and numerically demonstrated that the TMDI was more effective than the TMD with the same amount of additional auxiliary mass in reducing the vibrations of stochastically support-excited structural systems. A better performance was also found for suppressing the wind-induced vibrations of tall buildings by using TMDI [23]. Lazar et al. developed a tuned inerter damper (TID), a special case of TMDI without the attached mass, to reduce the seismic-induced vibrations of a SDOF system [24] and cable-stayed bridges [25]. Numerical results showed that the TID could be an attractive alternative to the TMDs and other damper systems due to its small mass and overall size. Wen et al. [26] and Pietrosanti et al. [27] investigated the optimal design of tuned inerter-based dampers (i.e. TVMD, TMDI and TID) by minimizing different objective responses (displacement, acceleration, etc.) and evaluated their performances to reduce seismic- and wind-induced vibrations of structures. Hu and Chen [28] studied the optimal parameters of the inerter-based dynamic vibrations absorbers (DVAs) with different configurations based on the H_2 and H_∞ optimizations. Numerical results showed that more than 20% and 10% improvement could be obtained for the H_∞ and H_2 performances respectively. The inerter-based DVA was also found more efficient than the traditional TMD in reducing the response of a continuum beam under harmonic excitation [29].

Critical literature reviews reveal that inerter-based devices can be utilized to further improve the performance of the conventional TMD by increasing its inertial mass in the TMD. However, it should be noted that almost all studies focused on mitigating the seismic-induced

and wind-induced vibrations of onshore structures. Very limited studies applied inerter-based control systems in the offshore structures. To the best knowledge of the authors, only two papers (Refs. [30, 31]) investigated the effectiveness of applying inerter-based passive control method to mitigate wind- and wave-induced vibrations of offshore wind turbines, and no open literature reports the feasibility of applying inerter in the offshore SSP. For a SSP system, the mass of the original structure is huge, the added mass will also be very large even a commonly used percentage (normally 2% to 5% of the primary structure) is applied. The inerter-based device will have great application potentials in SSP vibration control owing to the special mass amplification characteristic of the device.

In the present study, an inerter-based device is proposed to be added between the SSP and THP, i.e. forming a tuned heave plate inerter (THPI) system, to further improve the performance of THP for SSP heave motion mitigation. Analytical studies are performed to investigate the effectiveness of the proposed method. Compared to those devices applied in the onshore structures, the equation of motion of offshore structure is much more complicated due to the nonlinear damping and wave-induced force in the ocean environment. The paper is organized as follows: the analytical models for SSPs with different control devices (FHP, THP and THPI) are stochastically derived in Section 2.2; the parameter optimizations are introduced in Section 2.3 and the effectiveness of different control methods are discussed in Section 2.4; Section 2.5 investigates the influences of the size and original depth of heave plate on the control effectiveness; Section 2.6 presents a realization of the proposed inerter device; and finally some concluding remarks are made in Section 2.7.

2.2 Analytical Models of SSPs without and with Different Control Devices

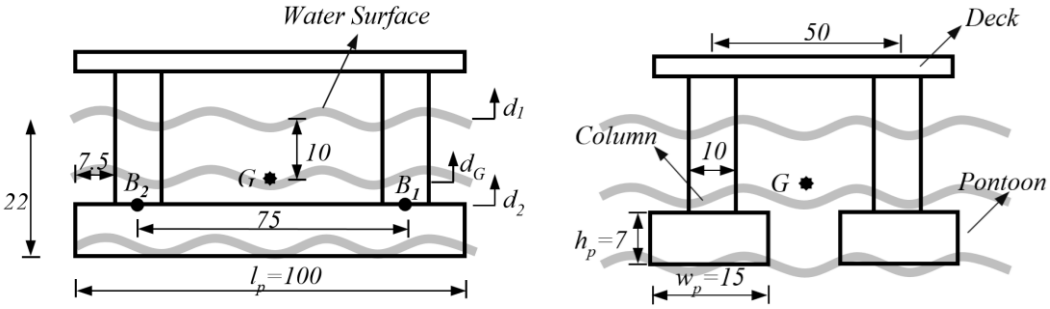

(a) Front view (b) Side view

Figure 2-1 Dimensions of an example SSP (unit: m)

In this section, the analytical models of SSPs with different control devices are established, and the mean square heave motions of different systems are stochastically formulated. In particular, three control devices, i.e. FHP, THP and THPI are considered. For comparison, the analytical model for SSP without any control device is also presented. The problem discussed

in the present study in nature is a hydrodynamic problem, which is very complex. To simplify the analysis a few assumptions are made in the present study: (1) the influence of mooring system and the coupling effect from the other motions (i.e. surge, sway, yaw, pitch, and roll) are neglected. This is a reasonable assumption, since the dominate frequencies of these motions are far from that of the heave motion, the coupling between the heave and other motions is therefore negligible [32, 33]; (2) vortex-induced vibration (VIV) of SSP is also disregarded because its amplitude is much smaller compared to the heave motion [34]. Figure 2-1 shows a typical SSP adopted from Ref. [32]. It can be seen that this SSP consists of one deck, two pontoons and four vertical columns. The dimensions of the key components are shown in the figure, the rectangular pontoons have a length of 100 m, a width of 15 m and a height of 7 m, the diameter of the vertical cylindrical columns is 10 m. G is the centre of gravity of the SSP and it locates at 10 m under the water surface [32].

2.2.1 Analytical Model of SSP with FHP

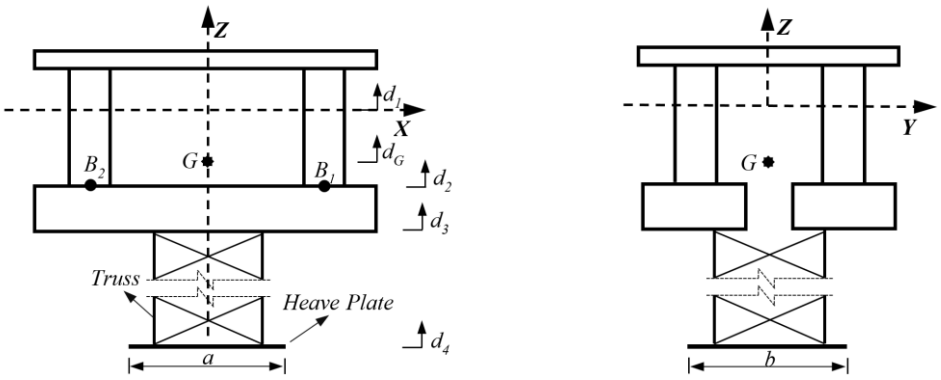

(a) Front view (b) Side view

Figure 2-2 Schematic view of a SSP with a FHP

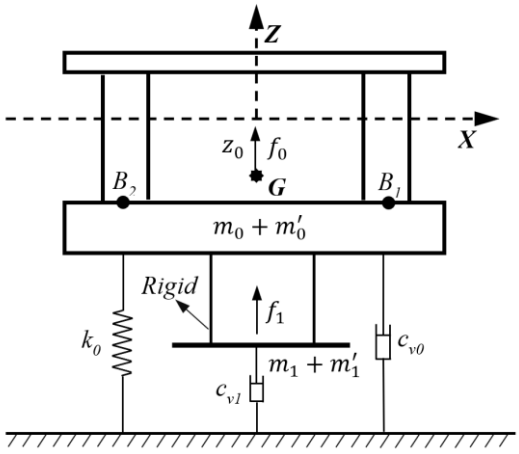

Figure 2-3 Analytical model of a SSP with a FHP

The FHP system is commonly utilized to increase the draft and damping of SSP and thus suppress the heave motion. Figure 2-2 shows a schematic view of a SSP with a FHP, in which

a heave plate is rigidly connected to the pontoons by the truss structures. Figure 2-3 shows the analytical model of a SSP with a FHP. In which, m_0 and m_1 are the physical masses of SSP and heave plate respectively, m_0' and m_1' are the corresponding added masses resulting from the fact that the submerged body can impart an acceleration to some of the surrounding fluid. m_0' and m_1' can be calculated as

$$m_0' = 2\rho c_{a0} V_p \tag{2.1}$$

$$m_1' = \rho c_{a1} V_R \tag{2.2}$$

where ρ is the density of seawater; c_{a0} and c_{a1} are the added mass coefficients of pontoons and heave plate respectively, which can be obtained from [32] and [35]; $V_p = l_p w_p h_p$ is the volume of one pontoon, and l_p, w_p and h_p are the length, width and height of the pontoon (see Figure 2-1), respectively; $V_R = \frac{\pi}{4} a^2 b$ is the reference volume [35] of the heave plate, with a and b representing the length and width of the rectangular heave plate, respectively.

In Figure 2-3, k_0 is the restoring stiffness provided by the surrounding water, and it can be calculated as [30]

$$k_0 = \rho g A_w \tag{2.3}$$

in which g is gravitational acceleration and A_w is the waterplane area of SSP. c_{v0} and c_{v1} are the inherent damping provided by the water to the SSP and heave plate respectively, and they are

$$c_{v0} = \frac{1}{2} \rho c_{d0} A_0 \tag{2.4}$$

$$c_{v1} = \frac{1}{2} \rho c_{d1} A_1 \tag{2.5}$$

where c_{d0} and c_{d1} are the drag coefficients of the pontoons and heave plate respectively, and they can be obtained from DNV-RP-H103 [35]; A_0 and A_1 are the projected areas of the pontoons and heave plate in the vertical direction.

The dynamic equilibrium equation of SSP with FHP then can be written as follows:

$$\sum_{j=0}^{1} (m_j + m_j') \ddot{z}_0(t) + \sum_{j=0}^{1} c_{rj}\, \dot{z}_0(t) + \sum_{j=0}^{1} c_{vj}\, \dot{z}_0(t) |\dot{z}_0(t)| + k_0 z_0(t) = \sum_{j=0}^{1} f_j\,(t) \tag{2.6}$$

where j is the ID of the SSP and heave plate, with "0" denoting SSP and "1" representing heave plate; c_{rj} is the radiation damping, and it is neglected in this research due to the relatively small wave radiation at low-frequency oscillations of SSP [36]; $f_j(t)$ is the wave

induced force on SSP or heave plate; $z_0(t)$, $\dot{z}_0(t)$ and $\ddot{z}_0(t)$ are the vertical displacement, velocity and acceleration of SSP/ heave plate, respectively.

In Equation (2.6), the nonlinear viscous damping term can be linearized and approximated as [37]

$$\dot{z}_0|\dot{z}_0| \approx \frac{8}{3\pi}\omega Z_0 \dot{z}_0 \tag{2.7}$$

where Z_0 is the amplitude of heave motion and ω is the frequency of the wave excitation in rad/s.

Based on the undamped Morison's equation, the wave induced force on SSP $f_0(t)$ can be evaluated by summing those on the pontoons and columns together, i.e. [32]

$$f_0(\mathrm{t}) = 2\int_{l_2}^{l_1} \rho A_p\,(1 + c_{a0}) a_{d3}\,dx + P_{B1}\frac{A_w}{2} + P_{B2}\frac{A_w}{2} \tag{2.8}$$

in which the first term considers the contribution of the pontoons and the last two terms are the contributions from the columns. In Equation (2.8), A_p is the cross-sectional area of one pontoon; a_{d3} is the vertical wave acceleration at the depth of d_3; l_1 and l_2 are the X-coordinates of the front and back ends of the pontoon respectively; P_{B1} and P_{B2} are the wave pressures at points B_1 and B_2, respectively, the calculation of which are briefly introduced as follows.

In the present study, the SSP is assumed located in the deep water, and an infinite water depth is assumed. In this case, the velocity potential of wave can be expressed as [32]:

$$\phi(x, z, t) = \frac{g\zeta_a}{\omega} e^{kz} \cos(\omega t - kx) \tag{2.9}$$

where x and z denote the horizontal and vertical coordinates, respectively; ζ_a is the amplitude of wave, which is half of the wave height H_s; k is the wave number which can be estimated from the following equation

$$\omega^2 = kg \tanh kd \tag{2.10}$$

where d is the depth of water. For the case of deep water ($d \geq 0.5L_w$, L_w is the wave length), $\tanh kd \approx 1$.

By differentiating the wave potential, the velocity and acceleration of water particles in the vertical direction can be obtained as

$$v_z = \frac{\partial \phi}{\partial z} = \omega \zeta_a e^{kz} \cos(\omega t - kx) \tag{2.11}$$

$$a_z = \frac{\partial v_z}{\partial t} = -\omega^2 \zeta_a e^{kz} \sin(\omega t - kx) \tag{2.12}$$

Based on the Bernoulli's equation, the wave pressures at Points B_1 and B_2 can be calculated by

$$P_{B1} = -\rho \frac{\partial \phi(x_1, d_2, t)}{\partial t} = \rho g \zeta_a e^{kd_2} \sin(\omega t - kx_1) \tag{2.13}$$

$$P_{B2} = -\rho \frac{\partial \phi(x_2, d_2, t)}{\partial t} = \rho g \zeta_a e^{kd_2} \sin(\omega t - kx_2) \tag{2.14}$$

where x_1 and x_2 are the X-coordinates of Points B_1 and B_2, respectively; d_2 is the depth of the bottom of columns.

Substituting Equations (2.12), (2.13) and (2.14) into Equation (2.8), the wave induced force on the SSP $f_0(t)$ then can be estimated. The wave induced force on the heave plate $f_1(t)$ can be similarly approximated by the following equation:

$$f_1(t) = \rho c_{a1} V_R a_{d4} \tag{2.15}$$

where a_{d4} is the vertical wave acceleration at the depth of d_4 (see Figure 2-2(a)).

Substituting Equations (2.7), (2.8) and (2.15) into Equation (2.6), Equation (2.6) can be expressed in the frequency domain as:

$$\left[-\omega^2 \sum_{j=0}^{1} (m_j + m_j') + \frac{8}{3\pi} Z_0 i\omega^2 \sum_{j=0}^{1} c_{vj} + k_0 \right] Z_0 e^{i\omega t} = \sum_{j=0}^{1} F_j \, e^{i\omega t} \tag{2.16}$$

where i is the complex number. Solving Equation (2.16), the heave motion transfer function of SSP with FHP can be derived as

$$Z_0(i\omega) = \sqrt{\frac{-\left[-\omega^2 \sum_{j=0}^{1}(m_j+m_j')+k_0\right]^2 + \sqrt{\left[-\omega^2 \sum_{j=0}^{1}(m_j+m_j')+k_0\right]^4 + 4\left(\frac{8}{3\pi}\omega^2 \sum_{j=0}^{n} c_{vj}\right)^2 \left(\sum_{j=0}^{n} F_j\right)^2}}{2\left(\frac{8}{3\pi}\omega^2 \sum_{j=0}^{n} c_{vj}\right)^2}} \tag{2.17}$$

The heave motion of SSP without any control device can be easily calculated based on Equation (2.17) by setting m_1, m_1', c_{v1}, and F_1 equal to 0.

2.2.2 Analytical Model of SSP with THP/THPI

Figure 2-4 shows the analytical model of a SSP with a THP or THPI. As shown in Figure 2-4, the heave plate is no longer fixed with SSP, but is connected to the SSP via a spring with the stiffness of k_n and a system component E_n. When E_n is a damper (Figure 2-5(a)), the system is a SSP-THP system; if E_n is an inerter-based device (Figure 2-5(b)), the system becomes

SSP-THPI. Different inerter layouts, in terms of how spring, damper and inerter components are arranged, have been studied by different researchers (e.g. Refs. [21, 22, 24, 26]). In the present study, only the arrangement shown in Figure 2-5(b) is considered since this arrangement can result in an evident control effectiveness based on a previous study [28]. In this layout, the inerter m_b is in parallel with a damper with a damping coefficient c_2, and then in series with a spring with a stiffness k_3.

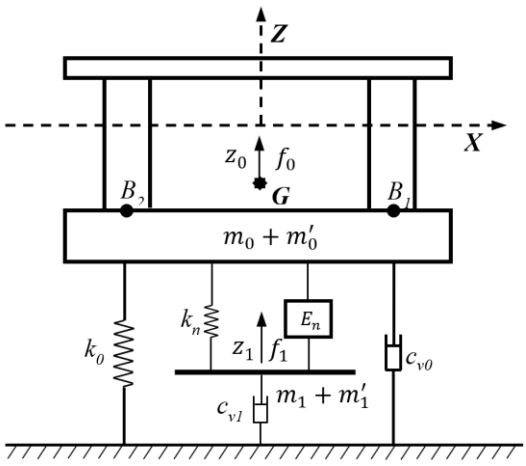

Figure 2-4 Analytical model of a SSP with a THP/THPI ($n = 1,2$)

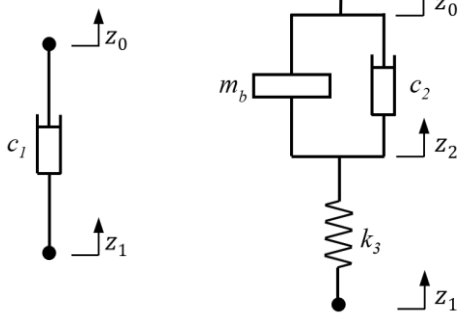

(a) Damper E_1 (b) Inerter-based system E_2

Figure 2-5 System components

According to Figure 2-4, the dynamic equilibrium equations of SSP with THP/THPI can be written as

$$(m_0 + m_0')\ddot{z}_0(t) = f_0(t) - k_0 z_0(t) - c_{v0}'\dot{z}_0(t) - k_n[z_0(t) - z_1(t)] + f_n'(t) \quad (2.18)$$

$$m_1 + m_1')\ddot{z}_1(t) = f_1(t) - k_n[z_1(t) - z_0(t)] - c_{v1}'\dot{z}_1(t) - f_n'(t) \quad (2.19)$$

where z_1, $\dot{z}_1$ and $\ddot{z}_1$ are the vertical displacement, velocity and acceleration of the heave plate, respectively; n is the device ID with "1" and "2" denoting THP and THPI, respectively; c_{v0}' and c_{v1}' are the linearized inherent damping of SSP and heave plate respectively, which are determined through an iterative method during the solution process; $f_n'(t)$ is the force generated by the system component E_n (see Figure 2-5) which can be expressed as follows:

For THP (n=1),

$$f_1'(t) = c_1[\dot{z}_1(t) - \dot{z}_0(t)] \quad (2.20)$$

For THPI (n=2),

$$f_2'(t) = k_3[z_1(t) - z_2(t)] = m_b[\ddot{z}_2(t) - \ddot{z}_0(t)] + c_2[\dot{z}_2(t) - \dot{z}_0(t)] \quad (2.21)$$

where c_1 is the damping coefficient of THP, and m_b is the inertance of the inerter.

Let $s = i\omega$, Equations (2.18) and (2.19) can be expressed in the Laplace domain as follows:

$$(m_0 + m_0')s^2 z_0(s) = f_0(s) - k_0 z_0(s) - c_{v0}' s z_0(s) - k_n[z_0(s) - z_1(s)] + f_n'(s) \quad (2.22)$$

$$(m_1 + m_1')s^2 z_1(s) = f_1(s) - k_n[z_1(s) - z_0(s)] - c_{v1}' s z_1(s) - f_n'(s) \quad (2.23)$$

Similarly, Equations (2.20) and (2.21) can be written as

$$f_n'(s) = \alpha_n(s)[z_1(s) - z_0(s)] \quad (2.24)$$

where

$$\alpha_n(s) = \begin{cases} c_1 s & n = 1 \\ \dfrac{1}{\dfrac{1}{k_3} + \dfrac{1}{m_b s^2 + c_2 s}} & n = 2 \end{cases} \quad (2.25)$$

Substituting Equation (2.24) into Equations (2.22) and (2.23), the heave motion transfer function $Z_0(i\omega)$ of SSP can be obtained as follows through some tedious while straightforward derivations:

$$Z_0(i\omega) = \frac{[(m_1+m_1')s^2+k_n+c_{v1}'s+\alpha_n(s)]F_0(s)+[k_n+\alpha_n(s)]F_1(s)}{[(m_0+m_0')s^2+k_0+c_{v0}'s+k_n+\alpha_n(s)][(m_1+m_1')s^2+k_n+c_{v1}'s+\alpha_n(s)]-[k_n+\alpha_n(s)]^2} \quad (2.26)$$

To simplify the above equation, the following dimensionless parameters are defined, and they are tabulated in Table 2-1.

Table 2-1 Dimensionless parameters for the THP and THPI systems

No	Term	Representation
1	Heave plate to SSP mass ratio	$\mu = \dfrac{m_1 + m_1'}{m_0 + m_0'}$
2	Inertance to heave plate mass ratio	$\delta = \dfrac{m_b}{m_1 + m_1'}$
3	Inherent damping ratio of SSP	$\zeta_{v0} = \dfrac{c_{v0}'}{2(m_0 + m_0')\omega_s}$
4	Inherent damping ratio of heave plate	$\zeta_{v1} = \dfrac{c_{v1}'}{2(m_1 + m_1')\omega_n}$
5	Damping ratio of THP/THPI	$\zeta_n = \dfrac{c_n}{2(m_1 + m_1')\omega_n}$
6	Corner frequency ratio	$\eta = \dfrac{\omega_b}{\omega_2}$
7	Natural frequency ratio of THP/THPI	$\gamma_n = \dfrac{\omega_n}{\omega_s}$

in which ω_s is the natural frequency of SSP; ω_n is the natural frequency of THP/THPI (n=1, 2); ω_b is the corner frequency of THPI. These frequencies can be calculated by

$$\omega_s = \sqrt{\frac{k_0}{m_0 + m_0'}} \quad (2.27)$$

$$\omega_n = \sqrt{\frac{k_n}{m_1 + m_1'}} \ (n = 1, 2) \tag{2.28}$$

$$\omega_b = \sqrt{\frac{k_3}{m_b}} \tag{2.29}$$

Based on these dimensionless parameters, Equation (2.26) can be simplified and expressed in a dimensionless form as follows:

$$Z_0(i\omega) = \frac{[\beta_2(s) + \beta_{1n}(s)]\frac{F_0(s)}{m_0 + m_0'} + [\beta_4(s) + \beta_{1n}(s)]\frac{F_1(s)}{m_0 + m_0'}}{[\beta_3(s) + \beta_{1n}(s)][\beta_2(s) + \beta_{1n}(s)] - [\beta_4(s) + \beta_{1n}(s)]^2} \tag{2.30}$$

where

$$\beta_{1n}(s) = \begin{cases} 2\mu\zeta_1\gamma_1\omega_s s & n = 1 \\ \dfrac{1}{\dfrac{1}{\mu\delta\eta^2\gamma_2^2\omega_s^2} + \dfrac{1}{\mu\delta s^2 + 2\mu\gamma_2\zeta_2\omega_s s}} & n = 2 \end{cases} \tag{2.31}$$

$$\beta_2(s) = \mu s^2 + \mu\gamma_n^2\omega_s^2 + 2\zeta_{v1}\mu\gamma_n\omega_s s \tag{2.32}$$

$$\beta_3(s) = s^2 + \omega_s^2 + 2\zeta_{v0}\omega_s s + \mu\gamma_n^2\omega_s^2 \tag{2.33}$$

$$\beta_4(s) = \mu\gamma_n^2\omega_s^2 \tag{2.34}$$

2.2.3 Heave Response Spectrum of SSP

In Sections 2.2.1 and 2.2.2, the expressions of the heave motion transfer function $Z_0(i\omega)$ are obtained for SSP with different control methods. Assuming the system is subjected to the sea wave loading with a spectrum $S(\omega)$, the heave response spectrum of SSP can be written as

$$S_Z(\omega) = S(\omega)|Z_0(i\omega)|^2 \tag{2.35}$$

In the present study, the commonly used JONSWAP spectrum [38] is adopted to represent the power spectral density (PSD) function of the wave surface elevation as follows:

$$S(\omega) = a^* H_s^2 \frac{\omega^{-5}}{\omega_0^{-4}} \exp\left[-1.25(\omega/\omega_0)^{-4}\right] \gamma^{\exp\left[-\frac{(\omega-\omega_0)^2}{2\tau^2\omega_0^2}\right]} \tag{2.36}$$

in which H_s is the wave height, ω_0 is the peak frequency, and

$$a^* = \frac{0.0624}{0.230 + 0.0336\gamma - 0.185(1.9 + \gamma)^{-1}} \tag{2.37}$$

where γ is the peakedness parameter and τ is a shape parameter. When $\omega \leq \omega_0$, $\tau = \tau_a$, and $\tau = \tau_b$ for $\omega > \omega_0$. The average values of these quantities are given as $\gamma = 3.30$, $\tau_a = 0.07$ and $\tau_b = 0.09$ [37].

Without loss of generality, six wave conditions are considered in the present study to investigate the influences of wave height and wave frequency/period on the heave response of SSP. Table 2-2 summarizes the corresponding parameters for the six typical loading conditions. As shown in Table 2-2, these include the working conditions in South China Sea (SCS) and Gulf of Mexico (GM), 10-year waves in SCS and North West Shelf of Australia (NWSA), and 100-year waves in SCS and GM [16, 39]. It should be noted that 10-year and 100-year wave denote the wave condition with the return period of 10 and 100 years, respectively. Figure 2-6 shows the corresponding JONSWAP spectra of the six wave conditions. As will be shown in the example, the natural frequency of SSP is $\omega_s = 0.2040$ rad/s, which falls outside the dominant wave frequencies, this is consistent with the basic design principle of offshore floating structures.

Table 2-2 Summary of the six typical sea wave conditions

Case No.	Wave Descriptions	Wave Height H_s/m	Wave Period T_0/s
L1	Working condition in SCS	6.00	11.20
L2	Working condition in GM	3.96	9.00
L3	10-year wave in SCS	11.10	13.60
L4	10-year wave in NWSA	10.00	12.50
L5	100-year wave in SCS	13.30	15.50
L6	100-year wave in GM	12.20	14.00

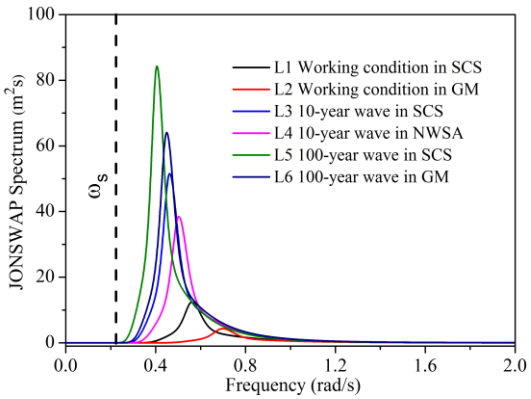

Figure 2-6 JONSWAP spectra of the six typical sea wave conditions

2.3 Parameter Optimization

To achieve the best performance of the control devices, the parameters of the dampers should be optimized. In the present study, the mean square heave motion of the SSP is of interest, and the optimization is to obtain the minimum value of the following J performance index [40]

$$J = \int_{-\infty}^{\infty} S_z(\omega)\, d\omega \tag{2.38}$$

where $S_z(\omega)$ is the heave response spectrum of SSP as formulated in Equation (2.35). In particular, for THP, the optimization is achieved by solving the following minimization problem

$$\min_{\gamma_1,\zeta_1}(J_{THP}(L_u)),\ u = 1,2,\cdots,6 \tag{2.39}$$

and for the THPI system, it becomes

$$\min_{\gamma_2,\eta,\delta,\zeta_2}(J_{THPI}(L_u))\ \ u = 1,2,\cdots,6 \tag{2.40}$$

where L_u denotes the u^{th} wave condition; J_{THP} and J_{THPI} are the J performance of THP and THPI systems, respectively.

Equation (2.38) is a H_2 norm problem. For a primary structure without inherent damping, the exact algebraic solutions can be found. However, it is very difficult to find the algebraic solutions in the optimization for a primary structure with damping, especially for the problem in the present study, in which the inherent damping varies with the frequency and motion amplitude. Furthermore, more than two design parameters need be optimized for THPI, which increases the workload and difficulty in the optimization. Considering these facts, the constrained nonlinear minimization method (command fmincon) with multiple start points in the commercial software package MATLAB (version R2017a) is adopted in the present study. This method can efficiently find a constrained minimum value of a function with several variables. Table 2-3 gives the derived optimal parameters for the THP and THPI systems under the six different sea wave loading conditions based on the example SSP with a 50×50 m heave plate and an original heave plate depth of -100 m as will be discussed in Section 2.4.

Table 2-3 Optimal design parameters for the THP and THPI systems

Case No.	THP		THPI			
	γ_1	ζ_1	γ_2	η	δ	ζ_2
L1	2.861	0.030	2.793	1.129	0.027	0.003
L2	3.227	0.076	3.391	1.356	0.053	0.007
L3	2.650	0.063	2.502	1.225	0.060	0.010
L4	2.699	0.049	2.644	1.191	0.045	0.007
L5	2.356	0.079	2.279	1.264	0.080	0.015
L6	2.516	0.067	2.450	1.239	0.065	0.012

As given in Table 2-3, it is clear that both the optimal natural frequency ratios of the THP (γ_1) and THPI (γ_2) systems are far from 1.0 in all load cases. This is different from the TMD optimization under the white-noise or seismic/wind excitations, in which the optimal natural frequency ratio is around unity to make the TMD resonate with the original structure to be controlled. For a floating structure (including SSP), the fundamental vibration frequency is required to fall outside the range of the wave dominant frequency during design to avoid the possible resonance. In other words, the THP and THPI should be tuned near the wave dominant frequency rather than the natural frequency of SSP to realize the best vibration control performance. These results are consistent with those reported by many other researchers (such as, Refs. [14, 16]). In addition, for a given wave condition, similar frequency ratios can be found for the THP and THPI in most cases, because the tuning principles of the two control methods are identical.

2.4 Effectiveness of Different Methods for SSP Vibration Control

In this section, the effectiveness of using FHP, THP and THPI to mitigate the heave motion of SSP are investigated. A typical SSP as shown in Figure 2-1 is adopted as the example, the dimensions of the SSP are given in the figure. The total mass of the SSP is 26432 tonnes. As reported in previous studies [13, 14, 16, 39], various heave plates with the size ranging from 14×14 m to 75×75 m have been adopted to reduce the vibrations of offshore platforms. In this section, without loss of generality, a steel heave plate with a cross section of 50×50 m and a thickness of 0.2 m is considered. The mass of the heave plate is 3900 tonnes, which gives a heave plate to SSP mass ratio (μ in Table 2-1) of 15%, and this is within the normally adopted mass ratio of the heave plate (7%-27% [39, 41]). The original depth of the heave plate is assumed as $-100\ m$. The influences of the size and original depth of the heave plate on the performance of heave motion suppression will be further investigated in the next subsection.

In order to examine the effectiveness of adding an inerter-based device to further improve the performance of the THP system, the following reduction ratio is introduced

$$\psi(L_u) = \frac{J_{THP}(L_u) - J_{THPI}(L_u)}{J_{THP}(L_u)} \times 100\% \tag{2.41}$$

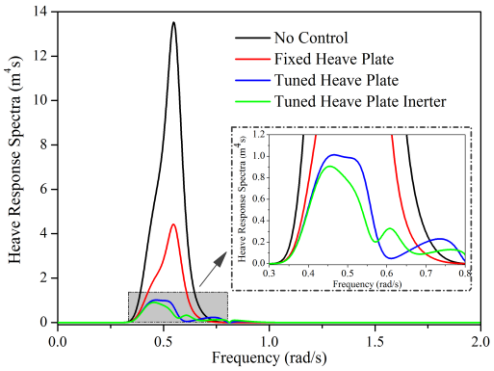

(a) L1

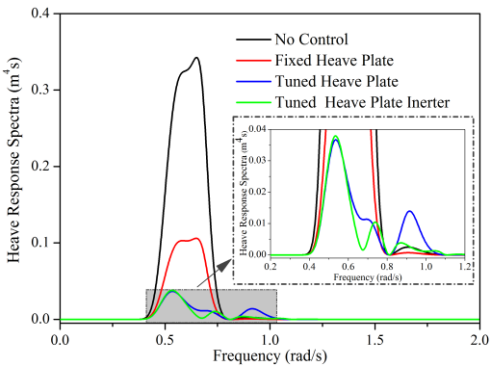

(b) L2

Figure 2-7 Heave response spectra of different SSPs subjected to the working wave conditions

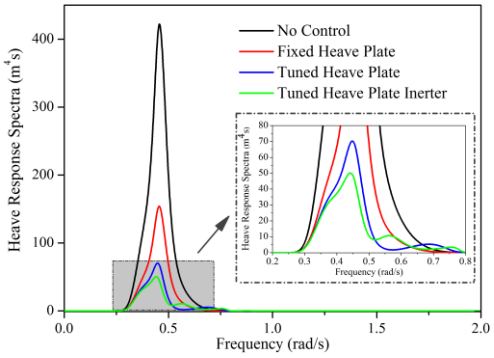

(a) L3

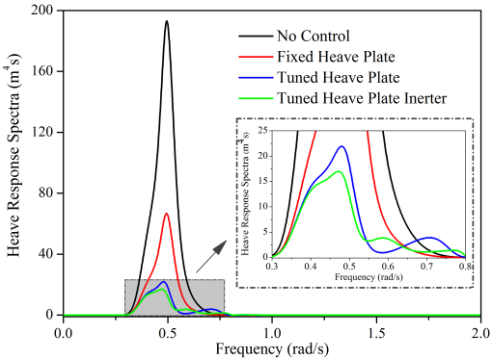

(b) L4

Figure 2-8 Heave response spectra of different SSPs subjected to the 10-year waves

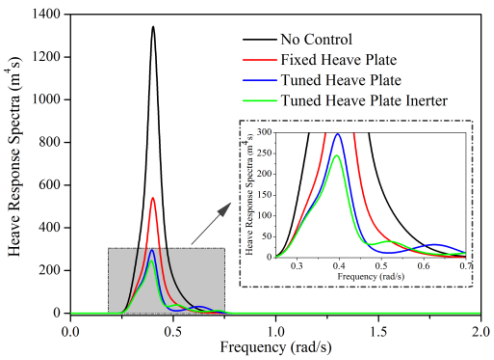

(a) L5

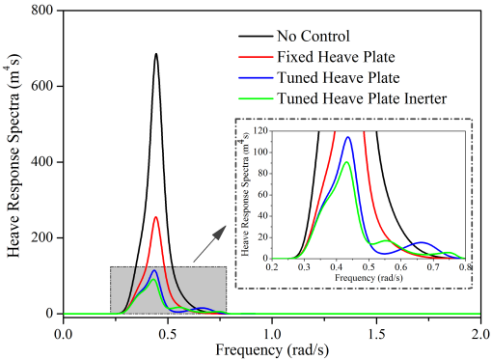

(b) L6

Figure 2-9 Heave response spectra of different SSPs subjected to the 100-year waves

The heave response spectra of the SSP with different control devices subjected to different wave conditions are shown in Figure 2-7 to Figure 2-9. In particular, Figure 2-7 shows the results under the working conditions, Figure 2-8 plots the results under the 10-year waves and Figure 2-9 shows those under the 100-year waves. The following general conclusions can be drawn based on the analytical results: adding the FHP can significantly reduce the heave motion of SSP; THP system is more effective compared to the FHP system; and adding an

inerter-based device to the THP system (i.e. forming a THPI system) can further improve the control efficiency. In particular, as shown in Figure 2-7 to Figure 2-9, the heave response spectra of the uncontrolled SSP and SSP-FHP system show a one-peak characteristic, and these peaks correspond to the dominant frequency of the external wave loading. When the THP is applied, another peak appears in the high-frequency range. This is because as shown in Figure 2-4 the inclusion of the moveable heave plate adds another DOF to the system. When the THPI system is applied, one more peak (i.e. in total three peaks) which corresponds to the DOF of the inerter appears. The results also show that although one more peak appears in the SSP-THPI system compared to the SSP-THP system, the peak at the dominant frequency of the wave load decreases in the SSP-THPI system in most cases (L1, L3, L4, L5 and L6). This is because, as indicated in Ref. [42], damping is the dominant factor to limit the vibration amplitude for a tuned dynamic vibration absorber (DVA). When the inerter device is added to the SSP-THP system, the damping of the SSP-THPI system is larger than that in the SSP-THP system. In the load case L2 (Figure 2-7(b)), the peak at the dominant wave load in the SSP-THPI system slightly increases compared to the SSP-THP system, but an obvious decrease appears at the second peak of the SSP-THP system (within 0.8-1.1 rad/s), which in turn results in the most evident motion suppression in the load case L2. According to Figure 2-7 to Figure 2-9, the J performance indices (Equation (2.38)) of the SSP controlled by the THP and THPI systems under different wave conditions can be obtained, and the further reduction ratios are then calculated by Equation (2.41). Figure 2-10 summarizes the performance differences between the THP and THPI systems. It can be seen that, by adding an inerter to the THP system, the control effectiveness can be further improved by 11.30% (for load case L5) to 18.99% (for load case L2). This improvement is comparable with the results reported by Hu and Chen [28], in which the effectiveness of using inerter to improve the performance of TMD was investigated, and they indicated that when inerter was added to the TMD system according to the layout as shown in Figure 2-5(b), the H_2 control performance was further improved by 8%-13%.

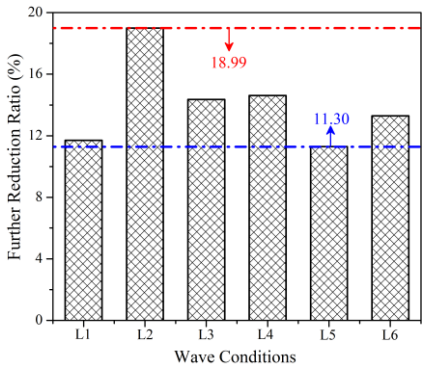

Figure 2-10 Reduction ratios of the SSP-THPI system under different wave conditions compared to the SSP-THP system

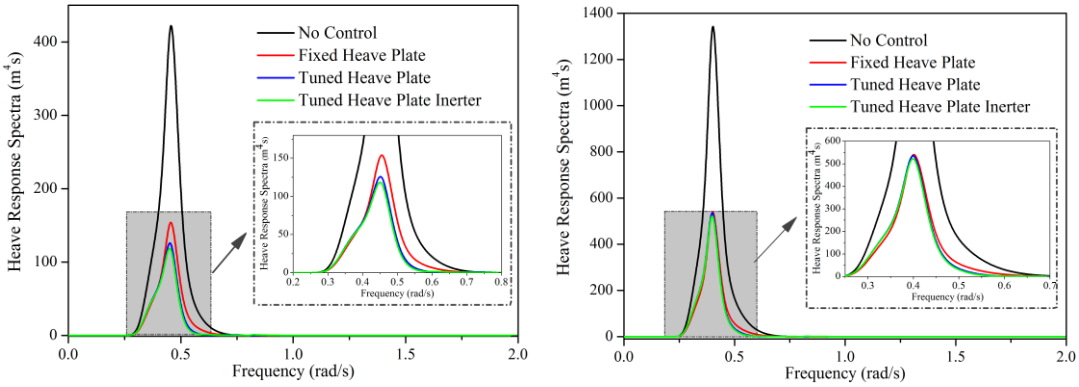

(a) L3 (b) L5

Figure 2-11 Heave response spectra of SSPs with mistuning THP and THPI systems

In the present study, optimal designs of the THP and THPI system are obtained for each wave condition. However, the SSP with the optimized THP and THPI may be subject to other worse wave loadings. Although this is an extreme situation which should be avoided in practice, it is quite imperative to investigate the robustness of the THP and THPI system. To examine the robustness, the THP and THPI optimized for the load case L1 (i.e. working condition in SCS) are utilized to control the heave motion of SSP in load cases L3 and L5 (i.e. 10-year and 100-year waves in SCS). Figure 2-11 illustrates the heave response spectra of SSPs with the mistuning THP and THPI in load case L3 and L5, respectively. It can be found that the mistuning THP and THPI systems are still effective in reducing the heave motion of SSP although the control performances decrease.

As mentioned above, the effectiveness and robustness of different control systems are investigated in the frequency domain. To make these results more intuitive, the effectiveness of FHP, THP and THPI systems is further studied in the time domain. Compared to the frequency-domain analysis, the nonlinear viscous damping term (referring to Equation (2.7)) can be solved directly in the time domain, which can further improve the accuracy of analysis. The design parameters of the THP and THPI systems, i.e. spring stiffness, damping coefficients and inertance, can be easily calculated based on the optimal results tabulated in Table 2-3 and the wave-excited force time histories on the platform and heave plate can also be generated through some tedious while straightforward derivations. After obtaining the wave-excited force time histories, the dynamic equilibrium equations of SSP with different control systems (Equations (2.6), (2.18) and (2.19)) are solved in MATLAB. Figure 2-12 shows the heave motion time histories of SSP with the FHP, THP and THPI systems. For comparison, the heave motion time history of SSP without any control is also given. It should be noted that only working condition, 10-year and 100-year waves in SCS (i.e. L1, L3 and L5) are selected for the time-domain analysis. Some general conclusions can be drawn from this figure: the FHP system can significantly reduce the heave response of SSP; the THP and THPI

systems are more effective compared to the FHP system; adding an inerter-based device to the THP system can further improve its control performance due to the increase of damping in the system. These conclusions are consistent with those obtained in the frequency domain, which further demonstrate the effectiveness of the proposed method.

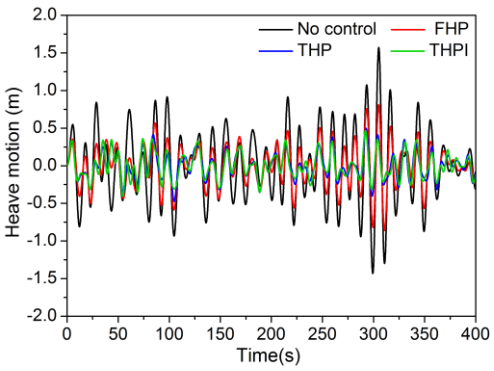

(a) L1

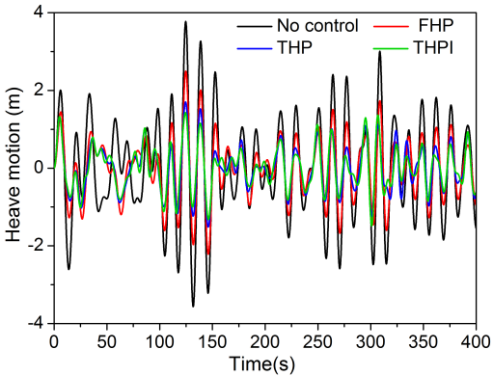

(b) L3

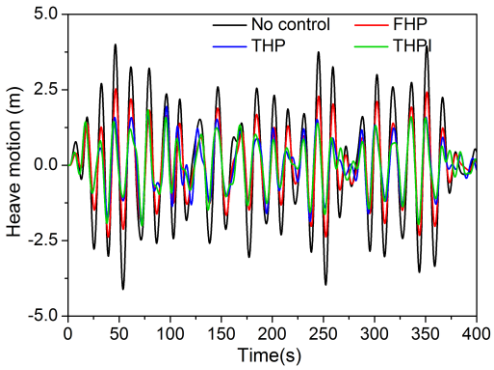

(c) L5

Figure 2-12 Heave motion time histories of SSP with different control systems

2.5 Parametric Studies

In Section 2.4, a 50×50 m heave plate with the original depth of -100 m is assumed to study the control performances of FHP, THP and THPI systems under different wave conditions. In reality, the size and original depth of the heave plate can vary in very large ranges. This section performs parametric studies to investigate the influences of the size and original depth of heave plate on the effectiveness of different control methods.

2.5.1 Influence of the Heave Plate Size

Previous studies reveal that the performance of a TMD system generally increases with the increment of the auxiliary mass. For the THP and THPI systems, the contribution of the heave plate cannot be simply regarded as the auxiliary mass only because the plate size not only determines the auxiliary mass but also affects the inherent damping and wave-induced force

to the heave plate. To investigate the influence of the size of the heave plate, the side length of the heave plate varies from 20 m to 60 m with an increment of 10 m, while the thickness of the plate is kept at 0.2 m. To preclude the influence of original heave plate depth, it is assumed as -100 m in this section.

Table 2-4 Optimal natural frequency ratio γ_1 of the THP system

Heave Plate		Case No.					
No.	Size (m)	L1	L2	L3	L4	L5	L6
1	20×20	2.961	3.521	3.020	3.141	2.951	2.961
2	30×30	2.745	3.500	2.790	2.898	2.543	2.745
3	40×40	2.630	3.318	2.673	2.819	2.483	2.630
4	50×50	2.516	3.227	2.650	2.699	2.356	2.516
5	60×60	2.355	3.214	2.398	2.512	2.184	2.355

Table 2-5 Optimal damping ratio ζ_1 of the THP system

Heave Plate		Case No.					
No.	Size (m)	L1	L2	L3	L4	L5	L6
1	20×20	0	0	0	0	0	0
2	30×30	0	0.018	0	0	0	0
3	40×40	0.050	0.027	0.050	0.045	0.054	0.050
4	50×50	0.067	0.076	0.063	0.049	0.079	0.067
5	60×60	0.059	0.075	0.053	0.034	0.081	0.059

Table 2-6 Optimal natural frequency ratio γ_2 of the THPI system

Heave Plate		Case No.					
No.	Size (m)	L1	L2	L3	L4	L5	L6
1	20×20	2.974	3.497	2.991	3.121	2.875	2.974
2	30×30	2.755	3.465	2.802	2.927	2.647	2.755
3	40×40	2.606	3.226	2.65	2.796	2.435	2.606
4	50×50	2.450	3.391	2.502	2.644	2.279	2.450
5	60×60	2.269	3.212	2.312	2.415	2.100	2.269

Table 2-7 Optimal damping ratio ζ_2 of the THPI system

Heave Plate		Case No.					
No.	Size (m)	L1	L2	L3	L4	L5	L6
1	20×20	0.025	0.058	0.009	0	0.072	0.025
2	30×30	0.025	0.001	0.001	0.009	0.018	0.025
3	40×40	0.006	0.001	0.006	0.004	0.008	0.006
4	50×50	0.012	0.007	0.010	0.007	0.015	0.012
5	60×60	0.010	0.006	0.009	0.005	0.017	0.010

Table 2-8 Optimal corner frequency ratio η of the THPI system

Heave Plate		Case No.					
No.	Size (m)	L1	L2	L3	L4	L5	L6
1	20×20	1.097	1.098	1.100	1.099	1.087	1.097
2	30×30	1.087	1.033	1.088	1.100	1.075	1.087
3	40×40	1.147	1.024	1.147	1.139	1.148	1.147
4	50×50	1.239	1.356	1.225	1.191	1.264	1.239
5	60×60	1.285	1.391	1.265	1.214	1.362	1.285

Table 2-9 Optimal inertance-mass ratio δ of the THPI system

Heave Plate		Case No.					
No.	Size (m)	L1	L2	L3	L4	L5	L6
1	20×20	0.010	0.023	0.001	0.001	0.009	0.010
2	30×30	0.009	0.010	0.013	0.001	0.009	0.009
3	40×40	0.047	0.016	0.046	0.036	0.057	0.047
4	50×50	0.065	0.053	0.060	0.045	0.080	0.065
5	60×60	0.060	0.040	0.054	0.035	0.082	0.060

Table 2-4 to Table 2-9 list the optimal parameters for the THP and THPI systems with different sizes of heave plate. Some interesting properties can be acquired from these results. As shown in Table 2-4 and Table 2-6, it is obvious that both the THP and THPI systems are tuned near the wave dominant frequency again rather than the natural frequency of SSP due to the reason as discussed above, and γ_1 and γ_2 are therefore much larger than unity. Another interesting characteristic is that under the majority of loading conditions, the optimal damping ratio for the THP system (ζ_1 in Table 2-5) in the cases with small plate (20×20 m and 30×30 m) is 0, which is the lower bound of the parameter in the optimization. This phenomenon indicates that the inherent damping of the heave plate, namely the viscous damping provided by the water (ζ_{v1} in Table 2-1), exceeds the required damping for the THP to achieve the optimal performance. By probing the dynamic equilibrium equation (Equation (2.6)) and the formula for linearizing the nonlinear damping (Equation (2.7)), it can be seen that the inherent damping term in Equation (2.6) is intrinsically a function of frequency and the amplitude of heave motion. In the cases with small heave plate, the heave motion of the system (SSP together with THP) is large, which can lead to considerable inherent damping. Due to this significant damping, the required optimal damping becomes 0. However, this characteristic does not appear in the optimal damping ratio for the THPI system (ζ_2) as tabulated in Table 2-7. This is because as shown in Figure 2-5(b), the inerter-based system consists of an inerter, a damper and a spring but not just a single damper as shown in the THP system (Figure 2-5(a)), which means the damping ratio ζ_2, the corner frequency ratio η and the inertance-mass ratio δ as

tabulated in Table 2-1 all contribute to the damping term, i.e. the three components form a "composite" damping to the system. To achieve the best performance, the "composite" damping should approach zero instead of each component being zero. This actually can be examined according to Equation (2.25) (n=2). It can be calculated that α_2 is quite small in the THPI system, which is then consistent with that of THP.

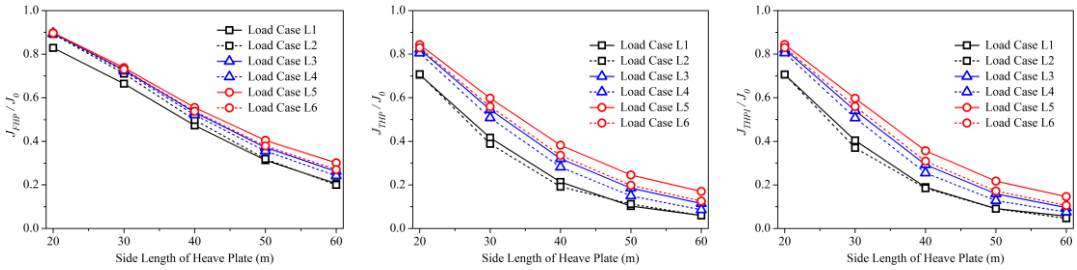

(a) FHP (b) THP (c) THPI

Figure 2-13 Normalized J performance of the FHP, THP and THPI systems with different heave plate sizes

Table 2-10 Influence of the size of the heave plate on the control performance of THPI system compared to the THP system (%)

Case No.	Heave Plate Size (m×m)				
	(a) 20×20	(b) 30×30	(c) 40×40	(d) 50×50	(e) 60×60
L1	-0.05	2.96	11.27	11.70	4.70
L2	0.20	4.74	3.70	18.99	21.42
L3	-0.05	0.86	8.52	14.36	16.22
L4	-0.05	0.07	9.43	14.62	12.48
L5	-0.03	0.09	6.72	11.30	14.13
L6	-0.09	-0.08	7.94	13.30	16.08

To investigate the influence of the size of heave plate, the J performances of SSP with FHP, THP and THPI systems are normalized by the J performance of the SSP without control (J_0). Figure 2-13 shows the corresponding results. It is found that the control performances of the FHP, THP and THPI systems are significantly improved by increasing the size of the heave plate. Table 2-10 tabulates the reduction ratio of the THPI system compared to the THP system for each wave condition. When the plate size is small (20×20 m and 30×30 m), some very small or even negative values are found, which indicates that the THPI system has almost identical or even worse performance compared to the THP system. To further illustrate the problem, the heave response spectra of a SSP with a heave plate of 20×20 m subjected to the working (L1), 10-year (L3) and 100-year (L5) SCS wave loadings are shown in Figure 2-14. As shown, for each wave condition, the heave response spectra of the systems with THP and THPI almost overlap with each other, which demonstrates that the THP and THPI systems with small plate size have nearly the same control performance in reducing the heave response

of SSP. This is primarily due to the fact that there exists a significant inherent damping for the small heave plate as discussed above, and the performances of the THP and THPI systems with small heave plate are mainly determined by their natural frequency ratio and the inherent damping provided by water.

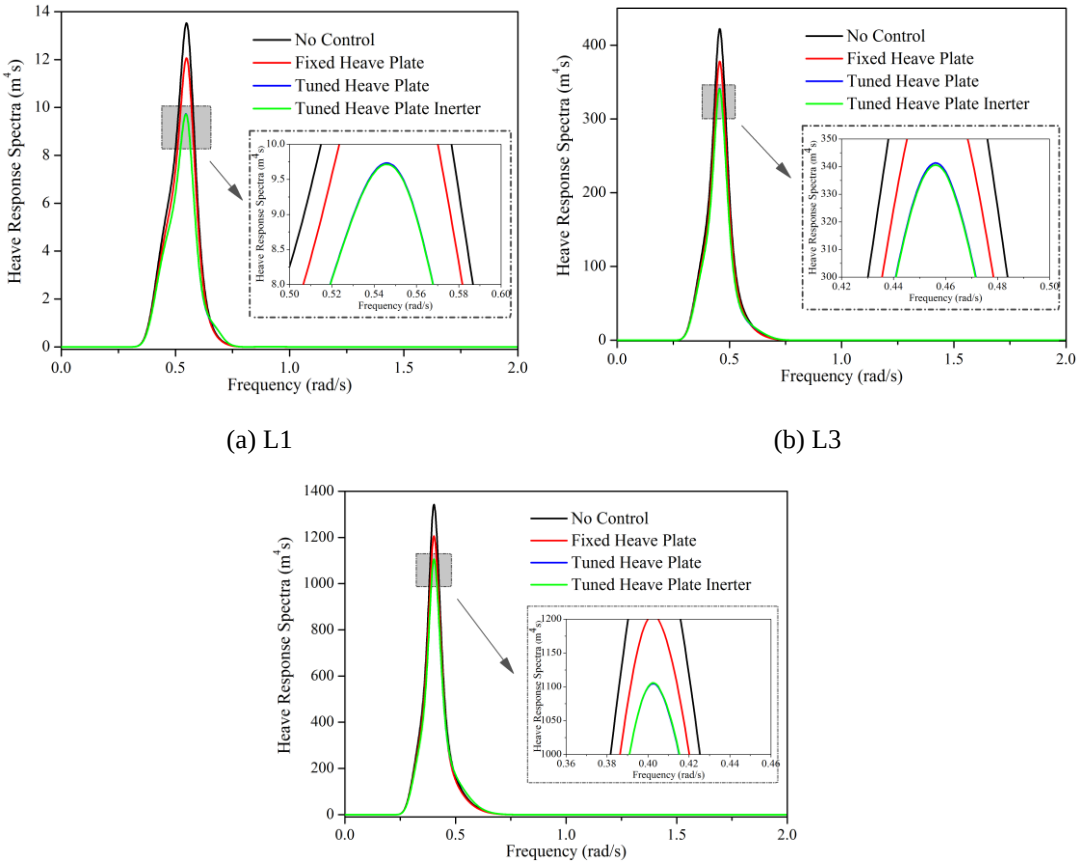

(a) L1 (b) L3

(c) L5

Figure 2-14 Heave response spectra of a SSP system and the SSP with a 20×20 m heave plate

Figure 2-15 graphically shows the reduction ratios that are tabulated in Table 2-10. It is observed that when the size of the heave plate is larger than 40×40 m, the THPI can further improve the performance of THP obviously. As shown, the maximum increment reaches 21.42% when a SSP with a 60×60 m heave plate is subjected to the load case L2. Increasing the size of the heave plate generally leads to better control performance, but it does not necessarily monotonously increase the control performance. For example, in the load case L1, the performance of the SSP with a 60×60 m heave plate is actually smaller than that controlled by a 50×50 m heave plate. This is again due to the fact that the size of the heave plate not only contributes to the auxiliary mass but also influences the inherent damping and wave-induced force as discussed above.

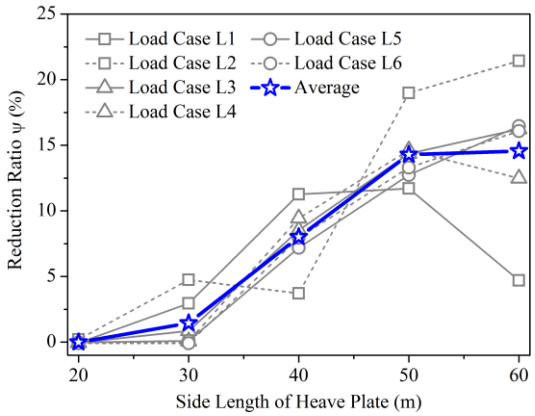

Figure 2-15 Reduction ratios of the THPI system compared to the THP system

2.5.2 Influence of the Original Depth of Heave Plate

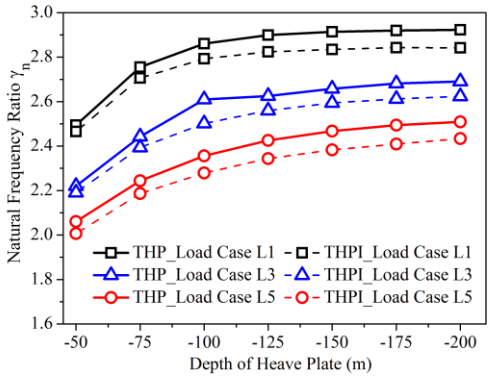

(a) Optimal frequency ratios γ_n of THP and THPI

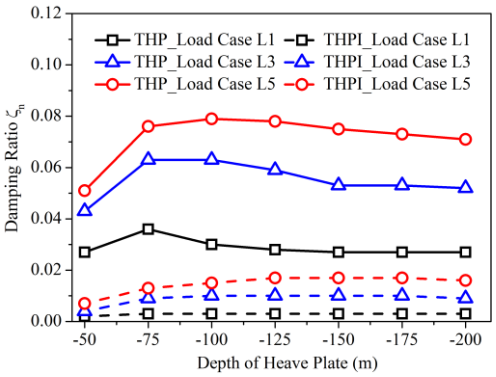

(b) Optimal damping ratios ζ_n of THP and THPI

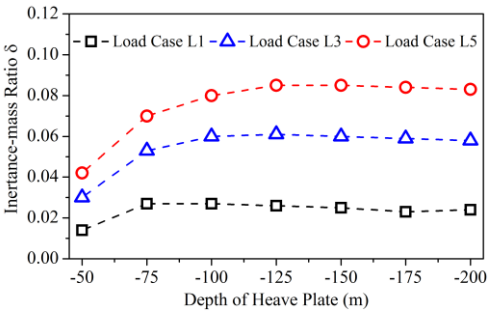

(c) Inertance-mass ratio δ of THPI

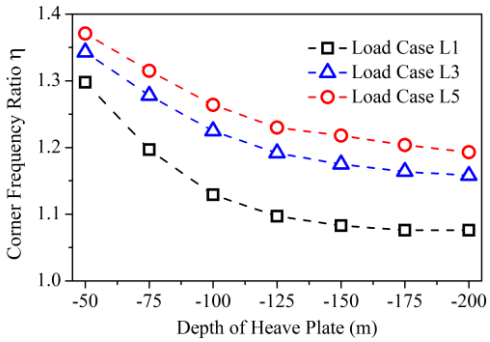

(d) Corner frequency ratio η of THPI

Figure 2-16 Optimal parameters of the THP and THPI systems with different original depths

To reduce the influence of the wave-excited force, heave plate should be deployed with enough depth. Deeper heave plate will inevitably increase the cost for installation and maintenance. It is important to find a reasonable original depth for the heave plate. This section investigates the influence of the depth of heave plate on the performance of THPI. Three wave conditions in SCS, i.e. L1, L3 and L5, are selected for the analyses. The original depth of the heave plate

varies from -50 m to -200 m with an increment of -25 m, and the size of the heave plate is assumed as 50×50 m in this section.

Figure 2-16 shows the optimal parameters for the THP and THPI systems with the heave plate deploying at different depths. As shown in Figure 2-16(a), the optimal frequency ratios of the THP and THPI systems vary with different original depths. When the depth is less than 100 m, both the optimal frequency ratios for the THP and THPI systems increase obviously with the depth. However, when the depth exceeds 100 m, the optimal frequency ratios become almost a constant. For the optimal damping ratios (Figure 2-16(b)) and the inertance to mass ratio (Figure 2-16(c)), a similar trend is observed, i.e. they increase obviously when the original depth of the heave plate is less than 100 m, while the increment becomes less evident when the depth is larger than 100 m. For the corner frequency ratio η, an opposite trend is however obtained. As shown in Figure 2-16(d), η decreases obviously when the depth of the heave plate is small and the slope of the curve becomes smaller when the depth is larger than 100 m.

Figure 2-17 illustrates the normalized J performance of the SSPs with FHP, THP and THPI systems at different heave plate depths under different load cases. It is found that the control performances of FHP, THP and THPI systems can be improved by increasing the depth of the heave plate, but the extents of improvement decrease gradually with the increase of the depth. As shown, when the original heave plate depth is larger than 100 m, the improvements for different cases are not obvious.

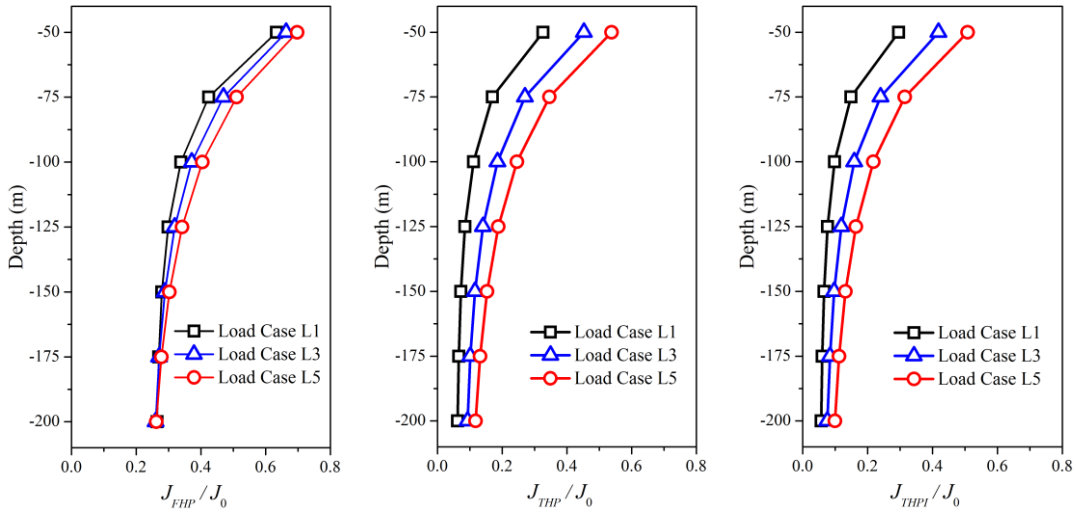

(a) FHP (b) THP (c) THPI

Figure 2-17 Normalized J performance of FHP, THP and THPI systems with different plate depths

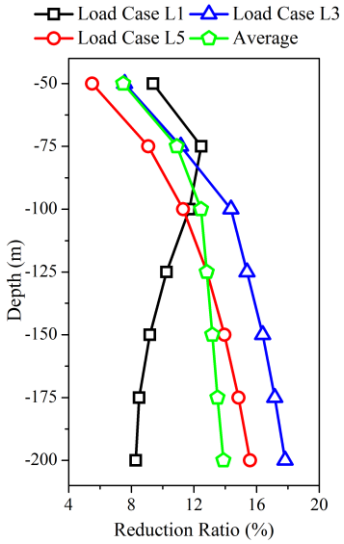

Figure 2-18 Reduction ratios of THPI with different heave plate depths and the average values

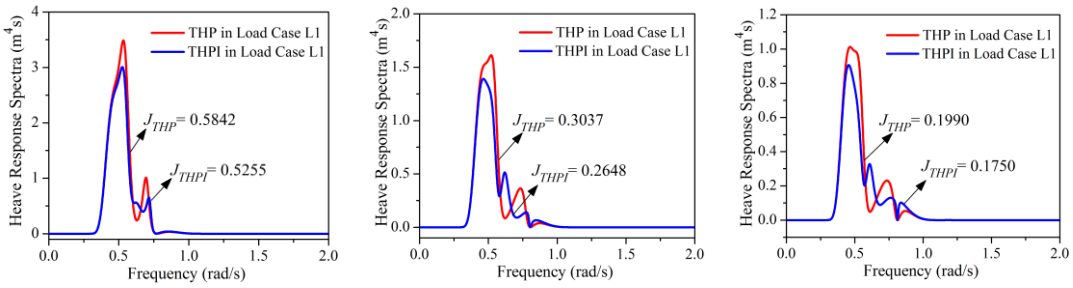

(a) Depth of -50 m in L1 (b) Depth of -75 m in L1 (c) Depth of -100 m in L1

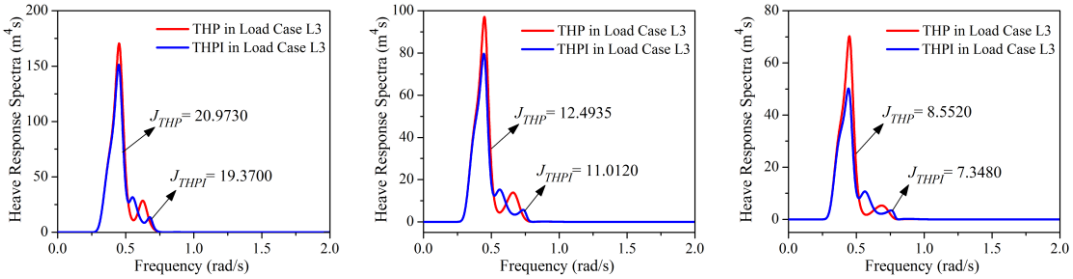

(d) Depth of -50 m in L3 (e) Depth of -75 m in L3 (f) Depth of -100 m in L3

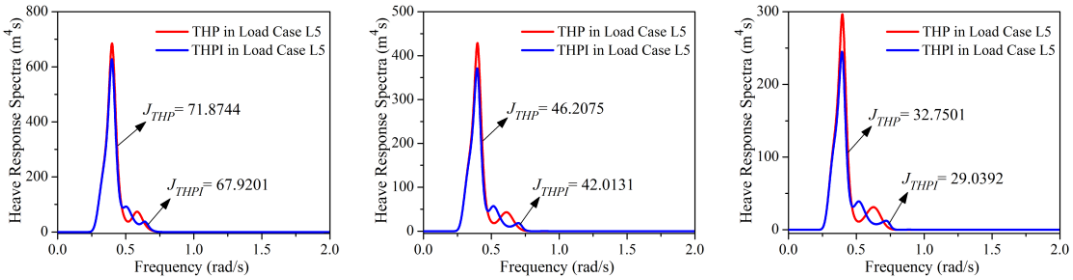

(g) Depth of -50 m in L5 (h) Depth of -75 m in L5 (i) Depth of -100 m in L5

Figure 2-19 Heave response spectra of the SSP with THP and THPI at original heave plate depth of -50 m, -75 m and -100 m

To demonstrate the effect of inerter, the reduction ratios of THPI system (compared to the THP system) at different original depths of the heave plate are illustrated in Figure 2-18. For load cases L3 and L5, the reduction ratio increases with the growth of the heave plate depth. It is interesting to find that in the load case L1, the maximum reduction ratio is achieved at the depth of -75 m, and the effect of inerter then becomes less obvious. To illustrate the reason, the heave response spectra of the SSP with THP and THPI at the original heave plate depth of -50 m, -75 m and -100 m are illustrated in Figure 2-19, and the corresponding values of the *J* performance index are also shown in the sub-figures. As shown, for load cases L3 (Figure 2-19(d), (e) and (f)) and L5 (Figure 2-19 (g), (h) and (i)), the heave response spectra at the dominant wave frequency (i.e. the first peaks in the figures) in the SSP-THPI system (the blue curve) are more evidently suppressed with the increment of the original heave plate depth, which in turn results in the monolithic control performance improvement as shown in Figure 2-18. For load case L1, the installing of the inerter device to the THP system does not obviously influence the heave response spectra at the dominant wave frequency. As shown in Figure 2-19(a), (b) and (c), the response spectrum ratios at the dominant wave frequency with different original heave plate depth are almost the same. While both the shapes of the SSP-THP and SSP-THPI systems are slightly changed under the different water depths. Since load case L1 is a working condition, the *J* value for each case is very small. The very small variations in the shapes of the heave response spectra result in the obvious enclosed area changes and therefore lead to the evident reduction ratio variations. The average reduction ratios of these load cases are also plotted in Figure 2-18. As shown, the average reduction ratio increases with the growth of the heave plate depth, but the performance improvement is not obvious when the depth exceeds 100 m. The above results show that for the SSP shown in Figure 2-1, deploying the heave plate at an original depth of -100 m might be a good option in terms of control effectiveness and economic perspective.

2.6 Realization of the Inerter

The above analytical results demonstrate that the effectiveness of THP system can be further enhanced by forming a THPI system. As discussed above, the analytical model of the THPI system can be represented by Figure 2-5(b). The spring and damper elements in Figure 2-5(b) are commercially available and they can be selected after the corresponding stiffness and damping coefficient are determined based on the optimization method as presented in Section 2.3. The essence of the problem then becomes how to develop an efficient and suitable inerter for the THPI.

As reviewed in the introduction, previous studies on inerter mainly focused on the analytical studies, and very limited studies (e.g. Refs. [18, 21]) reported the realization of an inerter.

Smith et al. [18] developed an inerter driven by a rack and pinion system as shown in Figure 2-20. An inertance of 726 kg was achieved by using a flywheel with a weight of 0.225 kg. In other words, the mass was amplified 3227 times by using this mechanism. Ikago et al. [21] proposed another type of inerter as shown in Figure 2-21. As shown, a ball screw was utilized to transform the linear motion into the high-speed rotational motion of an internal tube immersed in the viscous fluid, which in turn provided significant damping force and inertial force to the primary system. A flywheel was installed in the prototype to increase its rotational moment of inertia. With such a design, a mass amplification of 175 times was achieved as reported in Ref. [21]. Recently, it was also reported that the mass amplifications of several thousand [43] and 1.5 million folds [44] have been respectively realized by using the ball-screw and hydraulic inerter. For the conventional inerters, they are normally designed to be very compact due to the limited space between the storeys of building structures where these inerters are normally applied to. In the ocean environment, no such constraint exists, the size of the inerter can be larger, which can result in more evident mass amplification effect since the inertance is related to the radius of the flywheel.

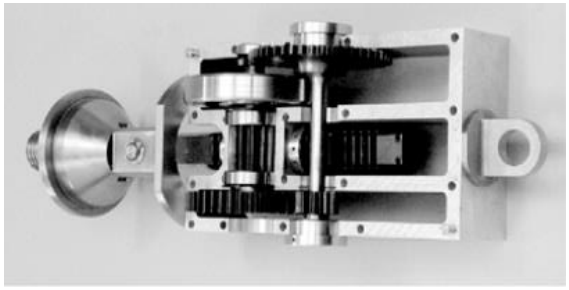

Figure 2-20 Rack-and-pinion inerter developed by Smith et al. [18]

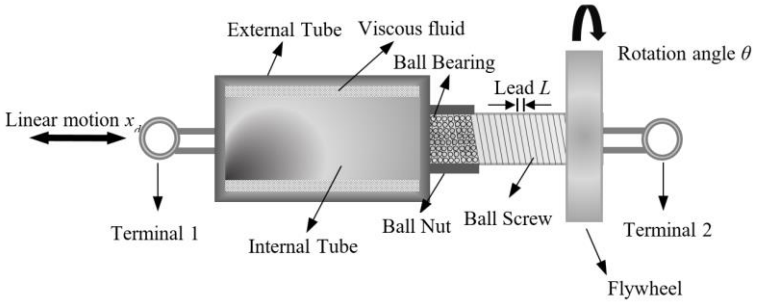

Figure 2-21 Schematic representation of the inerter developed by Ikago et al. [21]

In the present paper, a novel waterwheel inerter device, which is inspired by the waterwheel, is proposed. Figure 2-22 shows the schematic view of the proposed device. It can be seen that this novel inerter includes a waterwheel and a ball screw, and these two components are connected together by many truss structures. The waterwheel consists of an outer plate and two lateral plates (Figure 2-22(c)), and it is divided into a number of small cabins along the circumferential direction by the diaphragms. The inner and outer radii of the waterwheel are

r_0 and r_1 respectively. Similar to the design as shown in Figure 2-21, the ball screw is utilized to transform the linear motion into the rotational motion of the waterwheel in this inerter. Compared to Ref. [21], this novel waterwheel inerter has the following obvious advantage: the mass of the device is concentrated at the waterwheel, which is with a distance of r_0 from the rotating axis (the axis of the ball screw), as will be demonstrated in Equation (2.48), this design can generate larger inertance to the system. Moreover, the water within the cabins can contribute to the physical mass of the inerter, which further increases the inertance.

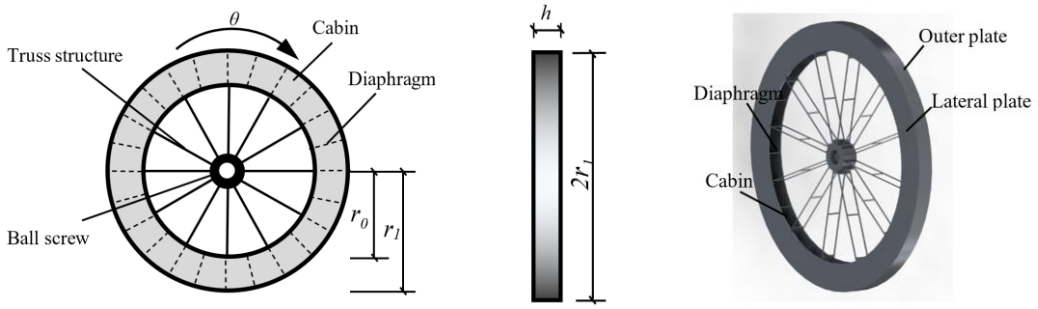

(a) Front view (b) Side view (c) 3D view

Figure 2-22 Schematic view of the proposed waterwheel inerter

As mentioned above, a ball screw is utilized to convert the linear motion into the rotational motion of the waterwheel. Therefore, the rotational angle θ of the shaft connected to the waterwheel can be written as [40]

$$\theta = \frac{2\pi}{L} x_d \tag{2.42}$$

where x_d is the relative displacement between Terminals 1 and 2 (refer to Figure 2-21) and L is the lead of the ball screw. The angular velocity $\dot{\theta}$ and angular acceleration $\ddot{\theta}$ therefore can be expressed as follows:

$$\dot{\theta} = \frac{2\pi}{L} \dot{x}_d \tag{2.43}$$

$$\ddot{\theta} = \frac{2\pi}{L} \ddot{x}_d \tag{2.44}$$

where, $\dot{x}_d$ and $\ddot{x}_d$ are the velocity and acceleration respectively.

For a rotating waterwheel, the inertial torque T_0 can be calculated by

$$T_0 = I\ddot{\theta} \tag{2.45}$$

where I is the moment of inertia of the waterwheel inerter, which includes two components I_1 and I_2, in which I_1 is from the constrained water and lateral plates and I_2 is from the outer plate, and they can be calculated as follows:

$$I_1 = \frac{1}{2} m_{w1}(r_1^2 + r_0^2) = \frac{1}{2}\{\rho\pi h - 2\rho\pi t + 2\rho_s\pi t\}(r_1^4 - r_0^4) \quad (2.46)$$

$$I_2 = m_{w2} r_1^2 = 2\rho_s\pi h t r_1^3 \quad (2.47)$$

where m_{w1} is the mass of the constrained water and lateral plates and m_{w2} is the mass of the outer plate; ρ is the density of water; ρ_s is the density of steel; h is the depth of the waterwheel; t is the thickness of steel plate. It should be noted that the mass of the diaphragms is ignored in the Equations (2.46) and (2.47) since it is quite small compared to the other components.

By neglecting the friction force in the ball screw, the axial force of the waterwheel caused by the inertial torque T_0 is

$$F_d = \frac{2\pi}{L} T_0 = \left(\frac{2\pi}{L}\right)^2 \left\{\frac{1}{2}(\rho\pi h - 2\rho\pi t + 2\rho_s\pi t)(r_1^4 - r_0^4) + 2\rho_s\pi h t r_1^3\right\} \ddot{x}_d \quad (2.48)$$

and the inertance is

$$m_e = \left(\frac{2\pi}{L}\right)^2 \left\{\frac{1}{2}(\rho\pi h - 2\rho\pi t + 2\rho_s\pi t)(r_1^4 - r_0^4) + 2\rho_s\pi h t r_1^3\right\} \quad (2.49)$$

It should be noted that r_0 and r_1 are very small in the design as proposed by Ikago et al. [21]. While in the current design, there is no constraint for the dimension of the inerter, I_1 and I_2 in Equations (2.46) and (2.47) can be large, which in turn can result in larger inertance to the device. Moreover, an inner tube was immersed in the viscous fluid in Ref. [21] to provide the damping force to the system as discussed above. For the proposed inerter, it is directly installed in the sea. The sea water can also provide some damping force to the system. However, as the kinematic viscosity of water ν is very small (which is $1.003 \times 10^{-6}\ m^2/s$ at the temperature of $20°C$ [45]), the viscous damping force in the tangential direction caused by the shear deformation of the water is very small and can be neglected. In this case, a damper as shown in Figure 2-5(b) is required to provide the damping force, and the damper can be selected after the damping coefficient is determined by the parameter optimization as discussed. In fact, using an additional damper to provide damping is a common practice for the inerter design. For example, Smith et al. [18] and Papageorgiou et al. [46] adopted the similar design.

Table 2-11 Example design parameters of the waterwheel inerter for the 50×50 m THPI under L3

Parameters	L (m)	h (m)	t (m)	r_0 (m)	r_1 (m)
Value	0.05	0.2	0.005	0.5	0.858

To demonstrate the effectiveness of the proposed waterwheel inerter for SSP heave motion suppression, the load case L3 is adopted as an example in this section. As given in Table 2-3, the optimal frequency ratio γ_2, corner frequency ratio η, inertance-mass ratio δ and damping

ratio ζ_2 of the THPI are 2.502, 1.225, 0.060 and 0.010, respectively. For the investigated SSP, the natural frequency is 0.2040 rad/s, and the secondary mass (which includes the physical mass and added mass of heave plate, namely $m_1 + m_1'$ in Equation (2.19) is 62300 tonnes. According to Table 2-1 and Equation (2.29), the stiffness k_3, damping coefficient c_2 and inertance m_b of the THPI can be calculated, and they are 37 kN/m, 101 kN·s/m and 3738 tonnes, respectively. As mentioned above, the spring and damper can be selected from the commercial products. For the waterwheel inerter, the parameters tabulated in Table 2-11 can be used to achieve the required inertance of 3738 tonnes based on Equation (2.49). It should be noted that the total physical mass of the inerter (including the mass of the waterwheel and constrained water in the cabins) is 0.636 tonnes, i.e. a mass amplification of 5873 times is achieved by this waterwheel inerter.

2.7 Conclusions

This paper carries out analytical studies on the effectiveness of using THPI system to control the heave motion of offshore SSP. For comparison, the SSP without any control device and controlled by FHP and THP are also investigated. The mean square heave motions of the SSP controlled by different devices are stochastically derived and the optimal values for different parameters are obtained by solving a H_2 optimization problem. The heave motions of the SSP without and with different control devices subjected to six wave conditions are analyzed and discussed. Analytical results reveal that:

(1) Compared to the FHP and THP systems, the THPI system can lead to better control performance. The THPI system can further reduce the heave motion up to about 19% compared to the THP system.

(2) The size of the heave plate can significantly influence the control effectiveness of THPI. Increasing the size of the heave plate generally leads to better control performance, but the increase in the control performance of THPI is not monotonic with the heave plate size.

(3) The depth of the heave plate obviously influences the control performance of THPI especially when the depth of the heave plate is small. For the example SSP considered in the analyses, the influence of depth on the heave motion control can be neglected when the depth of the heave plate is larger than 100 m.

(4) A novel waterwheel inerter is schematically suggested to realize the THPI for SSP heave motion control. Compared to the conventional designs, the size of the proposed inerter can be larger and the mass is concentrated at the edge of the device which increases the mass amplification effect.

It should be noted that only the analytical studies are performed in the present study. To further demonstrate the effectiveness of the proposed method, extensive numerical and experimental studies are necessary, and they will be further investigated in future studies.

2.8 References

[1] Kandasamy R, Cui F, Townsend N, Foo CC, Guo J, Shenoi A et al. A review of vibration control methods for marine offshore structures. Ocean Eng. 2016;127:279-97.

[2] Thiagarajan K, Troesch AW. Effects of appendages and small currents on the hydrodynamic heave damping of TLP columns. J Offshore Mech Arct Eng. 1998:37-42.

[3] Tao L, Lim KY, Thiagarajan K. Heave response of classic spar with variable geometry. J Offshore Mech Arct Eng. 2004;126:90-5.

[4] Downie M, Graham J, Hall C, Incecik A, Nygaard I. An experimental investigation of motion control devices for truss spars. Mar Struct. 2000;13:75-90.

[5] Tao L, Cai S. Heave motion suppression of a Spar with a heave plate. Ocean Eng. 2004;31:669-92.

[6] Subbulakshmi A, Jose J, Sundaravadivelu R, Selvam RP. Effect of Viscous Damping on Hydrodynamic Response of Spar with Heave Plate. Aquat Procedia. 2015;4:508-15.

[7] An S, Faltinsen OM. An experimental and numerical study of heave added mass and damping of horizontally submerged and perforated rectangular plates. J Fluids Struct. 2013;39:87-101.

[8] Kaynia AM, Biggs JM, Veneziano D. Seismic effectiveness of tuned mass dampers. J Struct Div. 1981;107:1465-84.

[9] Jangid R. Optimum multiple tuned mass dampers for base-excited undamped system. Earthq Eng Struct Dyn. 1999;28:1041-9.

[10] Bi K, Hao H. Using pipe-in-pipe systems for subsea pipeline vibration control. Eng Struct. 2016;109:75-84.

[11] Zuo H, Bi K, Hao H. Using multiple tuned mass dampers to control offshore wind turbine vibrations under multiple hazards. Eng Struct. 2017;141:303-15.

[12] Nikoo HM, Bi K, Hao H. Effectiveness of using pipe-in-pipe (PIP) concept to reduce vortex-induced vibrations (VIV): Three-dimensional two-way FSI analysis. Ocean Eng. 2018;148:263-76.

[13] Zhu H, Ou J, Zhai G. Conceptual design of a deep draft semi-submersible platform with a moveable heave-plate. J Ocean U China. 2012;11:7-12.

[14] Liu K, Ou J. A novel tuned heave plate system for heave motion suppression and energy harvesting on semi-submersible platforms. Sci China Technol Sci. 2016;59:897-912.

[15] Zhu H, Hu C, Liu Y. Optimum Design of a Passive Suspension System of a Semisubmersible for Pitching Reduction. J Dyn Syst Meas Control. 2016;138:121003.

[16] Liu K, Liang H, Ou J. Numerical investigation of a tuned heave plate energy-harvesting system of a semi-submersible platform. Energies. 2016;9:82.

[17] Smith MC. Synthesis of mechanical networks: the inerter. IEEE Trans Automat Contr. 2002;47:1648-62.

[18] Smith MC, Wang FC. Performance Benefits in Passive Vehicle Suspensions Employing Inerters. Veh Syst Dyn. 2004;42:235-57.

[19] Papageorgiou C, Smith MC. Positive real synthesis using matrix inequalities for mechanical networks: application to vehicle suspension. IEEE T Contr Syst T. 2006;14:423-35.

[20] Hwang JS, Kim J, Kim YM. Rotational inertia dampers with toggle bracing for vibration control of a building structure. Eng Struct. 2007;29:1201-8.

[21] Ikago K, Saito K, Inoue N. Seismic control of single-degree-of-freedom structure using tuned viscous mass damper. Earthq Eng Struct Dyn. 2012;41:453-74.

[22] Marian L, Giaralis A. Optimal design of a novel tuned mass-damper–inerter (TMDI) passive vibration control configuration for stochastically support-excited structural systems. Probabilistic Eng Mech. 2014;38:156-64.

[23] Giaralis A, Petrini F. Wind-Induced Vibration Mitigation in Tall Buildings Using the Tuned Mass-Damper-Inerter. J Struct Eng. 2017;143:04017127.

[24] Lazar IF, Neild SA, Wagg DJ. Using an inerter-based device for structural vibration suppression. Earthq Eng Struct Dyn. 2014;43:1129-47.

[25] Lazar I, Neild S, Wagg D. Vibration suppression of cables using tuned inerter dampers. Eng Struct. 2016;122:62-71.

[26] Wen Y, Chen Z, Hua X. Design and Evaluation of Tuned Inerter-Based Dampers for the Seismic Control of MDOF Structures. J Struct Eng. 2016;143:04016207.

[27] Pietrosanti D, De Angelis M, Basili M. Optimal design and performance evaluation of systems with Tuned Mass Damper Inerter (TMDI). Earthq Eng Struct Dyn. 2017;46:1367-88.

[28] Hu Y, Chen MZQ. Performance evaluation for inerter-based dynamic vibration absorbers. Int J Mech Sci. 2015;99:297-307.

[29] Jin X, Chen MZQ, Huang Z. Minimization of the beam response using inerter-based passive vibration control configurations. Int J Mech Sci. 2016;119:80-7.

[30] Hu Y, Chen MZQ. Passive structural control with inerters for a floating offshore wind turbine. The 36th Chinese Control Conference (CCC) IEEE; 2017. p. 9266-71.

[31] Hu Y, Chen MZQ. Inerter-based passive structural control for load mitigation of wind turbines. The 29th Chinese Control And Decision Conference (CCDC): IEEE; 2017. p. 3056-61.

[32] Faltinsen O. Sea loads on ships and offshore structures: Cambridge university press; 1993.

[33] Taflanidis AA, Angelides DC, Scruggs JT. Simulation-based robust design of mass dampers for response mitigation of tension leg platforms. Eng Struct. 2009;31:847-57.

[34] Veritas DN. Offshore standard DNV-OS-E301 position mooring. DNV: Norway. 2010.

[35] Veritas DN. Modelling and analysis of marine operations. Offshore Standard. 2011.

[36] Schellin T, Kirsch A. Low-frequency damping of a moored semisubmersible obtained from simulated extinction tests and mean wave drift forces. Appl Ocean Res. 1989;11:202-11.

[37] Chakrabarti SK. Hydrodynamics of offshore structures: WIT press; 1987.

[38] Hasselmann K, Barnett TP, Bouws E, Carlson H, Cartwright DE, Enke K et al. Measurements of wind-wave growth and swell decay during the Joint North Sea Wave Project (JONSWAP). Ergänzungsheft. 1973:8-12.

[39] Travanca J, Hao H. Control of wave-induced vibrations on floating production systems. Ocean Eng. 2017;141:35-52.

[40] Hoang N, Fujino Y, Warnitchai P. Optimal tuned mass damper for seismic applications and practical design formulas. Eng Struct. 2008;30:707-15.

[41] Waris MB, Ishihara T. Dynamic response analysis of floating offshore wind turbine with different types of heave plates and mooring systems by using a fully nonlinear model. Coupled Syst Mech. 2012;1:247-68.

[42] Den Hartog JP. Mechanical vibrations: Courier Corporation; 1985.

[43] Watanabe Y, Ikago K, Inoue N, Kida H, Nakaminami S, Tanaka H et al. Full-scale dynamic tests and analytical verification of a force-restricted tuned viscous mass damper. Proceedings of the 15th World Conference on Earthquake Engineering, Lisbon, Portugal, 2012.

[44] Nakaminami S, Kida H, Ikago K, Inoue N. Dynamic Testing of a Full-scale Hydraulic Inerter-Damper for the Seismic Protection of Civil Structures. Proceedings of the 7th International Conference on Advances in Experimental Structural Engineering; 2017. p. 57-79.

[45] Crittenden JC, Trussell RR, Hand DW, Howe KJ, Tchobanoglous G. MWH's water treatment: principles and design: John Wiley & Sons; 2012.

[46] Papageorgiou C, Houghton NE, Smith MC. Experimental testing and analysis of inerter devices. J Dyn Syst Meas Contr. 2009;131:011001.

CHAPTER 3 USING ROTATIONAL INERTIA DAMPER (RID) FOR HEAVE MOTION MITIGATION

Abstract[3]

Semi-submersible platforms (SSPs) have been widely used in offshore industries for energy exploitation. SSP is vulnerable to the heave motions and continuous heave motions may cause fatigue damage to the structural and nonstructural members or even sinking of the platform. It is therefore imperative to suppress the undesired heave motions of SSP. In the present study, a novel hydraulic rotational inertia damper (RID), which can amplify the fluid resistance of the submerged plates, is proposed based on the concept of inerter to mitigate the heave motions of SSP. Analytical studies are conducted in both the frequency and time domains to investigate the control effectiveness of the proposed method. For comparison, the responses of the SSP controlled by the commonly adopted fixed heave plate (FHP) and tuned heave plate (THP) are also calculated. Analytical results show that the proposed RID system is more effective in reducing the heave motions of SSP, and it can achieve the identical control performance of the FHP and THP systems by using a much smaller plate size, thus smaller physical mass (less than 0.8% of the mass of the heave plate in this research). Furthermore, it is found that the RID system performs better in the harsher wave conditions, and its effectiveness increases with the increase of wave height. The proposed method provides an attractive alternative to effectively and economically suppress the heave motions of SSP in the shallow sea.

3.1 Introduction

With the increasing demand for energy in the modern society, offshore energies have become a very important contributor to the global energy supply. As reported in 2012, offshore oil and gas provided 37% and 28% of the global energy [1], and these percentages are increasing in the recent years. To exploit offshore energies, various types of platforms have been developed, and they can be roughly categorized as the sea-bed-mounted platforms (e.g. the jack-up platform, gravity platform, etc.) and floating platforms (e.g. semi-submersible platform, tension leg platform and spar platform, etc.). The floating platforms can be deployed in the deep and ultra-deep waters, as well as in the shallow sea. As reported by the Bureau of Ocean Energy Management, Regulation and Enforcement (BOEMRE) [2], 34% of floating platforms are working in the shallow sea with the water depth less than 304.8 m. Among these floating platforms, semi-submersible platform (SSP) is most widely applied due to its wider range of

[3] This chapter was published in *Structural Control and Health Monitoring* with the full bibliographic citation as follows:
Ma R, Bi K, Hao H. A novel rotational inertia damper for heave motion suppression of semisubmersible platform in the shallow sea. Struct Control Health Monit. 2019;26:e2368. https://doi.org/10.1002/stc.2368.

applicable water depth, larger deck area, and bigger payload capacity. However, the shallow draft and large pontoons of SSP may lead to the excessive heave motion to the platform. These continuous vibrations may not only result in the fatigue damage to the structural/non-structural components but also affect the health of the crew and reduce the serviceability and efficiency of the platform. The aim of the present study is to propose a novel method to suppress the excessive heave motion of SSP in the shallow sea.

Considerable research efforts have been made to suppress the adverse vibrations of offshore platforms, and various control methods have been proposed. These methods can be roughly classified as the passive, active, semi-active and hybrid methods [3]. Compared to the other control systems, passive methods require no external energy input and are widely used in engineering practice. For SSP, the most commonly utilized passive method is to install a ballast or fixed heave plate (FHP) at the bottom of the platform to increase the added mass/damping of the system. The effectiveness of using FHP for SSP heave motion mitigation has been verified through both numerical and experimental studies by many researchers [4, 5]. Instead of rigidly connecting the SSP and heave plate, tuned heave plate (THP) has also been developed recently to further improve the performance of the control system based on the concept of tuned mass damper (TMD), a method that is widely applied in reducing the seismic-, wind- and wave-induced vibrations of engineering structures [6-10]. In this system, SSP and the heave plate is connected by carefully designed (i.e. tuned) springs and dampers. The THP concept was firstly proposed by Zhu et al. [11] in 2012, and was further developed to harvest the wave energy during the control process [12] and to control the pitch motion of SSP [13, 14].

The nature of FHP is to increase the draft of the platform by the added mass. Very large and heavy heave plate is therefore required to make this method effective. For the SSP-THP system, the added mass (the heave plate) is normally 1% to a few percent of the primary structure (SSP) in the conventional TMD design [15, 16]. For the offshore platform, the mass of the platform is huge, the added mass is therefore also very large. For example, the mass of a typical offshore platform reaches 51700 tonnes as reported in Liu and Ou [12], if a commonly used mass ratio of 2% is adopted to control the vibrations of the SSP, an additional mass of 1034 tonnes is required. This large mass not only increases the cost of SSP, but also significantly increases the install difficulty and maintenance cost. It would therefore be attractive to develop alternative techniques that can achieve a similar control performance but utilize a smaller auxiliary mass or a smaller plate.

A novel two-terminal mechanical device dubbed inerter by Smith [17] may shed some lights on achieving this objective. The most significant characteristic of inerter is the capability of generating an apparent mass that is much larger than its physical mass (i.e. the mass

amplification effect) by transforming the linear motion into high-speed rotational motion through the rack-and-pinion or a ball screw assembly. Due to this special characteristic, the inerter was initially utilized to improve the performance of the suspension system in Formula One racing cars under the name of J-damper [18, 19]. In recent years, this concept began to be introduced into civil engineering structures. Hwang et al. [20] proposed a rotational inertia viscous damper (RIVD) in association with a toggle bracing structure to reduce the seismic vibrations of building structures. This damper consisting of an internal tube driven by a ball screw and rotating in a chamber filled with viscous fluid, could provide a significant damping force to the primary structure by shearing the viscous fluid. Ikago et al. [21] extended the concept of the RIVD by developing a tuned viscous mass damper (TVMD), and conducted shaking table tests to verify its effectiveness. The experiment demonstrated that an apparent mass of 350 kg was achieved by a flywheel with a physical mass of 2 kg by using a ball screw mechanism. In other words, the physical mass of the flywheel was amplified 175 times by using this device. Recently, the mass amplification of several thousand folds was achieved by utilizing the similar mechanism [22]. Marian and Giaralis [23] proposed a tuned mass-damper-inerter (TMDI) by adding an inerter to the TMD system and demonstrated its effectiveness in reducing the vibrations of the stochastically support-excited structure. The TMDI system was also found to be effective in reducing the seismic-induced [24] and wind-induced [25] vibrations of building structures, minimizing the beam response [26] and enhancing the performance of base isolation system [27-29]. Lazar et al. developed a tuned inerter damper (TID), a special variant of TMDI without the attached mass, to suppress the seismic-induced responses of a single-degree-of-freedom (SDOF) system [30] and cables [31]. The results demonstrated that the TID system could be an excellent alternative to the conventional TMD system owing to its smaller physical mass and overall size. Hu and Chen [32, 33] proposed installing inerter-based device in the nacelle of the offshore wind turbine to control wind- and wave- induced vibrations of the tower. It should be noted that, similar to the TMD system, optimization should be applied to make these inerter-based devices effective, a considerable amount of research efforts [34-39] were also made on the optimal design and configuration of these inerter-based control systems based on the different performance indicators, e.g. the H_2 performance, H_∞ performance and reliability criteria.

Very recently, the authors proposed using inerter-based device to improve the control effectiveness of offshore SSP in the deep water [40], in which a novel waterwheel inerter was proposed to be installed between the SSP and heave plate to form a tuned heave plate inerter (THPI) to further improve the control effectiveness of the THP system. Analytical results show that the control effectiveness can be further improved by 11% to 19% compared to the conventional THP system depending on different sea wave conditions. However, it should be

noted that the control effectiveness is sensitive to the size (thus the mass) of the heave plate. When the heave plate is not big enough, the improvement on the control effectiveness is not prominent and under certain sea wave states the control effectiveness might be even slightly reduced [40]. In other words, the proposed method cannot reduce the mass of the heave plate although it can increase the control effectiveness by more than 10%. This is because the inerter device is a two-terminal device, and the control effectiveness is most evident if one end of the device can be connected to a fixed base, e.g., the ground, to best use the mass amplification effect as reported by some researchers [30, 41]. In the previous work [40], the waterwheel inerter was installed between the SSP and heave plate, the relative motion between the two ends of the device was therefore not large, which limited the control effectiveness. Same level of performance improvement was reported by other researchers on other types of structures [36] when similar arrangement was applied.

In the present study, another novel inerter-based damper dubbed rotational inertia damper (RID) is proposed to control the heave motion of SSP in the shallow water by using the currently available technologies. Compared to the installation of inerter damper between the platform and heave plate in the previous work [40], this inerter device is proposed to be installed between the seabed and SSP. This new proposed installation limits its application mainly to the SSP in the shallow sea, but as will be demonstrated in the numerical results, it makes the proposed device very effective in controlling the heave motion of SSP since it can apply not only inertial force but also significant damping force on the platform.

The present paper is organized as follows: the conceptual design and feasibility of applying RID system for SSP heave motion mitigation are introduced in Section 3.2; the analytical models for SSPs with different control systems (i.e. FHP, THP and RID) are developed and the equations of motion are derived in Section 3.3; Section 3.4 describes the selected wave conditions in this research; Section 3.5 reports the effectiveness of the FHP, THP and RID systems for SSP heave motion mitigation; and finally Section 3.6 summarizes the major conclusions of this work.

3.2 Rotational Inertia Damper and Its Mechanical Behavior

3.2.1 Proposed RID System and Feasibility Analysis

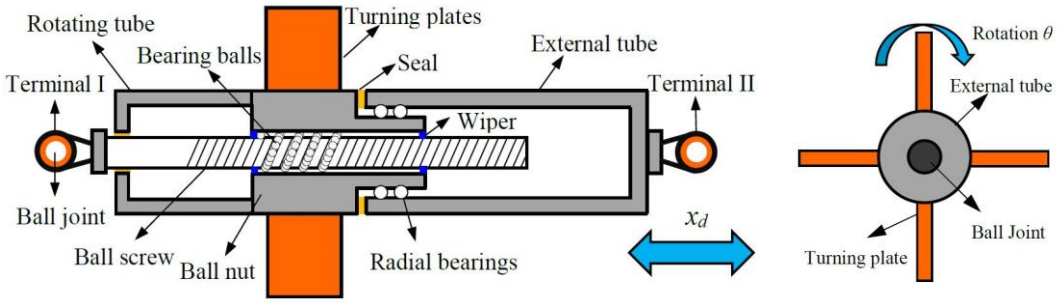

(a) Front view (b) Side view

Figure 3-1 Schematic drawing of the proposed rotational inertia damper

This paper employs an inerter-based device to suppress the heave motion of offshore SSP. Since SSPs are located in the ocean environment, it therefore can utilize the fluid resistance capability to enhance the control effectiveness. Inspired by this idea, a novel hydraulic rotational inertia damper (RID) as depicted in Figure 3-1 is proposed. As shown, the RID system consists of a ball screw system, radial bearings, an external tube, a rotating tube, two ball joints and a suit of turning plates. The ball screw system including a ball screw, a ball nut and many bearing balls can transform the heave motion into the high-speed rotational motions of the turning plates which are rigidly connected with the ball nut as shown in the figure. The radial bearings allow the ball nut to spin inside the external tube. The wipers are adopted to offer a good protection of the ball screw from swarf or rust and thus improve its durability. The RID system is enclosed by the external tube, rotating tube and seals to prevent the invasion from the foreign stuff such as marine growth. The two terminals of the RID are connected with the platform and seabed through the two ball joints. Except the wipers and seals which are made from rubber, all the other components are made from steel, special coating techniques therefore may be required to prevent the corrosion of these components in marine environment. It should be noted that only the conceptual design of the RID system is presented here, detailed design and manufacture will be investigated in the future.

Another issue is the feasibility of the proposed method, which is discussed here. As demonstrated in many previous studies [30, 41], the inerter-based device will be most effective when one terminal of the device is connected with the ground. The target of the proposed method is therefore for the platforms that are located in the shallow water (with the water depth smaller than 304.8 m in particular [2]), where fixing the device to the seabed is feasible. For the deep (304.8~1524 m) and ultra-deep waters (>1524 m) [2], the connection of the device to the seabed might be difficult due to the large water depth, the application of the proposed method may not be feasible.

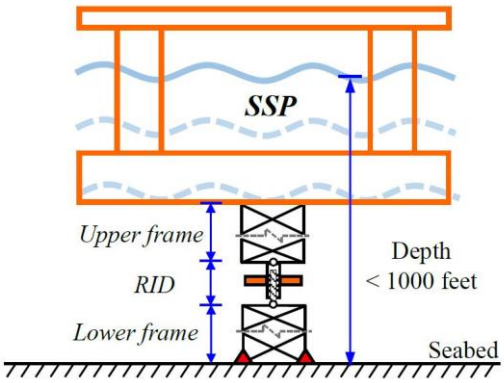

Figure 3-2 Realization of the proposed RID system for SSP heave motion suppression

For the shallow water, the sea-bed-mounted (i.e. fixed) platforms are most widely adopted. However, the most economic design of these fixed platforms is when the water depth is smaller than 137.16 m as reported in Ref. [42]. When the water depth is larger than 137.16 m, the supporting system should be designed with very large dimensions in order to reduce the lateral vibration of the platform resulting from wind and sea wave loadings. To solve this problem, a feasible arrangement as illustrated in Figure 3-2 is proposed in the present study. As shown, instead of constructing a monolithic supporting system, the supporting system is divided into two parts, i.e. the upper frame and the lower frame. The upper frame is rigidly connected with the platform and the lower frame is fixed to the seabed. The upper and lower frames are connected by the proposed RID device (Figure 3-1). The proposed arrangement has the following obvious advantages: (1) the supporting system is divided into two parts, which significantly reduces the length of each part, the dimensions of the supporting system therefore can be designed much smaller since it is well known that the stiffness of the supporting system is inversely proportional to the cube of the length (H) of the supporting system (i.e. proportional to $1/H^3$); (2) as will be demonstrated in the numerical results, to achieve the effective control of heave motion, the mass of the proposed inerter device is very small (refer to Figure 3-1), the additional cost on the proposed device is therefore limited; (3) the techniques (e.g. the supporting system fixing technology) that are applied in the fixed platform can be directly used in the proposed design, which will not increase the technical difficulties. On the other hand, this design (Figure 3-2) changes the fixed platform to a SSP, which makes use of buoyancy force to support the heavy platform. It however increases the heave motion of the platform, which needs to be effectively controlled. As will be demonstrated in the numerical results, with the proposed RID device, the heave motion of this untraditional SSP can be significantly reduced as compared to the conventionally adopted methods (i.e. FHP and THP). The proposed design is believed to be an attractive alternative when the platform is located in the shallow water especially when the water depth is between 137.16 and 304.8 m.

3.2.2 Mechanical Behavior of RID

The force diagram of the proposed RID system is illustrated in Figure 3-3. As shown, the relationship between the rotational motion and linear motion can be written as follows:

$$\theta = \frac{2\pi}{L} x_d \tag{3.1}$$

where θ is the rotational angle of the turning plates, x_d is the relative displacement between Terminals 1 and 2 (refer to Figure 3-1(a)), and L is the lead of the ball screw. Similarly, the angular velocity $\dot{\theta}$ and angular acceleration $\ddot{\theta}$ can be written as

$$\dot{\theta} = \frac{2\pi}{L} \dot{x}_d \tag{3.2}$$

$$\ddot{\theta} = \frac{2\pi}{L} \ddot{x}_d \tag{3.3}$$

where $\dot{x}_d$ and $\ddot{x}_d$ are the velocity and acceleration, respectively.

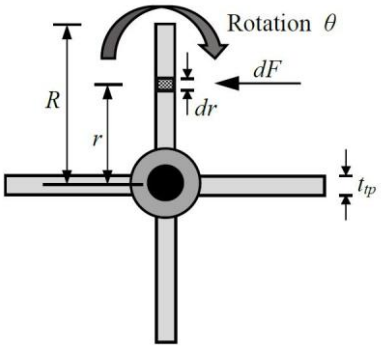

Figure 3-3 Force diagram of the proposed RID system

For the RID system shown in Figure 3-3, the torque applied on the device consists of two parts: the hydraulic torque provided by the water, and the inherent torque caused by the physical mass of the turning plates. As shown in Figure 3-3, the hydraulic torque applied on each turning plate can be calculated by

$$T_h = \int r \, dF \tag{3.4}$$

in which, R is the radius of the turning plate; dF is the hydrodynamic force at the radius of r, and it can be estimated by the Morison's equation as follows:

$$dF = \rho c_m a_t \, dV + \frac{1}{2} \rho c_d v_t |v_t| dA \tag{3.5}$$

where ρ is the density of seawater; $c_m = 1 + c_a$ is the inertia coefficient, with c_a denoting the added mass coefficient of the turning plate; c_d is the drag coefficient of the turning plate; $dV = l_{tp} t_{tp} \, dr$ and $dA = l_{tp} \, dr$, are the volume and area of the turning plate per unit radius

respectively, where l_{tp} and t_{tp} are the depth and thickness of the turning plate; $a_t = r\ddot{\theta}$ and $v_t = r\dot{\theta}$ are the tangential acceleration and velocity at the radius of r, respectively.

Substituting Equation (3.5) into Equation (3.4), the hydraulic torque T_h can be written as

$$T_h = \int r\, dF = \int_0^R \left(\rho c_m l_{tp} t_{tp} r^2 \ddot{\theta} + \frac{1}{2}\rho c_d l_{tp} r^3 \dot{\theta}\left|\dot{\theta}\right|\right) dr \tag{3.6}$$

For the inherent torque of each turning plate, it can be calculated by

$$T_i = I_{tp}\ddot{\theta} \tag{3.7}$$

where I_{tp} is the moment of inertia of each turning plate, which is

$$I_{tp} = \int r^2\, dm = \int_0^R \rho_s\, l_{tp} t_{tp} r^2\, dr \tag{3.8}$$

in which ρ_s is the density of the turning plate. The total torque T of the RID system is therefore

$$T = T_h + T_i \tag{3.9}$$

and it can be calculated as follows by substituting Equations (3.4) and (3.7) into Equation (3.9)

$$\begin{aligned} T &= \frac{1}{3}\rho c_m l_{tp} t_{tp} R^3 \ddot{\theta} + \frac{1}{8}\rho c_d l_{tp} R^4 \dot{\theta}\left|\dot{\theta}\right| + \frac{1}{3}\rho_s l_{tp} t_{tp} R^3 \ddot{\theta} \\ &= \frac{1}{3}(\rho c_m + \rho_s) l_{tp} t_{tp} R^3 \ddot{\theta} + \frac{1}{8}\rho c_d l_{tp} R^4 \dot{\theta}\left|\dot{\theta}\right| \end{aligned} \tag{3.10}$$

The relationship between the axial force *N* of the RID system and the total torque can be expressed as follows:

$$N = \frac{2\pi}{L} T \tag{3.11}$$

Substituting Equations (3.2), (3.3) and (3.10) into Equation (3.11), one obtains

$$N = m_e \ddot{x}_d + c_e \dot{x}_d |\dot{x}_d| \tag{3.12}$$

where

$$m_e = \frac{1}{3}\left(\frac{2\pi}{L}\right)^2 (\rho c_m + \rho_s) l_{tp} t_{tp} R^3 \tag{3.13}$$

$$c_e = \frac{1}{8}\left(\frac{2\pi}{L}\right)^3 \rho c_d l_{tp} R^4 \tag{3.14}$$

which represent the inertance (i.e. the amplified mass m_e) and the equivalent damping coefficient (c_e) of each turning plate, respectively. It should be noted that the inertance and damping will be collectively referred to as the fluid resistance in this research.

The above equations demonstrate that the RID system is capable of generating considerable inertial and damping forces to the primary structure through the amplification mechanism of the ball screw assembly. It should be noted that the frictions of the ball screw are disregarded in the above derivations since they are small compared to the inertial force (the first term in Equation (3.12)) and damping force (the second term in Equation (3.12)).

3.3 Analytical Models of SSP with Different Control Devices

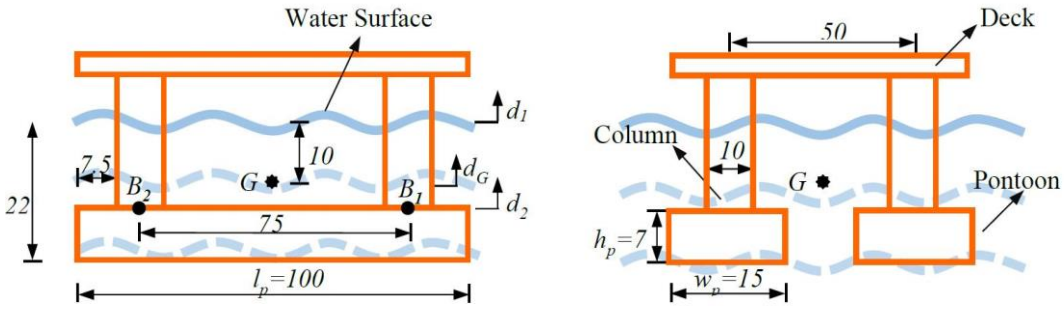

(a) Elevation (b) Side elevation

Figure 3-4 Dimensions of an example SSP (unit: m)

In the above section, a novel hydraulic RID system is proposed for the SSP heave motion suppression when the platform is located in the shallow sea, and the mechanical behaviour of the RID device is formulated. In this section, the analytical model of the SSP connected by the RID is established, and the equation of motion of the system is derived. For comparison, the analytical models of the SSP with FHP and THP are also derived. Based on these analytical models, the heave motion transfer functions of the SSP with different control systems are derived and the corresponding mean peak heave motions are formulated.

Figure 3-4 shows a typical SSP prototype as adopted from Faltinsen [43]. As shown, this SSP consists of one deck, two rectangular pontoons and four vertical columns. The dimension of the rectangular pontoons is 100 m (length) × 15 m (width) × 7 m (height), and the diameter of the vertical cylindrical columns is 10 m. G is the centre of gravity of the SSP, which locates at 10 m under the water surface as shown.

Considering the complexity of hydrodynamic problems, a few assumptions are made in the analytical modelling: (1) the influence of other motions (the surge, sway, yaw, pitch and roll) of the SSP on the heave motion is neglected [43, 44]. This is a reasonable assumption since the dominant frequencies of these motions are far from that of the heave motion, the coupling between the heave and other motions is therefore negligible; (2) the vortex-induced vibration (VIV) is not considered due to the fact that its contribution on the heave motion is not obvious [45].

3.3.1 Analytical Models of SSP with FHP/RID

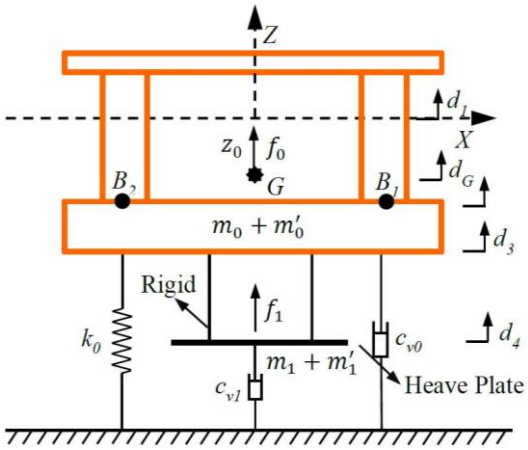

Figure 3-5 Analytical model of a SSP with FHP

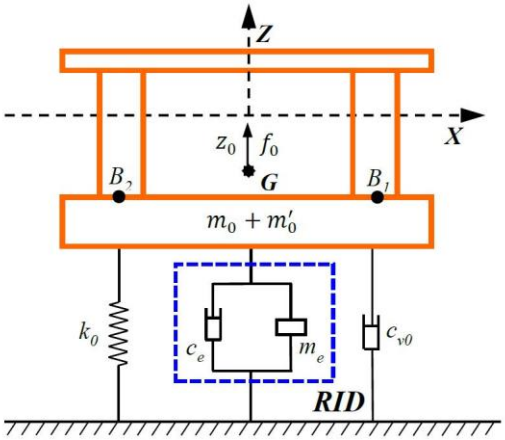

Figure 3-6 Analytical model of a SSP with RID

Figure 3-5 shows the analytical model of a SSP system with FHP. As shown, a heave plate is rigidly mounted below the pontoons of the SSP. According to the arrangement, the dynamic equilibrium equation of the system can be expressed as

$$\sum_{j=0}^{1}(m_j + m_j')\ddot{z}_0(t) + \sum_{j=0}^{1} c_{rj}\,\dot{z}_0(t) + \sum_{j=0}^{1} c_{vj}\,\dot{z}_0(t)|\dot{z}_0(t)| + k_0 z_0(t) = \sum_{j=0}^{1} f_j\,(t) \quad (3.15)$$

where j is the ID of the SSP and heave plate, with "0" and "1" denoting the SSP and heave plate, respectively; m_j is the physical mass of SSP or heave plate and m_j' is the corresponding added mass; c_{vj} is the inherent viscous damping provided by the surrounding water and c_{rj} is the radiation damping, which is ignored in this research owing to the relatively small wave radiation at low-frequency oscillations of SSP [43, 46]; $f_j(t)$ is the wave-induced force on SSP or heave plate; t is the time variable; k_0 is the restoring stiffness of SSP in the vertical direction, which depends on the waterplane area of the platform; and $z_0(t)$, $\dot{z}_0(t)$ and $\ddot{z}_0(t)$ are the displacement, velocity and acceleration of SSP in the vertical direction, respectively. These hydrodynamic parameters can be easily obtained through some straightforward derivations [43, 47].

To solve this equation in the frequency domain, the nonlinear viscous damping term should be firstly linearized, and it can be approximated as follows [48]

$$\dot{z}_0|\dot{z}_0| \approx \frac{8}{3\pi}\omega Z_a \dot{z}_0 \quad (3.16)$$

where ω is the circular frequency of the wave excitation and Z_a is the amplitude of heave motion. It should be noted that this linearization method has been commonly used in modelling the marine structures, and its effectiveness has been demonstrated in the previous study [49].

As the research focuses on the SSP operated in the shallow sea, the velocity potential of wave at location (x, z) and time t can be expressed as [43]:

$$\phi(x,z,t) = \frac{g\zeta_a}{\omega}\frac{\cosh k(z+h)}{\cosh kh}\cos(\omega t - kx) \tag{3.17}$$

where x and z denote the horizontal and vertical coordinates, respectively; g is the acceleration of gravity; ζ_a is the amplitude of wave, which is half of the wave height H_s; h is the water depth, which is taken as 200 m in this research; k is the wave number which can be estimated from the following equation

$$\omega^2 = kg\tanh kh \tag{3.18}$$

By differentiating the wave potential ϕ, the velocity and acceleration of water particles in the vertical direction can be calculated as follows:

$$v_z = \frac{\partial\phi}{\partial z} = \omega\zeta_a\frac{\sinh k(z+h)}{\sinh kh}\cos(\omega t - kx) \tag{3.19}$$

$$a_z = \frac{\partial v_z}{\partial t} = -\omega^2\zeta_a\frac{\sinh k(z+h)}{\sinh kh}\sin(\omega t - kx) \tag{3.20}$$

Based on the Bernoulli's equation, the wave pressures at points B_1 and B_2 (see Figure 3-5) can be calculated by

$$P_{B1} = -\rho\frac{\partial\phi(x_1,d_2,t)}{\partial t} = \rho g\zeta_a\frac{\cosh k(d_2+h)}{\cosh kh}\sin(\omega t - kx_1) \tag{3.21}$$

$$P_{B2} = -\rho\frac{\partial\phi(x_2,d_2,t)}{\partial t} = \rho g\zeta_a\frac{\cosh k(d_2+h)}{\cosh kh}\sin(\omega t - kx_2) \tag{3.22}$$

where x_1 and x_2 are the X-coordinates of points B_1 and B_2, respectively; d_2 is the depth of the bottom of columns.

According to the undamped Morison's equation, the wave-induced force on the SSP (f_0 in Equation (3.15)) can therefore be evaluated by summing the wave forces on the pontoons and columns respectively [43]:

$$f_0(\mathrm{t}) = 2\int_{l_2}^{l_1}\rho A_p\,(1+c_{a0})a_{d3}\,dx + P_{B1}\frac{A_w}{2} + P_{B2}\frac{A_w}{2} \tag{3.23}$$

in which A_p is the cross-sectional area of one pontoon; A_w is the waterplane area of SSP; c_{a0} is the added mass coefficient of pontoon; a_{d3} is the vertical wave acceleration at the depth of d_3, which can be calculated based on Equation (3.20); l_1 and l_2 are the X-coordinates of the front and back ends of the pontoon respectively.

Similarly, the wave force on the heave plate (f_1 in Equation (3.15)) can be estimated by

$$f_1(t) = \rho c_{a1} V_R a_{d4} \tag{3.24}$$

where c_{a1} is the added mass coefficient of heave plate; V_R is the reference volume of the heave plate [47]; a_{d4} is the vertical wave acceleration at the depth of d_4 (see Figure 3-5).

Substituting Equations (3.23) and (3.24) into Equation (3.15), it then can be expressed in the frequency domain as

$$\left[-\omega^2 \sum_{j=0}^{1}(m_j + m_j') + \frac{8}{3\pi} Z_0 i\omega^2 \sum_{j=0}^{1} c_{vj} + k_0\right] Z_0 e^{i\omega t} = \sum_{j=0}^{1} F_j \, e^{i\omega t} \tag{3.25}$$

where i is the imaginary unit. After solving Equation (3.25), the heave motion transfer function of SSP with FHP can be written as

$$Z_0(i\omega) = \sqrt{\frac{-\left[-\omega^2 \sum_{j=0}^{1}(m_j+m_j')+k_0\right]^2 + \sqrt{\left[-\omega^2 \sum_{j=0}^{1}(m_j+m_j')+k_0\right]^4 + 4\left(\frac{8}{3\pi}\omega^2 \sum_{j=0}^{n} c_{vj}\right)^2 \left(\sum_{j=0}^{n} F_j\right)^2}}{2\left(\frac{8}{3\pi}\omega^2 \sum_{j=0}^{n} c_{vj}\right)^2}} \tag{3.26}$$

For the SSP with a RID, the analytical model is illustrated in Figure 3-6. Comparing Figure 3-6 to Figure 3-5, it can be seen that the analytical models are similar. The only difference is that the heave plate in Figure 3-5 is replaced by the RID device in Figure 3-6, with m_e and c_e representing the inertance and equivalent damping coefficients of the RID system as derived in Section 3.2.2. Similar to Figure 3-5, the dynamic equilibrium equation of SSP with RID can be written as

$$(m_0 + m_0' + m_e)\ddot{z}_0(t) + c_{r0}\dot{z}_0(t) + (c_{v0} + c_e)\dot{z}_0(t)|\dot{z}_0(t)| + k_0 z_0(t) = f_0(t) \tag{3.27}$$

It should be noted that the wave force on the RID system is ignored in the above equation owing to its much smaller size compared to FHP. After similar derivation as FHP, the heave motion transfer function of SSP with RID can be written as follows:

$$Z_0(i\omega) = \sqrt{\frac{-\left[-\omega^2(m_0+m_0'+m_e)+k_0\right]^2 + \sqrt{\left[-\omega^2(m_0+m_0'+m_e)+k_0\right]^4 + 4\left[\frac{8}{3\pi}\omega^2(c_{v0}+c_e)\right]^2 (F_0)^2}}{2\left[\frac{8}{3\pi}\omega^2(c_{v0}+c_e)\right]^2}} \tag{3.28}$$

For comparison, the heave motion transfer function of SSP without any control device is also investigated in the present study, and it can be easily obtained by setting the parameters m_1, m_1', c_{v1}, and F_1 in Equation (3.28) to 0.

3.3.2 Analytical Model of SSP with THP

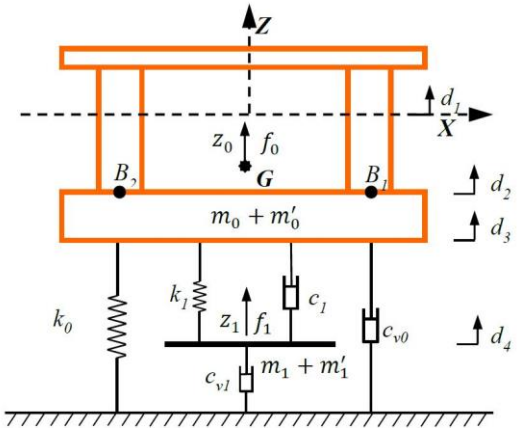

Figure 3-7 Analytical model of a SSP with THP

Figure 3-7 shows the schematic drawing of the SSP with a THP system. As shown, instead of the rigid connection as adopted in the SSP-FHP system (Figure 3-5), the heave plate is connected to the platform via a spring with the stiffness of k_1 and a damper with the damping coefficient of c_1 in the SSP-THP system. Based on Figure 3-7, the dynamic equilibrium equations of SSP with THP can be written as follows:

$$(m_0 + m_0')\ddot{z}_0(t) = f_0(t) - k_0 z_0(t) - c_{v0}'\dot{z}_0(t) - k_1[z_0(t) - z_1(t)] - c_1[\dot{z}_0(t) - \dot{z}_1(t)] \quad (3.29)$$

$$(m_1 + m_1')\ddot{z}_1(t) = f_1(t) - c_{v1}'\dot{z}_1(t) - k_1[z_1(t) - z_0(t)] - c_1[\dot{z}_1(t) - \dot{z}_0(t)] \quad (3.30)$$

where c_{v0}' and c_{v1}' are respectively the linearized inherent damping of SSP and heave plate, which can be determined through an iterative method in the analysis; $z_1(t)$, $\dot{z}_1(t)$ and $\ddot{z}_1(t)$ are the displacement, velocity and acceleration of the heave plate in the vertical direction, respectively.

The above equations can also be written in the Fourier domain as

$$(m_0 + m_0')s^2 z_0(s) = f_0(s) - k_0 z_0(s) - c_{v0}' s z_0(s) - k_1[z_0(s) - z_1(s)] - c_1 s[z_0(s) - z_1(s)] \quad (3.31)$$

$$(m_1 + m_1')s^2 z_1(s) = f_1(s) - c_{v1}' s z_1(s) - k_1[z_1(s) - z_0(s)] - c_1 s[z_1(s) - z_0(s)] \quad (3.32)$$

where $s = i\omega$. By some tedious yet straightforward derivations, the heave motion transfer function $Z_0(i\omega)$ of the SSP with THP can be expressed as

$$Z_0(i\omega) = \frac{[(m_1+m_1')s^2+k_1+c_{v1}'s+c_1s]F_0(s)+[k_1+c_1s]F_1(s)}{[(m_0+m_0')s^2+k_0+c_{v0}'s+k_1+c_1s][(m_1+m_1')s^2+k_1+c_{v1}'s+c_1s]-[k_1+c_1s]^2} \tag{3.33}$$

After deriving the heave motion transfer function $Z_0(i\omega)$, some non-dimensional parameters are introduced into Equation (3.33) to obtain its dimensionless expression. Table 3-1 tabulates these dimensionless parameters.

Table 3-1 Non-dimensional parameters for the SSP-THP system

No	Definition	Expressions
1	Mass ratio of THP	$\mu = \frac{m_1 + m_1'}{m_0 + m_0'}$
2	Frequency ratio of THP	$\gamma = \frac{\omega_1}{\omega_s}$
3	Damping ratio of THP	$\zeta = \frac{c_1}{2(m_1 + m_1')\omega_1}$
4	Inherent damping ratio of SSP	$\zeta_{v0} = \frac{c_{v0}'}{2(m_0 + m_0')\omega_s}$
5	Inherent Damping ratio of THP	$\zeta_{v1} = \frac{c_{v1}'}{2(m_1 + m_1')\omega_1}$

in which ω_s is the natural frequency of the SSP and ω_1 is the natural frequency of the THP. They can be calculated as follows:

$$\omega_s = \sqrt{\frac{k_0}{m_0 + m_0'}} \tag{3.34}$$

$$\omega_1 = \sqrt{\frac{k_1}{m_1 + m_1'}} \tag{3.35}$$

By introducing these dimensionless parameters as tabulated in Table 3-1, Equation (3.33) can be rewritten in a dimensionless form as

$$Z_0(i\omega) = \frac{(\mu s^2+\mu\gamma^2\omega_s^2+2\zeta_{v1}\mu\gamma\omega_s s+2\mu\zeta\gamma\omega_s s)\frac{F_0(s)}{m_0+m_0'}+(\mu\gamma^2\omega_s^2+2\mu\zeta\gamma\omega_s s)\frac{F_1(s)}{m_0+m_0'}}{(s^2+\omega_s^2+2\zeta_{v0}\omega_s s+\mu\gamma^2\omega_s^2+2\mu\zeta\gamma\omega_s s)(\mu s^2+\mu\gamma^2\omega_s^2+2\zeta_{v1}\mu\gamma\omega_s s+2\mu\zeta\gamma\omega_s s)-(\mu\gamma^2\omega_s^2+2\mu\zeta\gamma\omega_s s)^2} \tag{3.36}$$

3.3.3 Heave Response Spectrum and Mean Peak Heave Motion of SSP

In the previous subsections, the heave motion transfer functions for the SSP with different control systems are derived. The heave motion response spectrum then can be calculated as follows:

$$S_Z(\omega) = S(\omega)|Z_0(i\omega)|^2 \tag{3.37}$$

in which $S(\omega)$ is the power spectrum density (PSD) function of the wave loadings acting on the SSP. In this study, the widely applied Joint North Sea Wave Observation Projected (JONSWAP) spectrum is adopted to represent the power spectral density function of the wave surface elevation [50], which has the following expression

$$S(\omega) = a^* H_s^2 \frac{\omega^{-5}}{\omega_0^{-4}} \exp\left[-1.25(\omega/\omega_0)^{-4}\right] \gamma_w^{\exp\left[-\frac{(\omega-\omega_0)^2}{2\tau^2\omega_0^2}\right]} \tag{3.38}$$

where H_s is the wave height, ω_0 is the peak frequency, and

$$a^* = \frac{0.0624}{0.230 + 0.0336\gamma_w - 0.185(1.9 + \gamma_w)^{-1}} \tag{3.39}$$

in which γ_w is the peakedness factor with average value equaling to 3.3 [48]; τ is the shape parameter which equals to 0.07 for $\omega \leq \omega_0$ and 0.09 for $\omega > \omega_0$ [48].

To quantitatively evaluate the effectiveness of the different control methods, the mean peak heave motions (Z_{max}) of the SSP with different control systems are calculated based on the standard random vibration method [51].

3.4 Wave Conditions

Table 3-2 Summary of selected wave conditions

Case No.	Wave descriptions	Wave height H_s/m	Peak period T_0/s
L1	Working condition in SCS	6.00	11.20
L2	Working condition in GM	3.96	9.00
L3	10-year wave in SCS	11.10	13.60
L4	10-year wave in NWSA	10.00	12.50
L5	100-year wave in SCS	13.30	15.50
L6	100-year wave in GM	12.20	14.00

Without loss of generality, six wave conditions are adopted in this study to investigate the effectiveness of the FHP, THP, RID systems for SSP heave motion suppression in different sea states. The detailed information of these waves is tabulated in Table 3-2. As shown, these load cases consist of the working conditions in the South China Sea (SCS) and Gulf of Mexico (GM), 10-year waves in the SCS and North West Shelf of Australia (NWSA), and 100-year waves in the SCS and GM [14, 52]. It should be noted that all these areas are important oil and gas regions and a considerable amount of SSPs have been deployed. Additionally, among these wave conditions, the 10-year and 100-year waves represent the wave with the return period of 10 and 100 years, respectively. With the wave height and peak period of each wave condition

tabulated in Table 3-2, the JONSWAP spectra of these six wave conditions (Equation (3.38)) can be calculated and they are plotted in Figure 3-8. In the figure, ω_s=0.2040 rad/s is the fundamental natural frequency of the example SSP adopted in the present study. It can be found that ω_s falls outside the dominant wave frequencies of all wave conditions, which indicates the example SSP will be difficult to resonate with the wave loadings. This is actually the basic design principle for SSP in offshore industries.

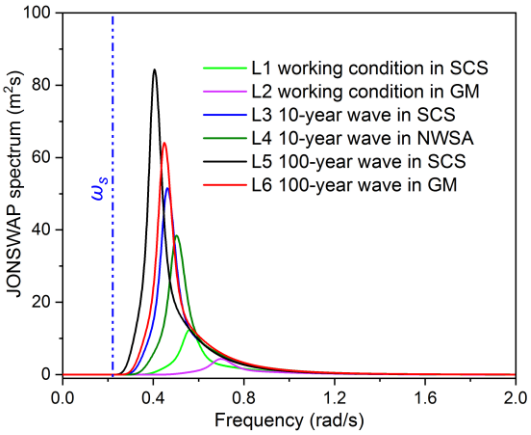

Figure 3-8 JONSWAP spectra of the six wave conditions

3.5 Result Discussions

In this section, the effectiveness of using RID system to reduce the heave motion of SSP is evaluated in the frequency (Section 3.5.2) and time (Section 3.5.3) domains respectively, and the results are compared with those obtained from the FHP and THP systems. It is obvious that, the THP system should be optimized to make this control system most effective, and the corresponding optimal parameters are determined through the numerical search method, which will be introduced in Section 3.5.1. For the FHP and RID systems, the optimization is not necessary since they are rigidly connected to the SSP.

The typical SSP shown in Figure 3-4 is selected as the example in the present study. The detailed dimensions of the SSP have been introduced in Section 3.3 and the total mass of the SSP is 26000 tonnes. Without loss of generality, a heave plate with a cross-section of 50×50 m and a thickness of 0.2 m is selected for the FHP and THP systems in this research according to previous works [12, 14, 52]. Since this research focuses on the SSP in the shallow sea, the deployed depth of the heave plate is assumed to be 100 m. For the RID system, four turning plates with the radius of 4 m, width of 1.0 m and thickness of 0.2 m are designed. With such designs, the masses of the heave plate and RID (excluding the mass of connecting systems) are 3900 and 24.96 tonnes respectively. The mass of the RID is only 0.64% of the heave plate. However, as will be demonstrated in the numerical example, RID can actually achieve better

control performance than the THP and FHP systems in most of the examined cases, which demonstrates the effectiveness and great application potential of the proposed method.

3.5.1 Optimization of the THP System

The THP system belongs to a variant of TMD, which must be optimized before application. In the present study, the mean peak heave motion Z_{max} of the SSP is of interest and is therefore selected as the performance indicator. Specifically speaking, the optimization of the THP system is achieved by solving the following minimization problem

$$\min_{\gamma\ \zeta}(Z_{max}(L_u)),\ u = 1, 2, \cdots, 6 \tag{3.40}$$

where L_u denotes the u^{th} wave condition.

For an undamped primary structure, the explicit expression can be given for the stiffness related parameter (γ in Equation (3.40)) and damping ratio (ζ) [53]. However, the algebraic expressions are difficult to be obtained for a damped primary structure, especially for the SSP system in the present study since the inherent damping of SSP and heave plate are not constants, and they vary with the frequency and motion amplitude as shown in Equation (3.16). Considering this fact, a numerical searching technique [54] is adopted to obtain the optimal parameters. The detailed description of this technique is out of the scope of the present study, interested readers can refer to Bakre and Jangid [54] for more details.

Figure 3-9 plots the contour of Z_{max} as functions of the frequency ratio γ and damping ratio ζ of the THP system in different loading cases, and the optimal values for these parameters are tabulated in Table 3-3. It can be seen that the optimal frequency ratio of the THP system is around 3.2 for load case L2, and about 2.8 for other load cases (i.e. L1, L3-L6). This is quite different from those obtained from a conventional structure-TMD system when the structure is subjected to the white-noise or seismic/wind excitations, in which the optimal frequency ratio is close to unity to ensure the TMD resonates with the primary structure and dissipates the vibration energy as much as possible. This can be attributed to the fact that the fundamental frequency of the SSP is required to fall outside the range of the wave dominant frequency during the design to preclude the possible resonances. In this case, the THP system should be tuned near the wave dominant frequency to achieve the best control performance. Similar results are also found in the other relevant references [12, 14, 40]. Additionally, it also can be seen from Figure 3-9 that the THP system is more sensitive to the variations of the frequency ratio γ than the damping ratio ζ.

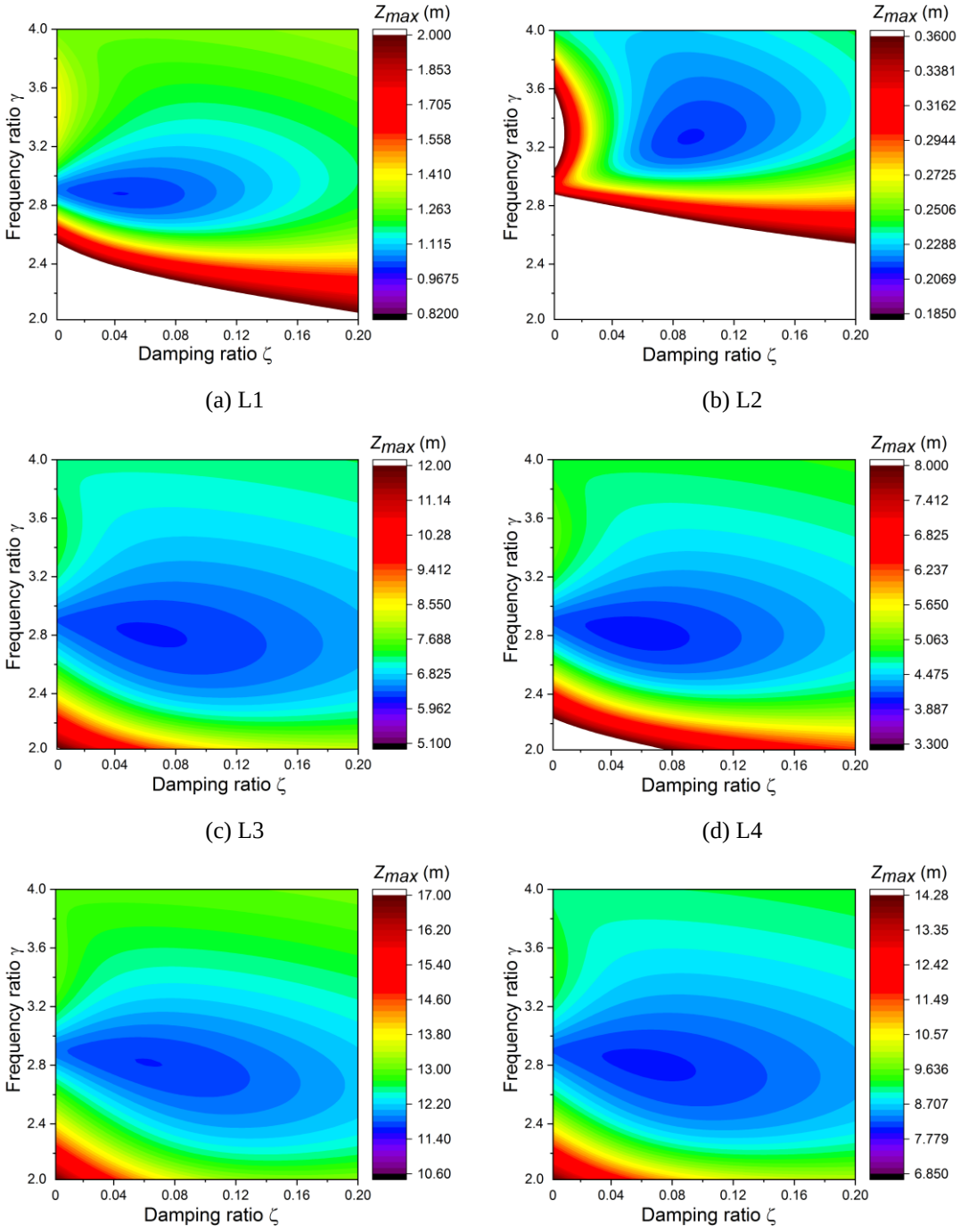

Figure 3-9 Contour plots of Z_{max} as functions of frequency ratio γ and damping ratio ζ for different load cases

Table 3-3 Optimal design parameters for the THP system

Case No.	L1	L2	L3	L4	L5	L6
γ	2.878	3.264	2.804	2.816	2.814	2.808
ζ	0.045	0.091	0.065	0.057	0.064	0.065

3.5.2 Effectiveness of Control Methods in the Frequency Domain

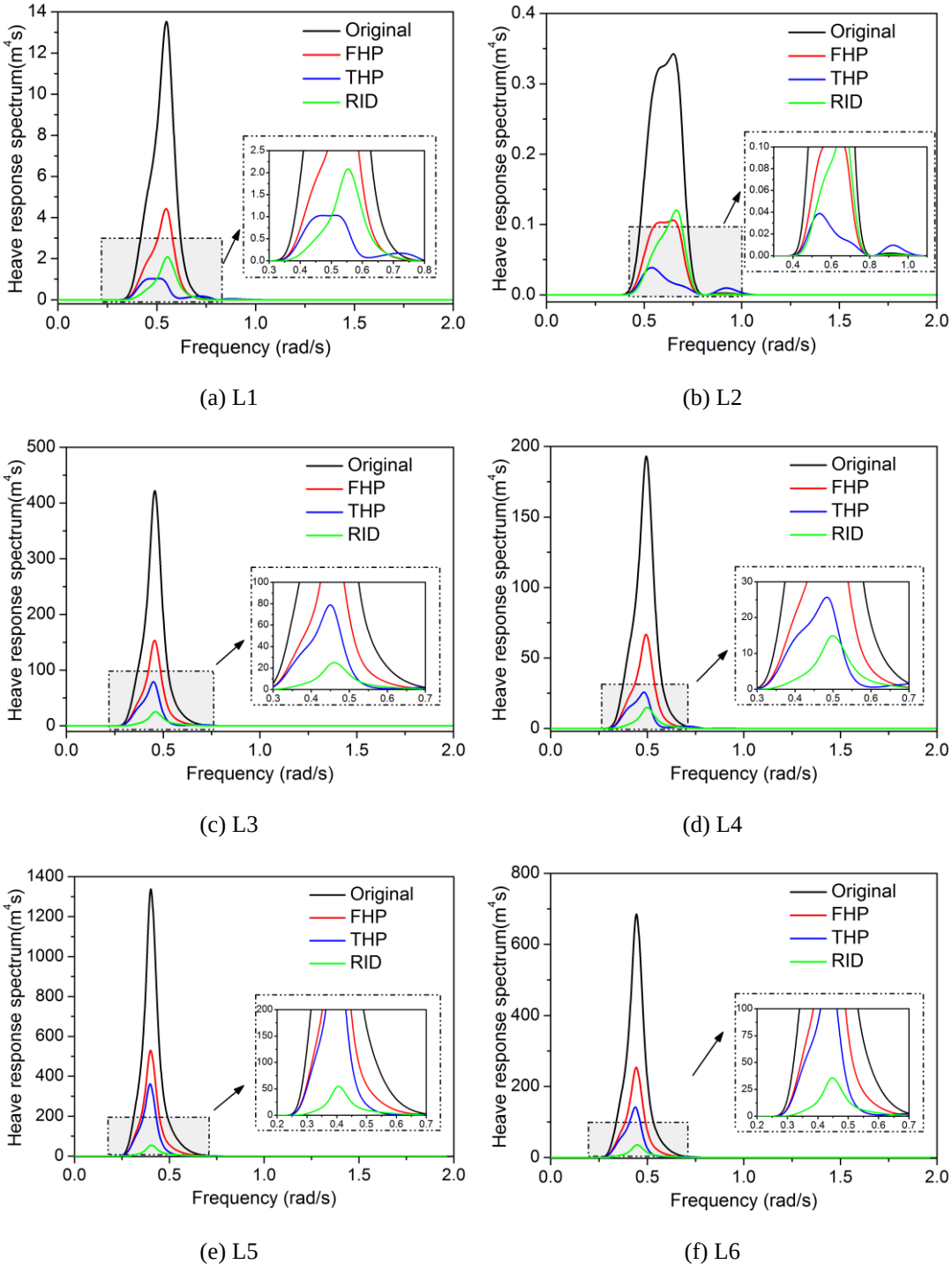

Figure 3-10 Influence of different control devices on the SSP heave response spectra under different loading scenarios

After obtaining the optimal design parameters of the THP system, the effectiveness of using FHP, THP and RID systems in reducing the heave motion of SSP are investigated in the frequency domain in this subsection. Figure 3-10 illustrates the heave response spectra of the SSP with different control devices under different loading scenarios, i.e. working condition waves (L1 and L2), 10-year waves (L3 and L4) and 100-year waves (L5 and L6). As shown,

all the control systems can significantly reduce the heave motion of the SSP, the THP and RID systems are more effective than the FHP system. In particular, as shown in Figure 3-10, the SSP-THP system performs the best in the working condition waves, and their heave response spectra show a two-peak characteristic since the moveable heave plate introduces another degree of freedom (DOF) into the system. For the uncontrolled SSP, SSP-FHP and SSP-RID systems, the heave response spectra show only one peak corresponding to the dominant frequency of the wave loading. As depicted in Figure 3-10(c), (d), (e) and (f), the SSP-RID system is most effective in the 10-year and 100-year wave conditions. Consistent with those in the working condition waves, the heave response spectra of the uncontrolled SSP, SSP-FHP and SSP-RID systems have one peak in the 10-year and 100-year waves. The heave response spectra of the SSP-THP system also show one-peak due to the fact that the peak in the high-frequency range is too small to be observed in these figures. The figure also shows that the control effectiveness of the THP decreases in the 10-year and 100-year waves compared to those in the working condition waves. However, the control effectiveness of the RID has a significant improvement in the 10-year and 100-year waves. The reason will be discussed in conjunction with the mean peak heave motion Z_{max} below.

Table 3-4 Mean peak heave motion Z_{max} of the SSP with and without control devices

Case No.	Z_{max} (m)				Reduction ratios (%)			
	Original	FHP	THP	RID	Original	FHP	THP	RID
L1	2.710	1.579	1.016	1.050	--	41.73	62.51	61.26
L2	0.557	0.315	0.214	0.297	--	43.45	61.58	46.68
L3	13.586	8.229	6.227	3.507	--	39.43	54.17	74.19
L4	9.557	5.688	4.039	2.746	--	40.48	57.74	71.27
L5	23.019	14.363	11.648	5.029	--	37.60	49.40	78.15
L6	17.111	10.434	8.044	4.152	--	39.02	52.99	75.73

To more straightforwardly show the control effectiveness, the mean peak heave motions (Z_{max}) of the SSP with different control systems are estimated based on the standard random vibration method as introduced in subsection 3.3.3 and the corresponding values are tabulated in Table 3-4.These results are compared with those obtained from the original platform (i.e. the SSP without any control device), and the corresponding reduction ratios are also included in the table. It is obvious that larger wave height results in larger mean peak heave motion. As shown in Table 3-4, the values of Z_{max} follow the variation trend of wave height, i.e. L2<L1<L4<L3<L6<L5. As for the reduction ratios, they are between 38% and 43% for the FHP system in different wave conditions, and the values range from 49% to 63% for the THP system and 47%-78% for the RID system. The RID system generally results in the best control effectiveness except for the working condition waves (i.e. L1 and L2).

The results in Table 3-4 also indicate that the reduction ratios of the SSP controlled by the FHP system under different waves are L5<L6<L3<L4<L1<L2, which are opposite to the changing of wave height. In other words, the control effectiveness of the FHP system decreases with the increase of wave height. This is because though the FHP increases the draft of the SSP system, it, on the other hand, also increases the force acting on the SSP-FHP system. As shown in Equation (3.15), the force applied on the SSP-FHP system includes two parts, the force acting on the SSP (f_0) and the force acting on the FHP (f_1). Wave with a larger height (i.e. more severe wave) can result in a very large force acting on the FHP, which in turn leads to larger structural responses and less reduction ratio. For the THP system, it is interesting to find that a similar trend as FHP (i.e. larger wave height results in smaller control effectiveness) is also found except for the loading cases L1 and L2, where the smaller wave height leads to smaller control effectiveness. This, on the other hand, contradicts with our intuition that the TMD system is more effective when the structural response is larger. It should be noted that our intuition is based on the assumption that the system behaves linearly. When the system is associated with nonlinear behaviors, an opposite trend might be observed. For example, as reported by Soto-Brito and Ruiz [55], when the TMD system was adopted to control seismic induced vibration of a 22-storey reinforced concrete frame, the control effectiveness of the TMD under the high-intensity excitations (of course with larger structural responses) was smaller than those due to the moderate excitations because of the nonlinear behaviour of the system under the high-intensity excitations. In the present study, the viscous damping force applied on the SSP is highly nonlinear, which results in the less evident control effectiveness when the wave height is larger. For the results for loading cases L1 and L2, the THP system optimized for L2 causes a more obvious response aggravation in the high frequency range (0.8-1.0 rad/s) compared to that in L1 (see Figure 3-10(a) and (b)). Moreover, the nonlinear effect under smaller wave loading is less significant compared to the one under more severe waves.

For the RID system, the order of reduction ratios follows the trend of wave height again, i.e. L2<L1<L4<L3<L6<L5. This is because larger structural responses lead to larger relative displacements (thus larger relative velocities and accelerations) between the two terminals, which in turn results in the larger resistant inertial and damping forces (Equation (3.12)) and more obvious control effectiveness. Besides the very small mass compared to the FHP and THP systems as mentioned above, the results also demonstrate another advantage of the proposed RID system, i.e. its control effectiveness increases with the wave height, namely it is more effective when the SSP is subjected to the harsher wave condition.

It should be noted that all the above results are obtained based on the size of the heave plate of 50×50 m and the radius of the RID of 4 m. To investigate the influence of the radius of the

RID system on the mean peak heave motion of SSP, Figure 3-11 shows the corresponding results when the radius of the RID system varies. It can be seen that when the radius of the RID system is small (around 1.5 m in L1 and L2, and around 1 m in all other cases), the control effectiveness is not evident, and when the radius reaches certain value, the mean heave motion reduces evidently with the increment of the RID radius. This is because as shown in Equations (3.13) and (3.14), the inertance and equivalent damping ratio of the RID device are proportional to the power of 3 and 4 respectively of the RID radius. Larger radius significantly increases the inertance and damping force provided by the RID device. Figure 3-11 shows the required radius of the RID system to achieve the identical mean peak heave motion as the FHP and THP systems, and Table 3-5 summarizes the corresponding physical mass ratios between the RID system and the FHP/THP systems. It can be seen that the mass ratios in all load cases are less than 0.8%. These results demonstrate that the RID system can achieve the equivalent control effectiveness of the FHP and THP systems with a very small physical mass. Moreover, it is also found that the required radius of the RID system in the 10-year and 100-year waves are smaller than those in the working wave conditions. This is because the control effectiveness of the RID improves with the larger wave height as discussed above.

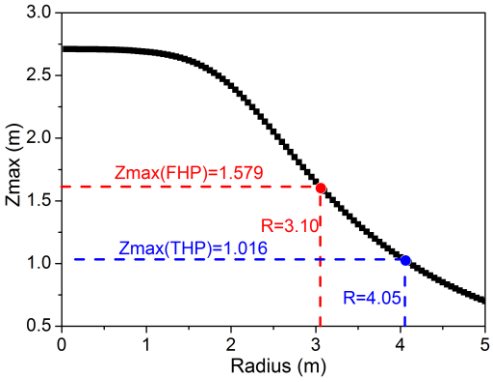

(a) L1

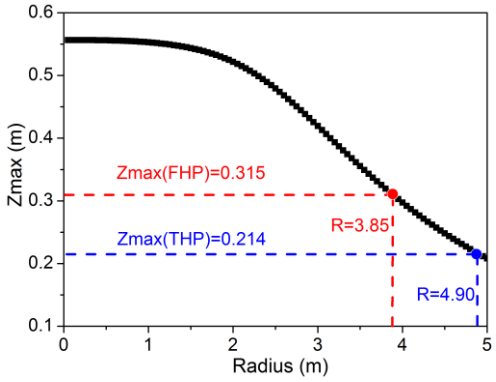

(b) L2

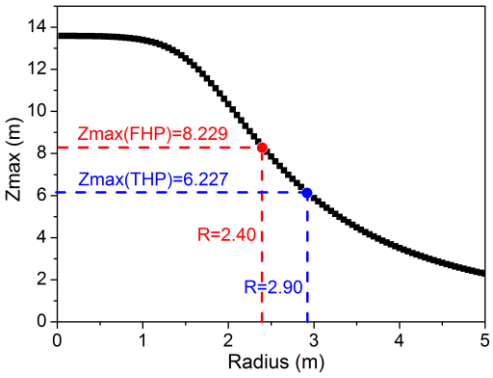

(c) L3

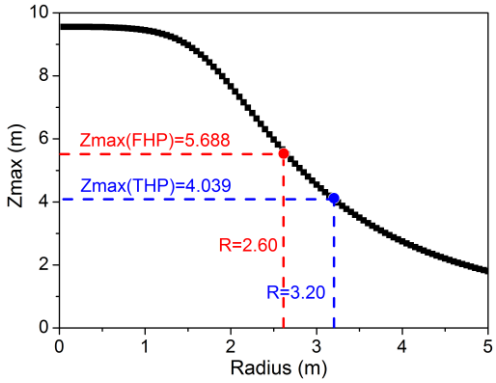

(d) L4

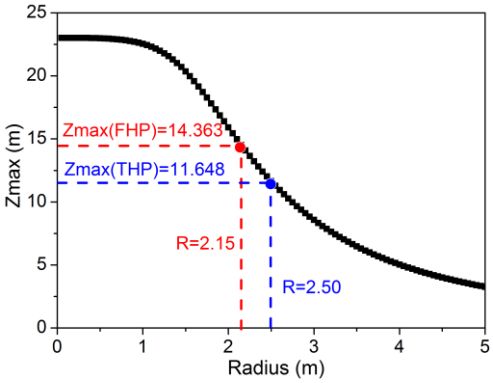

(e) L5

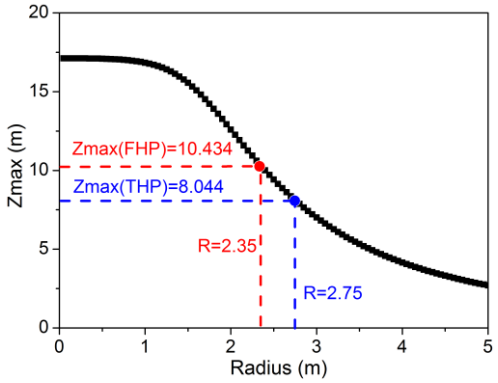

(f) L6

Figure 3-11 Influence of the RID radius on the mean peak heave motion under different load cases

Table 3-5 Summary of the physical mass ratios between the RID and FHP/THP systems (%)

Case No	L1	L2	L3	L4	L5	L6
FHP	0.50	0.62	0.38	0.42	0.34	0.38
THP	0.65	0.78	0.46	0.51	0.4	0.44

3.5.3 Effectiveness of Control Methods in the Time Domain

The effectiveness of the above control methods for SSP heave motion suppression are further investigated in the time-domain in this subsection. Instead of approximately considering the nonlinear damping in the frequency domain (Equation (3.16)), the results in the time domain are directly obtained by solving the dynamic equations of motion (Equations (3.15), (3.27), (3.29) and (3.30) respectively) by using the solver "ode 45" in MATLAB (version R2017 a) based on the Runge-Kutta method after the wave force time histories are obtained.

As discussed in Section 3.3.3, the JONSWAP spectrum is used to depict the PSD of the wave surface elevation, the sea surface elevation in the time domain then can be calculated as follows:

$$\eta(t) = \sum_{q=1}^{n} \sqrt{2\, d\omega S(\omega_q)}\cos(\omega_q t + \varphi(\omega_q)) \tag{3.41}$$

in which ω_q is the q^{th} frequency value, $d\omega$ is the frequency interval, and φ is the random phase angle uniformly distributed over the range of $[0, 2\pi]$.

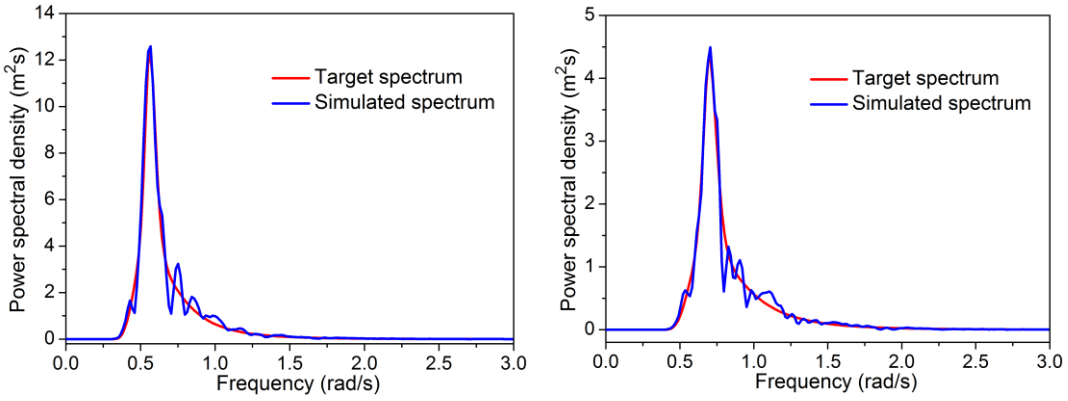

(a) L1

(b) L2

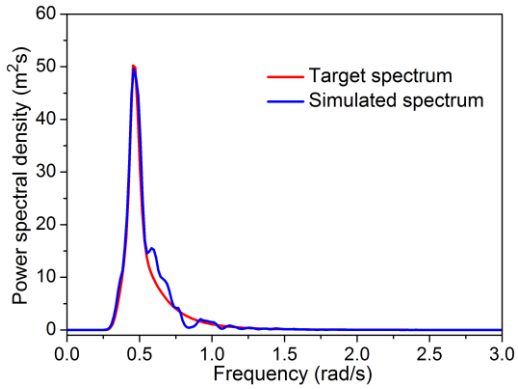

(c) L3

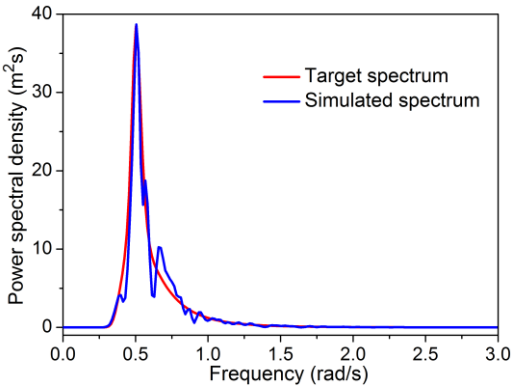

(d) L4

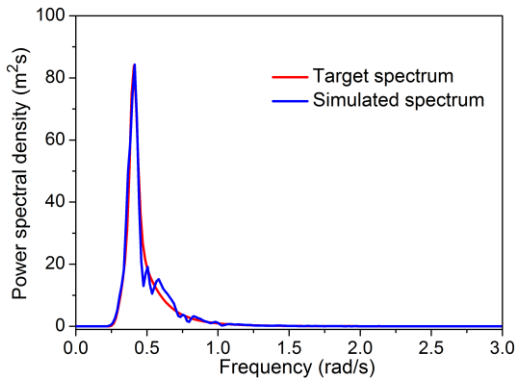

(e) L5

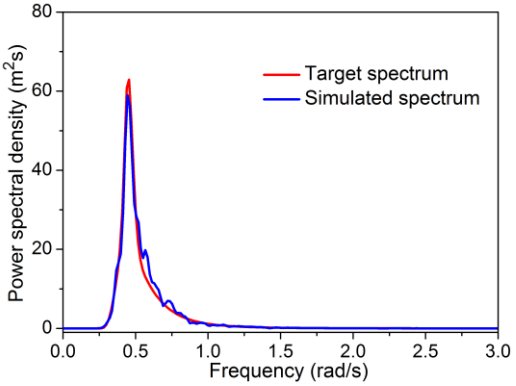

(f) L6

Figure 3-12 Comparison between the simulated and target PSDs for different load cases

After generating the sea surface elevation $\eta(t)$, the wave force time histories on the SSP and heave plate can be calculated according to Equations (3.23) and (3.24), respectively. Figure 3-12 shows the PSDs of the simulated sea surface elevation time histories and the target spectrum in different load cases. Good matches are obtained as shown. Figure 3-13 shows the wave force time histories on the SSP in different load cases. For conciseness, the wave force time histories on the heave plate are not shown.

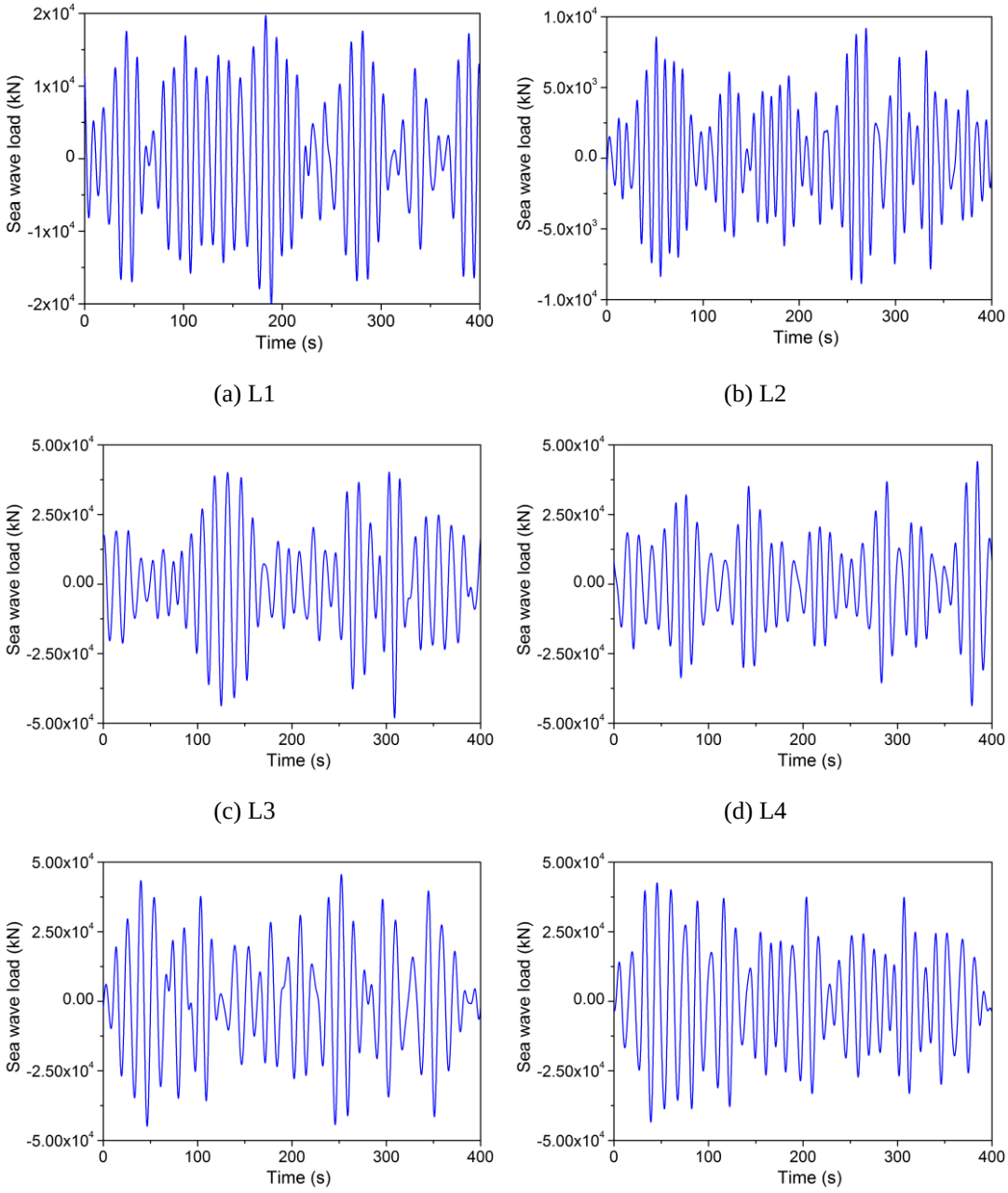

(a) L1 (b) L2

(c) L3 (d) L4

(e) L5 (f) L6

Figure 3-13 Wave force time histories on the SSP in different load cases

Figure 3-14 shows the heave motion time histories of the SSP without and with control devices, and Table 3-6 tabulates the root mean square (RMS) responses and the corresponding reduction ratios. Similar to the frequency-domain responses, the following general conclusions can be drawn based on the time-domain results in Figure 3-14: all the devices can evidently mitigate the heave motion of the SSP, the THP and RID systems are more effective compared to the FHP system, and the RID system is most effective especially when the SSP is subjected to the 10-year and 100-year waves.

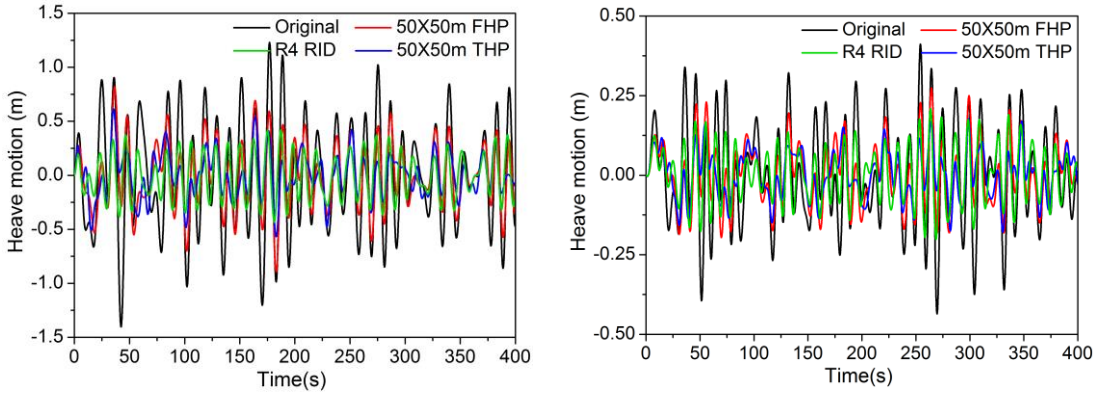

(a) L1

(b) L2

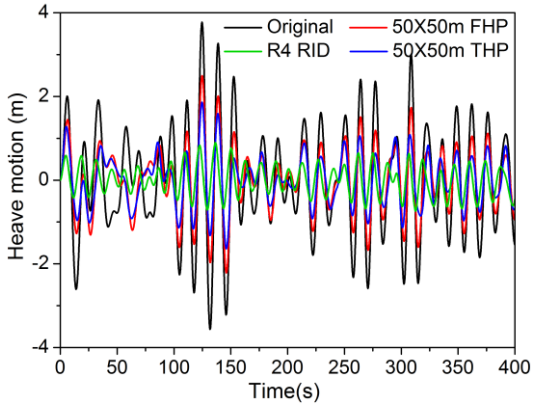

(c) L3

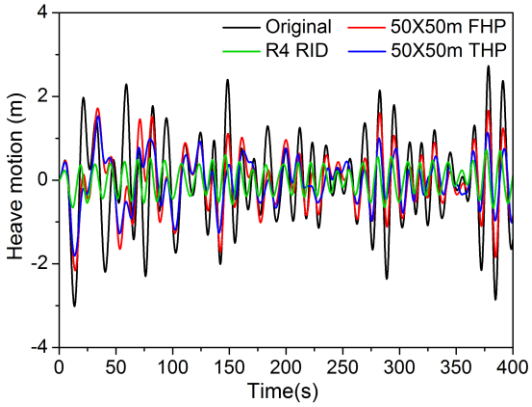

(d) L4

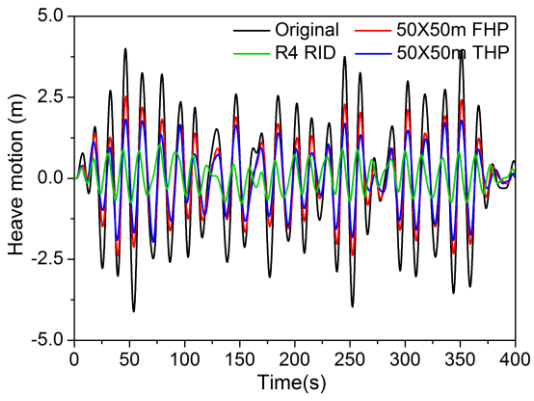

(e) L5

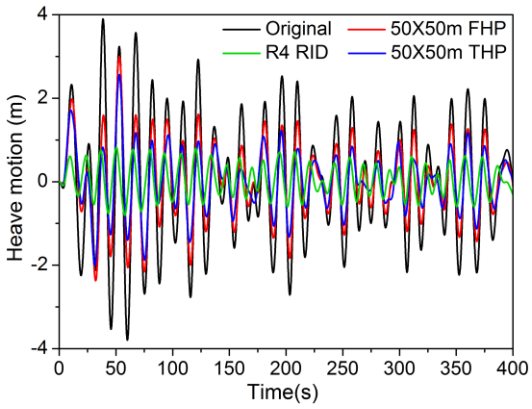

(f) L6

Figure 3-14 Heave motion time histories of the SSP without and with control devices in different load cases

Similar to Z_{max} in the frequency domain, the RMS responses of SSP (see Table 3-6) are also correlated positively with the wave height, i.e. L2<L1<L4<L3<L6<L5. As for the control effectiveness, Table 3-6 shows that the reduction ratios of 30-40%, 45-60%, and 44-75% are achieved for the FHP, THP and RID systems, respectively. In particular, the sequences of the reduction ratios of the FHP and THP systems are L4<L2<L6<L5<L3<L1 and L4<L5<L6<L2<L3<L1 respectively, which are different from those in the frequency domain,

and are not correlated with the wave height. This is because these results are obtained based on only one realization of the sea surface elevation, the random phase angles introduced in Equation (3.41) result in different responses. For the RID system, the sequence of the reduction ratio is L2<L1<L4<L3<L6<L5, which is consistent with that in the frequency domain and positively correlates with the wave height. These results demonstrate that the RID system is not sensitive to the random phase angles (i.e. the uncertainties) in the generation of the wave force. The reason is that the size of the RID system is quite small compared to the FHP and THP systems, the wave force on the RID system is therefore very small and ignorable. All the above results show that the RID system is an attractive and effective method in reducing the heave motion of SSP especially in severe load cases, and the control effectiveness of the RID system improves with the increase of wave height.

Table 3-6 RMS values and reduction ratios of different SSP systems under various loading scenarios

Case No.	RMS (m)				Reduction ratios (%)			
	Original	FHP	THP	RID	Original	FHP	THP	RID
L1	0.485	0.297	0.200	0.200	--	38.76	58.76	58.76
L2	0.152	0.097	0.073	0.085	--	36.18	51.97	44.08
L3	1.281	0.796	0.600	0.351	--	37.86	53.16	72.60
L4	1.056	0.719	0.561	0.316	--	31.91	46.88	70.08
L5	1.732	1.090	0.885	0.429	--	37.07	48.90	75.23
L6	1.424	0.907	0.704	0.378	--	36.31	50.56	73.46

3.6 Conclusions

This paper proposes a novel rotational inertia damper (RID) to mitigate the heave motion of SSP in the shallow sea based on the concept of inerter. The conceptual design and feasibility of the proposed RID system are firstly introduced. The analytical model of the SSP controlled by the RID system is then established. The control effectiveness of the RID system is investigated in both the frequency and time domains. For comparison, the effectiveness of the conventional control methods (i.e. the FHP and THP systems) are also studied. Based on the analytical results, the following conclusion can be drawn:

(1) The proposed RID system is capable of generating considerable inertial and damping forces to the SSP through the amplification mechanism of the ball screw assembly. It can be an attractive method for the SSP heave motion suppression when the platform is located in the shallow sea.

(2) The RID system can achieve the identical control performance of the FHP and THP systems by using a very small physical mass as compared to the heave plate. For all

the load cases investigated in the present study, the mass ratio is less than 0.8%. The device is very economic compared to the FHP and THP systems.

(3) Compared to the FHP and THP systems, the RID system can result in better control performance especially when the SSP is subjected to the harsher wave condition.

(4) The control effectiveness of the RID system increases with the increment of wave height, while for the THP and FHP systems, the control effectiveness generally decreases with the increment of wave height.

3.7 References

[1] Bollmann M. World ocean review: living with the oceans. 2010.

[2] Muehlenbachs L, Cohen MA, Gerarden T. The impact of water depth on safety and environmental performance in offshore oil and gas production. Energy Policy. 2013;55:699-705.

[3] Kandasamy R, Cui F, Townsend N, Foo CC, Guo J, Shenoi A et al. A review of vibration control methods for marine offshore structures. Ocean Eng. 2016;127:279-97.

[4] Tao L, Cai S. Heave motion suppression of a Spar with a heave plate. Ocean Eng. 2004;31:669-92.

[5] Subbulakshmi A, Sundaravadivelu R. Heave damping of spar platform for offshore wind turbine with heave plate. Ocean Eng. 2016;121:24-36.

[6] Kaynia AM, Biggs JM, Veneziano D. Seismic effectiveness of tuned mass dampers. J Struct Div. 1981;107:1465-84.

[7] Jangid R. Optimum Multiple Tuned Mass Dampers for base-excited undamped system. Earthq Eng Struct Dyn. 1999;28:1041-9.

[8] Bi K, Hao H. Using pipe-in-pipe systems for subsea pipeline vibration control. Eng Struct. 2016;109:75-84.

[9] Zuo H, Bi K, Hao H. Using multiple tuned mass dampers to control offshore wind turbine vibrations under multiple hazards. Eng Struct. 2017;141:303-15.

[10] Nikoo HM, Bi K, Hao H. Effectiveness of using pipe-in-pipe (PIP) concept to reduce vortex-induced vibrations (VIV): Three-dimensional two-way FSI analysis. Ocean Eng. 2018;148:263-76.

[11] Zhu H, Ou J, Zhai G. Conceptual design of a deep draft semi-submersible platform with a moveable heave-plate. J Ocean U China. 2012;11:7-12.

[12] Liu K, Ou J. A novel tuned heave plate system for heave motion suppression and energy harvesting on semi-submersible platforms. Sci China Technol Sci. 2016;59:897-912.

[13] Zhu H, Hu C, Liu Y. Optimum Design of a Passive Suspension System of a Semisubmersible for Pitching Reduction. J Dyn Syst Meas Control. 2016;138:121003.

[14] Liu K, Liang H, Ou J. Numerical investigation of a tuned heave plate energy-harvesting system of a semi-submersible platform. Energies. 2016;9:82.

[15] Sadek F, Mohraz B, Taylor AW, Chung RM. A method of estimating the parameters of tuned mass dampers for seismic applications. Earthq Eng Struct Dyn. 1997;26:617-35.

[16] Rana R, Soong T. Parametric study and simplified design of tuned mass dampers. Eng Struct. 1998;20:193-204.

[17] Smith MC. Synthesis of mechanical networks: the inerter. IEEE Trans Automat Contr. 2002;47:1648-62.

[18] Chen MZQ, Papageorgiou C, Scheibe F, Wang FC, Smith M. The missing mechanical circuit element. IEEE Circ Syst Mag. 2009;9:10-26.

[19] Papageorgiou C, Smith MC. Positive real synthesis using matrix inequalities for mechanical networks: application to vehicle suspension. IEEE T Contr Syst T. 2006;14:423-35.

[20] Hwang JS, Kim J, Kim YM. Rotational inertia dampers with toggle bracing for vibration control of a building structure. Eng Struct. 2007;29:1201-8.

[21] Ikago K, Saito K, Inoue N. Seismic control of single-degree-of-freedom structure using tuned viscous mass damper. Earthq Eng Struct Dyn. 2012;41:453-74.

[22] Watanabe Y, Ikago K, Inoue N, Kida H, Nakaminami S, Tanaka H et al. Full-scale dynamic tests and analytical verification of a force-restricted tuned viscous mass damper. Proceedings of the 15th World Conference on Earthquake Engineering, Lisbon, Portugal, 2012.

[23] Marian L, Giaralis A. Optimal design of a novel tuned mass-damper–inerter (TMDI) passive vibration control configuration for stochastically support-excited structural systems. Probabilistic Eng Mech. 2014;38:156-64.

[24] Pietrosanti D, De Angelis M, Basili M. Optimal design and performance evaluation of systems with Tuned Mass Damper Inerter (TMDI). Earthq Eng Struct Dyn. 2017;46:1367-88.

[25] Giaralis A, Petrini F. Wind-Induced Vibration Mitigation in Tall Buildings Using the Tuned Mass-Damper-Inerter. J Struct Eng. 2017;143:04017127.

[26] Jin X, Chen MZQ, Huang Z. Minimization of the beam response using inerter-based passive vibration control configurations. Int J Mech Sci. 2016;119:80-7.

[27] De Domenico D, Ricciardi G. An enhanced base isolation system equipped with optimal tuned mass damper inerter (TMDI). Earthq Eng Struct Dyn. 2018;47:1169-92.

[28] Wang FC, Hong MF, Chen CW. Building suspensions with inerters. P I Mech Eng C-J Mec. 2010;224:1605-16.

[29] De Domenico D, Ricciardi G. Improving the dynamic performance of base-isolated structures via tuned mass damper and inerter devices: A comparative study. Struct Contorl Health Monit. 2018:e2234.

[30] Lazar I, Neild S, Wagg D. Using an inerter-based device for structural vibration suppression. Earthq Eng Struct Dyn. 2014;43:1129-47.

[31] Lazar I, Neild S, Wagg D. Vibration suppression of cables using tuned inerter dampers. Eng Struct. 2016;122:62-71.

[32] Hu Y, Chen MZQ. Passive structural control with inerters for a floating offshore wind turbine. The 36th Chinese Control Conference (CCC) IEEE; 2017. p. 9266-71.

[33] Hu Y, Chen MZQ. Inerter-based passive structural control for load mitigation of wind turbines. The 29th Chinese Control And Decision Conference (CCDC): IEEE; 2017. p. 3056-61.

[34] Wen Y, Chen Z, Hua X. Design and Evaluation of Tuned Inerter-Based Dampers for the Seismic Control of MDOF Structures. J Struct Eng. 2016;143:04016207.

[35] Giaralis A, Taflanidis AA. Optimal tuned mass-damper-inerter (TMDI) design for seismically excited MDOF structures with model uncertainties based on reliability criteria. Struct Control Health Monit. 2018;25:e2082.

[36] Hu Y, Chen MZQ. Performance evaluation for inerter-based dynamic vibration absorbers. Int J Mech Sci. 2015;99:297-307.

[37] Pan C, Zhang R, Luo H, Li C, Shen H. Demand-based optimal design of oscillator with parallel-layout viscous inerter damper. Struct Control Health Monit. 2018;25:e2051.

[38] Barredo E, Blanco A, Colín J, Penagos VM, Abúndez A, Vela LG et al. Closed-form solutions for the optimal design of inerter-based dynamic vibration absorbers. Int J Mech Sci. 2018;144:41-53.

[39] Cao L, Li C. Tuned tandem mass dampers-inerters with broadband high effectiveness for structures under white noise base excitations. Struct Contorl Health Monit. 2019:e2319.

[40] Ma R, Bi K, Hao H. A Novel Rotational Inertia Damper (RID) for Heave Motion Suppression of Semi-submersible Platform (SSP) in the Shallow Sea Struct Contorl Health Monit. 2018:e2368.

[41] Chen MZQ, Hu Y, Huang L, Chen G. Influence of inerter on natural frequencies of vibration systems. J Sound Vib. 2014;333:1874-87.

[42] Reddy D, Arockiasamy M. Offshore structures. 1991.

[43] Faltinsen O. Sea loads on ships and offshore structures: Cambridge university press; 1993.

[44] Taflanidis AA, Angelides DC, Scruggs JT. Simulation-based robust design of mass dampers for response mitigation of tension leg platforms. Eng Struct. 2009;31:847-57.

[45] Veritas DN. Offshore standard DNV-OS-E301 position mooring. DNV: Norway. 2010.

[46] Schellin T, Kirsch A. Low-frequency damping of a moored semisubmersible obtained from simulated extinction tests and mean wave drift forces. Appl Ocean Res. 1989;11:202-11.

[47] Veritas DN. Modelling and analysis of marine operations. Offshore Standard. 2011.

[48] Chakrabarti SK. Hydrodynamics of offshore structures: WIT press; 1987.

[49] Burke BG. An analysis of marine risers for deep water. Journal of petroleum technology. 1974;26:455-65.

[50] Hasselmann K, Barnett TP, Bouws E, Carlson H, Cartwright DE, Enke K et al. Measurements of wind-wave growth and swell decay during the Joint North Sea Wave Project (JONSWAP). Ergänzungsheft. 1973:8-12.

[51] Der Kiureghian A. Structural response to stationary excitation. J Eng Mech Div. 1980;106:1195-213.

[52] Travanca J, Hao H. Control of wave-induced vibrations on floating production systems. Ocean Eng. 2017;141:35-52.

[53] Asami T, Nishihara O, Baz AM. Analytical solutions to H_∞ and H_2 optimization of dynamic vibration absorbers attached to damped linear systems. J Vib Acoust. 2002;124:284-95.

[54] Bakre S, Jangid R. Optimum parameters of tuned mass damper for damped main system. Struct Contorl Health Monit. 2007;14:448-70.

[55] Soto-Brito R, Ruiz SE. Influence of ground motion intensity on the effectiveness of tuned mass dampers. Earthq Eng Struct Dyn. 1999;28:1255-71.

CHAPTER 4 USING TWO RIDS TO SIMULTANEOUSLY CONTROL HEAVE AND PITCH MOTIONS

Abstract[4]

Semi-submersible platforms (SSPs) are widely applied for energy mining in the ocean. During their service lives, SSPs may be subjected to excessive heave and pitch motions induced by sea waves, which in turn may result in fatigue problems of structural components or even catastrophic capsizing. It is therefore important to mitigate the heave and pitch motions of SSP by all means. In the present study, a novel inerter-based control system, rotational inertia damper (RID), is proposed to simultaneously mitigate the heave and pitch motions of SSP in the shallow sea. The responses of SSP equipped with RID systems subjected to six typical wave conditions are calculated in the frequency and time domains respectively based on the developed analytical models and Simulink models. For comparison, the models and responses of SSP without and with traditional control devices, i.e. fixed heave plate (FHP) and tuned heave plate (THP), are also developed and calculated. The results reveal that the RID system can achieve almost the same or even better control effectiveness compared to the conventional systems with a much smaller additional mass to the SSP especially when the SSP is under harsher waves.

4.1 Introduction

Ocean provides modern society with many offshore fossil energies (e.g. oil and natural gas). To efficiently exploit these hydrocarbon resources, various types of platforms have been developed. These platforms can be roughly categorized into the fixed type (e.g. steel jack, jack-up platform, etc.) and the floating type (e.g. tension leg platform, semi-submersible platform, etc.). Among the floating-type platforms, the semi-submersible platform (SSP) is most widely used owing to its widely applicable water depth, big deck area and payload capacity. A large portion of SSPs are deployed in the shallow sea, where the water depth is less than 304.8 m according to the definition of the Bureau of Ocean Energy Management, Regulation and Enforcement (BOEMRE) [1]. On the other hand, offshore platforms are exposed to varieties of environmental loads like wind, sea wave and ocean current during their service lives, which could cause excessive motions or even capsize/sink these platforms [2]. It is therefore sorely imperative to reduce these adverse motions. Among these motions (i.e. heave, surge, sway, roll, pitch and yaw), the heave and pitch motions are of the most significant

[4] This chapter was published in *Engineering Structures* with the full bibliographic citation as follows:
Ma R, Bi K, Hao H. Using inerter-based control device to mitigate heave and pitch motions of semi-submersible platform in the shallow sea. Eng Struct. 2020;207:110248. https://doi.org/10.1016/j.engstruct.2020.110248.

importance and have attracted a lot of research attentions since their periods are close to the dominant periods of sea waves, which in turn may lead to the resonance of the floating platform. Considering the extensive application of SSP in the shallow sea and the excessive heave and pitch motions it may experience, this paper aims to simultaneously mitigate the heave and pitch motions of SSP in the shallow sea.

To achieve this objective, many control strategies including passive, semi-active, active and hybrid methods, have been proposed. Among which, the passive control method is most widely applied in engineering practices due to its simplicity and high level of reliability (e.g. external power independent). This paper focuses on the passive control method, and only literature related to the passive control is thereby briefly summarized in this section. For SSPs, the most commonly used passive control method is the fixed heave plate (FHP), which is normally installed at the bottom of the platform to increase its draft. Previous experimental and numerical studies [3-5] showed that the FHP system was effective in suppressing the heave motion of SSPs since it could endow the entire system with added mass and viscous damping in the heave direction. In recent years, tuned heave plate (THP) is proposed to further enhance the performance of the FHP system based on the concept of tuned mass damper (TMD), a passive control system that has been extensively applied for the vibration mitigation of onshore structures [6, 7] and offshore structures (e.g. Refs. [8-13]). Like the TMD system, the THP system comprises a heave plate acting as the secondary mass, and a spring and a dashpot utilized to connect the heave plate with the platform. Prior to its application, it is normally required to optimize (dubbed tune) the system by properly selecting the parameters for the spring and dashpot to achieve the best control performance. Previous studies (e.g. Ref. [14]) demonstrated that the THP system was more effective as compared to its counterpart FHP system. It should be noted that most previous studies [15, 16] proposed using a single heave plate installed at the centre of the platform, thus only the heave motion could be controlled. Instead of utilizing one single heave plate, Zhu et al. [17] proposed using multiple tuned heave plates to mitigate the pitch motion of a SSP induced by sea waves. Numerical results indicated that the pitch motion of SSP could be effectively reduced by the proposed multiple tuned heave plates. Liu et al. [18] conducted both experimental and numerical studies to evaluate the effectiveness of the multiple tuned heave plates on the vibration control of SSP. The results demonstrated that the multiple tuned heave plates could remarkably suppress both the heave and pitch motions of SSP.

On the other hand, similar to the TMD system, the control effectiveness of the THP system is also highly dependent on the mass ratio between the heave plate and platform. To make the system effective, a large heave plate (secondary mass) would be essential. The large secondary mass, however, increases not only the implementation cost of the THP system but also the

complexity of the suspension system. It would be attractive if the equivalent or better control performance can be realized by utilizing a much smaller mass/size of heave plate. Recently, a novel device dubbed inerter has been introduced into the vibration control of civil engineering structures, and the principal of this device may shed some light on the problem mentioned above. The inerter conceptually proposed by Smith [19] in the 2000s is a two-terminal mechanical element which can generate a resisting force proportional to the acceleration difference between its two terminals, with the proportionality dubbed as inertance. In the technological aspect, the inerter can be realized by means of ball screw assembly, rack-and-pinion and fluid [20, 21], and it has been shown to achieve the inertance several orders larger than its physical mass. Recognizing the significant mass amplification effect, researchers then introduce the inerter element into the TMD system to reduce the secondary mass of the system and developed many inerter-based TMD systems such as the tuned viscous mass damper (TVMD) [22], tuned mass-damper-inerter (TMDI) [23], tuned inerter damper (TID) [24, 25], electromagnetic inertial mass dampers (EIMD) [26-28], and tuned tandem mass dampers-inerters (TTMDI) [29], etc. These systems have been proved to be effective in mitigating seismic- [30, 31] and wind-induced [32, 33] vibrations of various structures, and improving the performance of base isolation systems [34-36]. Additionally, considerable research efforts are also dedicated to finding the optimal design of inerter-based control systems in recent years [37-39].

Very recently, the inerter-based control systems were introduced into offshore industries to reduce the vibrations of floating structures. Hu et al. [40] demonstrated the effectiveness of using inerter-based control system in suppressing the vibrations of a floating offshore wind turbine (FOWT) subjected to wind and wave loadings. Ma et al. [14] installed an inerter between the heave plate and SSP, and developed a tuned heave plate inerter (THPI) to reduce the heave motion of SSP when it is subjected to sea waves. The results demonstrated that the proposed THPI system outperformed the THP system, and the heave motion could be further reduced by about 19%. To further enhance the control effectiveness, an inerter-based device, rotational inertia damper (RID), was proposed to be installed between the SSP and seabed [41]. It was found the RID system could realize the identical or even better control performance compared to the FHP and THP systems by using only 0.8% mass of the conventional FHP and THP systems. The proposed RID device was therefore very economic compared to the FHP and THP systems. However, it should be noted that both the authors' previous studies [14, 41] controlled the heave motion of SSP only. As discussed above, SSP may experience excessive pitch motion during its service life, which should be controlled as well. This paper is an extension of the authors' previous study [41], and the RID systems are used to simultaneously control both the heave and pitch motions of SSP. Compared to the previous study, the

following obvious differences exist: (1) the designs are different: a single RID was used to control the heave motion only in Ref. [41], while both the heave and pitch motions are controlled in the present study by using two RIDs. Due to this design difference, the equations of motion of the system in the present study and Ref. [41] are different, and they are much more complicated in the present study; (2) the analytical model in the present study is more realistic compared to that in Ref. [41] since the vibration in the pitch direction is unavoidable in engineering practice, and it is important to suppress this adverse vibration as well; (3) the analytical model in the present study is also more precise as compared to that in Ref. [41] since the radiation damping is considered, and the analytical model is further validated in the present study by comparing the response amplitude operators (RAOs) of the heave and pitch motions with the previous experimental and numerical results [16]; (4) because both the heave and pitch motions are of interest in the present study, the optimization methods for the THP in the present study and Ref. [41] are different. In particular, a single-objective optimization method was used in Ref. [41], while a multi-objective optimization algorithm (for both the heave and pitch motions) is utilized in the present study.

The remaining of this paper is organized as follows: Section 4.2 develops the analytical models of SSP with different control systems in the frequency domain; the Simulink models of SSP with different control systems are developed in Section 4.3 to facilitate the investigation of time-domain control performances that will be presented in Section 4.5; in Section 4.4, six waves are selected to test the effectiveness of these control systems under different wave conditions, and the multi-objective genetic algorithm is introduced to determine the optimal parameters of the THP systems; Section 4.5 discusses the frequency- and time-domain control effectiveness of the FHP, THP and RID systems in reducing the heave and pitch motions of SSP; finally, the major conclusions of this research are drawn in Section 4.6.

4.2 Analytical Models of SSP with Different Control Systems

In this section, an analytical model of a SSP equipped with two RID systems is established. For comparison, the corresponding models of SSP with the conventional FHPs and THPs are developed as well. Based on these analytical models, the dynamic equilibrium equations of the SSP controlled by different control systems are derived and solved (Sections 4.2.2, 4.2.3 and 4.2.4), and the response amplitude operator (RAO) and response spectra are calculated. Moreover, the standard deviations of heave and pitch motions are also calculated to quantitatively evaluate the performances of the FHP, THP and RID systems.

4.2.1 SSP and RID models

In the present study, a practical SSP (i.e. the HYSY 981 platform) [16] is selected as the research objective. Figure 4-1 shows the schematic drawings of the platform and Table 4-1 tabulates the detailed physical properties. As shown, the SSP consists of four rectangular columns, two rectangular pontoons, and one deck. The total displacement (i.e. the physical mass) is 51700 tonnes, the operating draft is 19 m. In the figure, G is the centre of gravity of the platform.

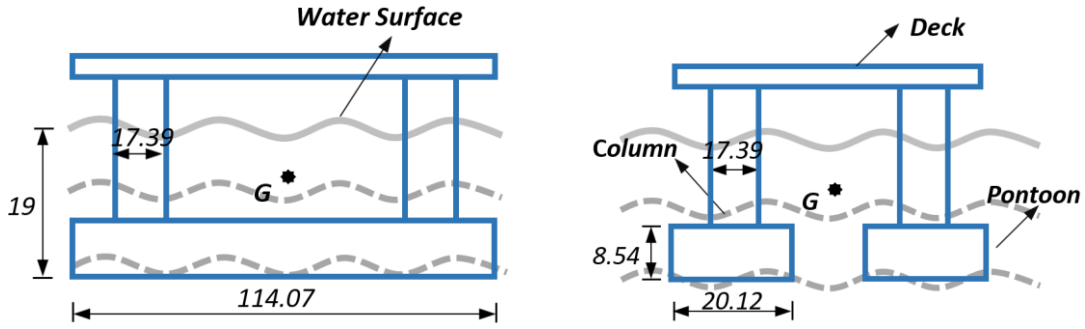

(a) Elevation view (b) Side view

Figure 4-1 Schematic drawings of the HYSY 981 platform (unit: m)

Table 4-1 Geometric properties of HYSY 981 platform

Properties	Value	Properties	Value
Deck (m)	77.47×74.38×8.60	Displacement (tonnes)	51700
Columns (m)	17.39×17.39×21.46	Roll radius of gyration (m)	33.30
Pontoons (m)	114.07×20.12×8.54	Pitch radius of gyration (m)	33.40
Operating draft (m)	19	Yaw radius of gyration (m)	35.00

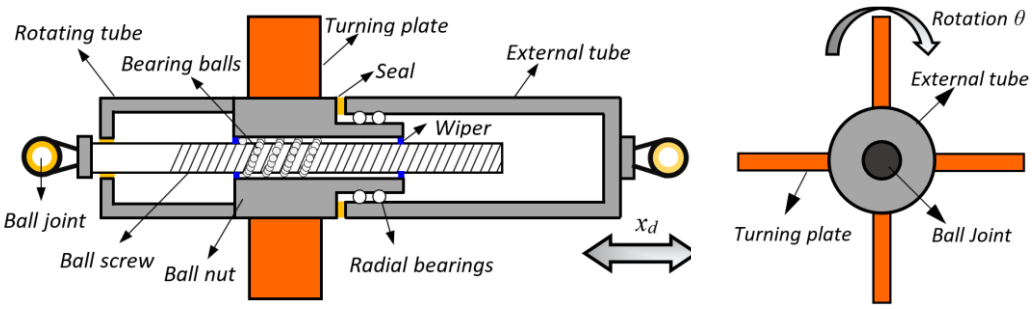

(a) Elevation view (b) Side view

Figure 4-2 Schematic drawings of the RID system

If a traditional THP with a mass ratio of 2% is applied to control the vibration of this platform, the required mass of heave plate is 1034 tonnes. There is no doubt that the huge auxiliary mass not only significantly increases the manufacture and maintenance costs of the platform, but also remarkably increases the design difficulty of the suspension systems. Instead of using THP, the novel RID system as proposed by the authors in Ref. [41] is adopted to mitigate both

the heave and pitch motions of the SSP in the present study. Figure 4-2 shows the schematic drawings of the RID system. As shown, this device consists of a ball screw assembly, an external tube, a rotating tube, ball joints, radial bearings and a suit of turning plates. The ball screw can convert the linear motion into the high-speed rotations of the turning plates, and thus amplify the resistant force of fluid.

Through some straightforward derivations, the ideal axial force $f_R(t)$ provided by the RID system can be calculated, and it has the following form [41]

$$f_R(t) = m_e\ddot{x}_d(t) + c_e\dot{x}_d(t)|\dot{x}_d(t)| \tag{4.1}$$

where

$$m_e = \frac{1}{3}\left(\frac{2\pi}{L}\right)^2 (\rho c_m + \rho_s) l_{tp} t_{tp} R^3 \tag{4.2}$$

and

$$c_e = \frac{1}{8}\left(\frac{2\pi}{L}\right)^3 \rho c_d l_{tp} R^4 \tag{4.3}$$

are the inertance (i.e. the equivalent mass) and equivalent damping coefficient of each turning plate, respectively; t is the time; L is the lead of ball screw; ρ is the density of seawater; c_m is the inertia coefficient; c_d is the drag coefficient of turning plate; l_{tp} is the depth of turning plate; t_{tp} is the thickness of turning plate; R is the radius of turning plate; $\dot{x}_d(t)$ and $\ddot{x}_d(t)$ are the relative velocity and acceleration, respectively. More details regarding the derivation can be found in Ref. [41].

4.2.2 Analytical Model of SSP-RID System

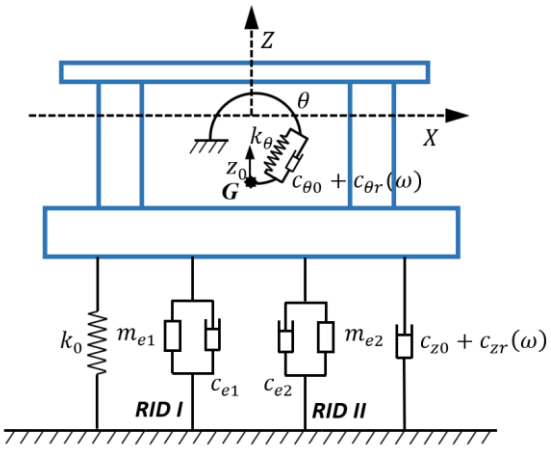

Figure 4-3 Analytical model of SSP-RID system

The proposed RID systems are installed between the SSP and seabed. The feasibility of this connection was justified in Ref. [41]. According to which, the water depth for economic application of this technique is between 137.16 and 304.8 m). To avoid repetition, this justification is not reported in the present study, and interested readers can find more detailed information in Ref. [41]. Figure 4-3 shows the analytical model of the SSP equipped with two RID systems, and the meaning of each parameter will be presented below. With such an analytical model, the dynamic equilibrium equations of the SSP with RIDs in the heave and pitch directions can be written as

$$m_0\ddot{z}_0(t) = f_0(t) + f_{res}(t) + f_{vic}(t) + f_{rad}(t) + f_{R1}(t) + f_{R2}(t) \tag{4.4}$$

$$m_\theta\ddot{\theta}(t) = \tau_\theta(t) + \tau_{res}(t) + \tau_{vic}(t) + \tau_{rad}(t) + \frac{L_s}{2}[f_{R1}(t) - f_{R2}(t)] \tag{4.5}$$

in which m_0 is the physical mass of the SSP; m_θ is the moment of inertia of the SSP; $\ddot{z}_0(t)$ is the acceleration in the heave direction; $\ddot{\theta}(t)$ is the angular acceleration in the pitch direction; $f_0(t)$ and $\tau_\theta(t)$ are the wave-excited forces on the SSP in the heave and pitch directions, respectively; $f_{R1}(t)$ and $f_{R2}(t)$ are the counteracting forces from RID I and II respectively, which are governed by Equation (4.1); L_s is the spacing between the RID I and II. Considering the dimension of the pontoon (i.e. the length of 114.07 m as shown in Table 4-1), L_s is taken as 60 m in the analysis. All the other items in Equations (4.4) and (4.5) are explained one by one as below.

$f_{res}(t)$ and $\tau_{res}(t)$ are the restoring forces on the SSP in the heave and pitch directions respectively, which arise when the platform is perturbed away from its equilibrium position, and they can be calculated by the following equations [42]:

$$f_{res}(t) = -k_0 z_0(t) \tag{4.6}$$

$$\tau_{res}(t) = -k_\theta \theta(t) \tag{4.7}$$

where $z_0(t)$ is the displacement of SSP in the heave direction; $\theta(t)$ is the angular displacement of the SSP in the pitch direction; k_0 and k_θ are respectively the restoring stiffnesses of the SSP in the heave and pitch directions (refer to Figure 4-3), and they can be calculated by

$$k_0 = \rho g A_w \tag{4.8}$$

$$k_\theta = \rho g V \overline{GM} \tag{4.9}$$

in which g is the gravitational acceleration, A_w is the waterplane area of platform, V is the displaced volume of water, $\overline{GM}$ is the meta-centric height of the SSP.

$f_{vic}(t)$ and $\tau_{vic}(t)$ are the viscous damping forces on the SSP in the heave and pitch directions respectively, which are induced due to the skin friction effect and viscous effect generated by the pressure distribution around the platform (i.e. the eddy-making damping) [42]. The viscous damping forces can be expressed as follows:

$$f_{vic}(t) = -c_{z0}\dot{z}_0(t) \tag{4.10}$$

$$\tau_{vic}(t) = -c_{\theta 0}\dot{\theta}(t) \tag{4.11}$$

where $\dot{z}_0(t)$ is the velocity of the SSP in the heave direction, $\dot{\theta}(t)$ is the angular velocity of the SSP in the pitch direction, and c_{z0} and $c_{\theta 0}$ are the viscous damping coefficients of the SSP in the heave and pitch directions respectively, which can be calculated based on the corresponding damping ratios. It is noteworthy that the damping ratios of the SSP in the heave and pitch directions have been identified through the previous free-decay tests in Ref. [16], and they are 4.48% and 7.61%, respectively. More information regarding the tests of SSP can be found in Appendix A.

In Equations (4.4) and (4.5), $f_{rad}(t)$ and $\tau_{rad}(t)$ are the radiation damping forces on the SSP in the heave and pitch directions respectively, and they result from the change in momentum of the fluid due to the motions of the SSP. According to Cummins's work [43], the radiation damping forces can be expressed as follows:

$$f_{rad}(t) = -m'_{0\_\infty}\ddot{z}_0(t) - \int_0^t K_0(t-t')\,\dot{z}_0(t')dt' \tag{4.12}$$

$$\tau_{rad}(t) = -m'_{\theta\_\infty}\ddot{\theta}(t) - \int_0^t K_\theta(t-t')\,\dot{\theta}(t')dt' \tag{4.13}$$

in which $m'_{0\_\infty} = \lim_{\omega\to\infty} m'_0(\omega)$ and $m'_{\theta\_\infty} = \lim_{\omega\to\infty} m'_\theta(\omega)$ are the infinite-frequency added masses of the SSP in the heave and pitch directions, respectively. In the present study, a toolbox developed by Perez and Fossen [44] is utilized to identify these infinite-frequency added masses (i.e. m'_{0_∞} and m'_{θ_∞}).The second term denotes the fluid-memory model which captures the energy transfer from the motions of platform to the radiated waves. The kernel of the convolution term (i.e. $K_0(t)$ and $K_\theta(t)$) is the impulse response function of the radiation, which is also known as retardation or memory function.

Substituting the above terms into Equations (4.4) and (4.5), one can obtain:

$$\begin{aligned}\left(m_0 + m'_{0\_\infty} + \sum_{j=1}^{2} m_{e\_j}\right)\ddot{z}_0(t) + c_{z0}\dot{z}_0(t) + \int_0^t K_0(t-t')\,\dot{z}_0(t')dt' \\ + \sum_{j=1}^{2} c_{e\_zj}\,\dot{z}_0(t)|\dot{z}_0(t)| + k_0 z_0(t) = f_0(t)\end{aligned} \tag{4.14}$$

$$\left(m_\theta + m'_{\theta\_\infty} + \sum_{j=1}^{2} m_{e\_\theta j}\right)\ddot{\theta}(t) + c_{\theta 0}\dot{\theta}(t) + \int_0^t K_\theta(t-t')\,\dot{\theta}(t')dt' + \sum_{j=1}^{2} c_{e\_\theta j}\,\dot{\theta}(t)\left|\dot{\theta}(t)\right| + k_\theta\theta(t) = \tau_\theta(t) \tag{4.15}$$

where j=1, 2 is the ID of the control system; m_{e_j} is the inertance (i.e. the amplified mass) of the RID system; $m_{e\_\theta j} = (\frac{L_s}{2})^2 m_{e\_j}$ is the moment of inertia provided by the RID system; c_{e_zj} is the viscous damping coefficient of the RID system in the heave direction; $c_{e\_\theta j} = (\frac{L_s}{2})^3 c_{e\_zj}$ is the viscous damping coefficient of the RID system in the pitch direction.

Obviously, Equations (4.14) and (4.15) cannot be directly transformed into the frequency domain due to the nonlinear damping force and the convolution term of the radiation force. Therefore, the nonlinear damping forces should be firstly linearized, and they can be linearized by the following equations [45]

$$\dot{z}_0(t)|\dot{z}_0(t)| \approx \frac{8}{3\pi}\omega Z_0 \dot{z}_0(t) \tag{4.16}$$

$$\dot{\theta}(t)\left|\dot{\theta}(t)\right| \approx \frac{8}{3\pi}\omega\theta_0\dot{\theta}(t) \tag{4.17}$$

in which Z_0 and θ_0 are respectively the motion amplitude of the SSP in the heave and pitch directions, which can be determined through an iterative process. It is noteworthy that this linearization method is widely applied in modelling marine structures, and its accuracy and effectiveness have been demonstrated in many previous studies (e.g. Ref. [46]).

As for the radiation forces in Equations (4.14) and (4.15), they can be expressed in the frequency domain as follows [42, 47]:

$$f_{rad}(s) = -m'_0(\omega)\ddot{z}_0(s) - c_{zr}(\omega)\dot{z}_0(s) \tag{4.18}$$

$$\tau_{rad}(s) = -m'_\theta(\omega)\ddot{\theta}(s) - c_{\theta r}(\omega)\dot{\theta}(s) \tag{4.19}$$

where $s = i\omega$ with i and ω representing the imaginary unit and frequency, respectively; $m'_0(\omega)$ and $m'_\theta(\omega)$ are the frequency-dependent added mass coefficients of the SSP in the heave and pitch directions, respectively; and $c_{zr}(\omega)$ and $c_{\theta r}(\omega)$ are the frequency-dependent damping coefficients of the SSP in the heave and pitch directions, respectively. These frequency-dependent coefficients can be calculated based on the potential theory, and many hydrodynamic codes have been developed in the past decades and implemented in the commercial software packages. In the present study, the commercial software ANSYS AQWA (version: R17.2 academic) is utilized to calculate these frequency-dependent coefficients. Moreover, the wave-excited forces on the SSP (i.e. f_0 and τ_θ) can be obtained from this

software package as well. It is worth noting that the wave-excited forces on the RID systems are ignored since they are much smaller compared to those on the SSP due to the very small size of the RID system.

After linearizing the nonlinear damping and obtaining the frequency-domain expression of the radiation forces, Equations (4.14) and (4.15) can be expressed in the Laplace domain as follows:

$$\left[m_0 + m_0'(\omega) + \sum_{j=1}^{2} m_{e\_j}\right]\ddot{z}_0(s) + \left[c_{z0} + c_{zr}(\omega) + \sum_{j=1}^{2} c'_{e\_zj}\right]\dot{z}_0(s) + k_0 z_0(s) = f_0(s) \tag{4.20}$$

$$\left[m_\theta + m_\theta'(\omega) + \sum_{j=1}^{2} m_{e\_\theta j}\right]\ddot{\theta}(s) + \left[c_{\theta 0} + c_{\theta r}(\omega) + \sum_{j=1}^{2} c'_{e\_\theta j}\right]\dot{\theta}(s) + k_\theta \theta(s) = \tau_\theta(s) \tag{4.21}$$

in which c'_{e_zj} and $c'_{e\_\theta j}$ are the linearized damping coefficients of the RID systems in the heave and pitch directions respectively, and they are

$$c'_{e\_zj} = \frac{8}{3\pi}\omega Z_0 c_{e\_zj} \tag{4.22}$$

$$c'_{e\_\theta j} = \frac{8}{3\pi}\omega \theta_0 c_{e\_\theta j} \tag{4.23}$$

For conciseness, Equations (4.20) and (4.21) can be rewritten in a more compact form as

$$[s^2\boldsymbol{M}_{RID} + s\boldsymbol{C}_{RID} + \boldsymbol{K}_{RID}]\boldsymbol{Z}_{RID}(s) = \boldsymbol{F}_{RID}(s) \tag{4.24}$$

where $\boldsymbol{Z}_{RID}(s)$ and $\boldsymbol{F}_{RID}(s)$ are the complex amplitude vectors of the motion and wave-excited force of the system, respectively; $\boldsymbol{M}_{RID}$, $\boldsymbol{C}_{RID}$ and $\boldsymbol{K}_{RID}$ respectively represent the mass, damping and stiffness matrices, and they can be expressed as follows:

$$\boldsymbol{M}_{RID} = \begin{bmatrix} m_0 + m_0'(\omega) + \sum_{j=1}^{2} m_{e\_j} & 0 \\ 0 & m_\theta + m_\theta'(\omega) + \sum_{j=1}^{2} m_{e\_\theta j} \end{bmatrix} \tag{4.25}$$

$$\boldsymbol{C}_{RID} = \begin{bmatrix} c_{z0} + c_{zr}(\omega) + \sum_{j=1}^{2} c'_{e\_zj} & 0 \\ 0 & c_{\theta 0} + c_{\theta r}(\omega) + \sum_{j=1}^{2} c'_{e\_\theta j} \end{bmatrix} \tag{4.26}$$

$$\boldsymbol{K}_{RID} = \begin{bmatrix} k_0 & 0 \\ 0 & k_\theta \end{bmatrix} \tag{4.27}$$

According to Equation (4.24), the motion of the SSP with RIDs can be calculated as

$$\boldsymbol{Z}_{RID}(s) = [\boldsymbol{\Lambda}_{RID}(s)]^{-1}\boldsymbol{F}_{RID}(s) \tag{4.28}$$

where $\boldsymbol{\Lambda}_{RID}(s)$ is the impedance matrix of the system, which has the following form:

$$\boldsymbol{\Lambda}_{RID}(s) = \begin{bmatrix} A_{11}(s) & A_{12}(s) \\ A_{21}(s) & A_{22}(s) \end{bmatrix} \tag{4.29}$$

The elements of the above matrix are summarized in Appendix B.

In the present study, the heave and pitch motions of the SSP without control are also calculated for comparison, and the corresponding responses can be obtained by setting the parameters related to the RID system (i.e. m_{e_j}, $m_{e\_\theta j}$, c'_{e_zj} and $c'_{e\_\theta j}$ in Equations (4.25) and (4.26), j=1, 2) equal to 0.

4.2.3 Analytical Model of SSP-FHP System

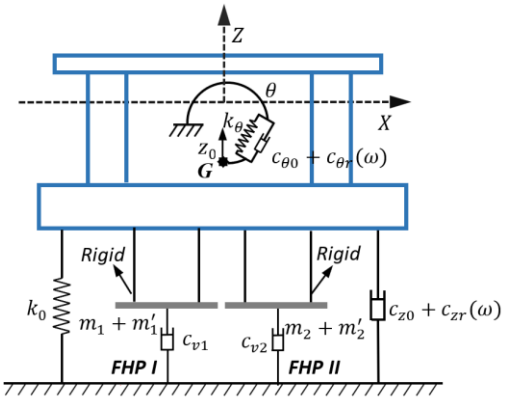

Figure 4-4 Analytical model of SSP-FHP system

Figure 4-4 illustrates the analytical model of the SSP equipped with two FHP systems (i.e. the SSP-FHP system). As shown, the heave plates are rigidly connected to the platform. In this figure, m_j, m'_j and c_{vj} are the physical mass, added mass and inherent damping coefficient of the heave plate respectively, and they can be calculated as follows:

$$m_j = \rho_s V_j \tag{4.30}$$

$$m'_j = \rho c_{aj} V_{Rj} \tag{4.31}$$

$$c_{vj} = \frac{1}{2}\rho c_{dj} A_j \tag{4.32}$$

in which j=1, 2; ρ_s is the density of steel; V_j is the volume of the j^{th} heave plate; c_{aj} is the added mass coefficient of the j^{th} heave plate; V_{Rj} is the reference volume of the j^{th} heave

plate; c_{dj} is the drag coefficient of the j^{th} heave plate; A_j is the projected area of the j^{th} heave plate in the vertical direction. These hydrodynamic coefficients can be determined according to Refs. [42, 48].

By following similar derivation processes in Section 4.2.2, the equation of motion of the SSP-FHP system can be derived as follows:

$$[s^2\boldsymbol{M}_{FHP} + s\boldsymbol{C}_{FHP} + \boldsymbol{K}_{FHP}]\boldsymbol{Z}_{FHP}(s) = \boldsymbol{F}_{FHP}(s) \tag{4.33}$$

in which $\boldsymbol{Z}_{FHP}(s)$ and $\boldsymbol{F}_{FHP}(s)$ are the complex amplitude vectors of the motion and wave-excited force of the system, respectively. $\boldsymbol{M}_{FHP}$, $\boldsymbol{C}_{FHP}$ and $\boldsymbol{K}_{FHP}$ respectively represent the mass, damping and stiffness matrices of the SSP-FHP system, and they are

$$\boldsymbol{M}_{FHP} = \begin{bmatrix} m_0 + m_0'(\omega) + \sum_{j=1}^{2}(m_j + m_j') & 0 \\ 0 & m_\theta + m_\theta'(\omega) + \sum_{j=1}^{2}(m_{\theta j} + m_{\theta j}') \end{bmatrix} \tag{4.34}$$

$$\boldsymbol{C}_{FHP} = \begin{bmatrix} c_{z0} + c_{zr}(\omega) + \sum_{j=1}^{2} c_{vj}' & 0 \\ 0 & c_{\theta 0} + c_{\theta r}(\omega) + \sum_{j=1}^{2} c_{\theta j}' \end{bmatrix} \tag{4.35}$$

$$\boldsymbol{K}_{FHP} = \begin{bmatrix} k_0 & 0 \\ 0 & k_\theta \end{bmatrix} \tag{4.36}$$

in which $m_{\theta j}$ and $m_{\theta j}'$ are the moment of inertia and the corresponding added moment of inertia of the heave plate in the pitch direction respectively, which can be calculated from m_j and m_j' through some straightforward derivations; c_{vj}' and $c_{\theta j}'$ are the linearized viscous damping coefficients of the heave plate in the heave and pitch directions, respectively, which are linearized according to Equations (4.22) and (4.23).

Then the motion of the SSP-FHP system can be written as

$$\boldsymbol{Z}_{FHP}(s) = [\boldsymbol{\Lambda}_{FHP}(s)]^{-1}\boldsymbol{F}_{FHP}(s) \tag{4.37}$$

where

$$\boldsymbol{\Lambda}_{FHP}(s) = \begin{bmatrix} B_{11}(s) & B_{12}(s) \\ B_{21}(s) & B_{22}(s) \end{bmatrix} \tag{4.38}$$

is the impedance matrix of the SSP-FHP system, and its detailed elements are also presented in Appendix B. It is worth noting that in the above derivations, the wave-excited forces on the

heave plates are neglected to simplify the analysis in the present study. This simplification is reasonable for the example SSP since the wave-excited force on the heave plate is much smaller than that on the SSP due to its deeper draft and smaller size compared to the platform [18, 49].

4.2.4 Analytical Model of SSP-THP System

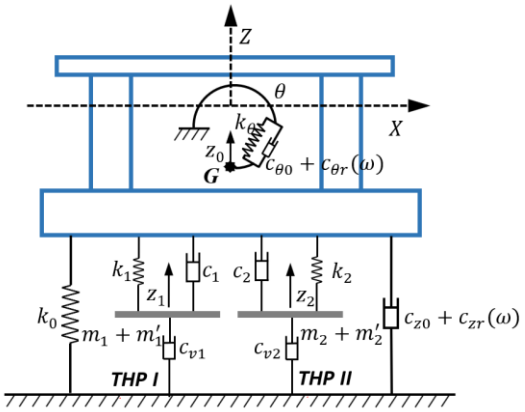

Figure 4-5 Analytical model of SSP-THP system

The analytical model of the SSP with two THPs (i.e. SSP-THP system) can be expressed by Figure 4-5. Different from the SSP-FHP system, each heave plate in the SSP-THP system is connected to the corresponding pontoon by a spring in parallel with a damper. Similarly, the dynamic equilibrium equation of the SSP-THP system can be written as follows:

$$[s^2\boldsymbol{M}_{THP} + s\boldsymbol{C}_{THP} + \boldsymbol{K}_{THP}]\boldsymbol{Z}_{THP}(s) = \boldsymbol{F}_{THP}(s) \tag{4.39}$$

in which $\boldsymbol{Z}_{THP}(s)$ and $\boldsymbol{F}_{THP}(s)$ are the complex amplitude vectors of the motion and wave-excited force of the system, respectively; $\boldsymbol{M}_{THP}$, $\boldsymbol{C}_{THP}$ and $\boldsymbol{K}_{THP}$ are the mass, damping and stiffness matrices of the SSP-THP system, and they are

$$\boldsymbol{M}_{THP} = \begin{bmatrix} m_0 + m_0'(\omega) & 0 & 0 & 0 \\ 0 & m_\theta + m_\theta'(\omega) & 0 & 0 \\ 0 & 0 & m_1 + m_1' & 0 \\ 0 & 0 & 0 & m_2 + m_2' \end{bmatrix} \tag{4.40}$$

$$\boldsymbol{C}_{THP} = \begin{bmatrix} c_{z0} + c_{zr}(\omega) + c_1 + c_2 & \frac{L_s}{2}(c_1 - c_2) & -c_1 & -c_2 \\ \frac{L_s}{2}(c_1 - c_2) & c_{\theta 0} + c_{\theta r}(\omega) + \left(\frac{L_s}{2}\right)^2 (c_1 + c_2) & -\frac{L_s}{2}c_1 & \frac{L_s}{2}c_2 \\ -c_1 & -\frac{L_s}{2}c_1 & c_1 + c_{v1}' & 0 \\ -c_2 & \frac{L_s}{2}c_2 & 0 & c_2 + c_{v2}' \end{bmatrix} \tag{4.41}$$

$$\boldsymbol{K}_{THP} = \begin{bmatrix} k_0 + k_1 + k_2 & \frac{L_S}{2}(k_1 - k_2) & -k_1 & -k_2 \\ \frac{L_S}{2}(k_1 - k_2) & k_\theta + \left(\frac{L_S}{2}\right)^2 (k_1 + k_2) & -\frac{L_S}{2}k_1 & \frac{L_S}{2}k_2 \\ -k_1 & -\frac{L_S}{2}k_1 & k_1 & 0 \\ -k_2 & \frac{L_S}{2}k_2 & 0 & k_2 \end{bmatrix} \tag{4.42}$$

in which k_j and c_j (j=1, 2) are the spring stiffness and damping coefficients of the THP systems respectively, and they will be determined through an optimization algorithm in Section 4.4.2.

Then the dynamic responses of the SSP-THP system can be calculated as follows:

$$\boldsymbol{Z}_{THP}(s) = \boldsymbol{\Lambda}_{THP}(s)^{-1}\boldsymbol{F}_{THP}(s) \tag{4.43}$$

where $\boldsymbol{\Lambda}_{THP}$ is the impedance matrix of the system, which can be expressed in the following form:

$$\boldsymbol{\Lambda}_{THP}(s) = \begin{bmatrix} C_{11}(s) & C_{12}(s) & C_{13}(s) & C_{14}(s) \\ C_{21}(s) & C_{22}(s) & C_{23}(s) & C_{24}(s) \\ C_{31}(s) & C_{32}(s) & C_{33}(s) & C_{34}(s) \\ C_{41}(s) & C_{42}(s) & C_{43}(s) & C_{44}(s) \end{bmatrix} \tag{4.44}$$

The specific elements of this matrix are given in Appendix B as well.

4.2.5 Response Spectrum and Validation

In the above subsections, the heave and pitch motions of the SSP without and with different control systems (i.e. the RID, FHP and THP systems) are derived. The corresponding response amplitude operator (RAO) of the SSP then can be calculated as follows:

$$RAO(\omega) = \frac{|Z_{n1}(\mathrm{s})|}{\xi_a} \tag{4.45}$$

in which $Z_{n1}(s)$ is the complex motion amplitude of the SSP in the heave or pitch direction (n=1, 2), which is the element $(n, 1)$ in the vectors $\boldsymbol{Z}_{RID}(s)$, $\boldsymbol{Z}_{FHP}(s)$, and $\boldsymbol{Z}_{THP}(s)$; $\xi_a = H_s/2$ is the wave amplitude, with H_s representing the significant wave height. It should be noted that Liu and Ou [16] carried out experimental and numerical studies on a 1:70 scaled model of the HYSY 981 platform, and the RAOs in the heave and pitch motions were obtained. To validate the accuracy of the analytical model developed in the present study, the experimental and numerical results obtained in Ref. [16] are compared with those obtained in the present study, and the comparisons are reported in Appendix A.

After obtaining the RAO, the response spectrum S_R of the SSP can be written as

$$S_R(\omega) = S(\omega)[RAO(\omega)]^2 \tag{4.46}$$

where $S(\omega)$ is the spectrum of the incident waves. In the present study, the JONSWAP spectrum is adopted to describe the power spectral density of wave surface elevation [50], and it is represented by the following equation:

$$S(\omega) = a^* H_s^2 \frac{\omega^{-5}}{\omega_0^{-4}} \exp\left[-1.25(\omega/\omega_0)^{-4}\right] \gamma_w^{\exp\left[-\frac{(\omega-\omega_0)^2}{2\tau^2\omega_0^2}\right]} \tag{4.47}$$

in which ω_0 is the peak frequency, and

$$a^* = \frac{0.0624}{0.230 + 0.0336\gamma_w - 0.185(1.9 + \gamma_w)^{-1}} \tag{4.48}$$

where γ_w is the peakedness factor with average value equalling to 3.3 [45]; τ is the shape parameter and equals to 0.07 for $\omega \leq \omega_0$ and 0.09 for $\omega > \omega_0$ [45].

Additionally, the standard deviation of the motion of the SSP is also calculated to quantitatively evaluate the effectiveness of different control systems, and it can be calculated by

$$\sigma = \sqrt{\int_0^\infty S_R(\omega)\, d\omega} \tag{4.49}$$

4.2.6 Practicality Analysis

As mentioned above, three control systems (i.e. the FHP, THP and RID systems) are utilized to control both the heave and pitch motions of the SSP. To illustrate the practicalities, the pros and cons of the FHP, THP and RID systems are discussed below: (1) in the FHP system, the heave plate is rigidly mounted to the SSP through frames, and the installation is relatively easy. However, the control effectiveness is affected by the draft of the heave plate. To make this method effective, the heave plate normally should be placed deep in the water in order to reduce wave-induced motions. The implementation of this system thus may be not easy especially when the platform is located in a harsh environment. Moreover, the control effectiveness of the FHP system is highly dependent on the size of the heave plate as demonstrated in Ref. [14]. A large plate size increases not only the cost of the heave plate but also the cost of the connection frames; (2) for the THP system, the heave plate is connected to the SSP through a set of spring and damper, the design and installation of which may be difficult especially when the mass of the heave plate is large. Similar to the FHP system, a large secondary mass (i.e. the heave plate) is required in order to make this system effective, which increases not only the cost of the project but also the complexity of the suspension system. However, compared to the FHP system, the THP system is normally more effective in reducing the motions of the SSP if the size of the heave plate is the same; (3) for the RID

system, as will be demonstrated in Section 4.5, it can most effectively control the motions of the SSP as compared to the other two systems, and the control effectiveness is achieved by utilizing a very small additional mass (only 1.6% of the physical mass of the heave plate in the present study), which can significantly decrease the construction cost. On the other hand, supporting frames are required in order to install the RID system to the seabed, however, no such supporting frames are required for the THP and FHP systems. The above brief discussions reveal that each system has its own pros and cons. Generally speaking, it is believed that the installation of the RID system is more economic compared to the FHP and THP systems. Moreover, the techniques for installing the RID system can refer to the well-matured techniques (e.g. the fixing technology for the fixed platforms), which thus will not increase the technical difficulties.

4.3 Simulink Models of SSP with Different Control Systems

In the above section, the equations of motion of the SSP controlled by the FHP, THP and RID systems are respectively derived in the frequency domain. As shown, nonlinear damping forces exist in these equations (e.g. Equations (4.14) and (4.15)). To solve the equilibrium equations in the frequency domain, all terms in the equations need to be linearized. Certain inaccuracies might be introduced due to these approximations. Time-domain analyses are thus performed in this section by directly solving the equations of motion, i.e. the approximations of these nonlinear damping forces are not necessary. Moreover, time-domain results (i.e. the heave and pitch motion time histories) are more straightforward and can provide another perspective to demonstrate the performances of different control systems. Given these facts, time-domain analyses are further performed by establishing Simulink models in the commercial software package MATLAB (R2017a).

Figure 4-6 shows the time-domain Simulink models of the SSP controlled by the RID, FHP and THP systems, respectively. On the left side of the Simulink models, the external forces including the wave forces and five feedback loops are input into the system. In particular, these feedback loops are the restoring force with regard to the displacement, the viscous damping force with regard to the velocity, the radiation damping force with regard to the velocity, and the two control forces generated by control systems. On the right side of these Simulink models, the heave and pitch motion time histories of the controlled SSP are outputted. A variable-step solver is adopted for these Simulink models. In the figure, the symbol $\frac{1}{s}$ is an integrator block that outputs the value of the integral of its input signal with respect to time, $|u|$ is the Abs block which outputs the absolute value of the input, and $\times$ is the product block which outputs

the result of multiplying two inputs. For the convenience of constructing Simulink models, some parameters are further defined for the RID, FHP and THP systems, respectively.

For the RID systems,

$$M = m_0 + m'_{0\_\infty} + \sum_{i=1}^{2} m_{e\_j} \tag{4.50}$$

$$I = m_\theta + m'_{\theta\_\infty} + \sum_{i=1}^{2} m_{e\_\theta j} \tag{4.51}$$

in which M and I are respectively the total mass and moment of inertia of the SSP controlled by the RID systems. Similarly, M and I of the SSP-FHP system as shown in Figure 4-6(b) can be calculated by

$$M = m_0 + m'_{0\_\infty} + \sum_{j=1}^{2} \left(m_j + m'_j\right) \tag{4.52}$$

$$I = m_\theta + m'_{\theta\_\infty} + \sum_{j=1}^{2} \left(m_{\theta j} + m'_{\theta j}\right) \tag{4.53}$$

For the SSP controlled by the THP systems, the following parameters are introduced as follows:

$$M_p = m_0 + m'_{0\_\infty} \tag{4.54}$$

$$I_p = m_\theta + m'_{\theta\_\infty} \tag{4.55}$$

$$M_1 = m_1 + m'_1 \tag{4.56}$$

$$M_2 = m_2 + m'_2 \tag{4.57}$$

where M_p and I_p are the total mass and moment of inertia of the uncontrolled SSP, respectively; M_1 and M_2 are respectively the total masses of THP I and II, which include the physical mass and added mass of the heave plate.

As indicated by Equations (4.12) and (4.13), the radiation force acted on the SSP consists of two components: the added-mass force proportional to the acceleration, and the damping force proportional to the velocity (i.e. the fluid-memory effect). The first component of the radiation force (i.e. the infinite-frequency mass) has been integrated into the total mass or moment of inertia of the SSP. As for the second component (e.g. $\int_0^t K_0(t-t')\,\dot{z}_0(t')dt'$ for the heave motion), it is time-consuming to be directly solved because it requires a discrete-time approximation of the convolution integral and enough past data to assess the convolution at each simulation step. Considering this fact, the second component of radiation force, i.e. the

radiation damping force, is approximated by using a linear state-space model. The state-space models in the heave and pitch directions can be respectively expressed by

$$\begin{cases} \dot{\boldsymbol{x}}_{z_r}(t) = \boldsymbol{A}_{z_r}\boldsymbol{x}_{z_r}(t) + \boldsymbol{B}_{z_r}\dot{z}_0(t) \\ y_{z_r}(t) = \boldsymbol{C}_{z_r}\boldsymbol{x}_{z_r}(t) \approx \int_0^t K_0(t-t')\,\dot{z}_0(t')dt' \end{cases} \tag{4.58}$$

$$\begin{cases} \dot{\boldsymbol{x}}_{\theta_r}(t) = \boldsymbol{A}_{\theta_r}\boldsymbol{x}_{\theta_r}(t) + \boldsymbol{B}_{\theta_r}\dot{\theta}(t) \\ y_{\theta_r}(t) = \boldsymbol{C}_{\theta_r}\boldsymbol{x}_{\theta_r}(t) \approx \int_0^t K_\theta(t-t')\,\dot{\theta}(t')dt' \end{cases} \tag{4.59}$$

in which $\boldsymbol{x}_{z_r}$ and $\boldsymbol{x}_{\theta_r}$ are the state vectors; $\dot{z}_0(t)$ and $\dot{\theta}(t)$ are the inputs of the system at time t; $y_{z_r}(t)$ and $y_{\theta_r}(t)$ are the outputs of the system at time t, i.e. the radiation damping forces; $\boldsymbol{A}_{z_r}$, $\boldsymbol{B}_{z_r}$, and $\boldsymbol{C}_{z_r}$ are the system matrices of the state-space model in the heave direction; $\boldsymbol{A}_{\theta_r}$, $\boldsymbol{B}_{\theta_r}$, and $\boldsymbol{C}_{\theta_r}$ are the system matrices of the state-space model in the pitch direction. These system matrices are also identified by using the MATLAB toolbox developed by Perez and Fossen [44]. Interested readers can find more details about the identification method in Ref. [44]. Additionally, it should be noted that other parameters in the Simulink models are the same as those in the frequency-domain analytical models.

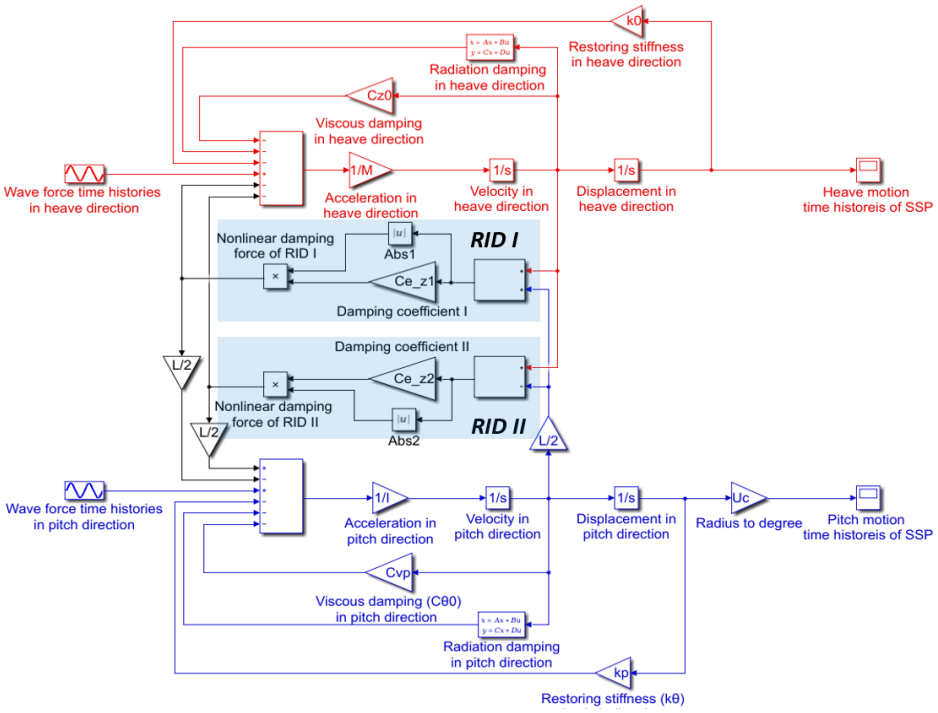

(a) SSP-RID system

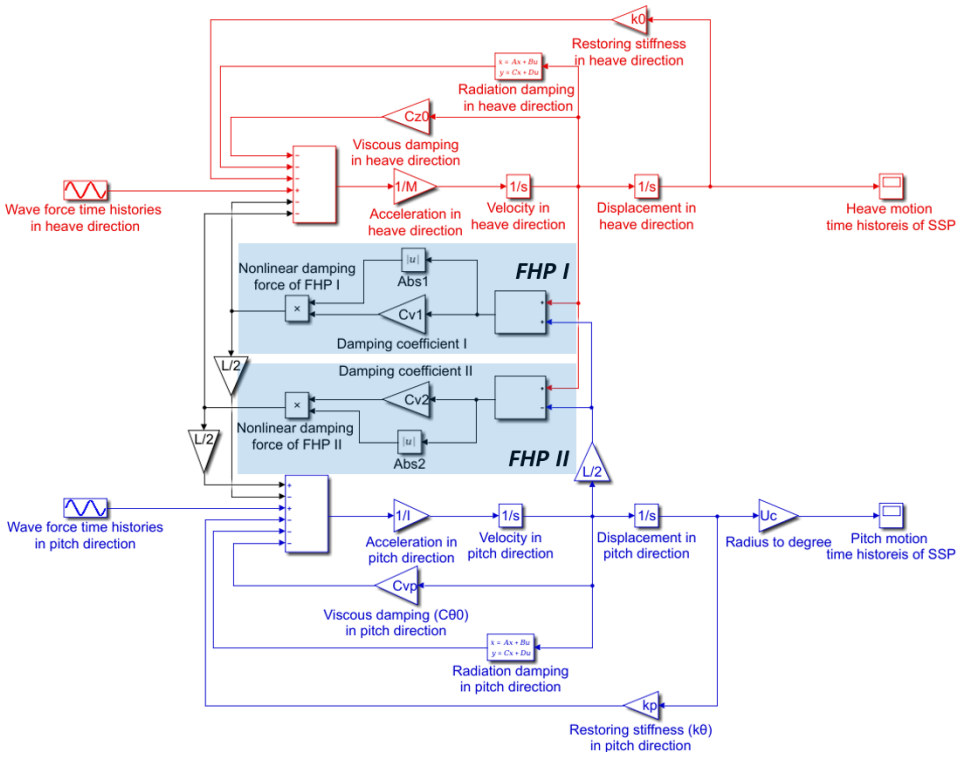

(b) SSP-FHP system

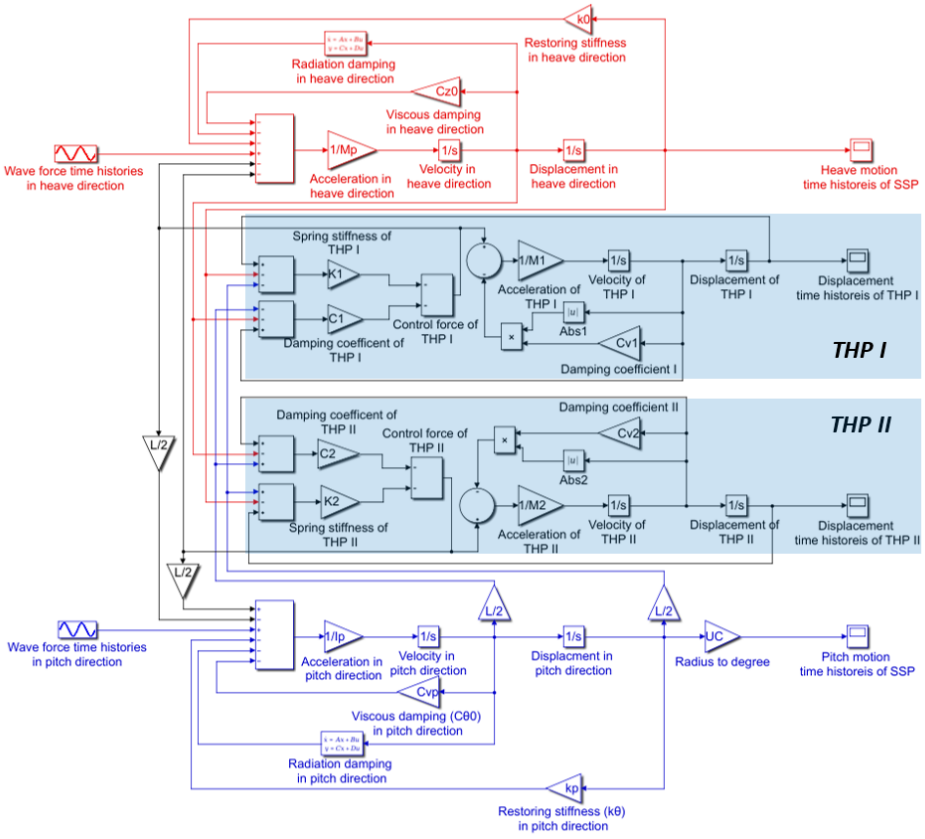

(c) SSP-THP system

Figure 4-6 Simulink models of the SSP with different control systems

4.4 Wave Selection and Optimization of THP System

4.4.1 Wave Selection

To evaluate the performance of different control systems (i.e. FHP, THP, and RID systems), six wave conditions are selected for the example SSP in the present study. All these wave conditions are chosen based on the recorded data at major oil and gas regions including South China Sea (SCS), Gulf of Mexico (GM) and North West Shelf of Australia (NWSA) [16, 49]. Table 4-2 tabulates the detailed information of selected waves, in which the working condition is defined as the wave experienced by the SSP during its normal operational condition, and 10-year and 100-year waves denote the wave with a return period of 10 and 100 years, respectively. Based on the given information, the JONSWAP spectrum of each wave can be determined according to Equation (4.47), and Figure 4-7 illustrates the corresponding spectra. The fundamental natural frequencies of the example SSP in the heave and pitch directions are also shown in the figure. For the example SSP, the fundamental natural frequencies in the heave (ω_s) and pitch (ω_p) directions are 0.290 rad/s and 0.108 rad/s, respectively. It can be observed that the fundamental natural frequency of the SSP in the heave direction falls inside the dominant frequency ranges of loading cases L3, L5 and L6, which indicates the SSP might resonate in the heave direction when it is subjected to these waves.

Table 4-2 Detailed information of the selected waves

Case No.	Wave descriptions	Significant wave height H_s (m)	Peak period T_0 (s)
L1	Working condition in SCS	6.00	11.20
L2	Working condition in GM	3.96	9.00
L3	10-year wave in SCS	11.10	13.60
L4	10-year wave in NWSA	10.00	12.50
L5	100-year wave in SCS	13.30	15.50
L6	100-year wave in GM	12.20	14.00

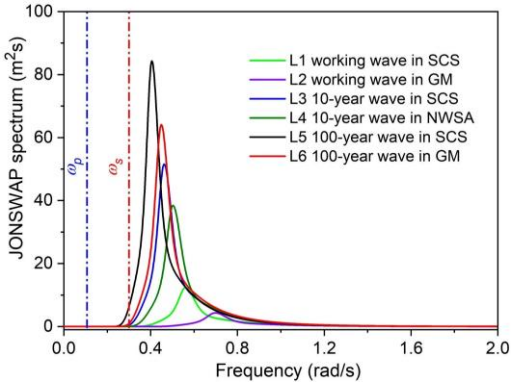

Figure 4-7 JONSWAP spectra of the selected waves

4.4.2 Optimization of THP System

To achieve the best control performance, the THP system should be firstly optimized (tuned). As mentioned above, this research focuses on reducing both the heave and pitch motions of the SSP subjected to wave loadings. To avoid possible mistuning scenarios, two objectives (i.e. both the heave and pitch motions of the SSP) should be optimized simultaneously, i.e. a multi-objective optimization problem should be solved. In the present study, a multi-objective genetic algorithm in MATLAB (i.e. the gamultiobj function) is adopted to determine the optimal parameters of this system. Different from the single-objective optimization, the multi-objective optimization method can generate a suit of optimal solutions, dubbed Pareto-optimal solutions. Without any extra subjective preference, each solution can be considered as acceptable due to the fact that the improvement of one objective leads to the degradation of another objective. According to Ref. [51], a total of 100 chromosomes and 200 generations are usually enough to generate reasonably good optimal results, and these numbers are used in the present study. Additionally, the value of "Pareto Fraction" is set as 0.3, which means 30 elite solutions will be returned after the optimization. As discussed in Section 4.4.1, the fundamental natural frequency of the SSP in the heave direction is much closer to the dominant frequency range of some loading cases and which in turn may result in the resonance of the platform, an optimal solution is thus chosen from the returned Pareto-optimal solutions by reducing the heave motion to the utmost extent. More detailed information regarding this multi-objective optimization method can be found in the user's guide of MATLAB [52].

For the SSP-THP system in the present study, the following optimization problem can be formulated:

$$\widetilde{\boldsymbol{Z}} = \text{argmin}\{\sigma_z, \sigma_\theta\}^T \tag{4.60}$$

in which $0 \leq \gamma_1 \leq 5$, $0 \leq \xi_1 \leq 1$, $0 \leq \gamma_2 \leq 5$, $0 \leq \xi_2 \leq 1$, σ_z and σ_θ are the standard deviations of the heave and pitch motions, respectively; γ_j and ξ_j (j=1, 2) are the non-dimensional natural frequency ratio and damping ratio of the THP system to be determined, and they are governed by

$$\gamma_j = \frac{\omega_j}{\omega_s} \tag{4.61}$$

$$\xi_j = \frac{c_j}{2(m_j + m_j')\omega_j} \tag{4.62}$$

where ω_j is the natural frequency of the THP system, which is $\sqrt{\frac{k_j}{m_j+m_j'}}$ (j=1, 2). Table 4-3 tabulates the optimal parameters of the THP system under different loading scenarios.

Table 4-3 Optimal parameters of the THP system under different wave conditions

Case No.	γ_1	ξ_1(%)	γ_2	ξ_2(%)
L1	2.125	0.779	2.144	2.676
L2	2.425	7.247	1.856	23.726
L3	1.977	2.922	2.066	2.669
L4	2.032	1.864	2.074	5.528
L5	1.979	2.940	1.901	32.818
L6	1.973	3.303	1.940	17.344

4.5 Results and Discussions

In the prior sections, the analytical and Simulink models of the SSP with different control systems are established, and six wave conditions are selected as input. In this section, the effectiveness of utilizing RID, FHP and THP systems to suppress the heave and pitch motions of SSP are investigated in the frequency and time domains, respectively. For comparison, the responses of the SSP without any control device (i.e. the original platform) are also discussed. As mentioned above, a classical floating platform HYSY 981 is selected as the example in this research, and its detailed information is tabulated in Table 4-1. Without loss of generality, two heave plates with a cross-section of 25×25 m and a thickness of 0.2 m are chosen for the FHP and THP systems in the present study by referring to previous studies [16, 18, 49], which corresponds to 3.77% of the mass of the SSP. As for the RID system, four turning plates with a radius of 2.5 m, a width of 1.0 m and a thickness of 0.2 m are adopted. With such designs, the physical mass of the RID systems is only about 1.6% of that of the heave plates (excluding the physical mass of connection systems). However, as will be demonstrated, with such a small mass, the designed RID system can achieve almost the same or even better control performance than the FHP and THP systems especially when the SSP is subjected to the extreme waves.

4.5.1 Control Effectiveness in the Frequency Domain

Figure 4-8 shows the heave response spectra of the SSP subjected to different loading cases, i.e. the working waves (L1 and L2), 10-year waves (L3 and L4) and 100-year waves (L5 and L6). It can be found that all these three control systems can obviously reduce the heave motion of the SSP, and the THP and RID systems are more effective as compared to the FHP system. More specifically, the THP system most evidently reduces the peak value of the spectra in the working wave conditions (L1 and L2), while the RID system is most efficient in the extreme wave scenarios (i.e. L3, L4, L5 and L6). This is due to the fact that the damping force provided by the RID system is a function of the velocity squared (see Equation (4.1)), and an extreme

wave scenario can result in a larger velocity of the platform, which in turn causes a bigger control force to the RID system, and thus more evident control effectiveness. Figure 4-8 also shows that the highest peak of the spectra of different systems (the original SSP, SSP-FHP, SSP-THP, and SSP-RID systems) under each wave appears between 0.3 rad/s and 0.75 rad/s, which corresponds to the dominant frequency of the corresponding wave. This demonstrates that the heave motion of SSP mostly results from the rigid-body motion induced by the wave, but not the resonant vibration of the SSP. This is also the reason why the optimal frequency ratios of the THP system (see Table 4-3) are different from the ordinary structure-TMD system subjected to the broadband loadings (e.g. earthquake, white noise, etc.), in which the optimal frequency ratio is generally close to unity (namely the optimal TMD frequency is close to the natural frequency of the vibrating main structure). Additionally, as shown in Figure 4-8(c), (e) and (f), another peak can be observed at 0.29 rad/s for the original SSP, which corresponds to the fundamental natural frequency of the SSP in the heave direction (ω_s) as mentioned above. This indicates that resonance of the SSP is triggered under these three wave conditions since the natural frequency ω_s falls inside the dominant frequency ranges of these loading cases as mentioned above. It is obvious that the resonant peak of the SSP can be significantly reduced by introducing the FHP, THP and especially RID systems. Another interesting phenomenon observed from the results is that the THP system can slightly lose its effectiveness within certain frequency range of each wave, i.e. the heave response spectra of the SSP-THP system can be slightly larger than the original SSP within certain frequency range (e.g. around 0.64 rad/s-0.70 rad/s in loading case L1). This is because, for the conventional TMD system (the THP system here), there exists an effective frequency range, and the structural responses outside this frequency range can be aggravated [53]. On the other hand, no such issue occurs in the RID system, which further demonstrates the effectiveness and advantages of the RID system.

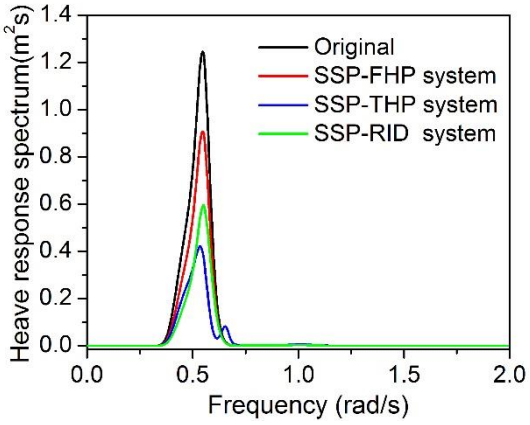

(a) L1

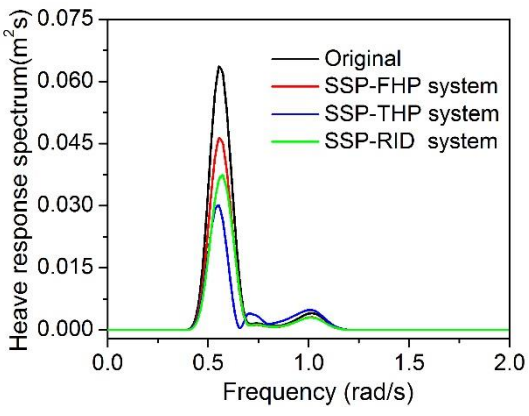

(b) L2

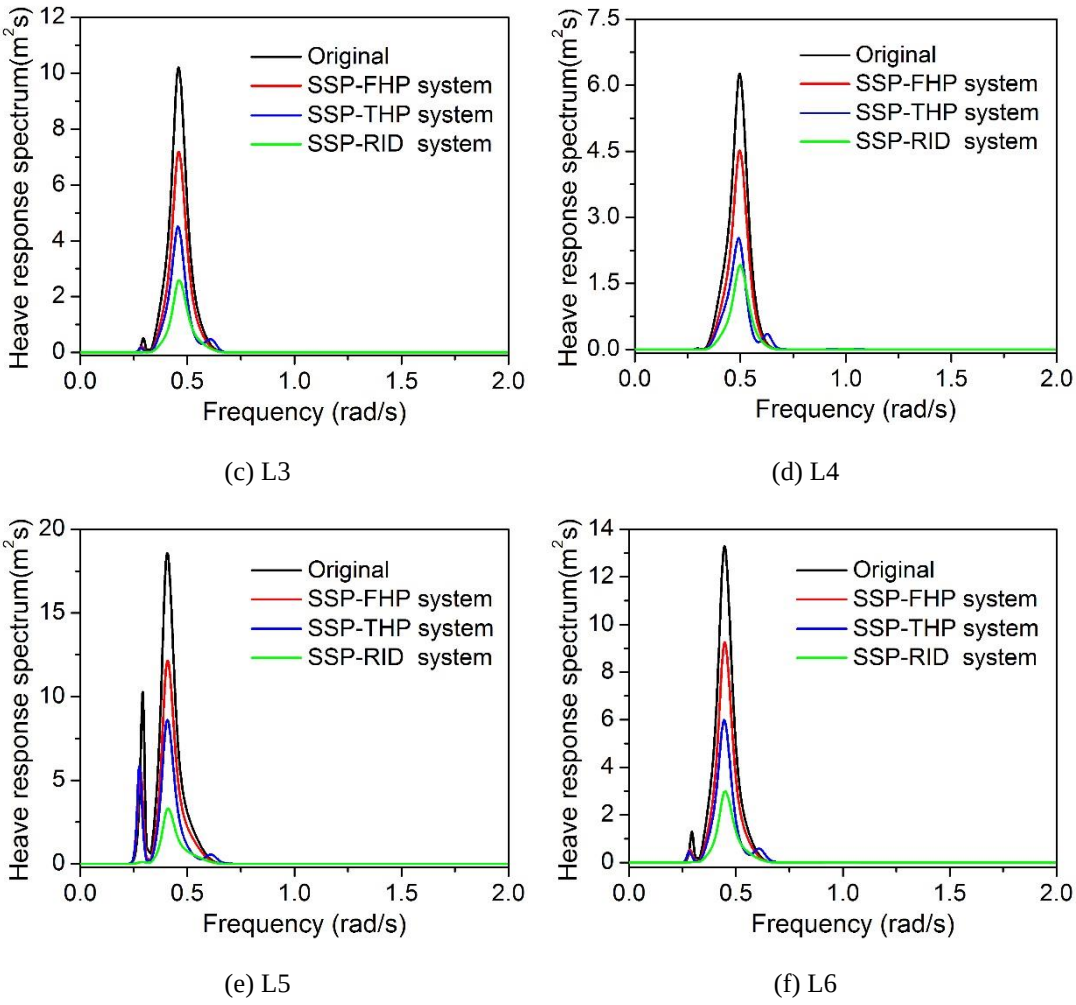

(c) L3 (d) L4

(e) L5 (f) L6

Figure 4-8 Heave response spectra of the SSP without and with control devices under different wave conditions

Figure 4-9 illustrates the pitch response spectra of the SSP with different control devices under different wave conditions. Similar to the results in the heave direction, all the FHP, THP and RID systems significantly reduce the peak value of the pitch response spectra of the SSP, and the THP and RID systems are more effective than the FHP system. The THP performs slightly better than the RID system under the working wave conditions L1 and L2 while the RID system outperforms the THP system in the extreme wave scenarios. On the other hand, different from that in the heave direction, the peak corresponding to the fundamental natural frequency of the SSP in the pitch direction (i.e. 0.108 rad/s) does not appear since the natural frequency (ω_p) falls outside the dominant frequency range of the considered waves as shown in Figure 4-7. The THP system is also found ineffective in reducing the pitch motion of SSP within a certain frequency range of each wave (e.g. around 0.8 rad/s-1.0 rad/s in loading case L2) due to the reason explained above. Similarly, the RID system performs better in reducing the pitch motion in the harsher wave conditions (see Figure 4-9(c). (d), (e) and (f)).

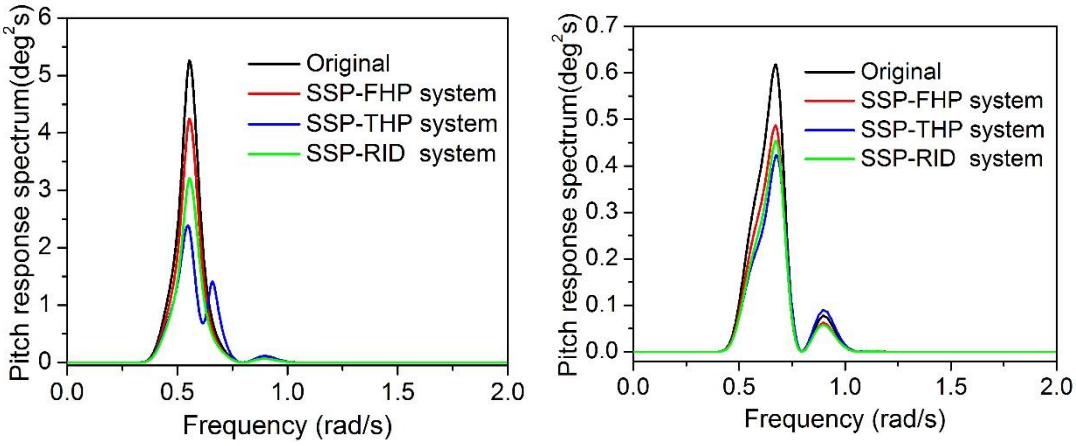

(a) L1

(b) L2

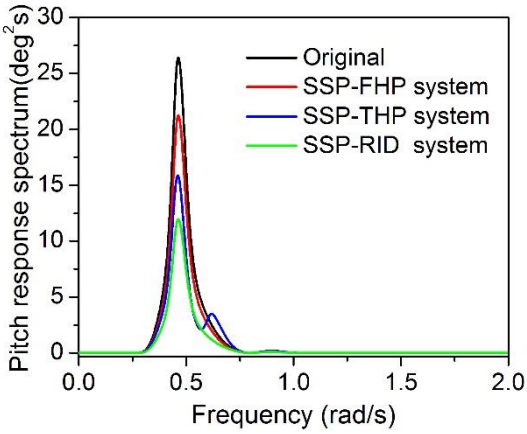

(c) L3

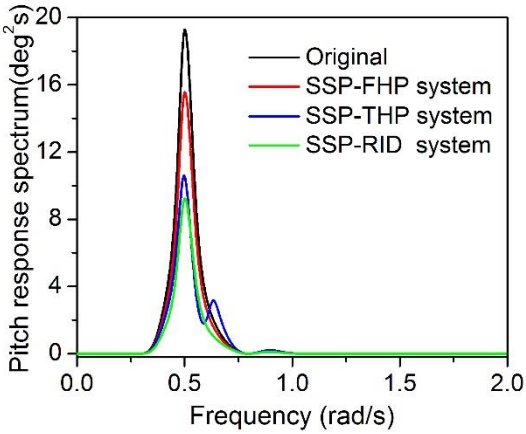

(d) L4

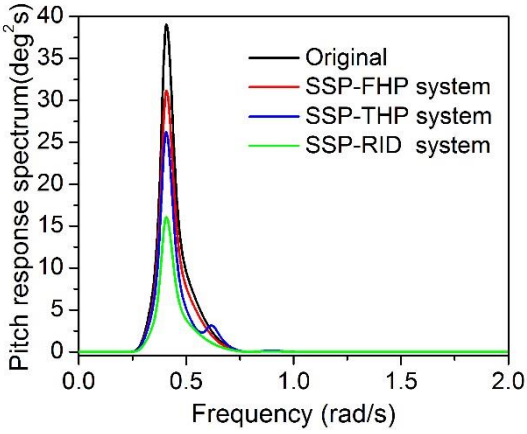

(e) L5

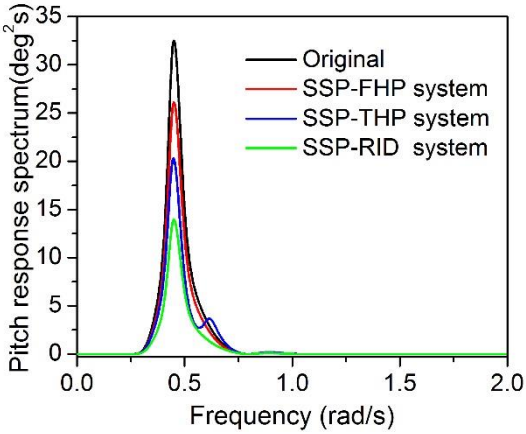

(f) L6

Figure 4-9 Pitch response spectra of the SSP without and with control devices under different wave conditions

For quantitative comparisons, the standard deviations of heave and pitch motions (i.e. σ_z and σ_θ) of the SSP without and with different control systems are calculated according to Equation (4.49), and the corresponding reduction ratios are also calculated:

$$\psi(L_u) = \frac{\sigma_0(L_u) - \sigma'(L_u)}{\sigma_0(L_u)} \times 100\% \tag{4.63}$$

in which L_u (u=1, 2, …, 6) is the number of the wave condition; σ_0 is the standard deviation of the original SSP, and σ' is the corresponding value of the SSP when it is controlled by the FHP, THP or RID system.

Table 4-4 Standard deviations of heave motion (σ_z) and corresponding reduction ratios of different control systems

Case No.	σ_z				Reduction ratio (%)			
	Original	FHP	THP	RID	Original	FHP	THP	RID
L1	0.381	0.323	0.236	0.259	--	15.18	37.99	32.13
L2	0.096	0.082	0.070	0.076	--	14.51	27.37	21.38
L3	1.021	0.849	0.674	0.515	--	16.89	34.04	49.52
L4	0.819	0.689	0.526	0.451	--	15.87	35.77	44.90
L5	1.400	1.136	0.963	0.578	--	18.82	31.20	58.68
L6	1.158	0.957	0.768	0.552	--	17.39	33.68	52.29

Table 4-5 Standard deviations of pitch motion (σ_θ) and corresponding reduction ratios of different control systems

Case No.	σ_θ				Reduction ratio (%)			
	Original	FHP	THP	RID	Original	FHP	THP	RID
L1	0.809	0.725	0.620	0.637	--	10.37	23.39	21.22
L2	0.324	0.289	0.278	0.276	--	10.82	14.24	14.66
L3	1.739	1.557	1.394	1.180	--	10.41	19.83	32.13
L4	1.504	1.349	1.179	1.052	--	10.34	21.64	30.06
L5	2.101	1.878	1.716	1.355	--	10.62	18.45	35.52
L6	1.924	1.723	1.551	1.270	--	10.45	19.49	33.99

Obviously, a larger wave height leads to the bigger structural responses, the biggest heave and pitch motions are thus obtained in the loading case L5. As tabulated in Table 4-4, the reduction ratios in the heave direction are between 14.51% and 18.82% for the FHP system, 27.37-37.99% for the THP system, and 21.38-58.68% for the RID system. Similar to the peak value of the spectra as shown in Figure 4-8, the RID system leads to the best control performance except under the working wave conditions. As for the pitch motion, the reduction ratios of the FHP, THP and RID systems are 10.34-10.82%, 14.24-23.39%, and 14.66-35.52%, respectively. Slightly different from the peak value of the pitch motion spectra (Figure 4-9(b)), it is interesting to find that the RID system is also the most effective in reducing the pitch motions of the SSP in loading case L2. This is due to the fact that the standard deviation (i.e. σ_z or σ_θ) is a statistical index calculated based on the response over the entire frequency range (i.e. it is related to the area enclosed by the corresponding response spectra), instead of the response at

a certain frequency. As shown in Figure 4-9(b), the peak of the pitch motion spectra for the SSP-RID system (the green curve) is higher than that of the SSP-THP system (the blue curve). However, there also exists another frequency range (around 0.80 rad/s-1.08 rad/s), in which the RID system outperforms the THP system. The enclosed area of the green curve is actually slightly smaller than that enclosed by the blue curve, which results in the better control effectiveness of the SSP-RID system in the entire frequency range.

It is also found that the orders of reduction ratios of the RID system in both the heave and pitch directions follow the variation trend of wave height (i.e. L2<L1<L4<L3<L6<L5). As mentioned above, the damping force generated by the RID system is a function of the velocity squared. The bigger the wave height is, the larger is the structural response (e.g. velocity), and thus the better is the control effectiveness of the RID system. For the FHP system, the reduction ratio of the heave motion also follows the wave height. As discussed above, the FHP system is similar to the RID system as it also provides SSP with the added mass and viscous damping. This means that the control effectiveness of the FHP system can increase with the increase of wave height. As for the pitch motion, interestingly, the reduction ratios in all the considered loading scenarios are almost the same as shown in Table 4-5, and the most evident control effectiveness is obtained in loading case L2. As shown in Figure 4-9(b), when the frequency is smaller than 0.68 rad/s, the frequency corresponds to the peak response spectrum, the differences between the pitch response spectra from the original SSP (the black curve) and the SSP-FHP system (the red curve) are marginally more evident compared to other cases (i.e. in Figure 4-9(a), (c), (d), (e) and (f), which in turn results in the slightly larger control effectiveness. For the THP system, generally speaking, both the heave and pitch motions follow the variation trend of L2<L5<L6<L3<L4<L1. It is interesting to find that the largest wave height does not necessarily result in the most evident control effectiveness, which contradicts with the common understanding that the control effectiveness of the TMD (i.e. the THP system here) is better when structural responses are larger. It is worth noting that this common understanding is made based on the assumption that structural behaviors are linear. In the present study, the viscous damping forces acted on the heave plates are linearized by Equation (4.16) and become a function of velocity. However, the excitation frequency (ω) and the corresponding motion amplitude are introduced into the linearized equations after the linearization. In other words, the damping forces would vary with the excitation frequencies, and are different from those in the linear "ordinary structures", in which the damping coefficients are constant and independent of frequency. Apparently, these frequency-dependent damping forces may significantly influence the control effectiveness of the THP system as also observed by some other researchers (e.g. Ref. [54]).

Table 4-5 also shows that the reduction ratios of the FHP, THP and RID systems in the pitch direction are less than those in the heave direction. This fact can be primarily attributed to the influence of the spacing between the two control devices (i.e. L_s in Equation (4.5)). Figure 4-10 shows the influence of spacing on the control effectiveness of different control systems when the SSP is subjected to loading case L3. Considering the dimensions of the platform, the spacing between the two control devices varies from 30 m to 80 m with an increment of 10 m. As shown, the spacing has an ignorable influence on the heave response of the SSP (Figure 4-10(a)), while it can significantly influence the pitch motion. A larger spacing leads to better control performances of the FHP, THP and RID systems in the pitch direction. The control effectiveness in the pitch direction is possible to exceed that in the heave direction when a larger spacing is adopted for the control systems. In practice, it is thus suggested to place the control system apart from each other as large as possible.

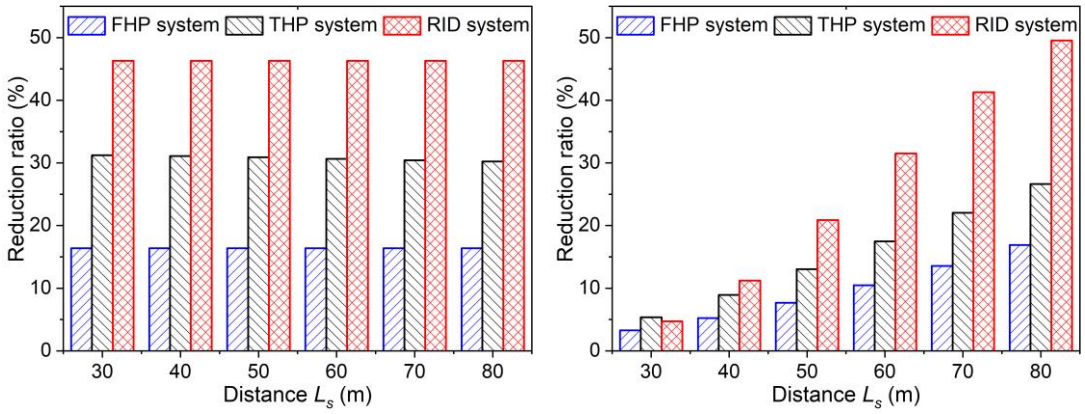

(a) Heave motion (b) Pitch motion

Figure 4-10 Influence of spacing on the reduction ratio of different control systems

It might be worth reiterating that all the above results are obtained based on the RID device with a radius of 2.5 m and the heave plate with a dimension of 25×25 m. The mass of the RID system is only 1.6% of that of the heave plate. However, the analytical results show that almost the same or even better control performance can be obtained by using the novel RID system, demonstrating the advantages of the proposed method.

4.5.2 Control Effectiveness in the Time Domain

The control effectiveness of the FHP, THP and RID systems is further evaluated in the time domain in this subsection. Figure 4-11 and Figure 4-12 show the heave and pitch motion time histories of the SSP without and with the FHP, THP and RID systems, and Table 4-6 and Table 4-7 tabulate the root mean square (RMS) values of the heave and pitch motions of the SSP subjected to different loading cases. The reduction ratios are also calculated based on Equation (4.63). It should be noted that the spacing between the two controlling devices is 60 m.

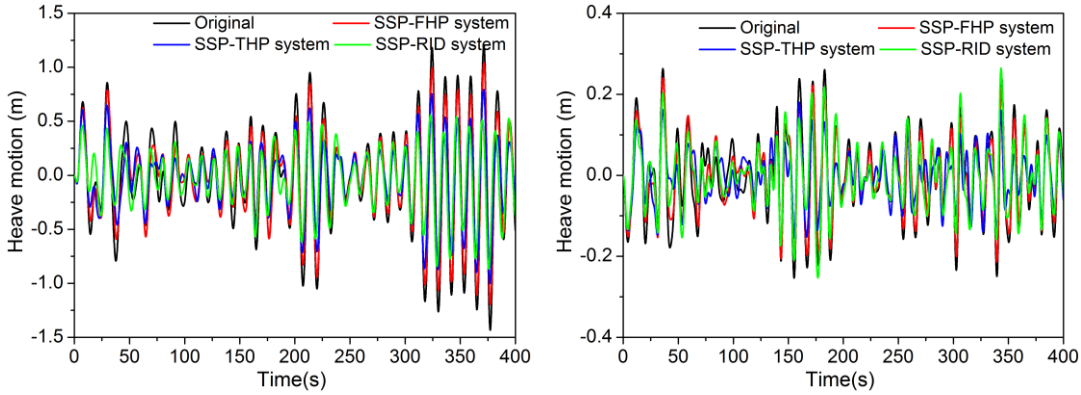

(a) L1

(b) L2

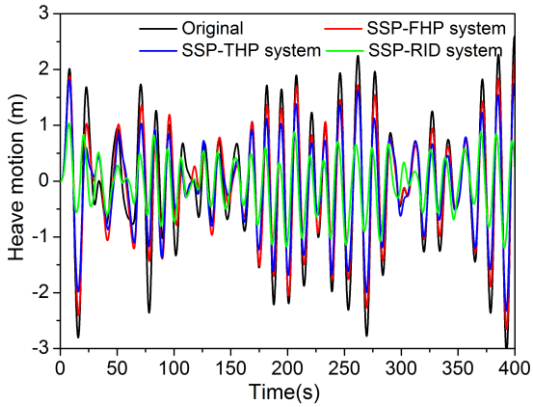

(c) L3

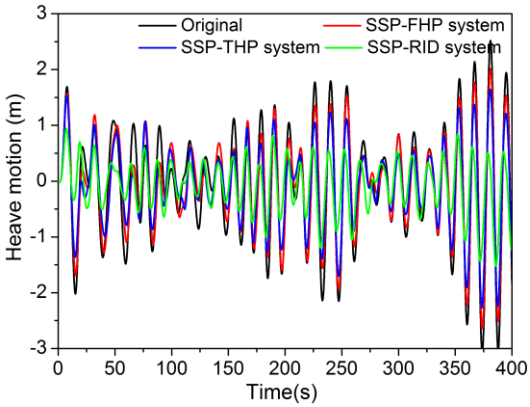

(d) L4

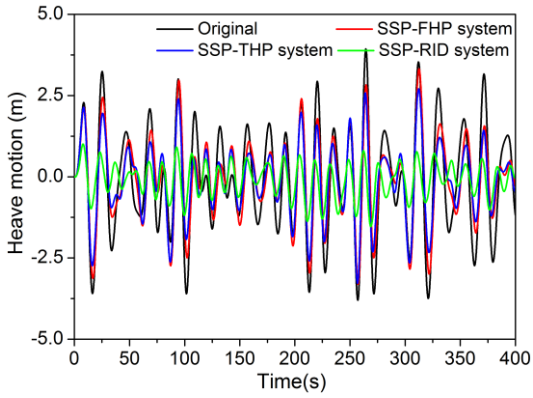

(e) L5

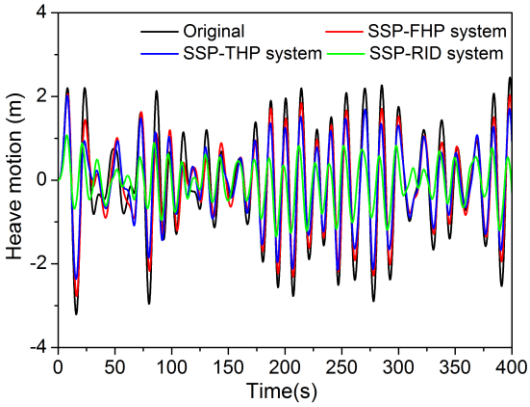

(f) L6

Figure 4-11 Heave motion time histories of the SSP without and with control devices under different wave conditions

It can be seen that both the RMS values in the heave and pitch directions increase with the wave height, and the maximum and minimum values occur in the loading cases L5 and L2, respectively. As for the control effectiveness, the reduction ratios of the FHP, THP and RID systems in the heave direction are 13.81-21.24%, 22.99-32.28%, and 19.14-67.95%, respectively. Compared to the FHP and THP systems, the RID system is most effective in reducing the heave motion except under loading case L2. As for the reduction ratios in the pitch direction, the corresponding values are 10.10-19.66%, 12.81-25.84% and 17.34-56.13%

respectively, and the RID system is the most effective control method in reducing the pitch motion of the SSP. The control effectiveness of the RID system in the heave and pitch directions are not consistent compared to the other two control devices. The reason might be, as discussed above, the effectiveness of the RID system is related to the relative accelerations between the two terminals of the device. In loading case L2, the wave height is relatively small, the control effectiveness of RID is therefore not obvious for the heave motion.

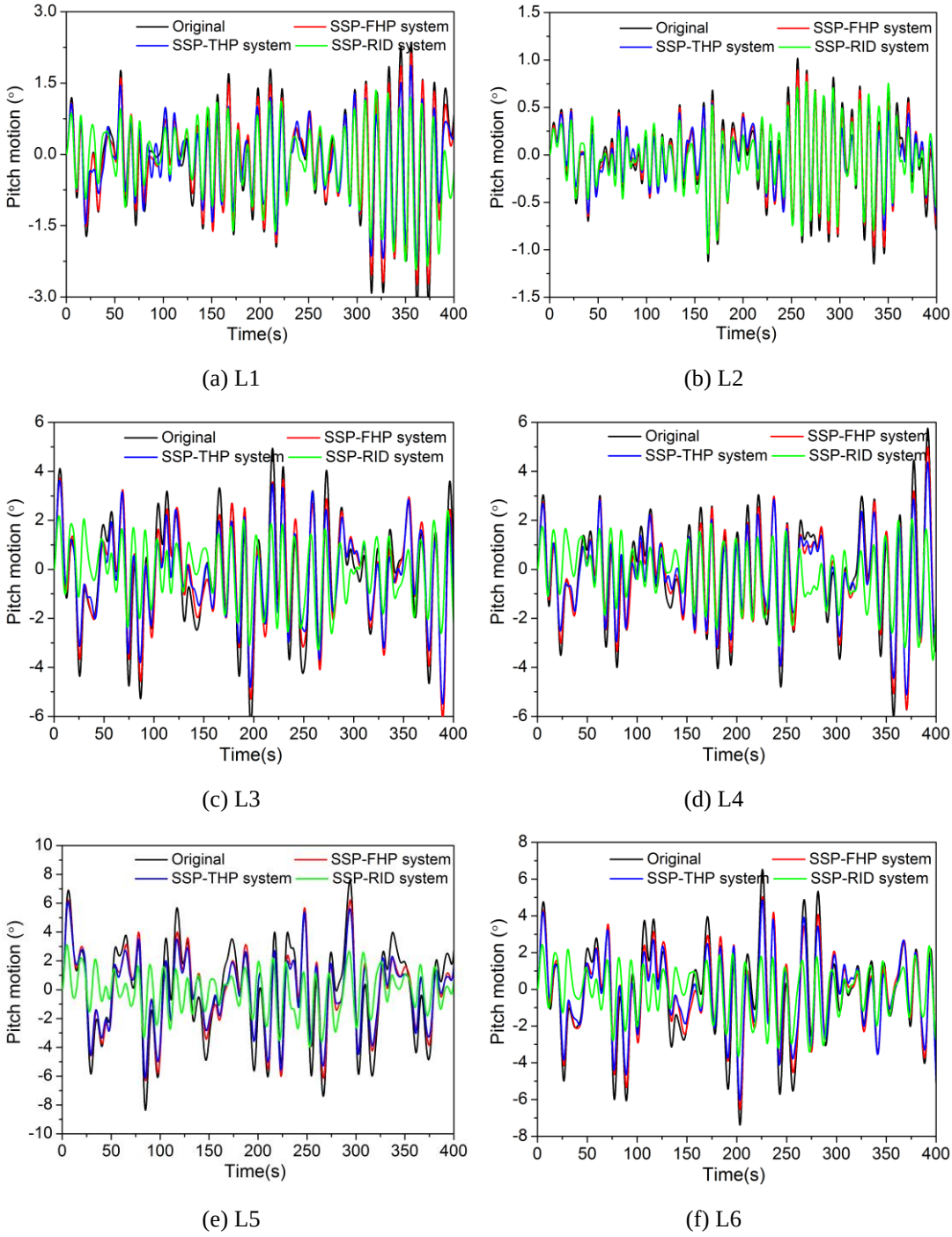

(a) L1 (b) L2

(c) L3 (d) L4

(e) L5 (f) L6

Figure 4-12 Pitch motion time histories of the SSP without and with control under different wave conditions

Furthermore, the reduction ratios of the RID and FHP systems in the heave and pitch directions are positively correlated with the wave height, i.e. the reduction ratios follow the variation trend of wave height L2<L1<L4<L3<L6<L5. As mentioned above, the bigger wave height can cause larger structural responses of the SSP, which in turn lead to larger control forces of the RID and FHP systems, and thus obtain better control performance. For the THP system, consistent with the observation in the frequency domain, no clear relationship between the reduction ratio and the wave height can be found. Besides the influence of nonlinear viscous damping forces as discussed in the frequency domain, the control effectiveness of the THP system in the time domain is also affected by the randomness introduced in the process of generating the wave force time histories for each wave condition.

Table 4-6 RMS values and corresponding reduction ratios of different control systems in the heave direction

Case No.	RMS (m)				Reduction ratio (%)			
	Original	FHP	THP	RID	Original	FHP	THP	RID
L1	0.465	0.398	0.315	0.285	--	14.34	32.28	38.66
L2	0.099	0.086	0.076	0.080	--	13.81	22.99	19.14
L3	1.099	0.920	0.798	0.483	--	16.25	27.38	56.04
L4	0.991	0.841	0.713	0.467	--	15.14	28.01	52.87
L5	1.631	1.285	1.111	0.523	--	21.24	31.89	67.95
L6	1.227	1.011	0.896	0.509	--	17.54	26.98	58.50

Table 4-7 RMS values and corresponding reduction ratios of different control systems in the pitch direction

Case No.	RMS (°)				Reduction ratio (%)			
	Original	FHP	THP	RID	Original	FHP	THP	RID
L1	1.022	0.913	0.784	0.775	--	10.68	23.27	24.19
L2	0.392	0.352	0.342	0.324	--	10.10	12.81	17.34
L3	2.201	1.920	1.714	1.219	--	12.74	22.14	44.61
L4	2.002	1.738	1.573	1.240	--	13.16	21.42	38.06
L5	3.208	2.577	2.379	1.407	--	19.66	25.84	56.13
L6	2.492	2.110	1.938	1.316	--	15.32	22.22	47.19

4.6 Conclusions

This study proposes using two RID systems to simultaneously mitigate the heave and pitch motions of SSP in the shallow sea. Analytical models of the SSP without control device and equipped with different control systems are developed, and the dynamic equilibrium equations are derived. The control effectiveness is compared and discussed in both the frequency and time domains. The results demonstrate that the RID systems can provide almost the same or

even better control performance in both the heave and pitch directions with a much smaller physical mass as compared to the FHP and THP systems. In the present study, the mass of the RID system is only about 1.6% of that of the FHP/THP system. Moreover, the spacing between the two control devices can significantly influence the performance of the FHP, THP, and RID systems in controlling the pitch response, and a larger spacing leads to better control effectiveness in the pitch direction.

4.7 Appendix A: Validation of Analytical Model

Figure 4-13 Scaled model of HYSY 981 platform in Ref. [16]

The validation is performed to ascertain the accuracy of the analytical model derived in the present study. As mentioned above, the HYSY 981 platform is adopted as the example SSP. Liu and Ou [16] carried out the free-decay tests on a 1:70 scaled model of this platform (see Figure 4-13) to determine the fundamental natural periods and the corresponding damping ratios for both the heave and pitch motions. Furthermore, regular wave tests were also performed for this SSP, and the RAOs of heave and pitch motions were obtained. Figure 4-14 shows the experimental RAOs when the platform was subjected to the regular waves with excitation frequency ranging from 0.3 rad/s to 1.2 rad/s (i.e. the blue square dots). Numerical simulations were also carried out in Ref. [16], and the corresponding results are shown in Figure 4-14 as well (see the red circular dots). To validate the analytical model in the present study, the corresponding heave and pitch RAOs of the uncontrolled SSP are also calculated, and Figure 4-14 also shows the results (see the black curves). It can be seen that for the heave motion, the results in the present study match both the experimental and numerical results well. For the pitch motion, there are some discrepancies between the present study and the experimental results especially when the excitation frequency is relatively high. The RAO curve, however, coincides well with the numerical results in Ref. [16]. As indicated in Ref. [16], these discrepancies were caused by the instability of the wave flume in generating high-frequency waves. These comparisons demonstrate the accuracy of the analytical model derived in this study.

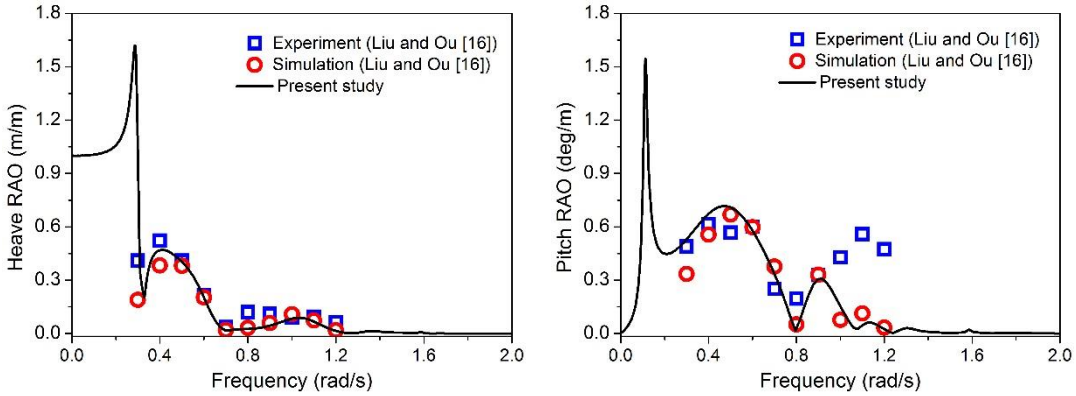

(a) Heave motion (b) Pitch motion

Figure 4-14 RAOs of the SSP obtained in the present study and in Ref. [16]

4.8 Appendix B: Elements of Matrices

$$A_{11}(s) = \left[m_0 + m_0'(\omega) + \sum_{j=1}^{2} m_{e\_j}\right]s^2 + \left[c_{zr}(\omega) + c_{z0} + \sum_{j=1}^{2} c_{e\_zj}'\right]s + k_0$$

$$A_{12}(s) = 0$$

$$A_{21}(s) = 0$$

$$A_{22}(s) = \left[m_\theta + m_\theta'(\omega) + \sum_{j=1}^{2} m_{e\_\theta j}\right]s^2 + \left[c_{\theta r}(\omega) + c_{\theta 0} + \sum_{j=1}^{2} c_{e\_\theta j}'\right]s + k_\theta$$

$$B_{11}(s) = \left[m_0 + m_0'(\omega) + \sum_{j=1}^{2}\left(m_j + m_j'\right)\right]s^2 + \left[c_{zr}(\omega) + c_{z0} + \sum_{j=1}^{2} c_{vj}'\right]s + k_0$$

$$B_{12}(s) = 0$$

$$B_{21}(s) = 0$$

$$B_{22}(s) = \left[m_\theta + m_\theta'(\omega) + \sum_{j=1}^{2}\left(m_{\theta j} + m_{\theta j}'\right)\right]s^2 + \left[c_{\theta r}(\omega) + c_{\theta 0} + \sum_{j=1}^{2} c_{\theta j}'\right]s + k_\theta$$

$$C_{11}(s) = [m_0 + m_0'(\omega)]s^2 + [c_{zr}(\omega) + c_{z0} + c_1 + c_2]s + k_0 + k_1 + k_2$$

$$C_{12}(s) = \frac{L_s}{2}(c_1 - c_2)s + \frac{L_s}{2}(k_1 - k_2)$$

$$C_{13}(s) = -c_1 s - k_1$$

$$C_{14}(s) = -c_2 s - k_2$$

$$C_{21}(s) = \frac{L_s}{2}(c_1 - c_2)s + \frac{L_s}{2}(k_1 - k_2)$$

$$C_{22}(s) = [m_\theta + m'_\theta(\omega)]s^2 + \left[c_{\theta r}(\omega) + c_{\theta 0} + \left(\frac{L_s}{2}\right)^2 (c_1 + c_2)\right]s + k_\theta + \left(\frac{L_s}{2}\right)^2 (k_1 + k_2)$$

$$C_{23}(s) = -\frac{L_s}{2}c_1 s - \frac{L_s}{2}k_1$$

$$C_{24}(s) = \frac{L_s}{2}c_2 s + \frac{L_s}{2}k_2$$

$$C_{31}(s) = -c_1 s - k_1$$

$$C_{32}(s) = -\frac{L_s}{2}c_1 s - \frac{L_s}{2}k_1$$

$$C_{33}(s) = (m_1 + m'_1)s^2 + (c_1 + c'_{v1})s + k_1$$

$$C_{34}(s) = 0$$

$$C_{41}(s) = -c_2 s - k_2$$

$$C_{42}(s) = \frac{L_s}{2}c_2 s + \frac{L_s}{2}k_2$$

$$C_{43}(s) = 0$$

$$C_{44}(s) = (m_2 + m'_2)s^2 + (c_2 + c'_{v2})s + k_2$$

4.9 References

[1] Muehlenbachs L, Cohen MA, Gerarden T. The impact of water depth on safety and environmental performance in offshore oil and gas production. Energy Policy. 2013;55:699-705.

[2] Moan T. Development of accidental collapse limit state criteria for offshore structures. Struct Saf. 2009;31:124-35.

[3] Tao L, Cai S. Heave motion suppression of a Spar with a heave plate. Ocean Eng. 2004;31:669-92.

[4] Li B, Huang Z, Low YM, Ou J. Experimental and numerical study of the effects of heave plate on the motion of a new deep draft multi-spar platform. J Mar Sci Tech. 2013;18:229-46.

[5] Subbulakshmi A, Sundaravadivelu R. Heave damping of spar platform for offshore wind turbine with heave plate. Ocean Eng. 2016;121:24-36.

[6] Kaynia AM, Biggs JM, Veneziano D. Seismic effectiveness of tuned mass dampers. J Struct Div. 1981;107:1465-84.

[7] Jangid R. Optimum Multiple Tuned Mass Dampers for base-excited undamped system. Earthq Eng Struct Dyn. 1999;28:1041-9.

[8] Colwell S, Basu B. Tuned liquid column dampers in offshore wind turbines for structural control. Eng Struct. 2009;31:358-68.

[9] Lackner MA, Rotea MA. Passive structural control of offshore wind turbines. Wind energy. 2011;14:373-88.

[10] Stewart GM, Lackner MA. The impact of passive tuned mass dampers and wind–wave misalignment on offshore wind turbine loads. Eng Struct. 2014;73:54-61.

[11] Bi K, Hao H. Using pipe-in-pipe systems for subsea pipeline vibration control. Eng Struct. 2016;109:75-84.

[12] Zuo H, Bi K, Hao H. Using multiple tuned mass dampers to control offshore wind turbine vibrations under multiple hazards. Eng Struct. 2017;141:303-15.

[13] Ghassempour M, Failla G, Arena F. Vibration mitigation in offshore wind turbines via tuned mass damper. Eng Struct. 2019;183:610-36.

[14] Ma R, Bi K, Hao H. Mitigation of heave response of semi-submersible platform (SSP) using tuned heave plate inerter (THPI). Eng Struct. 2018;177:357-73.

[15] Zhu H, Ou J, Zhai G. Conceptual design of a deep draft semi-submersible platform with a moveable heave-plate. J Ocean U China. 2012;11:7-12.

[16] Liu K, Ou J. A novel tuned heave plate system for heave motion suppression and energy harvesting on semi-submersible platforms. Sci China Technol Sci. 2016;59:897-912.

[17] Zhu H, Hu C, Liu Y. Optimum Design of a Passive Suspension System of a Semisubmersible for Pitching Reduction. J Dyn Syst Meas Control. 2016;138:121003.

[18] Liu K, Liang H, Ou J. Numerical investigation of a tuned heave plate energy-harvesting system of a semi-submersible platform. Energies. 2016;9:82.

[19] Smith MC. Synthesis of mechanical networks: the inerter. IEEE Trans Automat Contr. 2002;47:1648-62.

[20] Chen MZQ, Papageorgiou C, Scheibe F, Wang FC, Smith M. The missing mechanical circuit element. IEEE Circ Syst Mag. 2009;9:10-26.

[21] Swift S, Smith MC, Glover A, Papageorgiou C, Gartner B, Houghton NE. Design and modelling of a fluid inerter. Int J Control. 2013;86:2035-51.

[22] Ikago K, Saito K, Inoue N. Seismic control of single-degree-of-freedom structure using tuned viscous mass damper. Earthq Eng Struct Dyn. 2012;41:453-74.

[23] Pietrosanti D, De Angelis M, Basili M. Optimal design and performance evaluation of systems with Tuned Mass Damper Inerter (TMDI). Earthq Eng Struct Dyn. 2017;46:1367-88.

[24] Lazar I, Neild S, Wagg D. Using an inerter-based device for structural vibration suppression. Earthq Eng Struct Dyn. 2014;43:1129-47.

[25] Lazar I, Neild S, Wagg D. Vibration suppression of cables using tuned inerter dampers. Eng Struct. 2016;122:62-71.

[26] Nakamura Y, Fukukita A, Tamura K, Yamazaki I, Matsuoka T, Hiramoto K et al. Seismic response control using electromagnetic inertial mass dampers. Earthq Eng Struct Dyn. 2014;43:507-27.

[27] Zhu H, Li Y, Shen W, Zhu S. Mechanical and energy-harvesting model for electromagnetic inertial mass dampers. Mech Syst Signal Process. 2019;120:203-20.

[28] Li Y, Shen W, Zhu H. Vibration mitigation of stay cables using electromagnetic inertial mass dampers: Full-scale experiment and analysis. Eng Struct. 2019;200:109693.

[29] Cao L, Li C. Tuned tandem mass dampers-inerters with broadband high effectiveness for structures under white noise base excitations. Struct Contorl Health Monit. 2019:e2319.

[30] Wen Y, Chen Z, Hua X. Design and Evaluation of Tuned Inerter-Based Dampers for the Seismic Control of MDOF Structures. J Struct Eng. 2016;143:04016207.

[31] Zhang R, Zhao Z, Dai K. Seismic response mitigation of a wind turbine tower using a tuned parallel inerter mass system. Eng Struct. 2019;180:29-39.

[32] Giaralis A, Petrini F. Wind-Induced Vibration Mitigation in Tall Buildings Using the Tuned Mass-Damper-Inerter. J Struct Eng. 2017;143:04017127.

[33] Xu K, Bi K, Han Q, Li X, Du X. Using tuned mass damper inerter to mitigate vortex-induced vibration of long-span bridges: Analytical study. Eng Struct. 2019;182:101-11.

[34] Wang FC, Hong MF, Chen CW. Building suspensions with inerters. P I Mech Eng C-J Mec. 2010;224:1605-16.

[35] De Domenico D, Ricciardi G. An enhanced base isolation system equipped with optimal tuned mass damper inerter (TMDI). Earthq Eng Struct Dyn. 2018;47:1169-92.

[36] De Domenico D, Ricciardi G. Improving the dynamic performance of base-isolated structures via tuned mass damper and inerter devices: A comparative study. Struct Contorl Health Monit. 2018:e2234.

[37] Giaralis A, Taflanidis AA. Optimal tuned mass-damper-inerter (TMDI) design for seismically excited MDOF structures with model uncertainties based on reliability criteria. Struct Control Health Monit. 2018;25:e2082.

[38] Pan C, Zhang R, Luo H, Li C, Shen H. Demand-based optimal design of oscillator with parallel-layout viscous inerter damper. Struct Control Health Monit. 2018;25:e2051.

[39] Barredo E, Blanco A, Colín J, Penagos VM, Abúndez A, Vela LG et al. Closed-form solutions for the optimal design of inerter-based dynamic vibration absorbers. Int J Mech Sci. 2018;144:41-53.

[40] Hu Y, Wang J, Chen MZQ, Li Z, Sun Y. Load mitigation for a barge-type floating offshore wind turbine via inerter-based passive structural control. Eng Struct. 2018;177:198-209.

[41] Ma R, Bi K, Hao H. A novel rotational inertia damper for heave motion suppression of semisubmersible platform in the shallow sea. Struct Contorl Health Monit. 2019:e2368.

[42] Faltinsen O. Sea loads on ships and offshore structures: Cambridge university press; 1993.

[43] Cummins W. The impulse response function and ship motions. David Taylor Model Basin Washington DC; 1962.

[44] Perez T, Fossen TI. A matlab toolbox for parametric identification of radiation-force models of ships and offshore structures. Model Ident Control. 2009;30:1-15.

[45] Chakrabarti SK. Hydrodynamics of offshore structures: WIT press; 1987.

[46] Burke BG. An analysis of marine risers for deep water. J Pet Technol. 1974;26:455-65.

[47] Newman JN, Landweber L. Marine hydrodynamics. American Society of Mechanical Engineers; 1978.

[48] Veritas DN. Modelling and analysis of marine operations. Offshore Standard. 2011.

[49] Travanca J, Hao H. Control of wave-induced vibrations on floating production systems. Ocean Eng. 2017;141:35-52.

[50] Hasselmann K, Barnett TP, Bouws E, Carlson H, Cartwright DE, Enke K et al. Measurements of wind-wave growth and swell decay during the Joint North Sea Wave Project (JONSWAP). Ergänzungsheft. 1973:8-12.

[51] Deb K, Pratap A, Agarwal S, Meyarivan T. A fast and elitist multiobjective genetic algorithm: NSGA-II. IEEE T Evolut Comput. 2002;6:182-97.

[52] Guide MUs. The mathworks. Inc, Natick, MA. 1998;5:333.

[53] Asami T, Nishihara O, Baz AM. Analytical solutions to H_∞ and H_2 optimization of dynamic vibration absorbers attached to damped linear systems. J Vib Acoust. 2002;124:284-95.

[54] Soto-Brito R, Ruiz SE. Influence of ground motion intensity on the effectiveness of tuned mass dampers. Earthq Eng Struct Dyn. 1999;28:1255-71.

CHAPTER 5 DEVICE TESTS AND MECHANICAL MODEL OF RID

Abstract[5]

An inerter is a two-terminal mechanical device with the property of generating a resisting force that is proportional to the relative acceleration across its terminals. Due to its distinct mass amplification and negative stiffness effects, inerter has been applied to enhance the performance of conventional control systems, e.g. tuned mass damper (TMD) and vibration isolation system (VIS). Very recently, a novel inerter-based damper dubbed rotational inertia damper (RID) that is capable of generating a significant damping force was proposed by the authors to control the vibrations of offshore platforms, and its control effectiveness was examined through analytical studies. In the present study, a RID prototype was manufactured and tested under harmonic excitations for an in-depth understanding and demonstration of its mechanical behaviors. A precise mechanical model considering inerter nonlinearities is proposed to predict the behaviors of the RID, and the corresponding parameters are identified by using a nonlinear least-squares method based on the experimental results. The theoretical results predicted by the proposed mechanical model are then compared with the experimental results, good agreements are achieved. The results demonstrate that the developed RID has a good capacity for energy dissipation, and the proposed mechanical model is accurate in predicting the behaviors of the RID.

5.1 Introduction

Vibration control of instruments, mechanical device and engineering structures has been under investigation for more than one century, and various types of control systems have been developed and applied to suppress undesirable vibrations. These control systems can be broadly classified into passive, semi-active, active and hybrid groups [1]. Among these groups, the passive control method is most widely applied due to its simplicity and independence of external energy. Depending on the mechanism for vibration suppression, the passive control method can be further subdivided into three types: dynamic vibration absorber (DVA), vibration isolation system (VIS), and energy dissipator (ED) [2]. However, it should be noted that certain inherent issues exist in these traditional passive control systems. For example, the most generic DVA is an auxiliary system consisting of an additional mass and a spring-dashpot pair and its control effectiveness is highly relevant to the mass ratio between the additional

[5] This chapter was published in *Mechanical Systems and Signal Processing* with the full bibliographic citation as follows:
Ma R, Bi K, Hao H. A novel rotational inertia damper for amplifying fluid resistance: Experiment and mechanical model. Mech Syst Signal Process. 2021;149:107313. https://doi.org/10.1016/j.ymssp.2020.107313.

mass and host structure. In other words, a large additional mass is generally required for the superior control performances of conventional DVAs, which penalizes the practical application of DVA due to the increased cost and technical difficulty. Moreover, it is also demonstrated that the conventional VIS is effective only when the vibration frequency is larger than $\sqrt{2}$ times of the resonant frequency of the isolated structure, which indicates that the effective frequency range of conventional VIS is limited. On the other hand, the conventional VIS may also be impractical under some low-frequency vibrations since the isolated structure is required to be designed with a quite lower resonant frequency to guarantee the effectiveness.

To this end, it becomes a hot research topic to upgrade these conventional passive control systems by overcoming the above shortcomings, and some new control devices have been developed in the past decades. Among them, a two-terminal mechanical element firstly proposed by Smith [3] in 2002, dubbed inerter, has attracted a lot of attention from researchers. As the real counterpart of capacitor, the inerter is developed based on the force-current analogy between mechanical and electrical networks, which can be realized by various physical means, such as the ball screw assembly [4], rack-and-pinion [5], hydraulic [6], fluid [7, 8] and living hinge [9], etc. The most appealing characteristic of inerter is that it can generate the force proportional to the relative acceleration across its two terminals and the proportionality constant is called inertance with a unit of kilogram. This property endows the inerter with a mass amplification effect (also called inertance effect), i.e. achieving the inertance several orders of magnitude larger than its physical mass. This advantage enables the inerter to reduce the additional mass of conventional DVAs, and thus increase their application potentials. Another obvious characteristic of inerter is its negative stiffness effect, which indicates that a force can be generated to assist motion, not to oppose it [10]. An energy dissipating device with negative stiffness can have a larger motion amplitude, absorb more vibration energy, and thus realize better control performance. Moreover, the inerter does not respond to static loads and can thus avoid the amplification of static response [11]. These attractive advantages make inerters spread over a wide range of applications including automobile engineering, civil engineering and offshore engineering, etc.

In 2005, the inerter was commercially applied in automotive suspensions of high-performance racing cars under the name of “J damper” [12, 13], which successfully inspires possible applications in other fields, especially in the field of civil engineering. Due to its significant mass amplification effect, the inerter was initially used to reduce the additional mass of tuned mass damper (TMD), which is a classical form of DVA. Marian and Giaralis [14] proposed a tuned mass damper inerter (TMDI) by connecting the tuned mass via the inerter to either the ground or a different position from the one the TMD was already attached. It was demonstrated that the proposed TMDI could either reduce the additional mass of TMD or evidently improve

the performance of the TMD for a given mass ratio. Considering these performance benefits, the TMDI was then successfully applied to suppress the wind-induced vibrations of flexible structures [15] and tall buildings [16, 17], as well as the vortex-induced vibration (VIV) of bridge [18, 19]. In this aspect, Lazar et al. also proposed an inerter-based DVA termed as tuned inerter damper (TID) for the seismic-induced vibration reduction of multi-storey building [20] and stay cables [21]. It should be noted that the TID can be retrieved as the special case of the TMDI for a zero-value of the additional mass. Their results indicated that the optimized TID and TMD could realize almost identical performance at the same mass ratio, however, the TID was more attractive due to its small mass and overall size. Similarly, Wen et al. [22] and Shen et al. [23] also observed significant performance improvements of using TIDs in the seismic protection of multi-storey buildings. Moreover, the concept of TID was also extended into the active control system and an active tuned inerter damper (ATID) was proposed for smart structures [24]. It was found that the ATID could achieve similar control effectiveness to the TMD by using a smaller proof mass. Furthermore, it is worth mentioning that the inerter was also recently applied to improve the performance of nonlinear DVAs, e.g. nonlinear energy sink (NES) [25, 26].

Besides the applications to traditional DVAs, the inerter also has a high potential for improving the performance of traditional VIS. Hu et al. [27] proposed five inerter-based isolation configurations and derived the corresponding analytical solutions. Their results indicated that the inerter-based isolators outperformed the traditional VIS in terms of both the H_2 and H_∞ performances when the same inertance-to-mass (or mass) ratio was adopted. Alujević et al. [28] also investigated the control effectiveness of an inerter-based vibration isolator, where the inerter is connected in parallel with a spring and a dashpot. It was shown again that the incorporation of inerter could enhance the isolation performance of the traditional VIS. Recently, nonlinear inerter-based isolators were also developed [29, 30], and obvious performance improvements were observed as well. Moreover, some research efforts were also devoted to using the inerter-based devices to reduce the lateral displacement demand of base isolation system (BIS), which is a common vibration isolator in civil engineering. Some inertial mass dampers (IMDs), e.g. the “angular-mass” inertial damper [31] and “gyro-mass” damper [32], were initially applied to base-isolated buildings. It was found that these IMDs were effective in reducing the lateral displacement of superstructures. Later on, Domenico and Ricciardi [33] incorporated the TMDI into a base isolation system (BIS) for reducing the lateral displacement demand. Numerical results demonstrated that the BIS-TMDI could effectively reduce the lateral displacement demand with a limited mass. In order to realize the best performance, the optimal design of the BIS-TMDI system was investigated as well [34, 35]. Furthermore, it is well recognized that soil condition is a non-negligible parameter for the

seismic design and performance assessment of BIS. For this reason, the influence of soil conditions on the performance of the BIS-TMDI was comprehensively evaluated in Refs. [36, 37]. Interestingly, the inerter-based isolator was also found to possess a high application potential in preserving cultural heritage. Siami et al. [38] updated the isolation system of the famous statue of Michelangelo Buonarroti Pietà Rondanini by introducing the TMDI. The numerical results proved a significant reduction in the transmitted vibration to the statue due to the presence of the optimal TMDI, without imposing a large amount of mass or modification to the isolator.

In addition to inerter-based DVAs and VISs, many inerter-based energy dissipating devices were also developed to more effectively dissipate vibration energies of structures. Hwang et al. [39] proposed a rotational inertia viscous damper (RIVD), in which a ball screw was applied to transform the inter-storey drift into the rotation of a flywheel immersed in the viscous fluid, and the equivalent mass and damping of the controlled structure were thus increased. Similarly, Ikago et al [40] also developed a tuned viscous mass damper (TVMD) by using a ball-screw mechanism. It was demonstrated that the developed TVMD outperformed the conventional dampers with the same damping coefficient. Later on, Nakamura et al. [41] integrated the inertial mass damper and electromagnetic damper together for developing an electromagnetic inertial mass damper (EIMD), and a mechanical model was proposed to predict the behaviors of the EIMD. Analytical and experimental results indicated that the developed EIMD was capable of generating a large inertial force by rotating the flywheel and a controllable damping force by the electric generator. Zhu et al. [42, 43] extended the work of Nakamura et al. [41] by adding an energy harvesting circuit (EHC) into the EIMD for vibration control and energy harvesting simultaneously, derived a more accurate mechanical model to capture its nonlinear behavior, and then performed dynamic tests to validate the proposed model.

Recently, inerter-based control devices were introduced into the vibration control of offshore structures. Hu et al. [44] investigated the control effectiveness of a passive inerter-based control device in reducing the vibrations of a barge-type floating offshore wind turbine (FOWT). It was demonstrated that the developed inerter-based control device could improve the performances without the need for a larger working space. Ma et al. [45] proposed a novel tuned heave plate inerter (THPI) for the heave motion mitigation of floating platforms by incorporating an inerter element into conventional tuned heave plate (THP), in which the heave plate acted as the secondary mass in the system. The analytical results revealed that the THPI outperformed the conventional THP in reducing the heave motion of floating platforms. In Ref. [46], Sarkar and Fitzgerald used the TMDI system to control the vibration of a spar-type FOWT, and it was observed that the TMDI system could achieve better control performance with reductions in the stroke of the tuned mass. Moreover, Ma et al. [47] also proposed an

inerter-based vibration isolation system (IVIS) for the vibration control of a semi-submersible platform. The results demonstrated that the proposed IVIS is more effective in reducing heave motion and has a wider effective frequency range as compared to conventional VIS. Very recently, a novel inerter-based device, namely a rotational inertia damper (RID) was proposed by the authors to suppress the vibrations of floating platforms [48, 49]. Besides the mass amplification effect, the turning plates of RID immersed in the water could churn the water surrounding the device, which in turn led to a very large damping force due to the fluid resistance. Analytical results showed that the RID system could reach the same or even better control effectiveness of conventional fixed heave plate (FHP) and tuned heave plate (THP) by using only 0.8% of the mass of the FHP or THP.

It is worth mentioning that most previous studies focused on the analytical studies, only very limited experimental investigations were reported. Papageorgiou et al. [4] tested two kinds of inerter, which were driven by the ball screw and rack-and-pinion, respectively. It was found that the friction was the major parameter influencing the behaviors of inerter. Wang et al. [50] designed and tested a hydraulic inerter, in which a flywheel was driven by hydraulic means. The experimental results demonstrated the effectiveness of the developed hydraulic inerter. Swift et al. [7] examined the performance of a novel helical-tube inerter through harmonic excitations and estimated its inertance. Moreover, experimental studies were also performed to verify the realistic performances of other inerter-based devices, including the TVMD [40], EIMD [41, 42] and TMDI [51]. For the RID system proposed by the authors, the conceptual design and analytical studies have been reported in Ref. [48]. This paper is an extension of [48], reporting the experimental studies performed to examine the performances of the proposed device. A RID prototype was manufactured and systematically tested under harmonic excitations. A precise mechanical model considering inerter nonlinearities is then established, with its parameters identified by a nonlinear least-squares method based on the experimental results.

The remaining of this paper is organized as follows: the mechanical model considering nonlinearities is developed for the RID in Section 5.2; in Section 5.3, the RID prototype, experimental setup and loading scenarios are introduced; Section 5.4 presents the experimental results and analyzes the mechanical behaviors of the RID in both the air and water; model identifications are performed in Section 5.5, and the experimental and theoretical results are compared to evaluate the accuracy of the proposed mechanical model; finally, conclusions are drawn in Section 5.6.

5.2 Rotational Inertia Damper and Mechanical Model

5.2.1 Configuration and Working Principle

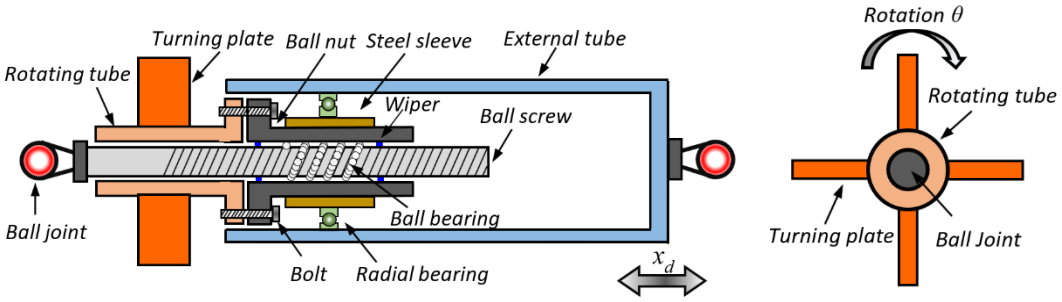

(a) Elevation view (b) Side view

Figure 5-1 Schematic drawing of RID

Figure 5-1 shows the schematic drawing of the inerter-based RID. As shown, the RID consists of a ball-screw assembly, a rotating tube, an external tube, one radial bearing, two ball joints and a set of turning plates. The ball nut is mounted to the external tube through the radial bearing and steel sleeve, it thus can spin inside the external tube. A steel sleeve is utilized to fill the gap between the ball nut and radial bearing. The turning plates are welded on the rotating tube, which is fixed to the ball nut through bolts. Wipers are adopted to protect the ball screw from swarf or rust and thus improve its durability. The ball screw assembly including a ball screw, a ball nut and bearing balls is a linear-to-rotary converter, which can transform the linear motion into the rotational motion of the ball nut, and thus the rotational motions of the turning plates immersed in the water. These rotating plates can generate a considerable damping effect. As will be demonstrated in the following sections, the developed RID can significantly amplify the fluid resistance against the relative motion across its two terminals.

5.2.2 Mechanical Model Considering Inerter Nonlinearities

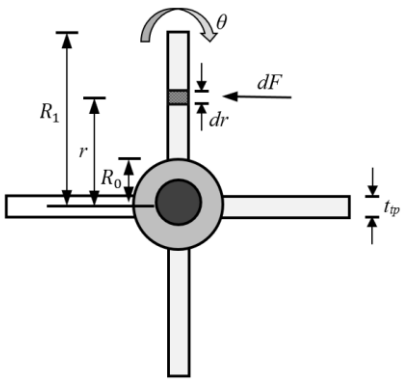

Figure 5-2 Force diagram of the proposed RID system

As shown in Figure 5-1, the ball screw is utilized to convert the linear motion into the rotations of turning plates. The rotational angle θ of turning plates can be written as follows:

$$\theta = \frac{2\pi}{L} x_d \tag{5.1}$$

in which x_d is the relative displacement across two ends of the RID system and L is the lead of the ball screw.

It is obvious that the total torque applied on the RID system consists of two parts: the hydraulic torque provided by the water, and the inherent torque due to the physical mass of turning plates. For the hydraulic torque acting on each turning plate, it can be calculated by:

$$T_h = \int r \, dF \tag{5.2}$$

where R_0 is the inner radius of rotating tube, R_1 is the outer radius of RID system, dF is the hydrodynamic force at the radius of r (see Figure 5-2), and it can be estimated in the form of Morison's equation as follows [52]:

$$dF = \rho c_m a_t \, dV + \frac{1}{2} \rho c_d v_t |v_t| dA \tag{5.3}$$

where ρ is the density of seawater; c_m is the inertia coefficient of turning plate; c_d is the drag coefficient of turning plate; $dV = l_{tp} t_{tp} \, dr$ and $dA = l_{tp} \, dr$ are the volume and area of the turning plate per unit radius, respectively, where l_{tp} and t_{tp} are the width and thickness of the turning plate, respectively; $a_t = r\ddot{\theta}$ and $v_t = r\dot{\theta}$ are respectively the tangential acceleration and velocity at the radius of r, with $\dot{\theta}$ and $\ddot{\theta}$ representing the angular velocity and angular acceleration of the rotating tube, respectively.

Substituting Equation (5.3) into Equation (5.2), one obtains:

$$T_h = \int r \, dF = \int_{R_0}^{R_1} \left(\rho c_m l_{tp} t_{tp} r^2 \ddot{\theta} + \frac{1}{2} \rho c_d l_{tp} r^3 \dot{\theta} |\dot{\theta}| \right) dr \tag{5.4}$$

For the inherent torque of each turning plate, it can be calculated by

$$T_i = I_{tp} \ddot{\theta} \tag{5.5}$$

where I_{tp} is the moment of inertia of each turning plate, which is

$$I_{tp} = \int r^2 \, dm = \int_{R_0}^{R_1} \rho_s \, l_{tp} t_{tp} r^2 \, dr \tag{5.6}$$

in which ρ_s is the density of the turning plate.

The total torque T of the RID system is therefore

$$T = T_h + T_i \tag{5.7}$$

and it can be calculated as follows by substituting Equations (5.4) and (5.5) into Equation (5.7)

$$T = \frac{1}{3}(\rho c_m + \rho_s) l_{tp} t_{tp} (R_1^3 - R_0^3)\ddot{\theta} + \frac{1}{8}\rho c_d l_{tp} (R_1^4 - R_0^4)\dot{\theta}|\dot{\theta}| \tag{5.8}$$

The axial force provided by the RID system (F_t) can therefore be calculated as follows:

$$F_t = \frac{2\pi}{L\eta} T \tag{5.9}$$

where η is the conversion efficiency of the ball screw, which can be affected by the various factors, e.g. the friction and skidding behavior between the balls and the inner raceway [53], etc. In the present study, the conversion efficiency is taken as an empirical value of 90% by referring to the work of Zhu et al. [42]. This is because, as will be introduced later, the ball screw assemblies in both studies are made by the same manufacturer, i.e. TBI.

Substituting Equations (5.1) and (5.8) into Equation (5.9), one obtains:

$$\begin{aligned} F_t = \frac{1}{3\eta}\left(\frac{2\pi}{L}\right)^2 (\rho c_m + \rho_s) l_{tp} t_{tp} (R_1^3 - R_0^3)\ddot{x}_d \\ + \frac{1}{8\eta}\left(\frac{2\pi}{L}\right)^3 \rho c_d l_{tp} (R_1^4 - R_0^4)\dot{x}_d |\dot{x}_d| \end{aligned} \tag{5.10}$$

It is obvious that the axial force is composed of the inertia force (the first term in Equation (5.10)) and nonlinear damping force (the second term in Equation (5.10)).

Previous experimental studies (e.g. Refs. [54, 55]) indicated that the performance of inerters could be influenced by some nonlinearities, e.g. parasitic damping, original structural mass and moment of inertia, and backlash effect. Strictly speaking, the original structural mass and moment of inertia might not be regarded as nonlinear terms since they are believed to be constants during the tests. However, the word "nonlinearities" is generally used to represent the adverse factors that influence the performance of ball-screw inerters. Without loss of generality, the original structural mass and moment of inertia are also incorporated into the nonlinearities of the RID prototype.

For the parasitic damping force, it can be expressed by [42]:

$$F_p = f_c \cdot sgn(\dot{x}_d) + c_v \dot{x}_d \tag{5.11}$$

where f_c is the Coulomb friction, c_v is the viscous friction coefficient, and sgn is the signum function. It should be noted that the parasitic damping corresponds to various mechanical losses of the RID prototype, which includes but not limited to the friction of the ball screw and ball bearing in the present study.

The inertia force due to the original mass and moment of inertia can be calculated as follows [41]:

$$F_i = m_r\ddot{x}_d + \frac{1}{\eta}\left(\frac{2\pi}{L}\right)^2 (J_{r1} + J_{r2})\ddot{x}_d \tag{5.12}$$

in which m_r is the original structural mass of the components that move linearly, including the mass of the long connecting rod, short connecting rod, ball screw and extension tube of the actuator as will be shown in Figure 5-6; J_{r1} is the original moment of inertia of some rotating components, including the moment of inertia of ball nut, steel sleeve, radial bearing and bolts, etc.; J_{r2} is the moment of inertia of the rotating tube.

As for the backlash effect, it is caused due to the clearances among the ball bearing, screw and nut tracks, and can result in the lost motion in the screw. In the present study, the backlash effect is not considered due to the fact that, as indicated by Brzeski et al. [56], the influence of the backlash effect on the performance of inerter is quite limited, and can be neglected in most applications. Moreover, in the process of manufacturing, some procedures (e.g. preloading) have been adopted to minimize the backlash effect of the ball screw assembly.

As a consequence, the total axial force F of the RID system can be written as follows:

$$F = N \cdot F_t + F_p + F_i \tag{5.13}$$

where N is the number of turning plate. Based on the definition here, it might be more appropriate to dub the axial force calculated by Equation (5.10) (namely F_t) as ideal axial force since the nonlinearities are not considered in the calculation.

Substituting Equations (5.11) and (5.12) into Equation (5.13), one obtains:

$$F = (N \cdot m_e + m_i)\ddot{x}_d + N \cdot c_e\dot{x}_d|\dot{x}_d| + f_c \cdot sgn(\dot{x}_d) + c_v\dot{x}_d \tag{5.14}$$

where

$$m_e = \frac{1}{3\eta}\left(\frac{2\pi}{L}\right)^2 (\rho c_m + \rho_s) l_{tp} t_{tp} (R_1^3 - R_0^3) \tag{5.15}$$

$$c_e = \frac{1}{8\eta}\left(\frac{2\pi}{L}\right)^3 \rho c_d l_{tp} (R_1^4 - R_0^4) \tag{5.16}$$

$$m_i = m_r + \frac{1}{\eta}\left(\frac{2\pi}{L}\right)^2 (J_{r1} + J_{r2}) \tag{5.17}$$

in which m_e is the inertance (i.e. equivalent mass) of the RID, c_e is the damping coefficient and m_i is the equivalent mass due to the original structural mass and moment of inertia in the RID.

In summary, the mechanical model of the RID system includes five components, namely the parts related to m_e, m_i, c_e, c_v and f_c respectively (see Figure 5-3 and Equation (5.14)). In particular, c_e and c_v result in the damping force to the RID, m_e and m_i lead to the inertial force, and f_c is the Coulomb friction. Figure 5-4 illustrates the schematic force-displacement relationship of different parts. Figure 5-4(a) and (b) respectively show the nonlinear and linear damping terms, which normally have an elliptical shape with the enclosed area representing dissipated energy [57]. Compared to that of the linear damping term, the closed area of the nonlinear damping term is larger due to its higher capacity of dissipating energy. Figure 5-4(c) illustrates the inertial term. It can be seen that no energy is dissipated by this term and the slope of the hysteresis curve is equal to $-(N \cdot m_e + m_i) \cdot \omega^2$ when the RID is subjected to a harmonic excitation with a circular frequency of ω. The negative slope is called the negative stiffness effect of inerter, which is proportional to the inertance. Figure 5-4(d) shows the Coulomb friction term, which is normally in a rectangular shape. The integrated mechanical behavior of the RID system thus can be formed by superposing all the terms together, and Figure 5-4(e) shows the corresponding hysteresis curve. It should be noted that Figure 5-4 only illustrates the force-displacement relationship of different components qualitatively, and the final shape of the hysteresis curve of RID depends on the contribution proportion of each component.

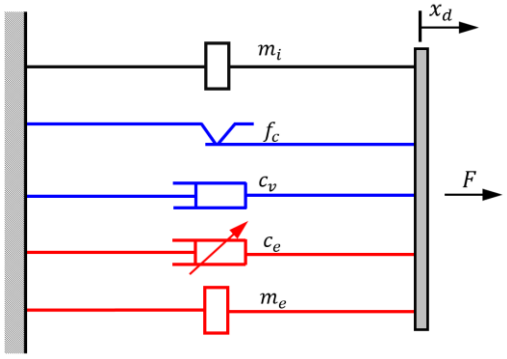

Figure 5-3 Proposed mechanical model for RID

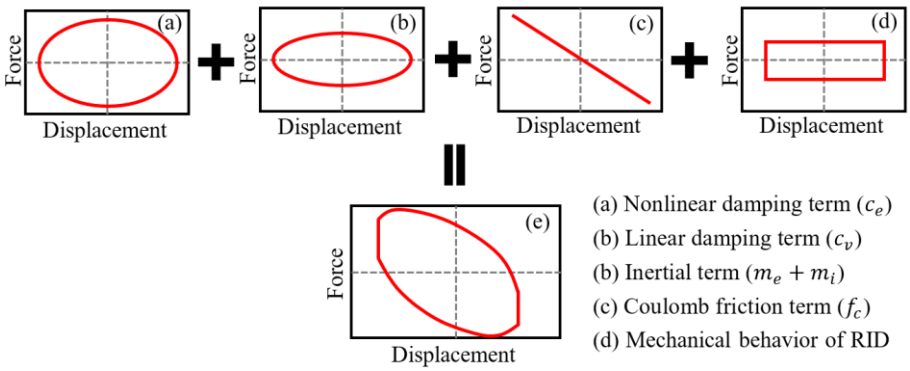

Figure 5-4 Illustration of mechanical behaviours of the RID considering inerter nonlinearities

5.3 RID Prototype and Experimental Setup

5.3.1 RID Prototype

Figure 5-5 shows the RID prototype manufactured for dynamic tests. Detailed specifications of this RID prototype are tabulated in Table 5-1. The outer diameter, length and stroke of this RID prototype were 60 mm, 265 mm and $\pm$50 mm, respectively. The structural mass m_r and the total weight of the RID prototype were 0.965 kg and 2.240 kg, respectively. A ball screw assembly made by the TBI MOTION (model No. SFV01210) was utilized to convert the linear motion to the rotational motions of turning plates. Considering the testing facilities, the mounting system of the RID prototype was slightly different from the schematic drawing as shown in Figure 5-1. As shown in Figure 5-5, a short connecting rod was utilized to connect the RID to a dynamic actuator, and a flange plate with bolts was used to fix the RID. To increase the corrosion resistance and durability, all components of the device were made of stainless steel. It is noted that, for simplicity, the waterproof function was not considered in the manufacturing. Four drainage holes were therefore drilled in the external tube to preclude the possible viscous damping caused by the water flowing in the small clearances among the ball screw, ball nut and bearing balls. It should also be noted that the star symbols in Table 5-1 represent that the parameters are determined by the model identification method that will be introduced in Section 5.5.

5.3.2 Test Rig and Instrumentation

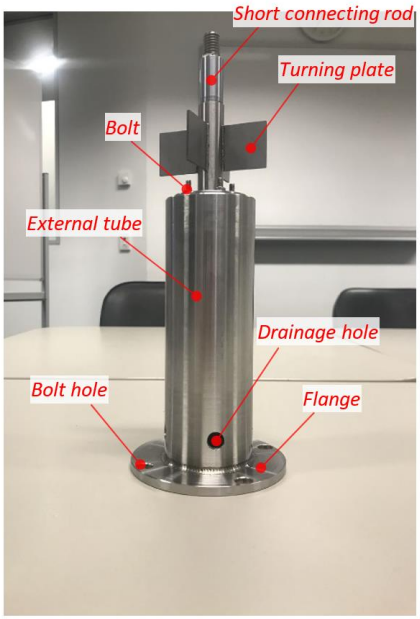

Figure 5-5 RID prototype

Figure 5-6 Test rig for the RID prototype

Figure 5-6 shows the test rig prepared for testing the RID prototype. As shown, the entire testing system consisted of a water tank, a tension/compression load cell, an actuator, an acquisition system, an aluminum base, steel screw clamps and a reaction frame. The water tank was made of acrylic plates, and its dimension was 1.0×1.0×1.0 m with a thickness of 0.01 m. During the test, the water was 0.6 m deep, and the position of the turning plates was roughly 0.3 m below the water surface. For the tests in the water, the influence of the reflected waves from tank walls should be carefully considered. In the present study, the ratio of the width of water tank (i.e. 1.0 m) and the diameter of turning plates (i.e. 0.068 m) was about 14.7, which is much larger than the common value of 5.0 in the previous experimental studies (e.g. Refs. [58, 59]). Therefore, the influence of the reflected waves was believed insignificant and could be neglected in the present study. The reaction frame was made of aluminum alloy, and it was rigid enough to eliminate the influence of structural vibration during the tests. Steel screw clamps were utilized to fix the reaction frame and the actuator. An electric actuator developed by Beijing Three Unite Testing System Co. Ltd (TUTS, http://www.tuts.com.cn) was utilized to test the RID prototype, and the displacement control mode was adopted to input the excitation. The actuator has a working frequency range of 0-50 Hz, a force range of 0-100 kg, and a maximum stroke of 200 mm. The displacement of RID was measured by a built-in sensing system in the actuator while the force was measured by the load cell as shown in the figure. The load cell was properly adjusted before each test to eliminate the influence of gravity force. These measured displacements and forces were collected synchronously and recorded through the data acquisition system, with a sampling frequency of 500 Hz.

5.3.3 Loading Scenarios

The RID prototype was tested under the sinusoidal excitations with different frequencies (0.5, 1.0, 1.5, 2.0, 2.5 and 3.0 Hz) and different amplitudes (5, 10, 15, 20, 25 and 30 mm). It should be noted that these frequencies were chosen according to the frequency range of the scaled regular waves since the RID would be mounted on a platform and further tested in a wave flume. The entire testing procedure was divided into the following steps: Step 1: the RID prototype was tested in the air (namely without water in the water tank) to demonstrate the fundamental behaviors of the conventional inerter; Step 2: the RID prototype without turning plates was tested in the water to identify the nonlinearities in the proposed mechanical model, and the detailed identification procedures will be introduced in Section 5.5; Step 3: the RID prototype with turning plates was tested in the water. A total of 20 cycles were run for each loading scenario.

Table 5-1 Primary design parameters of the RID prototype

Items	Parameters	Value
RID	Length (mm)	245
	Outer diameter (mm)	60
	Total weight (kg)	2.24
	Stroke (mm)	± 50
	Coulomb friction f_c (N)	16.378*
	Viscous friction coefficient c_v (N·s/m)	200.641*
	Original structural mass m_r (kg)	0.965
	Original moment of inertia J_{r1} (kg·m^2)	3.652×10^{-5}*
Ball screw	Diameter (mm)	12
	Lead L (mm)	10
	Conversion efficiency η (%)	90
Rotating tube	Weight (kg)	0.110
	Moment of inertia J_{r2} (kg·m^2)	2.30×10^{-5}
Turning plate	Length l_{tp} (mm)	30
	Outer radius R_1 (mm)	34
	Inner radius R_0 (mm)	9
	Thickness t_{tp} (mm)	2
	Number N	4
	Weight (kg)	0.049
Water tank	Length (m)	1
	Width (m)	1
	Height (m)	1
	Thickness (m)	0.01
	Height of water surface (m)	0.6

5.4 Experimental Results and Discussions

The experimental results are analyzed and discussed in this section. It is worth mentioning that, although 20 cycles were run in each loading scenario, only one cycle in the "steady state" is shown in each loading scenario for conciseness. Moreover, a low pass filter (0-15 Hz) is utilized to pre-process all the measured data to reduce the interference of high-frequency noise.

5.4.1 RID Prototype Tested without Water

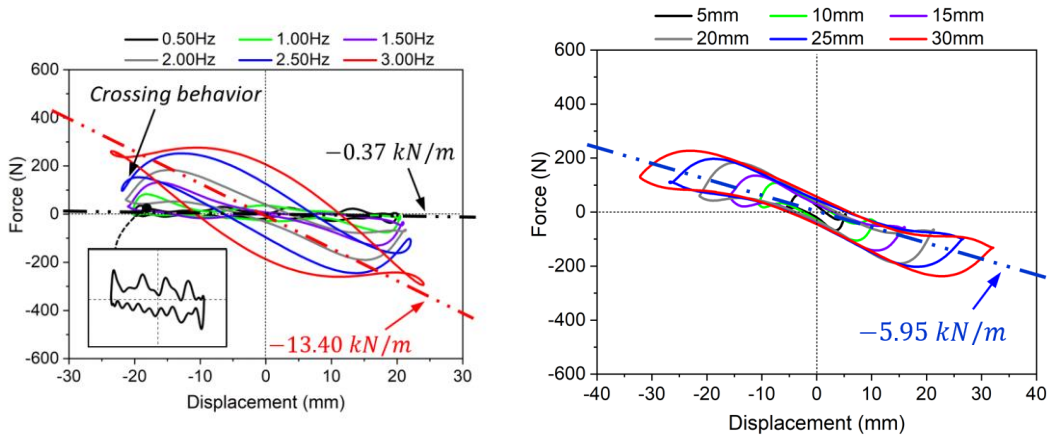

(a) Different frequencies (f=0.5, 1.0, 1.5, 2.0, 2.5 and 3.0 Hz, a=20 mm)

(b) Different amplitudes (a=5, 10, 15, 20, 25 and 30 mm, f=2.0 Hz)

Figure 5-7 Hysteretic behaviors of the RID prototype tested in the air

Figure 5-7 shows the hysteretic behaviors of the RID prototype under the sinusoidal excitations with different frequencies (f) and amplitudes (a) when the device was tested in the air. In these cases, the RID prototype was essentially a conventional inerter, and the extra inertance and damping provided by the water did not exist. As will be demonstrated in Section 5.5, the total inertance (i.e. $N \cdot m_e + m_i$) of the RID prototype was 37.70 kg. The corresponding mass amplification factor was thus about 108 according to the parameters of the device, namely the actual physical mass of the device was amplified by 108 times. It is noteworthy that the physical mass in the calculation was not the total weight of the RID prototype, but the mass of the rotating components (including the ball nut, steel sleeve, rotating tube and turning plates), which was 0.349 kg for the RID prototype.

Figure 5-7(a) shows the influence of excitation frequency on the hysteretic behavior when the excitation amplitude was 20 mm. It can be seen that an obvious negative slope exhibited in the hysteretic loops, and the slope increased with the increment of excitation frequency. This is because, as discussed in Section 5.2, the negative stiffness of the inerter was proportional to the squared excitation frequency ω^2, and a larger excitation frequency obviously resulted in a larger slope. The theoretical results (i.e. $-(N \cdot m_e + m_i) \cdot \omega^2$) when the excitation frequency f=0.5 Hz (the dashed black line in the figure) and f=3.0 Hz (the dashed red line) are plotted in the figure. As shown, the slopes of the experimental hysteresis curves agreed well with the corresponding theoretical negative stiffness. It is worth mentioning that, different from the positive stiffness where a force is developed to oppose the applied motion, the force assists the motion in the device with a negative stiffness. For the investigated RID, a large inertia force was developed due to the mass amplification effect of the inerter, which further drove the motion of the actuator. This was also evidenced by the maximum displacement of the

device. As shown, the maximum displacement was larger than the specified amplitude of 20 mm, and this effect was more evident when the excitation frequency was relatively high (see the blue and red solid curves in Figure 5-7(a)). Similar phenomenon was reported in some previous studies (e.g. Ref. [41]), and they attributed this phenomenon to the inertia and little damping (parasitic damping only) of the system when oscillation occurred. In these cases, the large inertia force in the device could drive the actuator to keep moving for a certain distance along the original direction though the inputted displacement had already altered its direction. Moreover, the parasitic damping in the system was small and not big enough to dissipate energy efficiently, the maximum displacement therefore exceeded the preassigned excitation amplitude, which further resulted in the crossing behaviors in the hysteresis curves: as shown in the blue and red solid curves in Figure 5-7(a), two obvious crosses appeared at the ends of each curve. These effects were however less evident when the excitation frequency was relatively low since the developed inertia force was not significant. Figure 5-7(a) also shows that a lot of fluctuations existed in the hysteresis curve when the excitation frequency was 0.5 Hz (see the subfigure in Figure 5-7(a)), while the curve became smoother when the frequency was larger. This could be primarily attributed to the influence of the torque ripples in the ball screw drive, which generally appear at the low-speed rotation. When the excitation frequency became larger, the inertial and damping forces were significantly increased, and the influence of torque ripples thus became marginal. More information about the torque ripples can be found in Ref. [60].

Figure 5-7(b) shows the influence of excitation amplitude on the hysteresis curve of the RID prototype when it was tested in the air. The excitation frequency f was fixed at 2 Hz while the amplitude a varied from 5 to 30 mm with an increment of 5 mm. As shown, all the hysteresis curves were similar and with a prolate shape, indicating that the energy dissipation capacity of the damper was limited. This is because only the parasitic damping force (see Equation (5.11)) dissipated energy in these cases. As will be demonstrated in Section 5.4.2, the energy dissipation capacity of the RID could be significantly improved when it was deployed in the water. Moreover, it is also found that all the hysteresis curves showed almost the same slope, i.e. the same negative stiffness. This is due to the fact that the negative stiffness was only related to the excitation frequency while not influenced by the excitation amplitude. Furthermore, the theoretical negative stiffness of the RID in these cases was equal to -5.95 kN/m (see the blue dashed line), which also coincided well with the slopes of the experimental hysteresis curves.

5.4.2 RID Prototype Tested in Water

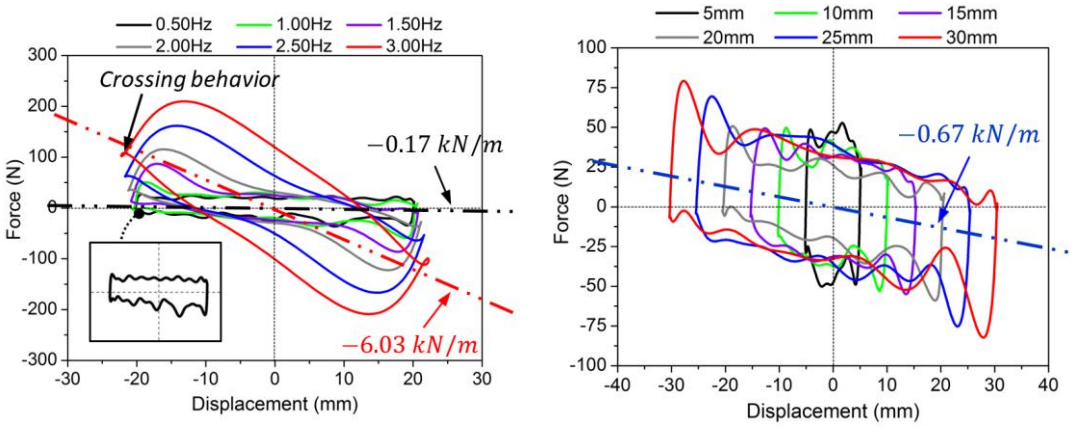

(a) Different frequencies (f=0.5, 1.0, 1.5, 2.0, 2.5 and 3.0 Hz, a=20 mm)

(b) Different amplitudes (a=5, 10, 15, 20, 25 and 30 mm, f=1.0 Hz)

Figure 5-8 Hysteretic behaviors of the RID prototype without turning plates tested in the water

The RID prototype was then tested in the water and its mechanical behaviors are discussed in this section. As mentioned in Section 5.3.3, the RID prototype without turning plates was firstly tested in order to identify the inerter nonlinearities in the proposed mechanical model. Figure 5-8 shows the hysteresis curves of the RID prototype without turning plates under the sinusoidal excitations with different frequencies and amplitudes. The theoretical negative stiffness is also highlighted by the dashed line in the figure. In particular, the black, red and blue dashed lines show the theoretical results when the excitation frequencies were 0.5, 3.0 (see Figure 5-8(a)) and 1.0 Hz (see Figure 5-8(b)), respectively. It can be seen from Figure 5-8 that the results were similar to those obtained in Figure 5-7. Namely: (1) as shown in Figure 5-8(a), the negatives stiffness effect was found in the damper, and it increased with the increment of excitation frequency; (2) as shown in Figure 5-8(b), the shapes of curves were similar and the slopes of the hysteresis curves were almost identical when the excitation amplitude increased from 5 to 30 mm; (3) the theoretical negative stiffness agreed well with the slopes of the experimental hysteresis curves. On the other hand, some differences also existed between Figure 5-7 and Figure 5-8: (1) as shown in Figure 5-8(a), the crossing behavior was only found in the hysteresis curve at the frequency of 3.0 Hz (i.e. the red solid curve in the figure) and it was less evident as compared to those in Figure 5-7(a). As mentioned above, the crossing behavior was primarily caused by the inertia force when damping is small. Since there was no turning plate in these tests, the inertia force of the RID prototype was smaller, and the corresponding crossing behavior was thus less significant; (2) all the curves in Figure 5-8(b) had more evident fluctuations compared to those in Figure 5-7(b). This was primarily because of the influence of torque ripples, which were more obvious at low-speed rotation. In particular, the excitation frequency in Figure 5-8(b) was smaller than that in Figure 5-7(b),

which lead to more evident fluctuations. Furthermore, as shown in Figure 5-8(a), the hysteresis curve was roughly with a rectangular shape (see the subfigure in Figure 5-8(a)) and had a very small slope (with a negative stiffness of -0.17 kN/m) when the excitation frequency was 0.5 Hz, which indicated that the Coulomb friction force (see Figure 5-4(c)) dominated the force in the damper while the viscous damping and inertial forces were insignificant under the excitation frequency of 0.5 Hz. This result will be utilized to identify the Coulomb friction force of the RID prototype in Section 5.5.1.

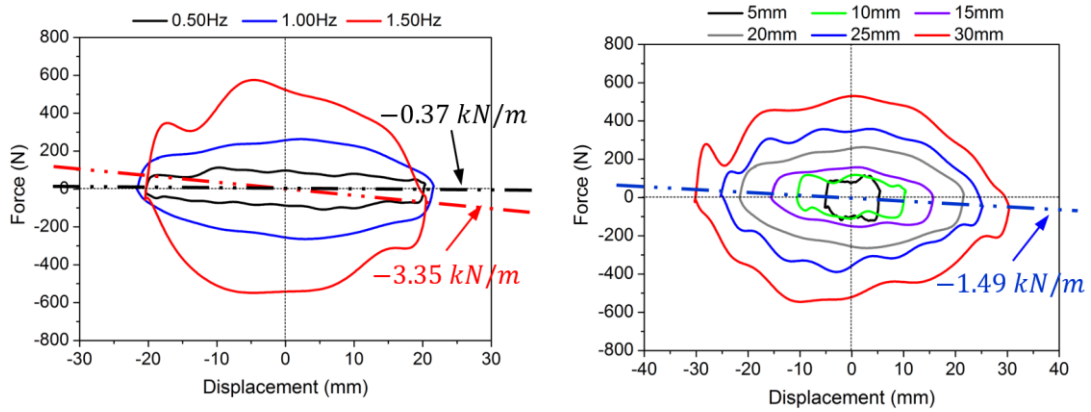

(a) Different frequencies (f=0.5, 1.0 and 1.5 Hz, a=20 mm)

(b) Different amplitudes (a=5, 10, 15, 20, 25 and 30 mm, f=1.0 Hz)

Figure 5-9 Hysteretic behaviors of the RID prototype with turning plates tested in the water

Figure 5-9 shows the hysteresis curves of the RID prototype with turning plates when it was tested in the water. Figure 5-9(a) shows the results when the excitation frequencies were 0.5, 1.0 and 1.5 Hz and the amplitude was 20 mm. It should be noted that the tests with excitation frequencies of 2.0, 2.5 and 3.0 Hz were not performed due to the output limitation of the actuator. A shown, the hysteresis curve roughly showed an elliptical shape, but tended to be a circle with the increase of the excitation frequency. Compared to the results in Figure 5-8(a), the energy dissipation capacity (i.e. the enclosed area of a particular hysteresis curve) was significantly increased when the excitation frequency and amplitude were the same. This was attributed to the nonlinear damping forces provided by the turning plates rotating in the water. Moreover, the theoretical negative stiffnesses of the 0.5 Hz and 1.5 Hz excitations were also highlighted by using the black and red dashed lines, respectively. It was found that the theoretical negative stiffnesses agreed well with the slopes of the experimental hysteresis curves. However, these negative stiffnesses in Figure 5-9(a) were not as obvious as those in Figure 5-7 and Figure 5-8. This is due to the fact that the nonlinear damping force proportional to the squared velocity was significantly larger than the inertial force proportional to the acceleration (see Figure 5-3 and Figure 5-4) when the turning plates rotated in the water. In other words, the nonlinear damping force dominated the responses of the damper when the RID prototype was deployed in the water.

Figure 5-9(b) shows the influence of excitation amplitude on the hysteresis curves of the RID prototype when it was tested in the water. The amplitude varied from 5 to 30 mm with an increment of 5 mm and the excitation frequency was fixed at 1.0 Hz. It is worth mentioning that the theoretical negative stiffness was represented by the blue dashed line in the figure. As shown, all the hysteresis curves were roughly elliptical, and more energy was dissipated when the excitation amplitude increased. Moreover, similar to Figure 5-9(a), the theoretical negative stiffness also agreed well with the slopes of these hysteresis curves although it was not evident due to the significant damping effect of RID. Furthermore, different from the results in Figure 5-7, more fluctuations existed in the hysteresis curves as shown in Figure 5-9. This is because the force of the RID in the water was also affected by the surrounding flow field, which could be changed by the turning plates during the tests.

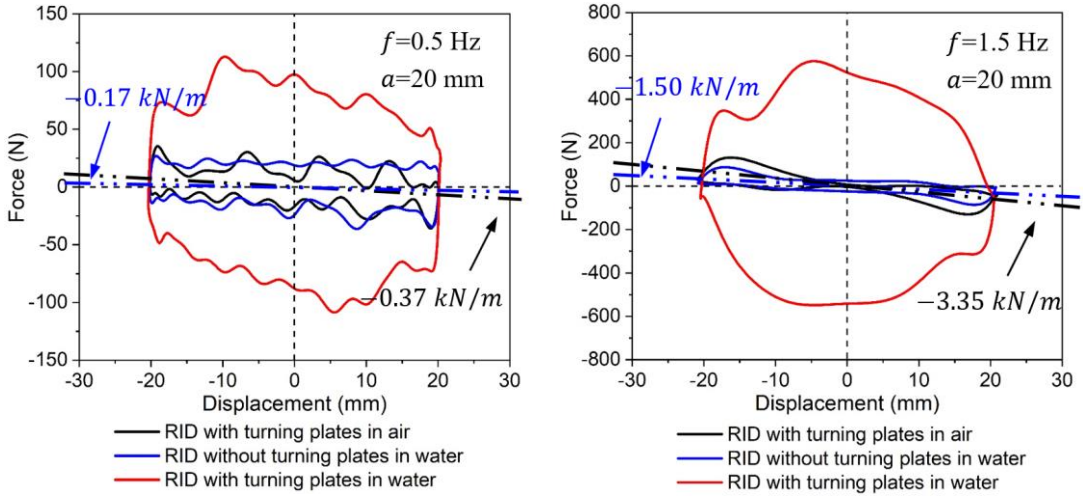

(a) 0.5 Hz and 20 mm (b) 1.5 Hz and 20 mm

Figure 5-10 Comparison of the hysteresis curves for different test conditions

For an in-depth understanding of the RID performance, Figure 5-10 shows the comparison of the hysteresis curves for different test conditions, i.e. with/without turning plates and in/out of water. Two loading cases are considered in the comparison: one is the harmonic excitation with a frequency of 0.5 Hz and an amplitude of 20 mm, and another one is the harmonic excitation with a frequency of 1.5 Hz and an amplitude of 20 mm. In this figure, the black and blue dashed lines denote the expected negative stiffnesses of the RID with turning plates and the RID without turning plates, respectively. Similarly, these expected negative stiffnesses matched well with the slopes of hysteresis curves. Moreover, the hysteresis curves of both the RID with turning plates in the air and the RID without turning plate in the water were prolate shape with small enclosed areas no matter under the 0.5 Hz or 1.5 Hz excitations. This fact indicates that these two configurations have a limited capacity of dissipating energy. Compared to either the RID with turning plates in the air or the RID without turning plates in the water, the RID with turning plates in the water had a larger enclosed area of the hysteresis

curve, indicating it was more effective in reducing the vibration energy. It should be noted that the RID with turning plates in the air is not compared with the RID without turning plates due to the principle of the single variable. Specifically speaking, there are two variables (i.e. the turning plates and water) in these two configurations and it is thus not reasonable to compare directly.

To qualitatively demonstrate the energy dissipation capability of the RID under different test conditions, the equivalent viscous damping ratio (ξ_{eq}) is also examined, which can be calculated as follows [61]:

$$\xi_{eq} = \frac{A_h}{4\pi A_e} = \frac{A_h}{2\pi K_{eq} X_m^2} = \frac{A_h}{2\pi F_m X_m} \tag{5.18}$$

$$F_m = \frac{|F_{max}| + |F_{min}|}{2} \tag{5.19}$$

$$X_m = \frac{|X_{max}| + |X_{min}|}{2} \tag{5.20}$$

in which A_h is the dissipated energy of RID per cycle; F_m is the average peak force, with F_{max} and F_{min} representing the maximum and minimum forces of RID per cycle; X_m is the average displacement, with X_{max} and X_{min} denoting the maximum and minimum displacement of RID per cycle; K_{eq} is the stiffness of the equivalent linear elastic system; A_e is the elastic strain energy.

Table 5-2 Equivalent viscous damping ratios of the RID for different test conditions

Frequency f (Hz)	Equivalent viscous damping ratio ξ_{eq}		
	RID with turning plates in air	RID without turning plates in water	RID with turning plates in water
0.5	0.251	0.385	0.437
1.5	0.164	0.207	0.461

Table 5-2 tabulates the equivalent viscous damping ratios (ξ_{eq}) of the RID for different test conditions. As shown, the equivalent viscous damping ratios of the RID with turning plates in the water are obviously bigger than that of either the RID with turning plates in the air or the RID without turning plates in the water. Taken the 1.5 Hz excitation as an example, the equivalent viscous damping ratio of the RID with turning plates in the water is almost 3 and 2.3 times of those of the RID with turning plates in the air and the RID without turning plates in the water, respectively. These facts demonstrate that the RID has a superior energy dissipation capacity when the turning plates are rotating in the water. Moreover, it is also found that the equivalent viscous damping ratio of more than 0.4 can be realized by the RID with turning plates in the water no matter under the 0.5 or 1.5 Hz excitation. However, the

equivalent viscous damping ratios of the RID with turning plates in the air and the RID without turning plates in the water decrease significantly when the frequency increases from 0.5 Hz to 1.5 Hz. This may be because as defined in Equation (5.18), besides the dissipated energy A_h, the equivalent viscous damping ratio is also directly relevant to the peak force of RID [62]. Comparing the results in Figure 5-10(a) and (b), it can be found that the peak forces under the 1.5 Hz excitation are obviously larger than those under the 0.5 Hz excitation.

5.5 Mechanical Model Identification

Section 5.2 presented the mechanical model of the RID system. It is obvious that the parameters in the mechanical model (i.e. Equation (5.14)) need to be identified based on the experimental results. In this section, the parameters in the mechanical model are identified by using some of the experimental data as reported in Section 5.4, and the accuracy of the mechanical model is further validated by the remaining experimental results not used for parameter identification. It should be noted that three cycles of "steady-state" results are utilized in the parameter identifications, and all the experimental data are pre-processed by a low pass filter (0-15 Hz) to decrease the contamination of high-frequency noise as discussed in Section 5.4.

The nonlinear least-squares method in MATLAB (version R2017a) is utilized for the parameter identification, and its mathematical expression can be given as follows:

$$\psi = \min \left(\sum \left| F_{exp}(X_{exp}) - F_{th}(X_{exp}, P_i) \right|^2 \right) \tag{5.21}$$

in which F_{exp} is the force measured in the experiment; X_{exp} is the system input, namely the displacement; F_{th} is the theoretical force calculated based on the identified parameters; P_i is the parameters to be identified, which includes the parameters related to the inerter nonlinearities (namely Coulomb friction force f_c, original moment of inertia J_{r1} and viscous friction coefficient c_v) and two coefficients in the (ideal) axial force (i.e. inertia coefficient c_m and drag coefficient c_d). The identifications of these parameters are introduced in the following two subsections respectively, and the reasons why these parameters need to be identified are also discussed.

5.5.1 Identification of Inerter Nonlinearities

The experimental results of the RID prototype without turning plates excited in the water are utilized to identify the inerter nonlinearities in this section. These data are used for inerter nonlinearity identification due to the following reasons: (1) the inerter nonlinearities of the RID prototype in the water might be different from those in the air due to the influence of

water. The RID system developed in the present study aims to be installed in the offshore environment, the experimental results in the water are thus more relevant for the identification; (2) as indicated in Equation (5.14), the viscous damping term of the RID consists of two parts, i.e. the viscous friction force and the nonlinear damping force provided by the rotating turning plates. Using the experimental results of the RID prototype without turning plates can eliminate the influence of damping force provided by the turning plates during the identification process.

The Coulomb friction force f_c is firstly identified. As discussed in Section 5.4.2, the Coulomb friction force dominated the response of the RID prototype when the excitation frequency was 0.5 Hz, and the corresponding inertial and viscous damping forces were insignificant. The experimental data of the RID prototype without turning plates excited by the sinusoidal displacement with a frequency of 0.5 Hz and an amplitude of 20 mm (i.e. the black solid line in Figure 5-8(a)) is thus taken out for identification. The identified Coulomb friction force f_c is 16.378 N for the RID prototype.

The original moment of inertia J_{r1} is difficult to be calculated accurately due to the irregular shape and mass distribution of the ball nut and radial bearings (see Figure 5-1), and the viscous friction coefficient c_v is another parameter not easy to be determined. These two parameters are thus identified through experimental results. According to Li et al. [40], these two parameters are more sensitive to the high-frequency excitations. The experimental data of the RID prototype without turning plates excited by the sinusoidal displacement with a frequency of 3.0 Hz and an amplitude of 20 mm is used to identify these two parameters. The identified c_v and J_{r1} are 200.641 N·s/m and 3.652×10^{-5} kg·m^2, respectively. After identifying the original moment of inertia J_{r1}, the total inertance of the RID prototype can be calculated according to Equation (5.14), and it is 37.70 kg.

To demonstrate the accuracy of the identified parameters, Figure 5-11 compares the experimental and analytical results of the RID without turning plates under the other two sets of sinusoidal excitations with different frequencies and amplitudes (i.e. 2.5 Hz and 20 mm, 1.0 Hz and 15 mm). In particular, the analytical results of the RID without turning plates are calculated based on Equation (5.14). It should be noted that the parameters relevant to the turning plates (i.e. m_e, c_e and J_{r2}) in Equation (5.14) are equal to 0 in the calculations since there are no turning plates in the system. As shown, good agreements are achieved when the identified nonlinear parameters are used in the calculations. Moreover, these three nonlinearities (f_c, c_v and J_{r1}) are assumed as constants during the tests, i.e. they are not varying with the variation of excitation frequency and amplitude (Liu et al. [8]).

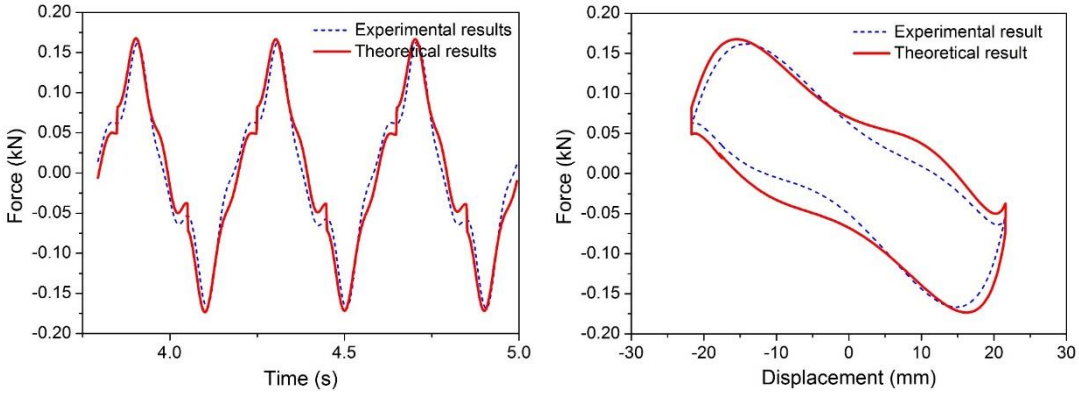

(a) f=2.5 Hz, a=20 mm

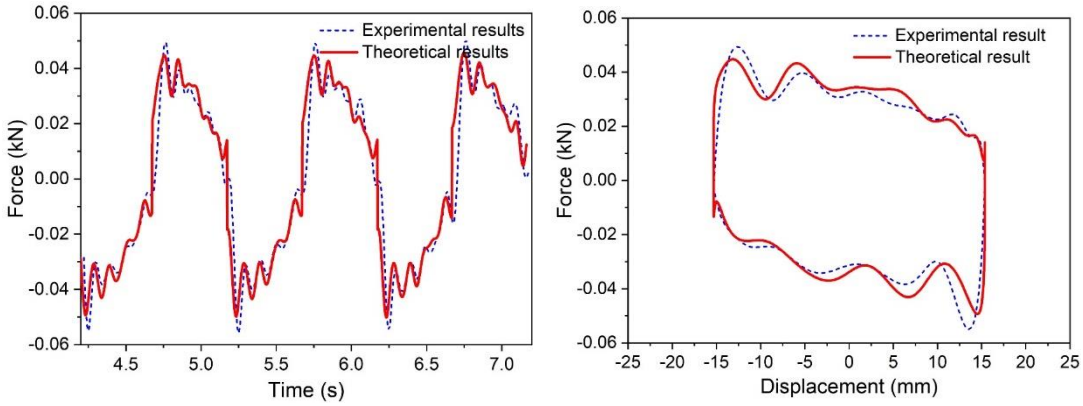

(b) f=1.0 Hz, a=15 mm

Figure 5-11 Comparisons of the experimental and analytical results of the RID prototype without turning plates excited in the water

5.5.2 Identification of Inertia and Drag Coefficients

After identifying the inerter nonlinearities, the next step is to identify the inertance m_e and equivalent damping coefficient c_e in the proposed mechanical model. Since the physical dimensions of turning plates (e.g. length, thickness, and radius, etc.) and the properties of ball screw (e.g. the lead and conversion efficiency) are determinate, the identifications of the inertance m_e and equivalent damping coefficient c_e are essentially to identify the inertia coefficient c_m and drag coefficient c_d in Equation (5.14). The nonlinear least-squares method is utilized again to identify these two parameters.

Table 5-3 tabulates the identified inertia and drag coefficients for all the loading scenarios. It can be seen that all the inertia coefficients are identified equaling to zero while the drag coefficient varies with both the excitation frequency and amplitude. This is because, as will be demonstrated by the sensitivity analysis in the Appendix, the inertia coefficient c_m is much less sensitive compared to the drag coefficient c_d. From another point of view, these results indicate that the force of the RID is governed by the damping force rather than the inertial

force. The variation of the drag coefficient is because the hydrodynamic force of a rigid body oscillating in the fluid is affected by two non-dimensional parameters, namely the Keulegan-Carpenter (KC) number and frequency number (β), which are defined as follows:

$$KC = \frac{2\pi a}{D} \tag{5.22}$$

$$\beta = \frac{D^2 f}{\vartheta} \tag{5.23}$$

where a is the excitation amplitude; $D = 2R_1$ is the characteristic dimension of the RID prototype, which is the diameter of turning plates in the present study; f is the excitation frequency; ϑ is the kinematic viscosity of water, which is $1.004 \times 10^{-6} m^2/s$ at 20℃. Figure 5-12 shows the drag coefficient C_d of the RID prototype over a variety of KC numbers calculated according to Equation (5.22) when the excitation frequency was 1 Hz. As shown, the drag coefficient c_d is highly dependent on the KC number, it decreases significantly when the KC number is relatively small and tends to be a constant with the increase of the KC number. Similar relationships were reported in some previous experimental studies (e.g. Refs. [63, 64]). For the frequency number β, it is 4605 based on Equation (5.23).

Table 5-3 Identified inertia and drag coefficients for the RID prototype

Case No	Frequency (Hz)	Amplitude (mm)	Inertia coefficient c_m	Drag coefficient c_d
1	0.5	20	0	2.905
2	1.0	20	0	2.068
3	1.5	20	0	2.466
4	1.0	5	0	10.451
5	1.0	10	0	3.065
6	1.0	15	0	2.232
7	1.0	20	0	2.069
8	1.0	25	0	2.299
9	1.0	30	0	2.353

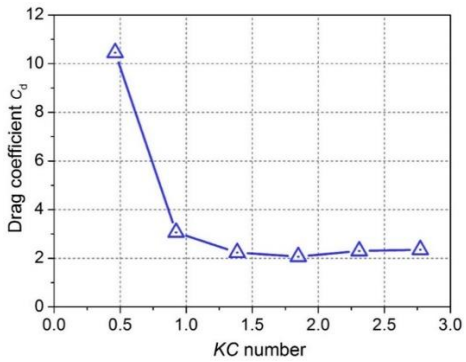

Figure 5-12 Drag coefficient of the RID prototype under different KC numbers (β=4605)

Based on the identified inertia and drag coefficients, the analytical forces of the RID can be calculated based on Equation (5.14). Figure 5-13 and Figure 5-14 compare the experimental and analytical results, and the corresponding differences are summarized in Table 5-4. In particular, Figure 5-13 shows the results when the amplitude was 20 mm while the excitation frequency varied from 0.5 to 1.5 Hz (i.e. Cases 1-3 in Table 5-3), and Figure 5-14 shows the results when the excitation frequency was fixed at 1 Hz while the amplitude varied from 5 to 30 mm (i.e. Cases 4-9 in Table 5-3). It can be seen that, except Case 4, good agreements are found in all the cases which are with a wide range of excitation frequencies and amplitudes. As shown in Table 5-4, the difference between the peak force is less than 9.13% and the difference between the dissipated energy is less than 3.21%, which demonstrate the accuracy of the mechanical model. For Case 4 (i.e. Figure 5-14(a)), the differences are relatively large, with a value of 24.01% and 5.41% for the peak force and dissipated energy respectively. This discrepancy might be attributed to the fact that the drag coefficient c_d in this case (i.e. KC=0.46) is 10.451 (see Table 5-3), which is much larger than those in other cases, so the effect of torque ripple is more evident.

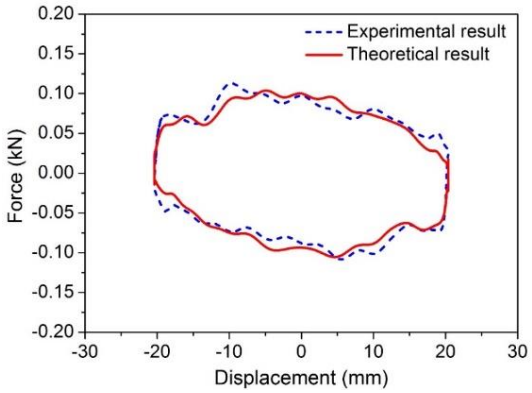

(a) f=0.5 Hz, a=20 mm

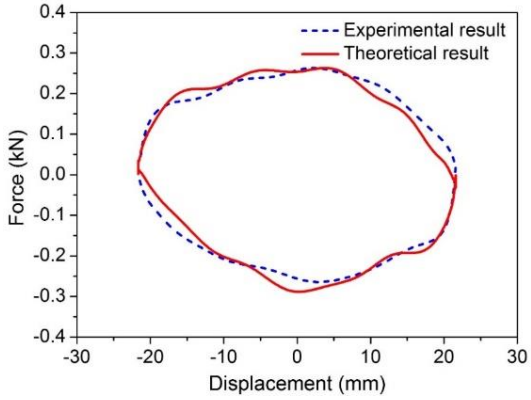

(b) f=1.0 Hz, a=20 mm

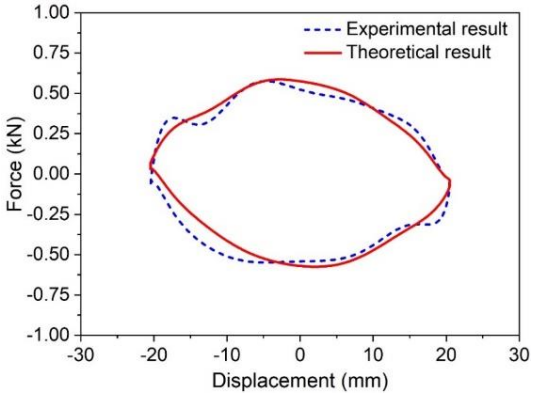

(c) f=1.5 Hz, a=20 mm

Figure 5-13 Comparisons of the experimental and analytical hysteretic behaviors of the RID prototype under the sinusoidal excitations with different frequencies

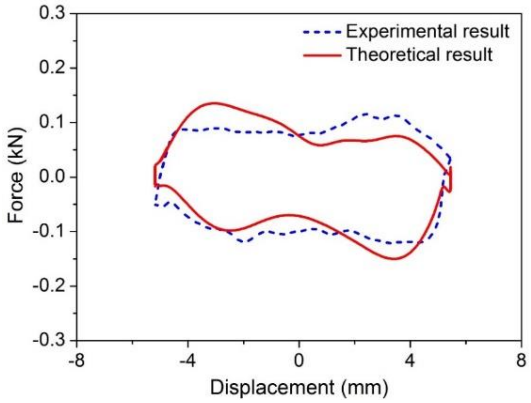

(a) f=1.0 Hz, a=5 mm

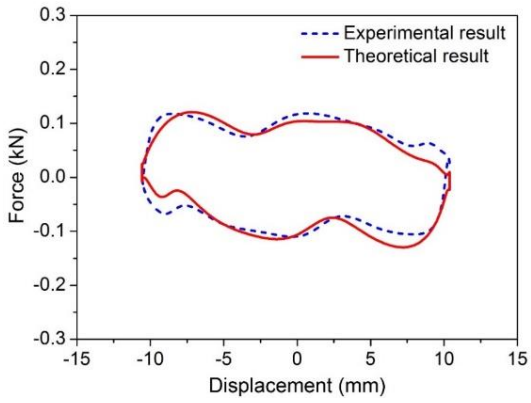

(b) f=1.0 Hz, a=10 mm

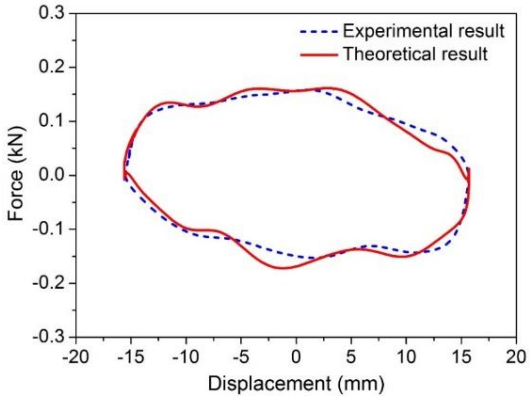

(c) f=1.0 Hz, a=15 mm

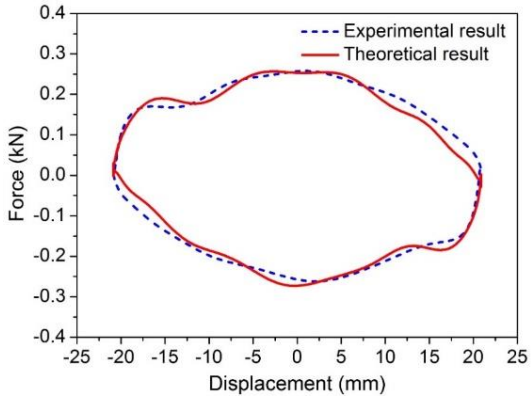

(d) f=1.0 Hz, a=20 mm

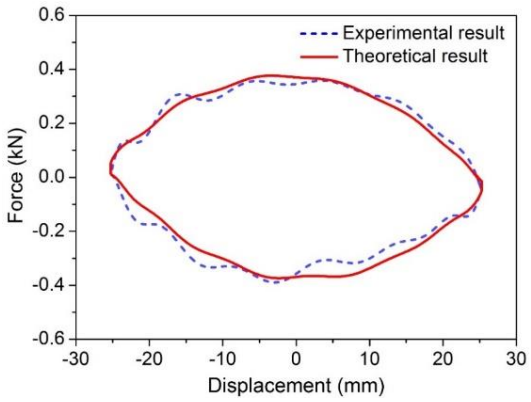

(e) f=1.0 Hz, a=25 mm

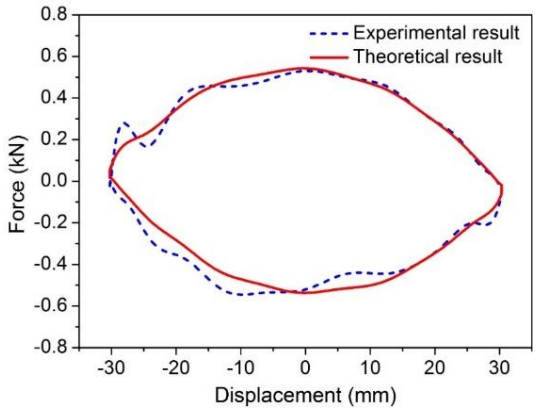

(f) f=1.0 Hz, a=30 mm

Figure 5-14 Comparisons of the experimental and analytical hysteretic behaviors of the RID prototype under the sinusoidal excitations with different amplitudes

Table 5-4 Differences between the experimental and analytical results

No	Peak force (N)			Dissipated energy ($N \cdot m$)		
	Experimental	Analytical	Difference (%)	Experimental	Analytical	Difference (%)
1	112.82	103.82	7.98	6.34	6.16	2.74
2	264.16	288.28	9.13	17.06	16.79	1.57
3	575.40	586.14	1.87	33.31	32.43	2.64
4	121.01	150.06	24.01	1.91	1.81	5.41
5	118.31	120.58	1.92	3.66	3.54	3.21
6	158.25	161.40	1.99	7.46	7.53	0.93
7	262.00	273.03	4.21	15.82	15.32	3.17
8	389.32	373.87	3.97	26.28	26.28	0.02
9	545.24	536.74	1.56	45.63	44.83	1.74

5.6 Conclusions

In the present study, a RID prototype was manufactured and systematically tested by using a series of harmonic excitations with different frequencies and amplitudes. A nonlinear mechanical model considering inerter nonlinearities is proposed to capture the behaviors of the RID prototype, and the parameters in the mechanical model are identified based on experimental results. The experimental data and the analytical results predicted by the proposed mechanical model are investigated and compared. Based on the results, the following conclusions can be drawn:

(1) The RID deployed in the air (namely the ordinary inerter) has the mass amplification and negative stiffness effects. A mass amplification factor of 108 was obtained for the RID prototype in the present study.

(2) The proposed RID can generate significant damping force by rotating turning plates in the water, and an equivalent viscous damping ratio of more than 0.4 can be realized.

(3) The proposed mechanical model is accurate to predict the behaviors of the RID. For most cases considered in this paper, the differences between the experimental and analytical results are less than 9.13% and 3.12% in terms of the peak force and dissipated energy, respectively.

(4) The mechanical behaviors of RID are governed by the nonlinear damping force acting on the turning plates, and the inertial force acting on the turning plates is insignificant.

(5) The drag coefficient c_d is highly dependent on KC number and tends to be constant with the increase of KC number. The influence of KC number should be incorporated into the performance evaluation of RID.

The results also show that the mechanical model of RID was derived based on the classical Morison's equation with the following two merits: (1) the developed mechanical model could accurately capture the mechanical behaviors of the RID prototype; (2) all the parameters in the mechanical model have specific physical meanings, which would be beneficial for the design of RID. However, it should be noted that only this damping model was examined in the present study, there might exist some other damping models (e.g. the generic nonlinear model suggested in Ref. [57]) that could provide better result estimations while with physical meanings, which deserves further investigations.

5.7 Appendix: Sensitivity Analysis

A sensitivity analysis is performed to demonstrate the sensitivity of the inertia and drag coefficients on the axial force of the damper. Based on the finite difference method [65], the sensitivities can be obtained by differentiating Equation (5.14) with respect to the inertia and drag coefficients, and they are expressed as follows:

$$\chi_1 = \left|\frac{\partial F}{\partial c_m}\right| = \left|N \cdot \frac{1}{3\eta}\left(\frac{2\pi}{L}\right)^2 \rho l_{tp} t_{tp} (R_1^3 - R_0^3)\ddot{x}_d\right| \tag{5.24}$$

$$\chi_2 = \left|\frac{\partial F}{\partial c_d}\right| = \left|N \cdot \frac{1}{8\eta}\left(\frac{2\pi}{L}\right)^3 \rho l_{tp} (R_1^4 - R_0^4)\dot{x}_d|\dot{x}_d|\right| \tag{5.25}$$

where χ_1 and χ_2 are the sensitivity measures of the force from the damper with respect to the inertia and drag coefficients, respectively.

Assuming the harmonic excitation has an amplitude a and a circular frequency ω ($\omega = 2\pi f$), the displacement can be given by

$$x_d = a\sin(\omega t + \varphi) \tag{5.26}$$

in which, φ is the random phase angle. The velocity and acceleration of this harmonic excitation are thus:

$$\dot{x}_d = a\omega\cos(\omega t + \varphi) \tag{5.27}$$

$$\ddot{x}_d = -a\omega^2\sin(\omega t + \varphi) \tag{5.28}$$

Substituting Equations (5.27) and (5.28) into Equations (5.24) and (5.25), one obtains:

$$\chi_1 = \left|N \cdot \frac{1}{3\eta}\left(\frac{2\pi}{L}\right)^2 \rho l_{tp} t_{tp} (R_1^3 - R_0^3) a\omega^2 \sin(\omega t + \varphi)\right| \tag{5.29}$$

$$\chi_2 = \left| N \cdot \frac{1}{8\eta} \left(\frac{2\pi}{L}\right)^3 \rho l_{tp} (R_1^4 - R_0^4) a\omega \cos(\omega t + \varphi) \, |a\omega \cos(\omega t + \varphi)| \right| \tag{5.30}$$

Obviously, the sensitivity measures are amplitude-dependent, which means the influence of amplitude on the sensitivity analysis cannot be neglected. Therefore, two amplitudes (i.e. 5 mm and 30 mm) are considered in the calculation of sensitivity measures, and they correspond to the minimum and maximum amplitude in the RID test, respectively. It should be noted that the oscillation frequency is fixed to 2π rad/s (i.e. f=1 Hz). As shown in Figure 5-15(a), the maximum values of χ_1 and χ_2 are about 0.27 and 5.6 respectively when the vibration amplitude is 5 mm, with a relative ratio of about 1/21. When the vibration amplitude is 30 mm, the ratio is about 1/122 (see Figure 5-15(b)). These facts demonstrate that, for the amplitudes investigated in the present study (i.e. 5-30 mm), the overall force of RID is very sensitive to the variation of the drag coefficient, and relatively not sensitive to the variation of the inertia coefficient.

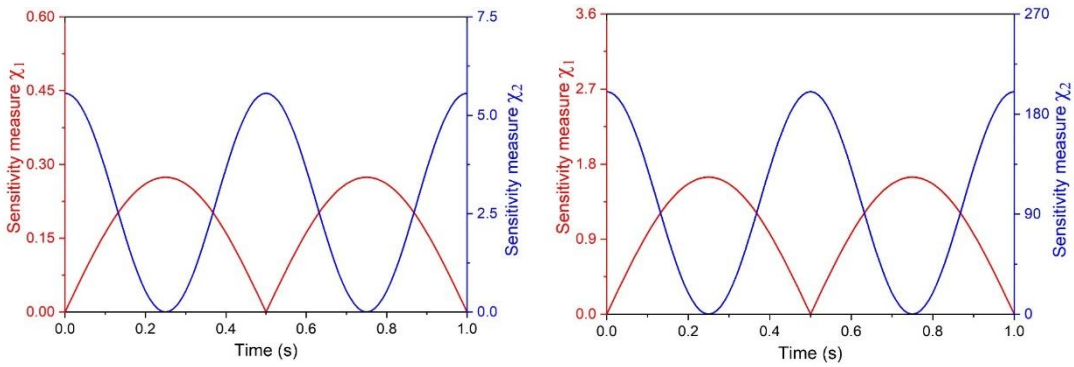

(a) 5 mm (b) 30 mm

Figure 5-15 Comparison between the sensitivity measures of the inertia and drag coefficients under different oscillation amplitudes

5.8 References

[1] Zuo H, Bi K, Hao H. A state-of-the-art review on the vibration mitigation of wind turbines. Renew Sust Energ Rev. 2020;121:109710.

[2] Parulekar Y, Reddy G. Passive response control systems for seismic response reduction: A state-of-the-art review. Int J Struct Stab Dyn. 2009;9:151-77.

[3] Smith MC. Synthesis of mechanical networks: the inerter. IEEE Trans Automat Contr. 2002;47:1648-62.

[4] Papageorgiou C, Houghton NE, Smith MC. Experimental testing and analysis of inerter devices. J Dyn Syst Meas Contr. 2009;131:011001.

[5] Brzeski P, Lazarek M, Perlikowski P. Experimental study of the novel tuned mass damper with inerter which enables changes of inertance. J Sound Vib. 2017;404:47-57.

[6] Wang FC, Hong MF, Lin TC. Designing and testing a hydraulic inerter. J Mech Eng Sci. 2010;225:66-72.

[7] Swift S, Smith MC, Glover A, Papageorgiou C, Gartner B, Houghton NE. Design and modelling of a fluid inerter. Int J Control. 2013;86:2035-51.

[8] Liu X, Jiang JZ, Titurus B, Harrison A. Model identification methodology for fluid-based inerters. Mech Syst Signal Process. 2018;106:479-94.

[9] John EDA, Wagg DJ. Design and testing of a frictionless mechanical inerter device using living-hinges. J Franklin Inst. 2019;356:7650-68.

[10] Lu L, Duan YF, Spencer BF, Lu X, Zhou Y. Inertial mass damper for mitigating cable vibration. Struct Control Health Monit. 2017;24:e1986.

[11] Shi X, Zhu S. Dynamic characteristics of stay cables with inerter dampers. J Sound Vib. 2018;423:287-305.

[12] Chen MZQ, Papageorgiou C, Scheibe F, Wang FC, Smith M. The missing mechanical circuit element. IEEE Circuits Syst Mag. 2009;9:10-26.

[13] Smith MC, Wang FC. Performance Benefits in Passive Vehicle Suspensions Employing Inerters. Veh Syst Dyn. 2004;42:235-57.

[14] Marian L, Giaralis A. Optimal design of a novel tuned mass-damper–inerter (TMDI) passive vibration control configuration for stochastically support-excited structural systems. Probabilistic Eng Mech. 2014;38:156-64.

[15] Dai J, Xu ZD, Gai PP. Tuned mass-damper-inerter control of wind-induced vibration of flexible structures based on inerter location. Eng Struct. 2019;199:109585.

[16] Giaralis A, Petrini F. Wind-Induced Vibration Mitigation in Tall Buildings Using the Tuned Mass-Damper-Inerter. J Struct Eng. 2017;143:04017127.

[17] Petrini F, Giaralis A, Wang Z. Optimal tuned mass-damper-inerter (TMDI) design in wind-excited tall buildings for occupants' comfort serviceability performance and energy harvesting. Eng Struct. 2019:109904.

[18] Xu K, Bi K, Han Q, Li X, Du X. Using tuned mass damper inerter to mitigate vortex-induced vibration of long-span bridges: Analytical study. Eng Struct. 2019;182:101-11.

[19] Dai J, Xu ZD, Gai PP, Hu ZW. Optimal design of tuned mass damper inerter with a Maxwell element for mitigating the vortex-induced vibration in bridges. Mech Syst Signal Process. 2021;148.

[20] Lazar IF, Neild SA, Wagg DJ. Using an inerter-based device for structural vibration suppression. Earthq Eng Struct Dyn. 2014;43:1129-47.

[21] Lazar IF, Neild SA, Wagg DJ. Vibration suppression of cables using tuned inerter dampers. Eng Struct. 2016;122:62-71.

[22] Wen Y, Chen Z, Hua X. Design and Evaluation of Tuned Inerter-Based Dampers for the Seismic Control of MDOF Structures. J Struct Eng. 2016;143:04016207.

[23] Shen W, Niyitangamahoro A, Feng Z, Zhu H. Tuned inerter dampers for civil structures subjected to earthquake ground motions: optimum design and seismic performance. Eng Struct. 2019;198:109470.

[24] Zhao G, Raze G, Paknejad A, Deraemaeker A, Kerschen G, Collette C. Active tuned inerter-damper for smart structures and its H_∞ optimisation. Mech Syst Signal Pr. 2019;129:470-8.

[25] Javidialesaadi A, Wierschem NE. An inerter-enhanced nonlinear energy sink. Mech Syst Signal Process. 2019;129:449-54.

[26] Chen HY, Mao XY, Ding H, Chen LQ. Elimination of multimode resonances of composite plate by inertial nonlinear energy sinks. Mech Syst Signal Process. 2020;135:106383.

[27] Hu Y, Chen MZQ, Shu Z, Huang L. Analysis and optimisation for inerter-based isolators via fixed-point theory and algebraic solution. J Sound Vib. 2015;346:17-36.

[28] Alujević N, Čakmak D, Wolf H, Jokić M. Passive and active vibration isolation systems using inerter. Journal of Sound and Vibration. 2018;418:163-83.

[29] De Haro Moraes F, Silveira M, Gonçalves PJP. On the dynamics of a vibration isolator with geometrically nonlinear inerter. Nonlinear Dyn. 2018;93:1325-40.

[30] Yang J, Jiang JZ, Neild SA. Dynamic analysis and performance evaluation of nonlinear inerter-based vibration isolators. Nonlinear Dyn. 2019;99:1823-39.

[31] Pradono MH, Iemura H, Igarashi A, Kalantari A. Application of angular-mass dampers to base-isolated benchmark building. Struct Control Health Monit. 2008;15:737-45.

[32] Saitoh M. On the performance of gyro-mass devices for displacement mitigation in base isolation systems. Struct Control Health Monit. 2012;19:246-59.

[33] De Domenico D, Ricciardi G. An enhanced base isolation system equipped with optimal tuned mass damper inerter (TMDI). Earthq Eng Struct Dyn. 2018;47:1169-92.

[34] Di Matteo A, Masnata C, Pirrotta A. Simplified analytical solution for the optimal design of Tuned Mass Damper Inerter for base isolated structures. Mech Syst Signal Pr. 2019;134:106337.

[35] Qian F, Luo Y, Sun H, Tai WC, Zuo L. Optimal tuned inerter dampers for performance enhancement of vibration isolation. Eng Struct. 2019;198:109464.

[36] Chen Q, Zhao Z, Zhang R, Pan C. Impact of soil–structure interaction on structures with inerter system. J Sound Vib. 2018;433:1-15.

[37] Zhao Z, Chen Q, Zhang R, Pan C, Jiang Y. Optimal design of an inerter isolation system considering the soil condition. Eng Struct. 2019;196:109324.

[38] Siami A, Karimi H, Cigada A, Zappa E, Sabbioni E. Parameter optimization of an inerter-based isolator for passive vibration control of Michelangelo's Rondanini Pietà. Mech Syst Signal Process. 2018;98:667-83.

[39] Hwang J, Kim J, Kim Y. Rotational inertia dampers with toggle bracing for vibration control of a building structure. Eng Struct. 2007;29:1201-8.

[40] Ikago K, Saito K, Inoue N. Seismic control of single-degree-of-freedom structure using tuned viscous mass damper. Earthq Eng Struct Dyn. 2012;41:453-74.

[41] Nakamura Y, Fukukita A, Tamura K, Yamazaki I, Matsuoka T, Hiramoto K et al. Seismic response control using electromagnetic inertial mass dampers. Earthq Eng Struct Dyn. 2014;43:507-27.

[42] Zhu H, Li Y, Shen W, Zhu S. Mechanical and energy-harvesting model for electromagnetic inertial mass dampers. Mech Syst Signal Process. 2019;120:203-20.

[43] Li Y, Shen W, Zhu H. Vibration mitigation of stay cables using electromagnetic inertial mass dampers: Full-scale experiment and analysis. Eng Struct. 2019;200:109693.

[44] Hu Y, Wang J, Chen MZQ, Li Z, Sun Y. Load mitigation for a barge-type floating offshore wind turbine via inerter-based passive structural control. Eng Struct. 2018;177:198-209.

[45] Ma R, Bi K, Hao H. Mitigation of heave response of semi-submersible platform (SSP) using tuned heave plate inerter (THPI). Eng Struct. 2018;177:357-73.

[46] Sarkar S, Fitzgerald B. Vibration control of spar-type floating offshore wind turbine towers using a tuned mass-damper-inerter. Struct Contorl Health Monit. 2019.

[47] Ma R, Bi K, Hao H. Heave motion mitigation of semi-submersible platform using inerter-based vibration isolation system (IVIS). Engineering Structures. 2020:110833.

[48] Ma R, Bi K, Hao H. A novel rotational inertia damper for heave motion suppression of semisubmersible platform in the shallow sea. Struct Contorl Health Monit. 2019:e2368.

[49] Ma R, Bi K, Hao H. Using inerter-based control device to mitigate heave and pitch motions of semi-submersible platform in the shallow sea. Eng Struct. 2020;207:110248.

[50] Wang FC, Hong MF, Lin TC. Designing and testing a hydraulic inerter. P I Mech Eng C-J Mec. 2011;225:66-72.

[51] Pietrosanti D, De Angelis M, Giaralis A. Experimental study and numerical modeling of nonlinear dynamic response of SDOF system equipped with tuned mass damper inerter (TMDI) tested on shaking table under harmonic excitation. Int J Mech Sci. 2020;184:105762.

[52] Morison J, Johnson J, Schaaf S. The force exerted by surface waves on piles. J Pet Technol. 1950;2:149-54.

[53] Harris T. An analytical method to predict skidding in thrust-loaded, angular-contact ball bearings. J Lubr Technol. 1971:17-23.

[54] Li C, Liang M, Wang Y, Dong Y. Vibration suppression using two-terminal flywheel. Part I: Modeling and characterization. J Vib Control. 2012;18:1096-105.

[55] Brzeski P, Perlikowski P. Effects of play and inerter nonlinearities on the performance of tuned mass damper. Nonlinear Dyn. 2017;88:1027-41.

[56] Brzeski P, Kapitaniak T, Perlikowski P. Novel type of tuned mass damper with inerter which enables changes of inertance. J Sound Vib. 2015;349:56-66.

[57] Di Paola M, Navarra G. Stochastic seismic analysis of MDOF structures with nonlinear viscous dampers. Struct Control Health Monit. 2009;16:303-18.

[58] Tian X, Tao L, Li X, Yang J. Hydrodynamic coefficients of oscillating flat plates at $0.15 \leq KC \leq 3.15$. J Mar Sci Tech. 2017;22:101-13.

[59] Tao L, Dray D. Hydrodynamic performance of solid and porous heave plates. Ocean Eng. 2008;35:1006-14.

[60] Kamalzadeh A, Erkorkmaz K. Accurate tracking controller design for high-speed drives. Int J Mach Tool Manu. 2007;47:1393-400.

[61] Priestley MN, Seible F, Calvi GM. Seismic design and retrofit of bridges: John Wiley & Sons; 1996.

[62] Li C, Bi K, Hao H, Zhang X, Van Tin D. Cyclic test and numerical study of precast segmental concrete columns with BFRP and TEED. Bull Earthq Eng. 2019;17:3475-94.

[63] Li J, Liu S, Zhao M, Teng B. Experimental investigation of the hydrodynamic characteristics of heave plates using forced oscillation. Ocean Eng. 2013;66:82-91.

[64] Liang H, Liu K, Li L, Ou J. Dynamic Performance Analysis of the Tuned Heave Plate System for Semi-Submersible Platform. China Ocean Eng. 2018;32:422-30.

[65] Haftka RT, Adelman HM. Recent developments in structural sensitivity analysis. Structural Optimization. 1989;1:137-51.

CHAPTER 6 WAVE FLUME TESTS OF SSP WITH RID

Abstract[6]

Semi-submersible platform (SSP) primarily consisting of a deck, columns and pontoons, is a specialized marine vessel for multiple functions, e.g. oil extraction, wind power generation and fish farming, etc. During their service lives, SSPs may be subjected to excessive vibrations resulting from wave loads, which in turn could reduce the production efficiency, cause long-term fatigue problems and even catastrophic sinking of SSP. It is therefore necessary to suppress the excessive vibrations of SSP. In the past decades, some vibration control methods have been proposed and developed, such as the fixed heave plate (FHP) and tuned heave plate (THP). Recently, the authors proposed using inerter-based control device, i.e. rotational inertia dampers (RIDs), to control the vibrations of SSPs, and the control effectiveness has been demonstrated through analytical studies. To further investigate the feasibility and effectiveness of the proposed method, wave flume tests are conducted and reported in the present study. In particular, a 1:70 scaled SSP model was manufactured, and the vibration characteristics of the platform were determined firstly through free vibration tests. After that, the bare and RID equipped SSPs were tested under regular and irregular waves. For comparison, the SSP equipped with the commonly used FHP was also tested. The experimental results demonstrate that both the RID and FHP systems are effective in reducing the heave motion of SSP. However, compared to the FHP, the RID system showed a much better control performance by using a very small physical mass. The wave flume tests demonstrated the superior vibration control performances of RID on SSP.

6.1 Introduction

Marine energy plays a significant role in the global energy sector and has attracted increasing interest in the past few decades. To exploit the marine energy, various types of floating platforms have been designed and built, such as the tension leg platform (TLP), spar-type platform, and semi-submersible platform (SSP), etc. Among these platforms, SSP is most widely used due to its many merits, e.g. the larger deck area and bigger payload capacity. However, SSP may be subject to excessive motions especially heave motion due to its shallow draft and large pontoons, which could cause health and safety problems to operators, reduce the platform productivity and even endanger the structural safety. It is therefore imperative to effectively suppress the excessive vibrations of SSPs.

Extensive research efforts have been dedicated to suppressing the excessive motions of

[6] Ma R, Bi K, Hao H. Wave flume tests of a semi-submersible platform controlled by a novel rotational inertia damper. 2020. (Under review)

offshore platforms in the past few decades, and various vibration control methods have been developed. For SSPs, the heave motion is generally the most crucial, and the most commonly used control method is to rigidly install a fixed heave plate (FHP) to the bottom of a SSP, with the aim of increasing the added mass and damping of the platform. In this regard, Thiagarajan and Troesch [1] performed experimental studies to quantify the damping effect of the heave plate. It was found that both the drag coefficient and current-induced damping were doubled by introducing the heave plate. Downie et al. [2] conducted wave basin tests to investigate the control effectiveness of the perforated and solid heave plates in the vibration control of a truss spar. The results demonstrated that the large solid heave plates were generally more effective since they could generate larger added masses compared to the perforated ones. Tao and Dray [3] studied the performances of the solid and porous heave plates by the forced oscillation tests. It was shown that the solid plates produced higher damping at large Keulegan Carpenter (KC) number while the porous plates generated higher damping at very low KC number. Moreover, Tao et al. [4, 5] also numerically investigated the motion suppression of a spar with a heave plate. It was shown that the heave plate could result in significant damping effect, and its performance could be significantly affected by the geometry configurations, e.g. the aspect ratio and diameter ratio. Furthermore, Subbulakshmi and Sundaravadivelu [6] performed detailed parametric studies to investigate the heave damping of a spar-type wind turbine with single and two heave plates, and various parameters were considered, e.g. the scaling ratio, diameter ratio, and heave plate position to diameter of heave plate ratio, etc. They concluded that the heave damping increased with the increment of the scaling ratio and diameter ratio, and recommended the optimal ranges for other parameters to more effectively reduce heave motion.

Besides the conventional FHP system, tuned heave plate (THP) was also proposed to mitigate the SSP heave motion based on the concept of tuned mass damper (TMD), a well-known control system that has been widely applied to reduce the structural vibrations induced by many vibration sources such as wind, earthquake and wave [7-11]. Different from the rigid connection in the FHP system, the heave plate in the THP system is connected to SSP via a connection system, i.e. springs in parallel with dampers. With such a design, the vibration energy of SSP could be transferred to the THP system, and then dissipated. The control effectiveness of using the THP system in reducing the SSP motions has also been well verified through experimental and numerical studies [12-15]. Although both the FHP and THP systems were demonstrated effective, large heave plates are normally required for both systems. For example, as indicated in Ref. [4], the FHP extension was suggested at least four times of the heave amplitude of the SSP in order to realize the optimum damping effect. As for the THP system, it also needs a large heave plate to achieve a large mass ratio between the heave plate

and SSP, and thus attain a superior control performance [13]. However, a large heave plate would hinder the extensive applications of these control systems due to the increasing cost and installation difficulties.

The recently hot-debated inerter system might shed some light on reducing the secondary mass of the conventional FHP and THP systems due to its mass amplification effect. The inerter proposed by Smith [16] is a two-terminal mechanical element with the capability of generating a resisting force proportional to the relative acceleration between its two terminals. In practice, inerter can be realized via various means, such as rack-and-pinion [17], fluid [18-20] and ball-screw assembly [17, 21]. It was reported in previous studies (e.g. Ref. [22]) that an inerter could achieve an equivalent mass (i.e. inertance) several orders larger than its physical mass. Due to this significant mass amplification effect, inerters have been widely applied in the structural vibration control recently, and a number of inerter-based dynamic vibration absorbers (DVAs) have been proposed, such as tuned viscous mass damper (TVMD) [23, 24], tuned mass-damper-inerter (TMDI) [25-27], tuned inerter damper (TID) [28-30], electromagnetic inertial mass dampers (EIMD) [31, 32], and tuned tandem mass dampers-inerter (TTMDI) [33], etc. These inerter-based DVAs were generally demonstrated more effective than conventional TMDs in suppressing the structural vibrations induced by various loads, e.g. wind [34, 35], earthquake [36, 37], and vortex [38, 39], etc.

Very recently, inerter-based control systems were also introduced into the vibration control of offshore platforms subjected to wave or wind loads. In this regard, Hu et al. [40] demonstrated the control effectiveness of using inerter-based control systems in suppressing the vibrations of a floating offshore wind turbine (FOWT) subjected to wind and wave loads. Sarkar and Fitzgerald [41] investigated the effectiveness of using the TMDI in reducing the vibrations of FOWT, and good control performance was observed. Ma et al. [42] proposed an inerter-based DVA, namely tuned heave plate inerter (THPI), to mitigate the heave motion of SSP subjected to wave load. It was found that the THPI could further improve the control effectiveness by about 19% compared to the THP system. To further improve the control effectiveness, Ma et al. [43, 44] proposed another inerter-based system, namely a rotational inertia damper (RID), for the vibration control of SSP. Analytical studies showed that the RID system could provide a significant damping effect by amplifying the fluid resistance and realize the same or even better control effectiveness as compared to the FHP by using a much smaller physical mass. Experimental studies on the RID device itself were also carried out by Ma et al. [45], and the results demonstrated the mass amplification and damping effects of the device. Very recently, Ma et al. [46] further applied an inerter-based vibration isolation system (IVIS) to mitigate the heave motion of SSP. Analytical results showed that, by introducing a parallel-connected inerter, the reduction ratio of the receiving body (the top part of a SSP) could be further

improved by more than 23%.

The above literature review reveals that some research efforts have been made to control the excessive motions of offshore platforms. However, most previous studies focused on analytical (e.g. Ref. [40, 41]) or numerical (e.g. Ref. [4, 5]) investigations, and very limited experimental works [1-3] have been carried out. As an extension of the authors' previous studies [43-45], this paper aims to experimentally investigate the feasibility and control effectiveness of using RID system in reducing the heave motion of SSP. Wave flume tests were designed and performed in the present study. In particular, a 1:70 scaled SSP model was manufactured, and the vibration characteristics of the platform were determined firstly through free vibration tests. After that, the bare SSP and the SSP equipped with RID (SSP-RID) were tested under regular and irregular waves. For comparison, the SSP equipped with the commonly used FHP (SSP-FHP) was also tested. The remaining of this paper is organized as follows: Section 6.2 presents the experimental setup, which includes the description of the scaled model, mooring system, control devices, instrumentations and test programs; Section 6.3 introduces the experimental results. In particular, the heave motion responses of the SSP without control and controlled by the RID and FHP systems are reported; finally, the conclusions are drawn in Section 6.4.

6.2 Experimental Setup

Wave flume tests were performed in the nonlinear wave flume in the State Key Laboratory of Coastal and Offshore Engineering, Dalian University of Technology, P. R. China. Figure 6-1(a) shows a photo of the wave flume. The wave flume is 60 m long, 4 m wide and 2.5 m deep, and the maximum working depth is 2.0 m. A motor-driven piston-type wavemaker is equipped at one end of the flume, which is capable of generating regular and irregular waves. A beach made with plastic "horsehair" is fixed at the other end of the wave flume to absorb incoming waves. Considering the dimension of the wave flume and the dimension of the selected SSP, the geometric scaling ratio of SSP was set at 1:70, and the water depth was fixed to 1.40 m, which corresponds to a water depth of about 100 m at full-scale according to the Froude scaling law.

6.2.1 Scaled SSP Model

A typical SSP [47] consisting of one deck, two pontoons, four columns and four cross braces was selected as the objective SSP in this paper. The length, width and depth of the SSP are 114.07 m, 78.64 m and 38.6 m respectively, and its displacement (i.e. the total mass) is 48206.8 tonnes. An overview of the dimensions and properties of the platform are tabulated in Table 6-1. The dimensions of the model after scaling are also shown in the table. Figure 6-1(b) shows

the scaled SSP model in the wave flume. The model was made of steel and designed to be very stiff, which could be considered as a rigid body with six-degree-of-freedom (6-DOF) in the water. It should be noted that the scaled model was placed in the middle of the wave flume to reduce the impact of reflected waves during the tests, and the longer side of the platform was along the longitudinal direction of the flume. In addition, the incident angle of the wave was along the longitudinal direction of the flume. i.e. the incident angle of the wave to the platform was 0°.

Table 6-1 Specifications of the selected SSP

Parts	Terms	Prototype	Scaled model (1:70)
Platform	Length (mm)	114070	1630
	Width (mm)	78640	1123
	Height (mm)	38600	551
	Displacement (kg)	48206800	140.54
	Draft (mm)	19000	271.43
	Center of gravity from water surface (mm)	5800	82.86
Pontoons	Length (mm)	114070	1630
	Width (mm)	20120	287
	Height (mm)	8540	122
Columns	Length (mm)	21460	307
	Width (mm)	17385	248
	Height (mm)	17385	248
Deck	Length (mm)	77470	1107
	Width (mm)	74380	1063
	Height(mm)	8600	123
Braces	Diameter (mm)	1800	26

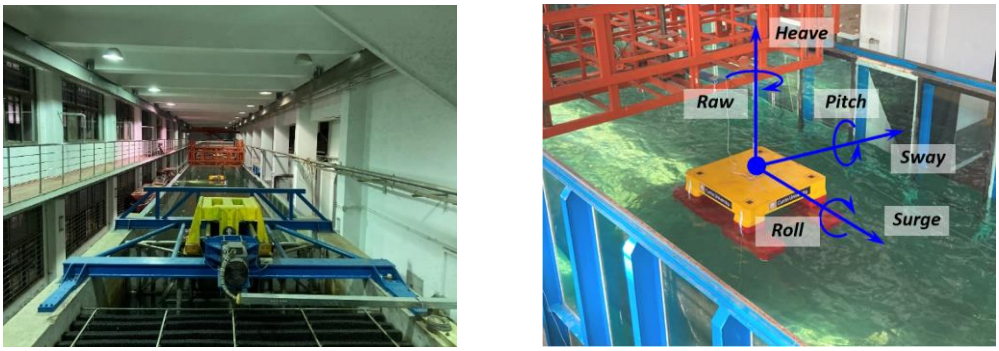

(a) Nonlinear wave flume (b) Scaled SSP with the DOFs

Figure 6-1 Scaled SSP in the wave flume

6.2.2 Mooring System

For the scaled model, a set of mooring system consisting of four steel wires with flexible

springs was adopted according to Ref. [47], with the aim of avoiding the SSP model drifting away during the tests. Table 6-2 summarizes the properties of the mooring system in the prototype and the scaled model, and Figure 6-2 shows the schematic layout. As shown in Figure 6-2(a), these mooring lines were positioned almost 90° apart. Each of them firstly passed through a V-shape fixed pulley mounted at the anchor point, and then connected to a spring, a load cell and a tensioner that was fixed to a rigid steel frame as shown in Figure 6-2(b). Specifically, the flexible springs were utilized to represent the stiffness of the mooring lines; the tensioners were installed to (slightly) adjust the initial length (i.e. the initial force) of the mooring lines when necessary; the load cells were deployed to measure the forces in the mooring lines, which will be presented in Section 6.2.4.

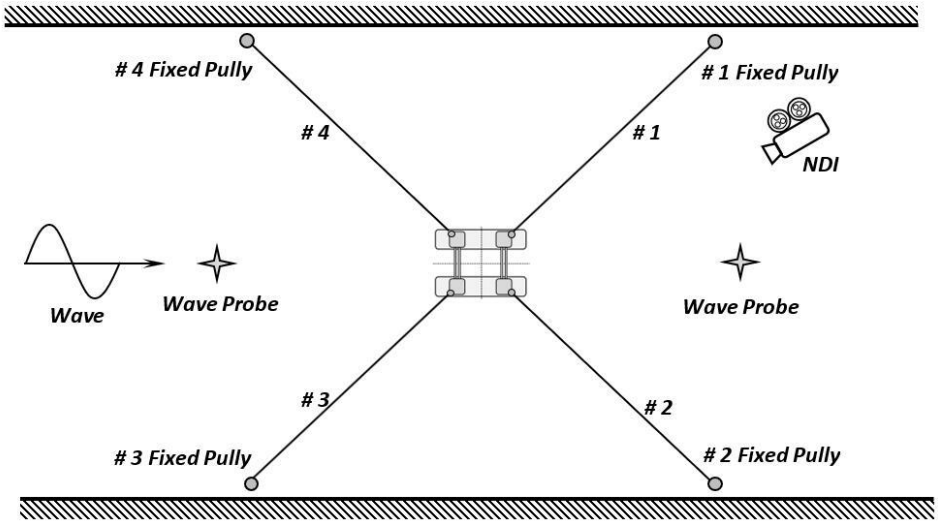

(a) Plan view

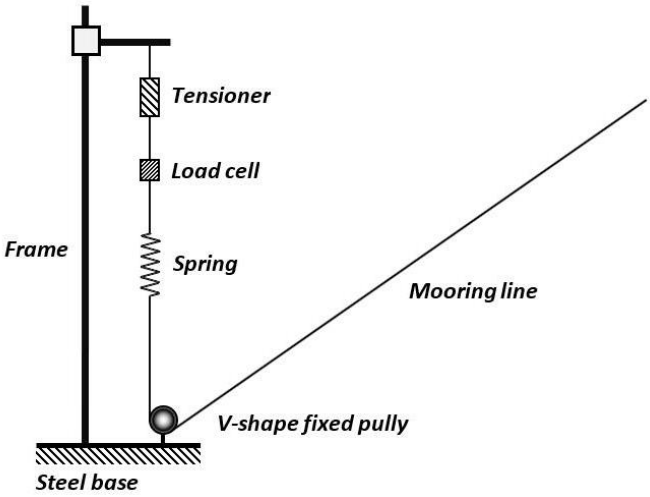

(b) Elevation view

Figure 6-2 Schematic layout of the designed mooring system

Table 6-2 Specifications of mooring lines

Terms	Diameter (m)	Length (m)	Net submerged weight (kg/m)	Spring stiffness (N/m)	Initial force (N)
Prototype	0.14	175	60.65	137000	2000000
Scaled model (1:70)	0.002	2.5	0.0124	28	5.83

6.2.3 RID and FHP

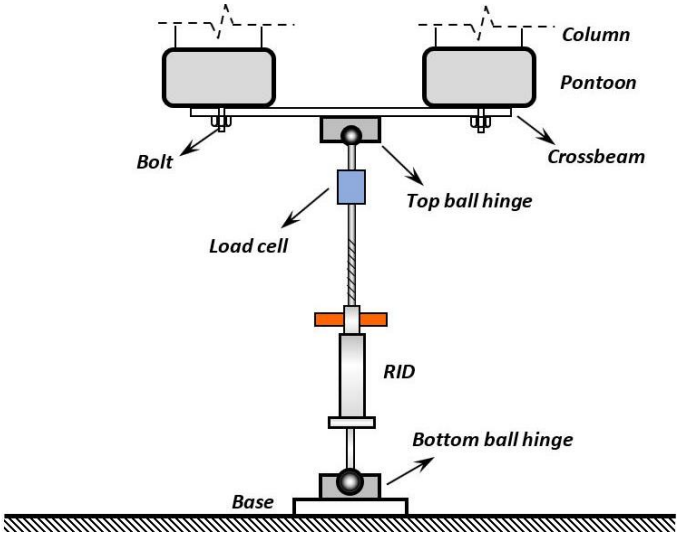

Figure 6-3 Schematic drawing of a SSP equipped with a RID

As indicated in the introduction, the primary objective of this paper is to experimentally investigate the control effectiveness of the RID and FHP systems in reducing the motions of the scaled SSP subjected to wave loads. It is well known that, compared to the other motions, the heave motion is generally most crucial and dominant the vibrations of a SSP since its natural period is the closest to the dominant period of the wave, which will also be demonstrated in Section 6.3.2. Given this fact, only the heave motion was of interest in the tests, and a single RID and a single FHP were mounted to the scaled model, respectively. A RID device similar to the one experimentally investigated by the authors in Ref. [45] was manufactured, and Table 6-3 lists the detailed specifications of the RID. In particular, a ball screw assembly made by the TBI MOTION (model No. SFV01210) was adopted to convert the linear motion to the rotations of two turning plates (see Figure 6-4(a)), and all components of the device were made of stainless steel to enhance corrosion resistance and durability. The outer diameter, length and stroke of the RID were 60 mm, 660 mm and $\pm$250 mm, respectively. The mass of the turning plates was 0.013 kg and the total mass of the RID was 3.3 kg. To make the RID effective, one end of the RID was fixed to the ground of the wave flume and the other end was fixed to the platform through the ball hinges at the two ends of the RID (Figure 6-3) as suggested in the authors' previous study [44]. It should be noted that, to avoid the possible eccentric load, the RID was installed in the middle of the platform through a cross beam as

shown in Figure 6-3. In addition, a waterproof load cell was attached to measure the resulted axial force. Figure 6-4 shows the on-site photos of the RID and the scaled model equipped with the RID.

As for the FHP, an aluminum alloy heave plate with a dimension of 0.4 m×0.4 m×0.01 m and a mass of 4.2 kg was manufactured, and Figure 6-5 and Figure 6-6 show the schematic drawing and on-site photos, respectively. As shown, the FHP system was placed under the platform and rigidly connected to the scaled model via a connecting rod. Similarly, the FHP system was also installed centrally through the cross beam. More detailed information about the FHP system can be found in Table 6-3.

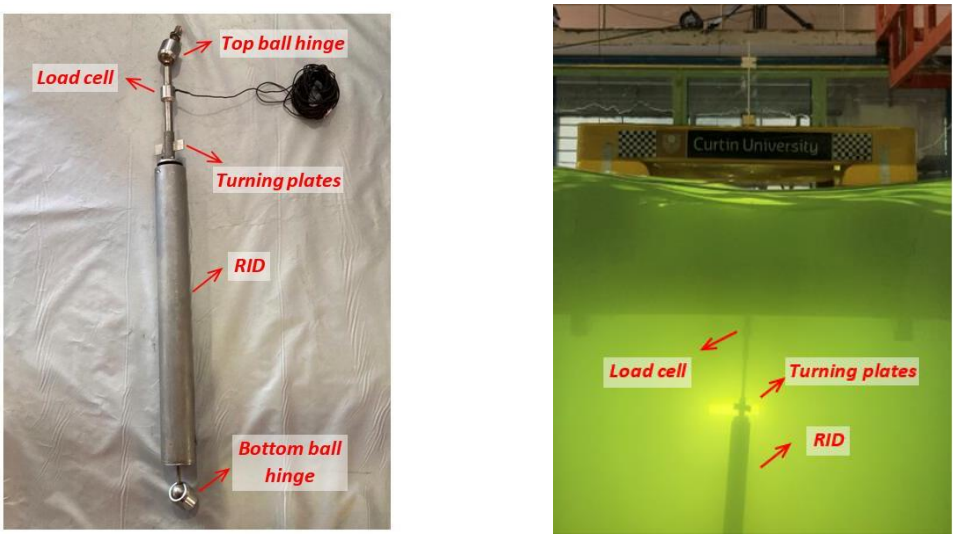

(a) RID (b) Scaled model equipped with the RID

Figure 6-4 On-site photos of the scaled model with RID

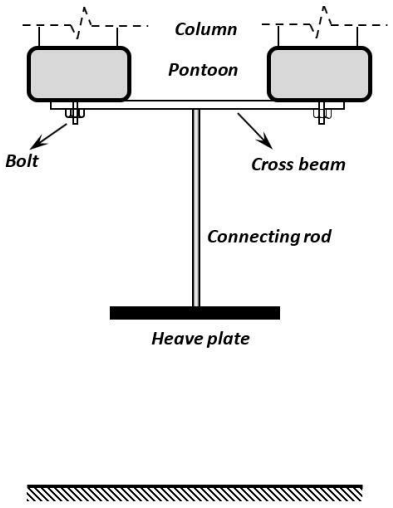

Figure 6-5 Schematic drawing of a SSP equipped with a FHP

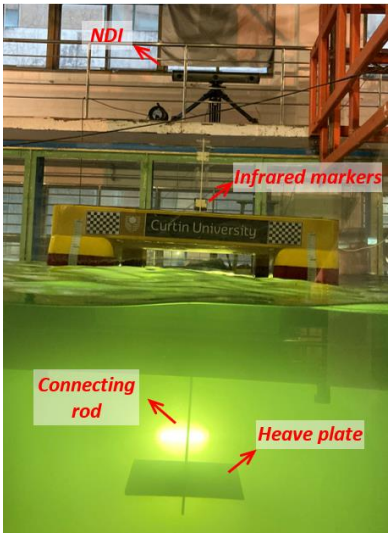

Figure 6-6 On-site photos of the scaled model with the FHP

Table 6-3 Specifications of the RID and FHP systems

Parts		Terms	Value
RID	Overall	Material	Stainless steel
		Length (mm)	660
		Outer diameter (mm)	60
		Weight (kg)	3.3
		Stroke (mm)	± 250
	Ball screw	Manufacturer	TBI Motion
		Model	SFV01210
		Diameter (mm)	12
		Lead (mm)	10
	Turning plates	Length (mm)	20
		Outer radius (mm)	30
		Inner radius (mm)	10
		Thickness (mm)	2
		Number	2
		Weight (kg)	0.013
FHP		Material	Aluminum alloy
		Length (mm)	400
		Width (mm)	400
		Thickness (mm)	10
		Weight (kg)	4.2
		Depth from water surface (mm)	714

6.2.4 Instrumentations

The instruments utilized in the wave flume tests are shown in Figure 6-2. Two wave probes were installed at the front and rear of the scaled model to measure wave elevation. Four load cells attached to the mooring lines were used to measure the tension forces of the mooring lines during the tests. Moreover, another load cell was utilized to measure the axial force when the SSP was equipped with the RID, as shown in Figure 6-4(b). These measured forces were collected and recorded by a data acquisition system. Furthermore, an optical motion capture system, namely NDI Optotrak Certus (see Figure 6-6), was utilized to measure the 6-DOF motions of the scaled model. This system was capable of precisely capturing the instantaneous positions of the SSP model by installing a planar rigid body with four infrared markers on the model (see Figure 6-6). All the measuring devices were calibrated before performing tests, and the acquisition frequency was set to 100 Hz.

6.2.5 Test Programs

In the present study, the wave flume tests were divided into four parts: (1) wave calibrations; (2) free vibration tests; (3) regular wave tests; and (4) irregular wave tests. In particular, the wave calibration tests were performed to ensure the accuracy of the generated waves, and the free vibration tests were applied to determine the natural periods of the scaled model.

In the regular wave tests, a total of 14 regular waves were considered with the scaled frequencies ranging from 0.837 rad/s to 7.530 rad/s. Table 6-4 gives the amplitudes and frequencies/periods of the full-scale and scaled regular waves. As shown, the amplitude of the scaled regular waves was taken to be 60 mm for R1-R9 and decreased to 30 mm when the excitation frequency was larger than 4.602 rad/s (i.e. R10-R14) due to the power limitation of the wavemaker.

Table 6-4 Amplitudes and periods of regular waves

No.	Full-scale waves			Scaled waves (1:70)		
	Amplitude (mm)	Frequency (rad/s)	Period (s)	Amplitude (mm)	Frequency (rad/s)	Period (s)
R1	4200	0.10	62.83	60	0.84	7.51
R2	4200	0.15	41.89	60	1.26	5.01
R3	4200	0.20	31.42	60	1.67	3.76
R4	4200	0.25	25.13	60	2.09	3.00
R5	4200	0.30	20.94	60	2.51	2.50
R6	4200	0.35	17.95	60	2.93	2.15
R7	4200	0.40	15.71	60	3.35	1.88
R8	4200	0.45	13.96	60	3.77	1.67
R9	4200	0.50	12.57	60	4.18	1.50
R10	2100	0.55	11.42	30	4.60	1.37
R11	2100	0.60	10.47	30	5.02	1.25
R12	2100	0.70	8.98	30	5.86	1.07
R13	2100	0.80	7.85	30	6.69	0.94
R14	2100	0.90	6.98	30	7.53	0.83

In the irregular wave tests, two irregular waves listed in Table 6-5 were considered, which correspond to the waves in the South China Sea (IR1) and the Gulf of Mexico (IR2) respectively with a one-year return period. The irregular waves were simulated based on the Joint North Sea Wave Project (JONSWAP) spectrum defined as follows [48]

$$S(\omega) = a^* H_s^2 \frac{\omega^{-5}}{\omega_0^{-4}} \exp\left[-1.25(\omega/\omega_0)^{-4}\right] \gamma_w^{\exp\left[-\frac{(\omega-\omega_0)^2}{2\tau^2\omega_0^2}\right]} \tag{6.1}$$

in which $S(\omega)$ is the power spectral density (PSD) function of the JONSWAP spectrum, H_s is

the significant wave height and ω_0 is the wave peak frequency which can be calculated based on T_0 tabulated in Table 6-5, ω is the wave frequency, and

$$a^* = \frac{0.0624}{0.230 + 0.0336\gamma_w - 0.185(1.9 + \gamma_w)^{-1}} \tag{6.2}$$

where γ_w is the peakedness factor with an average value of 3.3 [49]; τ is the shape parameter and it equals to 0.07 when $\omega \leq \omega_0$ and 0.09 when $\omega > \omega_0$ [49].

The duration of each irregular wave was 1260s, which corresponds to about 3 hours at the full scale. Meanwhile, each irregular wave was further divided into seven sub-waves with a duration of 180s to reduce the influence of reflected waves during the tests. In other words, each irregular wave included seven 180s sub-waves that were all compatible with the given JONSWAP spectra. In addition, the water surface was waited to be calm before the subsequent test to avoid the influence from the prior test.

Table 6-5 Significant heights and peak periods of irregular waves

No.	Full-scale waves		Scaled waves (1:70)	
	Significant height (m)	Peak Period (s)	Significant height (mm)	Peak Period (s)
IR1	6.00	11.2	85.70	1.33
IR2	3.96	9	56.57	1.08

6.3 Experimental Results and Discussions

6.3.1 Wave Calibrations

In practice, certain discrepancies unavoidably exist between the theoretical and actually generated waves. To evaluate the quality of the generated waves, calibrations were performed for the regular and irregular waves. Notably, the wave calibration tests were conducted in the absence of the SSP model.

6.3.1.1 Regular Waves

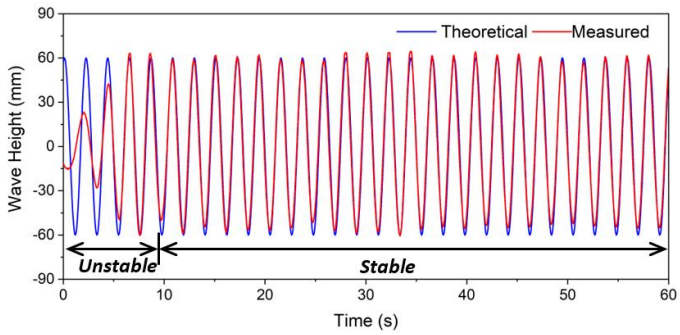

(a) R6

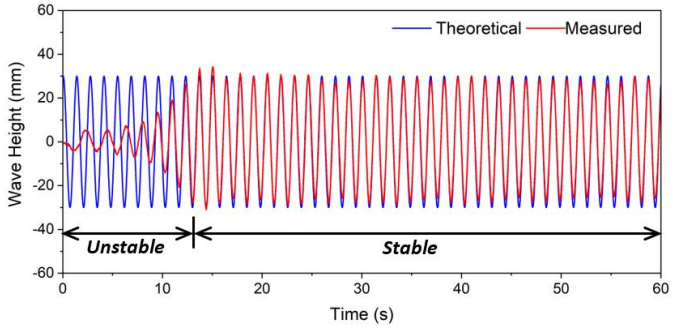

(b) R10

Figure 6-7 Theoretical and measured wave elevation time histories of regular waves

Table 6-6 Frequency and amplitude comparisons between theoretical and measured regular waves

No.	Theoretical waves		Measured waves			
	Amplitude (mm)	Frequency (rad/s)	Amplitude		Frequency	
			Value (mm)	Difference (%)	Value (rad/s)	Difference (%)
R1	60	0.84	56.59	5.69	0.84	0.00
R2	60	1.26	66.10	10.16	1.25	0.56
R3	60	1.67	62.96	4.94	1.68	0.12
R4	60	2.09	59.38	1.03	2.09	0.10
R5	60	2.51	48.39	19.35	2.51	0.04
R6	60	2.93	56.50	5.84	2.93	0.00
R7	60	3.35	54.11	9.82	3.35	0.06
R8	60	3.77	60.34	0.56	3.76	0.08
R9	60	4.18	56.15	6.41	4.18	0.05
R10	30	4.60	26.69	11.02	4.60	0.04
R11	30	5.02	30.62	2.06	5.02	0.06
R12	30	5.86	29.10	3.00	5.85	0.10
R13	30	6.69	29.30	2.35	6.69	0.07
R14	30	7.53	30.78	2.59	7.52	0.11

Two regular waves, i.e. R6 and R10, are taken out as examples to illustrate the quality of the generated regular waves. Figure 6-7 shows the theoretical and measured wave elevation time histories of the two regular waves. It should be noted that the measured wave elevation time histories include two parts, i.e. unstable and stable responses (see Figure 6-7), only the stable response would be utilized in the following analyses. Generally speaking, despite some minor discrepancies, very good repeatability was observed in the stable range between the theoretical and measured waves in terms of amplitudes and periods. Table 6-6 compares the frequencies and amplitudes of all the regular wave cases, and the corresponding differences are also tabulated in the table. It can be seen that most of the amplitude differences were less than 10% except R2, R5 and R10, and all the frequency differences were less than 0.56%, which

demonstrate the good quality of the regular waves. In addition, it is worth mentioning that the relatively large discrepancies in R2, R5 and R10 do not influence the response amplitude operators (RAOs) in Section 6.3.3 since the measured amplitude rather than the theoretical amplitude of the regular waves will be utilized in the calculation.

6.3.1.2 Irregular Waves

Figure 6-8 illustrates the wave elevation time histories of irregular waves IR1-1 and IR2-1, and Table 6-7 compares the statistics of the theoretical and all the measured irregular waves. Notably, the name "$IRi-j$" (i=1, 2 and j=1, 2, 3, 4, 5, 6, 7) denotes the j^{th} sub-wave of the i^{th} irregular wave. To quantify the quality of the irregular waves, the significant wave height $H_{1/3}$ and significant wave period $T_{1/3}$ of the measured irregular waves are calculated as follows:

$$H_{1/3} = \frac{1}{N/3}\sum_{i=1}^{N/3} H_i \tag{6.3}$$

$$T_{1/3} = \frac{1}{N/3}\sum_{i=1}^{N/3} T_i \tag{6.4}$$

in which N is the number of waves in the record; H_i is a series of wave height ranked from the highest to the lowest; T_i is the wave period corresponding to the i^{th} wave height H_i. For the theoretical values, they are tabulated in Table 6-5 as discussed above.

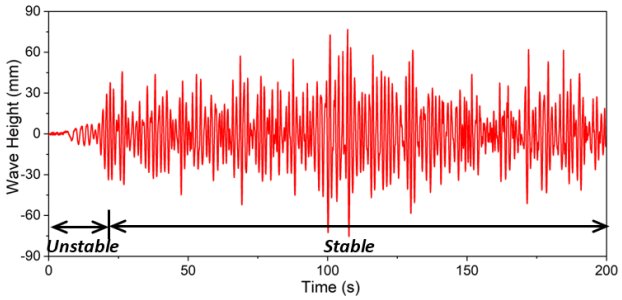

(a) IR1-1

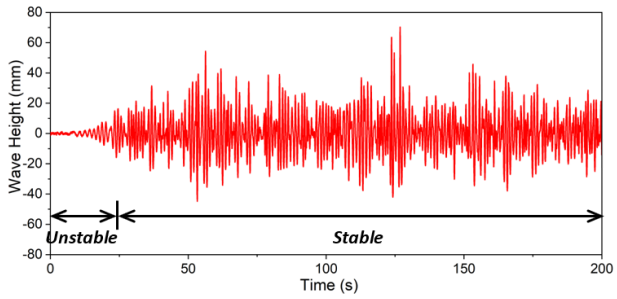

(b) IR2-1

Figure 6-8 Measured wave elevation time histories of irregular waves

Table 6-7 summarizes the significant wave height and significant wave period of all the 7 sub-

waves of each irregular wave, and the corresponding differences are also listed in the table. It can be seen that the differences of the significant wave height and significant wave period for IR1 were less than 7.47% and 1.35%, respectively. As for IR2, the differences of the significant wave height and significant wave period were less than 3.39% and 3.89%, respectively. Figure 6-9 shows the comparison between the theoretical (Equation (6.1)) and measured wave spectra. Similarly, good agreements are obtained as well. The above comparisons demonstrate the good quality of the generated irregular waves.

Table 6-7 Statistics of the theoretical and measured irregular waves

No.		Theoretical waves		Measured waves			
		Significant height H_s (mm)	Peak Period T_0 (s)	$H_{1/3}$		$T_{1/3}$	
				Value (mm)	Difference (%)	Value (s)	Difference (%)
IR1	1	85.70	1.33	79.29	7.47	1.33	0.15
	2			85.55	0.18	1.31	1.28
	3			81.17	5.29	1.31	1.20
	4			81.08	5.39	1.35	1.13
	5			82.64	3.57	1.35	1.35
	6			82.00	4.31	1.32	0.60
	7			83.86	2.15	1.34	1.05
IR2	1	56.57	1.08	58.49	3.39	1.08	0.28
	2			58.33	3.12	1.07	1.20
	3			55.88	1.23	1.05	2.59
	4			56.98	0.72	1.06	1.76
	5			54.82	3.10	1.06	1.76
	6			57.49	1.62	1.06	2.04
	7			58.04	2.59	1.04	3.89

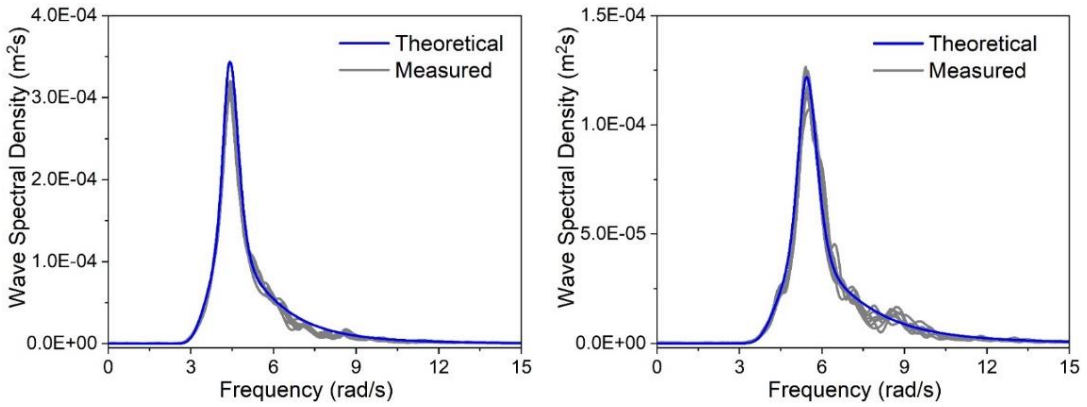

(a) IR1 (b) IR2

Figure 6-9 Theoretical and measured wave spectra

6.3.2 Free Vibration Tests

Table 6-8 Initial forces in the four mooring lines

Terms	Line 1	Line 2	Line 3	Line 4
Initial Force (N)	5.52	5.42	5.08	5.61
Difference (%)	5.33	7.04	12.84	3.77

As calculated in Table 6-2, when the SSP is in the original (balanced) position, the initial force in each mooring line should be 5.83 N. Before the free vibration test, the initial forces in the mooring lines were measured, and Table 6-8 lists the results. As shown, the measured initial forces were 5.52, 5.42, 5.08 and 5.61 N for Lines 1, 2, 3 and 4 respectively, which were slightly smaller than the theoretical value with a maximum difference of 12.84%. These discrepancies might be caused by the following facts that (1) the four mooring lines were not exactly symmetrical (see Figure 6-2(a)); and (2) the stiffness of the springs could not be exactly the same (Figure 6-2(b)). Since the aim of the present study is to investigate the effectiveness of applying different control systems for SSP heave motion mitigation, and the influence of these discrepancies does not affect the evaluation of the control effectiveness, therefore no further action was made to adjust the initial mooring line forces.

The free vibration tests were then carried out in the calm water to determine the natural periods of the scaled SSP in the six directions (see Figure 6-1(b)). In particular, the scaled model was applied a displacement/angle at a specific DOF and then released suddenly to let SSP oscillate freely. The motion time histories of free oscillations were captured by NDI, and the fast Fourier transform (FFT) technique was then utilized to identify the natural periods. The identified natural period of the SSP model is 14.90s for surge, 3.03s for roll, 16.38s for sway, 3.15s for pitch, 2.60s for heave, and 15.98s for raw. After scaling, the heave natural period of the prototype is 21.79s, which is close to the ocean wave period band normally ranging from 5s to 20s [50]. This fact indicates that the heave motion is most crucial for this platform, which is also the reason why the heave motion mitigation is of interest in this paper.

6.3.3 Regular Wave Tests

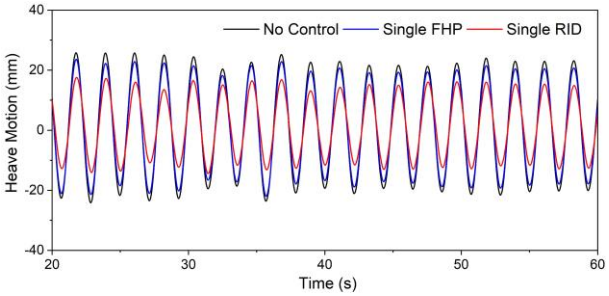

(a) R6

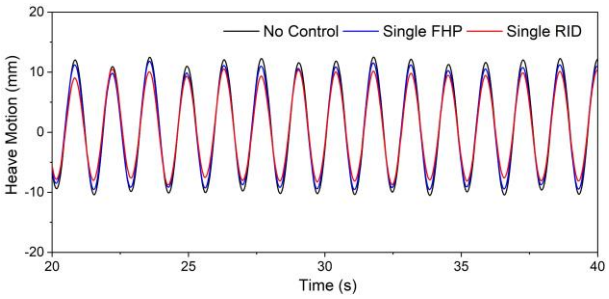

(b) R10

Figure 6-10 Heave motion time histories of the scaled model without and with different control systems under regular waves

Regular wave tests were performed to evaluate the control effectiveness of the RID and FHP systems in reducing the heave motion of the SSP model under regular waves. For comparison, the bare SSP (i.e. the SSP model without control) was also tested. Figure 6-10 shows the results when the SSP model was subjected to regular waves R6 and R10. As shown, both the RID and FHP systems were effective in reducing the heave motion of the SSP, and the RID system was more effective. In particular, the peak heave motions of the bare SSP, SSP-RID and SSP-FHP were respectively 22.49 mm, 14.29 mm and 19.91 mm for R6. As for R10, the peak heave motion of the bare SSP was 11.33 mm, which was reduced to 9.25 mm and 10.30 mm by introducing the RID and FHP systems, respectively. In other words, compared to the bare SSP, the reduction ratios for the RID and FHP systems were 36.5% and 11.5% respectively in Case R6, and 18.4% and 9.1% respectively for Case R10.

For floating platforms, the response amplitude operator (RAO) is commonly used to evaluate the behaviors of platform, which is defined as:

$$RAO(\omega) = \frac{a}{\xi_a} \tag{6.5}$$

in which a is the motion amplitude and ξ_a is the wave amplitude at a specific wave incident frequency ω. It should be noted that, the amplitude of the wave was not stable at the beginning (see Figure 6-7), the RAO values are determined when a and ξ_a reached the steady range of the time histories as mentioned above.

Figure 6-11 shows the heave RAO curves of the scaled model without and with different control systems. As shown in Table 6-4, the excitation frequencies of the regular waves varied from 0.84 rad/s to 7.53 rad/s, and as obtained in the free vibration tests the natural frequency of the bare SSP model in the heave direction was 2.41 rad/s, which is shown by the black dashed line in this figure. It can be seen from Figure 6-11 that, for the bare SSP, an obvious peak occurred at 2.09 rad/s due to the fact that this excitation frequency was close to the natural vibration frequency of the SSP (2.41 rad/s), and resonance occurred. In the pre-peak region (i.e. 0.84 rad/s-2.09 rad/s), the RAO values increased with the increment of the excitation

frequency and tended to be unity at very low excitation frequencies. In the post-peak region (i.e. 2.09 rad/s-7.53 rad/s), the RAO values decreased obviously especially in the range that is around the natural frequency of the SSP. It should be noted that another wave with the excitation frequency very close to the natural frequency of the SSP was also tested (2.51 rad/s in Case R5). Though this frequency was even closer to 2.41 rad/s compared to Case R4 (with the excitation frequency of 2.09 rad/s), the peak RAO value however did not occur in this case. This is because as numerically demonstrated by the authors [46], the RAO curve varies sharply around the natural frequency of the SSP, namely very significant change occurs within a very narrow excitation frequency range. It is believed that even larger RAO value could be obtained if the SSP was excited by a wave with the frequency between 2.09 rad/s (Case R4) and 2.41 rad/s, and the excitation frequency is closer to 2.41 rad/s, the larger RAO value would be obtained.

Figure 6-11 also shows that, for the SSP-FHP system, an obvious peak was also observed at 2.09 rad/s, which was caused by the resonance in the heave direction. By introducing the FHP system, the heave RAOs were slightly reduced when the wave excitation frequency was larger than 2.09 rad/s. It should be noted that, as mentioned above, the ocean wave period band normally ranges from 5s to 20s, which corresponds to 2.63 rad/s to 10.51 rad/s for the scaled model (which is displayed by the grey shaded area in the figure). In other words, the experimental results showed that the heave motion could be generally mitigated within the normal wave excitation range. However, it is also found that the heave RAOs of the SSP-FHP system were slightly increased in the pre-peak region. This is because the FHP system increased the total mass and thus reduced the natural frequency of the scaled model, which in turn amplified the RAOs in the pre-peak region.

Figure 6-11 also displays the RAO curve of the scaled SSP with the RID system. It should be noted that the data for Cases R1 and R2 are not available because the motions of SSP exceeded the maximum stroke of RID (i.e. $\pm$250 mm in Table 6-3) under these two regular waves. It is found that, when RID was applied, the heave motion could be obviously mitigated especially when the excitation frequency was relatively small (smaller than 5 rad/s as shown), and the RID system was more effective compared to the FHP system. The superior control effectiveness of RID was attributed to its superior energy dissipation capacity. To illustrate this effect, Figure 6-12 shows the hysteretic curves of the RID under regular waves R6 and R10. As shown, obvious negative slopes exhibited in the hysteretic loops, which were due to the negative stiffness effect of RID. It is also found that the hysteretic loops roughly showed an inclined elliptical shape with large enclosed areas, which demonstrates that the RID possessed a good capacity of dissipating vibration energy. In addition, a lot of fluctuations were observed in the hysteresis curves. As indicated in Ref. [45], these fluctuations could be

caused by various factors, e.g. the noise, disturbance of surrounding flow field, and torque ripples of the ball screw. It should be noted that the hysteretic curves shown in Figure 6-12 are not the accurate hysteretic curves of the RID: the axial displacement of the RID in the figure is not the accurate axial displacement of the RID, which is influenced by all the DOFs of the SSP and thus difficult to be obtained; In the figure, the heave motion of the SSP is directly used as the axial displacement of the RID, namely the influences from the other DOFs are ignored. This simplification will bring some inaccuracies, but is deemed acceptable since the SSP responses were governed by the heave motion.

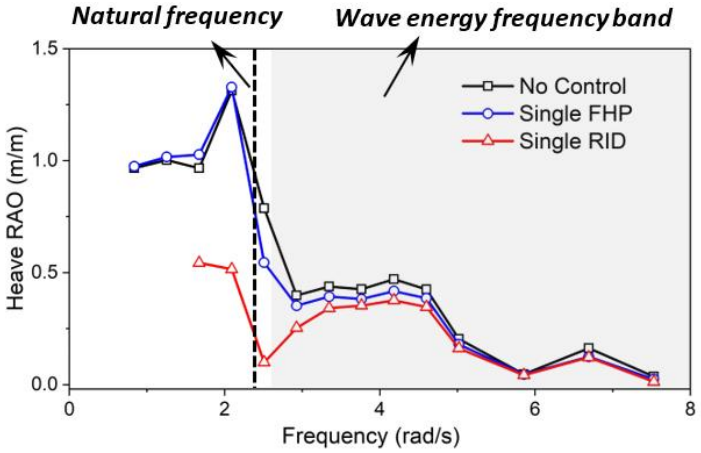

Figure 6-11 Heave RAO curves of the scaled model without and with different control systems

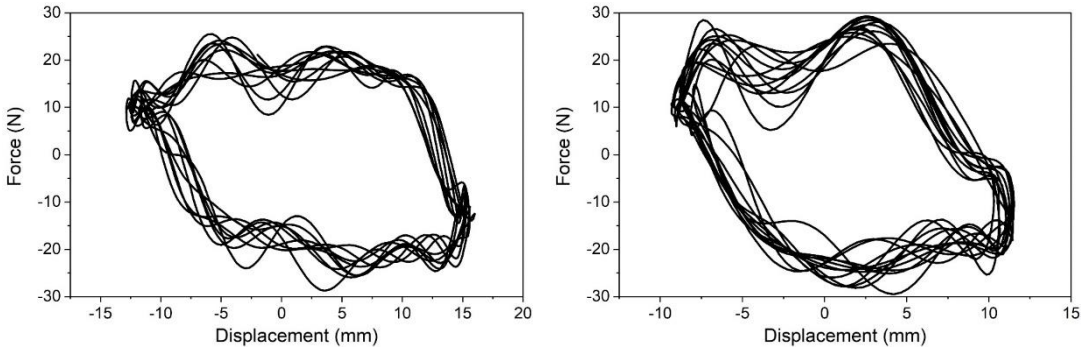

(a) R6 (b) R10

Figure 6-12 Hysteretic curves of the RID under regular waves

6.3.4 Irregular Wave Tests

In this subsection, the control effectiveness of the RID and FHP systems under irregular waves are investigated. Similarly, the bare SSP model was also tested for comparison. Figure 6-13 and Figure 6-14 show the example heave motion time histories of the scaled model without and with different control systems under irregular waves IR1 and IR2, respectively. It should be noted that only the first and second sub-waves of each irregular wave are taken out for illustration, for the other sub-waves, similar trends were observed.

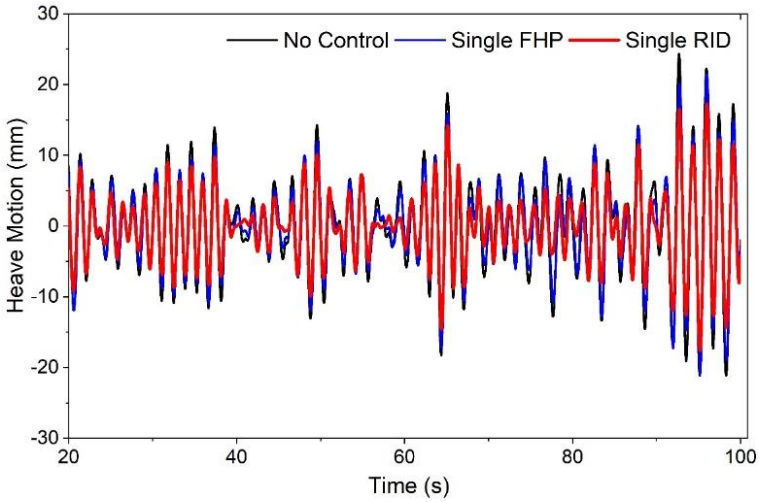

(a) IR1-1

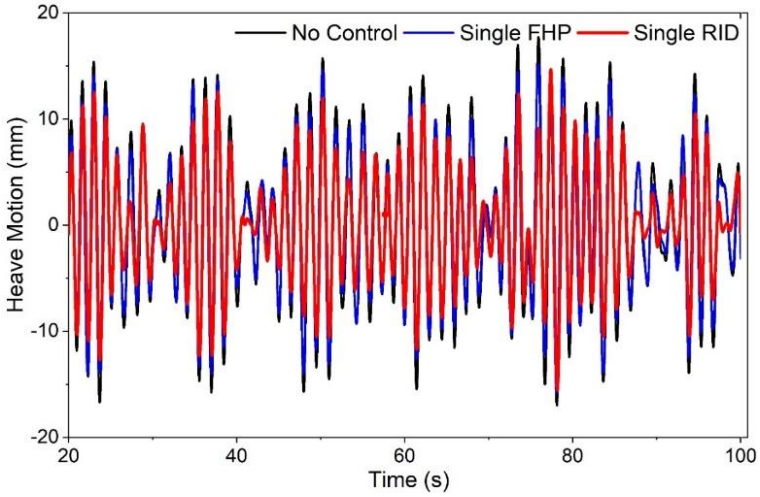

(b) IR1-2

Figure 6-13 Example heave motion time histories of the scaled model without and with different control systems under irregular waves IR1

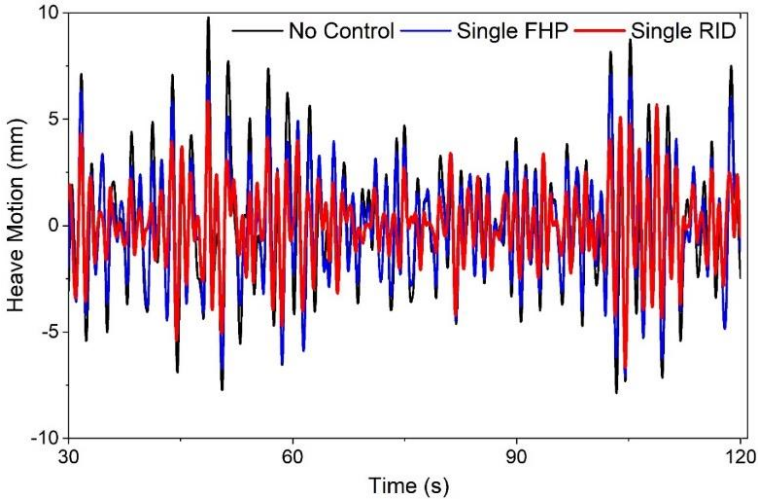

(a) IR2-1

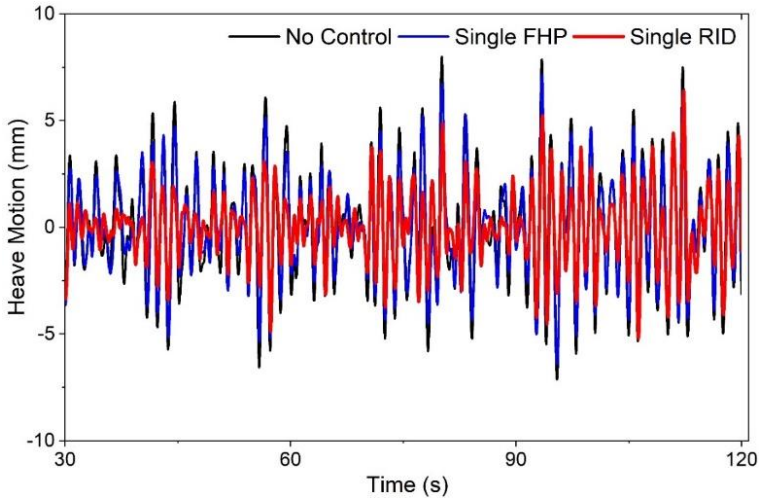

(b) IR2-2

Figure 6-14 Example heave motion time histories of the scaled model without and with different control systems under irregular waves IR2

As shown in the figures, both the RID and FHP systems could suppress the heave motion of the SSP, and the RID system was more effective. To quantitatively evaluate the control effectiveness, besides the maximum heave motion, the heave motion standard deviation (σ) is also calculated:

$$\sigma = \sqrt{\frac{\sum(Z_i - \mu)^2}{N}} \tag{6.6}$$

in which Z_i is the recorded heave motion; N is the number of data points; μ is the mean of Z_i (i=1, 2, 3,⋯, N). Table 6-9 and Table 6-10 tabulate the results and the corresponding reduction ratios are also calculated and summarized in the tables, in which ψ_max is the reduction ratio for the maximum response, and ψ_σ corresponds to the reduction ratio for the standard deviation. In addition, to minimize the influence of the unstable waves (see Figure 6-8), the steady responses with duration of 180s were extracted for the statistical results of each sub-wave.

The statistical results of the SSP model without and with different control systems under IR1 are listed in Table 6-9. It can be seen that both the maximum response and standard deviation under each sub-wave could be suppressed by using the RID or FHP system, and the RID system performed better under all the sub-waves. In particular, the average value of the maximum responses of the bare SSP was 25.52 mm, which was reduced to 20.10 mm and 23.07 mm by introducing the RID and FHP systems, respectively. The corresponding average reduction ratios were 21.24% and 9.60%, respectively. For the standard deviation, the average reduction ratios of the RID and FHP systems were 27.07% and 10.69%, respectively. Similar results are shown in Table 6-10, which tabulates the results when the SSPs were subjected to

IR2. It can be seen that, in average, when the FHP was installed, the maximum response and standard deviation of the heave motion could be reduced by 14.45% and 11.74%, respectively. When the RID was installed, the corresponding results were 28.27% and 38.72%, respectively. The above results clearly demonstrate the control effectiveness of the RID system in reducing the heave motion of the SSP.

Table 6-9 Statistics of the scaled model without and with different control systems under IR1

Systems	Terms	Sub-wave No.							Average
		1	2	3	4	5	6	7	
No Control	Max (mm)	25.71	26.27	23.03	27.02	26.55	22.86	27.19	25.52
	σ (mm)	7.53	7.50	7.47	7.28	7.43	7.39	7.30	7.41
FHP	Max (mm)	23.83	25.69	20.14	23.59	24.00	20.40	23.86	23.07
	σ (mm)	6.66	6.68	6.71	6.48	6.62	6.63	6.56	6.62
	ψ_Max (%)	7.31	2.21	12.55	12.69	9.60	10.76	12.25	9.60
	ψ_σ (%)	11.45	10.95	10.22	11.04	10.87	10.20	10.11	10.69
RID	Max (mm)	20.43	21.74	18.83	20.99	21.85	16.66	20.18	20.10
	σ (mm)	5.55	5.49	5.29	5.29	5.52	5.34	5.36	5.41
	ψ_Max (%)	20.54	17.24	18.24	22.32	17.70	27.12	25.78	21.24
	ψ_σ (%)	26.29	26.74	29.15	27.33	25.73	27.72	26.53	27.07

Table 6-10 Statistics of the scaled model without and with different control systems under IR2

Systems	Terms	Sub-wave No.							Average
		1	2	3	4	5	6	7	
No Control	Max (mm)	9.78	7.98	8.95	9.53	7.99	11.22	10.43	9.41
	σ (mm)	2.87	2.60	2.56	2.62	2.57	2.75	2.74	2.67
FHP	Max (mm)	8.26	7.14	6.89	9.03	7.46	8.89	8.71	8.05
	σ (mm)	2.50	2.28	2.23	2.34	2.32	2.42	2.42	2.36
	ψ_Max (%)	15.54	10.53	23.02	5.25	6.63	20.77	16.49	14.45
	ψ_σ (%)	13.05	12.28	12.80	10.71	9.95	11.94	11.44	11.74
RID	Max (mm)	6.39	6.39	6.90	8.33	5.75	7.31	6.15	6.75
	σ (mm)	1.68	1.63	1.64	1.68	1.74	1.70	1.39	1.64
	ψ_Max (%)	34.66	19.92	22.91	12.59	28.04	34.85	41.04	28.27
	ψ_σ (%)	41.51	37.48	36.03	35.95	32.39	38.34	49.32	38.72

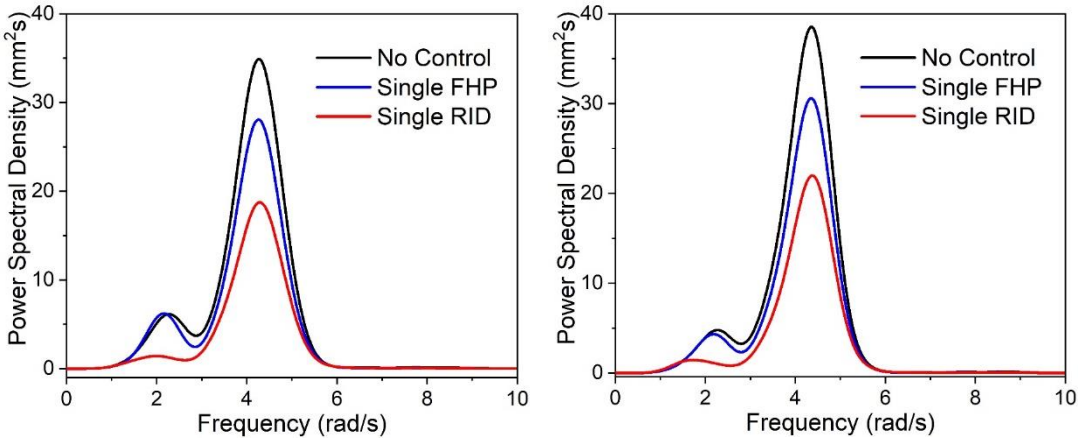

(a) IR1-1 (b) IR1-2

Figure 6-15 Heave motion PSDs of the scaled model without and with different control systems under irregular waves IR1

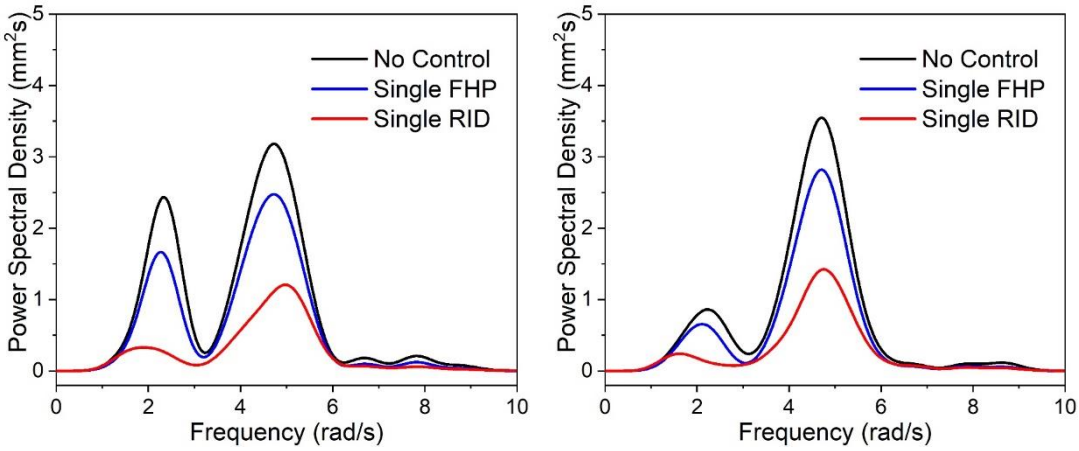

(a) IR2-1 (b) IR2-2

Figure 6-16 Heave motion PSDs of the scaled model without and with different control systems under irregular waves IR2

To further investigate the control effectiveness, Figure 6-15 and Figure 6-16 present the heave motion PSDs of the scaled model without and with different control systems under irregular waves IR1 and IR2, respectively. In general, similar to the time-domain results shown in Figure 6-13 and Figure 6-14, both the RID and FHP systems could reduce the heave motion PSD of the SSP model, and the control effectiveness of the RID system was more significant. For the bare SSP model, the PSD curve showed a two-peak characteristic. The first peak occurred around 2.4 rad/s, which corresponds to the natural frequency of the scaled model in the heave direction. As for the second peak, it was caused by the dominant frequency of the wave (see Figure 6-9) and obviously higher than the first one. This fact indicates that the heave motion of the SSP mainly came from the rigid-body motion induced by the waves rather than the resonance of the SSP. Similar results were found in Ref. [51]. By introducing the control systems especially the RID system, both the two peaks of PSD curves were significantly

suppressed, which demonstrates the control effectiveness of the RID and FHP systems. Moreover, it is also found that the first peak of PSD curve moved leftward after installing the control systems. This means that the natural frequency of the scaled model in the heave direction was reduced by both the RID and FHP systems. However, the working mechanisms of these two control systems are different. Specifically speaking, the FHP system increased the effective mass and thus decreased the natural frequency of the scaled model. As for the RID system, it decreased the natural frequency of the SSP mainly due to its negative stiffness effect, as observed in Figure 6-12. Different from the positive stiffness provided by springs, the negative stiffness produced by the RID could reduce the global stiffness, and thus decrease the natural frequency of the SSP. Furthermore, it is worth mentioning again that the physical mass of turning plates was only 0.013 kg in the tests. This fact demonstrates that the RID system could achieve good control performance by using turning plates with very small physical mass, which is consistent with the finding obtained in the previous analytical studies [43, 44].

6.4 Conclusions

This paper presented the wave flume tests of a SSP subjected to the wave load, with the aim of demonstrating the feasibility and control effectiveness of the RID and FHP systems in reducing the SSP heave motion. A 1:70 scaled SSP model was manufactured, and the vibration characteristics of the platform were determined firstly through free vibration tests. Then, the bare SSP, SSP-RID and SSP-FHP were tested under regular and irregular waves, respectively. Based on the experimental results, the following conclusions can be drawn:

(1) The RID system is feasible and effective in reducing the heave motion of SSP by using turning plates with very small physical mass, which provides an attractive alternative for the vibration control of offshore platforms.

(2) The conventional FHP system was effective in reducing the heave motion of SSP. For the regular waves, the heave RAOs in the normal wave excitation range were slightly reduced. As for the irregular waves, both the peak and standard deviation of the heave motion are mitigated, and the maximum reduction ratios of 14.45% for the maximum response and 11.74% for the standard deviation were realized.

(3) Compared to the FHP system, the RID system was more effective in reducing the heave motion of the SSP. For the regular waves, the heave RAOs are obviously reduced especially when the excitation frequency was relatively small. For the irregular waves, both the peak and standard deviation of the heave motion were mitigated more effectively, and the maximum reduction ratios of 28.27% for the

maximum response and 38.72% for the standard deviation were achieved.

6.5 References

[1] Thiagarajan K, Troesch AW. Effects of appendages and small currents on the hydrodynamic heave damping of TLP columns. J Offshore Mech Arct Eng. 1998:37-42.

[2] Downie M, Graham J, Hall C, Incecik A, Nygaard I. An experimental investigation of motion control devices for truss spars. Mar Struct. 2000;13:75-90.

[3] Tao L, Dray D. Hydrodynamic performance of solid and porous heave plates. Ocean Eng. 2008;35:1006-14.

[4] Tao L, Cai S. Heave motion suppression of a Spar with a heave plate. Ocean Eng. 2004;31:669-92.

[5] Tao L, Lim KY, Thiagarajan K. Heave response of classic spar with variable geometry. J Offshore Mech Arct Eng. 2004;126:90-5.

[6] Subbulakshmi A, Sundaravadivelu R. Heave damping of spar platform for offshore wind turbine with heave plate. Ocean Eng. 2016;121:24-36.

[7] Kaynia AM, Biggs JM, Veneziano D. Seismic effectiveness of tuned mass dampers. J Struct Div. 1981;107:1465-84.

[8] Jangid R. Optimum Multiple Tuned Mass Dampers for base-excited undamped system. Earthq Eng Struct D. 1999;28:1041-9.

[9] Bi K, Hao H. Using pipe-in-pipe systems for subsea pipeline vibration control. Eng Struct. 2016;109:75-84.

[10] Zuo H, Bi K, Hao H. Using multiple tuned mass dampers to control offshore wind turbine vibrations under multiple hazards. Eng Struct. 2017;141:303-15.

[11] Nikoo HM, Bi K, Hao H. Effectiveness of using pipe-in-pipe (PIP) concept to reduce vortex-induced vibrations (VIV): Three-dimensional two-way FSI analysis. Ocean Eng. 2018;148:263-76.

[12] Zhu H, Ou J, Zhai G. Conceptual design of a deep draft semi-submersible platform with a moveable heave-plate. J Ocean U China. 2012;11:7-12.

[13] Liu K, Ou J. A novel tuned heave plate system for heave motion suppression and energy harvesting on semi-submersible platforms. Sci China Technol Sci. 2016;59:897-912.

[14] Zhu H, Hu C, Liu Y. Optimum Design of a Passive Suspension System of a Semisubmersible for Pitching Reduction. J Dyn Syst Meas Control. 2016;138:121003.

[15] Liu K, Liang H, Ou J. Numerical investigation of a tuned heave plate energy-harvesting system of a semi-submersible platform. Energies. 2016;9:82.

[16] Smith MC. Synthesis of mechanical networks: the inerter. IEEE Trans Automat Contr. 2002;47:1648-62.

[17] Papageorgiou C, Houghton NE, Smith MC. Experimental testing and analysis of inerter devices. J Dyn Syst Meas Contr. 2009;131:011001.

[18] Wang FC, Hong MF, Lin TC. Designing and testing a hydraulic inerter. J Mech Eng Sci. 2010;225:66-72.

[19] Liu X, Jiang JZ, Titurus B, Harrison A. Model identification methodology for fluid-based inerters. Mech Syst Signal Process. 2018;106:479-94.

[20] De Domenico D, Deastra P, Ricciardi G, Sims ND, Wagg DJ. Novel fluid inerter based tuned mass dampers for optimised structural control of base-isolated buildings. J Franklin Inst. 2019;356:7626-49.

[21] Li C, Liang M, Wang Y, Dong Y. Vibration suppression using two-terminal flywheel. Part I: Modeling and characterization. J Vib Control. 2012;18:1096-105.

[22] Zhu H, Li Y, Shen W, Zhu S. Mechanical and energy-harvesting model for electromagnetic inertial mass dampers. Mech Syst Signal Process. 2019;120:203-20.

[23] Ikago K, Saito K, Inoue N. Seismic control of single-degree-of-freedom structure using tuned viscous mass damper. Earthq Eng Struct Dyn. 2012;41:453-74.

[24] Huang Z, Hua X, Chen Z, Niu H. Optimal design of TVMD with linear and nonlinear viscous damping for SDOF systems subjected to harmonic excitation. Struct Contorl Health Monit. 2019:e2413.

[25] Marian L, Giaralis A. Optimal design of a novel tuned mass-damper–inerter (TMDI) passive vibration control configuration for stochastically support-excited structural systems. Probabilistic Eng Mech. 2014;38:156-64.

[26] Pietrosanti D, De Angelis M, Basili M. Optimal design and performance evaluation of systems with Tuned Mass Damper Inerter (TMDI). Earthq Eng Struct Dyn. 2017;46:1367-88.

[27] Giaralis A, Taflanidis A. Optimal tuned mass-damper-inerter (TMDI) design for seismically excited MDOF structures with model uncertainties based on reliability criteria. Struct Contorl Health Monit. 2018;25:e2082.

[28] Lazar I, Neild S, Wagg D. Using an inerter-based device for structural vibration suppression. Earthq Eng Struct Dyn. 2014;43:1129-47.

[29] Lazar I, Neild S, Wagg D. Vibration suppression of cables using tuned inerter dampers. Eng Struct. 2016;122:62-71.

[30] Shen W, Niyitangamahoro A, Feng Z, Zhu H. Tuned inerter dampers for civil structures subjected to earthquake ground motions: optimum design and seismic performance. Eng Struct. 2019;198:109470.

[31] Nakamura Y, Fukukita A, Tamura K, Yamazaki I, Matsuoka T, Hiramoto K et al. Seismic response control using electromagnetic inertial mass dampers. Earthq Eng Struct Dyn. 2014;43:507-27.

[32] Li Y, Shen W, Zhu H. Vibration mitigation of stay cables using electromagnetic inertial mass dampers: Full-scale experiment and analysis. Eng Struct. 2019;200:109693.

[33] Cao L, Li C. Tuned tandem mass dampers-inerters with broadband high effectiveness for structures under white noise base excitations. Struct Contorl Health Monit. 2019:e2319.

[34] Giaralis A, Petrini F. Wind-Induced Vibration Mitigation in Tall Buildings Using the Tuned Mass-Damper-Inerter. J Struct Eng. 2017;143:04017127.

[35] Petrini F, Giaralis A, Wang Z. Optimal tuned mass-damper-inerter (TMDI) design in wind-excited tall buildings for occupants' comfort serviceability performance and energy harvesting. Eng Struct. 2020;204:109904.

[36] Zhang R, Zhao Z, Pan C. Influence of mechanical layout of inerter systems on seismic mitigation of storage tanks. Soil Dyn Earthq Eng. 2018;114:639-49.

[37] Zhang R, Zhao Z, Dai K. Seismic response mitigation of a wind turbine tower using a tuned parallel inerter mass system. Eng Struct. 2019;180:29-39.

[38] Xu K, Bi K, Han Q, Li X, Du X. Using tuned mass damper inerter to mitigate vortex-induced vibration of long-span bridges: Analytical study. Eng Struct. 2019;182:101-11.

[39] Xu K, Bi K, Ge Y, Zhao L, Han Q, Du X. Performance evaluation of inerter-based dampers for vortex-induced vibration control of long-span bridges: A comparative study. Struct Control Health Monit. 2020;27:e2529.

[40] Hu Y, Wang J, Chen MZQ, Li Z, Sun Y. Load mitigation for a barge-type floating offshore wind turbine via inerter-based passive structural control. Eng Struct. 2018;177:198-209.

[41] Sarkar S, Fitzgerald B. Vibration control of spar-type floating offshore wind turbine towers using a tuned mass-damper-inerter. Struct Control Health Monit. 2019;27:e2471.

[42] Ma R, Bi K, Hao H. Mitigation of heave response of semi-submersible platform (SSP) using tuned heave plate inerter (THPI). Eng Struct. 2018;177:357-73.

[43] Ma R, Bi K, Hao H. Using inerter-based control device to mitigate heave and pitch motions of semi-submersible platform in the shallow sea. Eng Struct. 2020;207:110248.

[44] Ma R, Bi K, Hao H. A novel rotational inertia damper for heave motion suppression of semisubmersible platform in the shallow sea. Struct Control Health Monit. 2019;26:e2368.

[45] Ma R, Bi K, Hao H. A novel rotational inertia damper for amplifying fluid resistance: Experiment and mechanical model. Mech Syst Signal Process. 2021;149:107313.

[46] Ma R, Bi K, Hao H. Heave motion mitigation of semi-submersible platform using inerter-based vibration isolation system (IVIS). Eng Struct. 2020;219:110833.

[47] Fan T, Qiao D, Yan J, Chen C, Ou J. Experimental verification of a semi-submersible platform with truncated mooring system based on static and damping equivalence. Ships Offshore Struct. 2017;12:1145-53.

[48] Hasselmann K, Barnett TP, Bouws E, Carlson H, Cartwright DE, Enke K et al. Measurements of wind-wave growth and swell decay during the Joint North Sea Wave Project (JONSWAP). Ergänzungsheft. 1973:8-12.

[49] Chakrabarti SK. Hydrodynamics of offshore structures: WIT press; 1987.

[50] Pham TD, Shin H. Validation of a 750 kW semi-submersible floating offshore wind turbine numerical model with model test data, part I: Model-I. Int J Nav Archit Ocean Eng. 2019;11:980-92.

[51] Qiao D, Ou J. Global responses analysis of a semi-submersible platform with different mooring models in South China Sea. Ships Offshore Struct. 2012;8:441-56.

CHAPTER 7 INERTER-BASED VIBRATION ISOLATION SYSTEM (IVIS) FOR HEAVE MOTION MITIGATION

Abstract[7]

This paper develops an inerter-based vibration isolation system (IVIS) for heave motion mitigation of semi-submersible platforms (SSPs) subjected to sea waves. An analytical model of a classical SSP equipped with IVIS is first established and validated by comparing the heave response amplitude operator (RAO) with the previous experimental and numerical results, and the corresponding equations of motion are derived. Optimization analyses are performed to search for the optimum inertance-to-mass ratio of IVIS by minimizing the heave motion standard deviation of the SSP. A case study is carried out to demonstrate the control performance of IVIS in the frequency and time domains. The results indicate that the proposed IVIS is more effective and has a wider effective frequency range compared to the conventional vibration isolation system (VIS). By introducing a parallel-connected inerter, the reduction ratio of the receiving body can be further improved by more than 23%. More importantly, the IVIS can achieve the best control performance under different wave conditions by adjusting the inertance in the system. The proposed IVIS is an attractive alternative to the conventional vibration isolation systems for offshore platforms.

7.1 Introduction

Semi-submersible platform (SSP) is a specialized marine vessel consisting of pontoons, columns, topsides, etc. Due to its obvious merits (e.g. the wide applicable water depth, big deck area, and large payload capacity), SSP is widely applied as the floating foundation for the oil rigs, offshore wind turbines and wave energy converters. For a SSP operating in the water, it normally can be modelled as a rigid body with six degrees-of-freedom (DOFs), including three translations (surge, sway and heave) and three rotations (roll, pitch and yaw). Among these motions, the heave motion is most critical [1] since the fundamental natural period of a SSP in the heave direction is generally close to the wave dominant period, and a large heave motion is therefore expected during its service life because of resonances. The excessive heave motion not only degrades the performance of crew members, but also results in fatigue problems of structural components, and/or even capsize/sink the platform. It is therefore imperative to suppress the adverse heave motion of a SSP subjected to sea waves.

Vibration control of offshore platforms is a hot research topic in the past decades. Many

[7] This chapter was published in *Engineering Structures* with the full bibliographic citation as follows:
Ma R, Bi K, Hao H. Heave motion mitigation of semi-submersible platform using inerter-based vibration isolation system (IVIS). Eng Struct. 2020;219:110833. https://doi.org/10.1016/j.engstruct.2020.110833.

different control methods, such as passive, semi-active, active and hybrid, have been proposed and developed [2, 3]. Among these methods, the passive control method is the most extensively used due to its simplicity and independence of external energy. For the floating platform, the most conventional passive control method is to mount a fixed heave plate (FHP) at the bottom of the columns or under the pontoons. These heave plates can introduce extra damping and added mass into the system, and consequently reduce the heave motion [4, 5]. Theoretical and experimental studies revealed that the FHP system could be an effective solution in reducing the heave motion of a SSP. However, the control effectiveness of the FHP system may be limited in some cases, e.g. when the plate size is not big enough and/or when it is installed with not enough depth. To improve the control performance, Liu and Ou [6] proposed the concept of tuned heave plate (THP), in which the heave plate was connected to the platform via a set of spring and damper rather than the rigid connection as adopted in the FHP system. Essentially, the THP system can be considered as a variant of tuned mass damper (TMD), a well-known dynamic vibration absorber (DVA) widely applied to suppress the vibrations of engineering structures [7-10]. Similar to TMD, the THP system should be carefully optimized before application, i.e. setting reasonable values for the spring stiffness and damping coefficient. The analytical results showed that the optimized THP system was more effective in mitigating the heave motion of a SSP than the FHP system [6]. However, the extensive application of the THP system is constrained due to the following reasons: (1) similar to the TMD system, the control effectiveness of the THP system depends heavily on the mass ratio between the heave plate and platform, a very large secondary mass (i.e. heave plate) is generally required to achieve good effectiveness. On the other hand, the large secondary mass not only increases the implementation cost of the project but also makes the suspension system very complex and not straightforward to fabricate; (2) different from the conventional TMD system, the fundamental natural period of the THP system must be tuned near the wave dominant period in order to achieve the best control performance [11]. In other words, the optimal fundamental natural period of the THP system will be different when the SSP is subjected to different waves (e.g. the waves with different peak periods). This requires the parameters of the suspension system being changeable with the wave condition, which is hard to realize in most applications. Besides the FHP and THP systems, the vibration isolation system (VIS) was also introduced to control the motions of offshore platforms [12-14]. Different from the working principle of the FHP and THP systems, the VIS is to isolate the upper structures (e.g. crane, oil tree and other vibration-sensitive apparatuses) from the vibratory motions by releasing the rigid constraints between the deck and columns. It is well-known that the vibration attenuation of the conventional VIS is only effective when the input frequencies are larger than $\sqrt{2}$ times of the fundamental natural frequency of the isolated component. For the input frequencies below $\sqrt{2}$ times of the fundamental natural frequency,

the responses of the isolated component would be aggravated rather than suppressed. In other words, the effective frequency range of the conventional VIS is limited. Given the issues in these conventional control methods, it is of particular significance to propose a more effective control method for the mitigation of the heave motion of SSP.

Inerter is a two-terminal mechanical element with the property of generating the resisting force proportional to the relative acceleration between its two terminals, in which the proportionality constant is called inertance [15]. In practice, the inerter can be realized through a flywheel driven by rack-and-pinion, fluid or a ball-screw assembly, and the required inertance can be easily achieved by choosing the gear ratio or the diameter of the flywheel [16, 17]. As reported in Ref. [18], the inerter is capable of achieving an inertance several orders larger than its physical mass. This significant mass amplification effect sheds light on the possibility of upgrading the conventional control systems. Given the obvious mass amplification effect, the inerter was firstly utilized to reduce the secondary mass of TMD systems, and a number of inerter-based DVAs have been proposed, such as tuned mass-damper-inerter (TMDI) [19-22], tuned inerter damper (TID) [23-25], and tuned tandem mass dampers-inerter (TTMDI) [26], etc. As demonstrated, the incorporation of inerter can significantly improve the performance of the TMD system in reducing the vibrations induced by various loading scenarios [27-31]. Similarly, inerter is also found to possess a high application potential in the vibration control of floating platforms owing to the obvious mass amplification effect. Hu et al. [32] demonstrated the effectiveness of using inerter-based control system in suppressing the wind- and wave-induced vibrations of a floating offshore wind turbine (FOWT). Ma et al. [33-35] developed two kinds of inerter-based damper, i.e. tuned heave plate inerter (THPI) and rotational inertia damper (RID), to mitigate the heave and pitch motions of semi-submersible platform subjected to wave loadings. Compared to the conventional THP system, these two inerter-based dampers show better control performance by utilizing a much smaller physical mass. Moreover, inerter is also very useful in vibration isolation systems. In this aspect, the inerter was initially incorporated into the suspension system to improve the isolating performance of vehicles [36-38]. In recent years, inerter was introduced into the base-isolated structural systems (BISs) in civil engineering structures, to reduce lateral displacement demands [39-44]. In addition, the configuration and optimization of the inerter-based vibration isolation systems were also investigated [45-48]. However, so far, inerter has not been introduced into the vibration isolation system of SSP, and its influence on the heave motion mitigation is unclear.

Considering the evident advantages of inerter devices, this paper proposes an inerter-based vibration isolation system (IVIS) to isolate the upper structures of SSP from its substructures (namely columns or pontoons), and thus reduces their vibrations. The remaining of this paper

is organized as follows: Section 7.2 develops the analytical model of a SSP equipped with IVIS; in Section 7.3, a classical platform is chosen for this research, and the validation is performed; Section 7.4 examines the control effectiveness of IVIS in reducing the heave motion of SSP, and investigates the optimal design of IVIS; in Section 7.5, a case study is performed to demonstrate the frequency- and time-domain isolating performances of IVIS; finally, the major conclusions of this paper are drawn in Section 7.6.

7.2 Analytical Model of SSP with IVIS

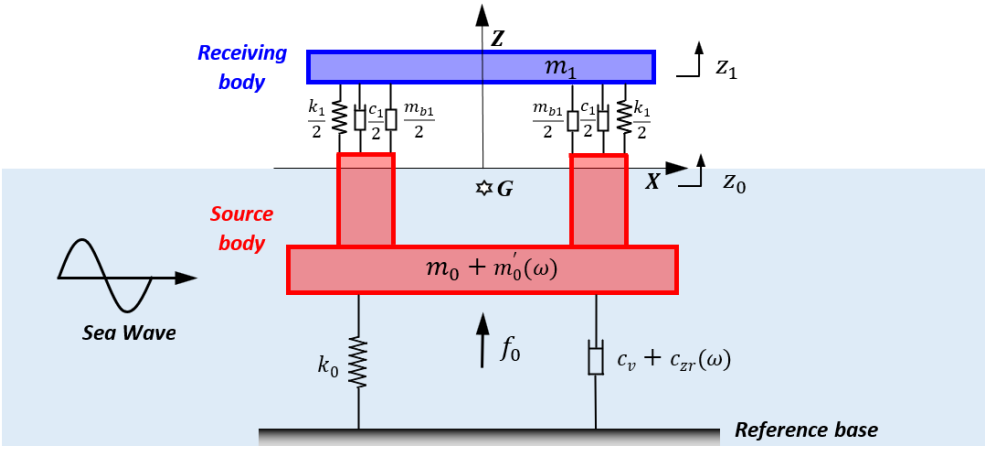

Figure 7-1 Analytical model of the SSP with IVIS

For a SSP, most vibration-sensitive apparatuses (e.g. crane, dry oil tree, risers, etc.) are mounted on the deck, and the pontoons and columns are mainly utilized to provide buoyancy. Therefore, similar to the previous study [14], the SSP is divided into two parts: the upper part (i.e. the receiving body, primarily including the deck and apparatuses above) and the lower part (i.e. the source body, primarily including pontoons and columns). Moreover, as mentioned in the previous study [45], there exist many configurations for the inerter-based vibration isolation system, e.g. parallel-connected inerter and serial-connected inerter. In the present study, only the parallel-connected inerter is considered due to its attractive merits as will be demonstrated in this paper. Figure 7-1 shows the analytical model of the SSP equipped with IVIS. As shown, the rigid constraints between the deck and columns are replaced by a set of springs, dashpots and inerters. More specifically, the receiving and source bodies have the mass of m_1 and $m_0 + m_0'(\omega)$ respectively (where m_0 is the physical mass of the source body, and $m_0'(\omega)$ is the frequency-dependent added mass that is caused by the fact that the vibrating SSP can impart an acceleration to the surrounding sea water, which in turn results in the inertial force to the platform), and they are interconnected by two springs (with a total stiffness of k_1), two viscous dampers (with a total damping coefficient of c_1), and two inerters (with a total inertance of m_{b1}). The source body is attached to the reference base via a spring k_0 and a damper $c_v + c_{zr}(\omega)$ (where c_v is the damping coefficient of the SSP in the heave direction,

and $c_{zr}(\omega)$ is the frequency-dependent radiation damping coefficient), and excited by the wave-induced force f_0. Notably, the reference base is not a real physical base, and it is a representation of the support provided by water. The detailed representation of these parameters will be introduced later.

The equations of motion of the SSP with IVIS can be written as follows:

$$m_0\ddot{z}_0(t) = f_0(t) + f_{res}(t) + f_{vic}(t) + f_{rad}(t) + f_{IVIS}(t) \tag{7.1}$$

$$m_1\ddot{z}_1(t) = -f_{IVIS}(t) \tag{7.2}$$

in which $\ddot{z}_0$ and $\ddot{z}_1$ are the acceleration of the source and receiving bodies, respectively. f_{IVIS} is the force provided by the IVIS, which can be expressed as follows:

$$f_{IVIS}(t) = -k_1[z_0(t) - z_1(t)] - c_1[\dot{z}_0(t) - \dot{z}_1(t)] - m_{b1}[\ddot{z}_0(t) - \ddot{z}_1(t)] \tag{7.3}$$

where z_0 and z_1 are the displacement of the source and receiving bodies, respectively, and $\dot{z}_0$ and $\dot{z}_1$ are the corresponding velocities.

In Equation (7.1), $f_{res}(t)$ is the restoring force arising when the SSP is perturbed away from its equilibrium position, and it can be written as follows [49]:

$$f_{res}(t) = -k_0 z_0(t) \tag{7.4}$$

$$k_0 = \rho g A_w \tag{7.5}$$

where k_0 is the restoring stiffness of the SSP in the heave direction, ρ is the density of water, g is the gravitational acceleration, A_w is the waterplane area of platform.

As for the viscous damping force acting on the SSP, it can be calculated by

$$f_{vic}(t) = -c_v\dot{z}_0(t) \tag{7.6}$$

in which c_v is the damping coefficient of the SSP as mentioned above, which can be calculated based on the corresponding damping ratio.

$f_{rad}(t)$ is the radiation force due to the change in momentum of the fluid resulting from the motions of SSP. According to Cummins's work [50], it can be calculated as

$$f_{rad}(t) = -m_\infty\ddot{z}_0(t) - \int_0^t K_0(t-t')\,\dot{z}_0(t')dt' \tag{7.7}$$

in which, m_∞ is the infinite-frequency added mass of the SSP in the heave direction. The integral term is the fluid-memory model which captures the energy transferring from the platform motion to the radiated waves, and $K_0(t)$ is the impulse response function of the radiation in the heave direction.

Substituting Equations (7.3)-(7.7) into Equations (7.1) and (7.2), one obtains

$$(m_0 + m_\infty)\ddot{z}_0(t) = f_0(t) - k_0 z_0(t) - c_v \dot{z}_0(t) - \int_0^t K_0(t-t')\,\dot{z}_0(t')dt' - k_1[z_0(t) - z_1(t)] - c_1[\dot{z}_0(t) - \dot{z}_1(t)] - m_{b1}[\ddot{z}_0(t) - \ddot{z}_1(t)] \quad (7.8)$$

$$m_1\ddot{z}_1(t) = -k_1[z_1(t) - z_0(t)] - c_1[\dot{z}_1(t) - \dot{z}_0(t)] - m_{b1}[\ddot{z}_1(t) - \ddot{z}_0(t)] \quad (7.9)$$

Obviously, Equation (7.8) cannot be directly transformed into the frequency domain due to the convolution term of the radiation force. To simplify the analysis, Equation (7.7) is expressed in the frequency domain as follows [49, 51]:

$$f_{rad}(s) = -m_0'(\omega)\ddot{z}_0(s) - c_{zr}(\omega)\dot{z}_0(s) \quad (7.10)$$

where $s = i\omega$ with ω denoting the excitation frequency and i representing the imaginary unit (i.e. $i = \sqrt{-1}$); $m_0'(\omega)$ is the frequency-dependent added mass of the SSP in the heave direction; $c_{zr}(\omega)$ is the frequency-dependent radiation damping coefficient. These frequency-dependent coefficients can be calculated based on the potential theory, and many hydrodynamic codes (e.g. ANSYS AQWA) have been developed and implemented in the commercial software packages.

After introducing the frequency-domain radiation force, Equations (7.8) and (7.9) can be expressed in the Laplace domain as follows:

$$\{[m_0 + m_0'(\omega) + m_{b1}]s^2 + [c_v' + c_{zr}(\omega) + c_1]s + k_0 + k_1\}Z_0(s) - [m_{b1}s^2 + c_1 s + k_1]Z_1(s) = F_0(s) \quad (7.11)$$

$$[(m_1 + m_{b1})s^2 + c_1 s + k_1]Z_1(s) - [m_{b1}s^2 + c_1 s + k_1]Z_0(s) = 0 \quad (7.12)$$

in which $Z_1(s)$ and $Z_0(s)$ are the complex motion amplitudes of the receiving and source bodies, respectively, and $F_0(s)$ is the complex amplitude of the wave-excited force acting on the SSP. The complex motion amplitudes of the receiving and source bodies are therefore

$$Z_1(s) = \frac{[m_{b1}s^2+c_1s+k_1]F_0(s)}{\{[m_0+m_0'(\omega)+m_{b1}]s^2+[c_v'+c_{zr}(\omega)+c_1]s+k_0+k_1\}[(m_1+m_{b1})s^2+c_1s+k_1]-[m_{b1}s^2+c_1s+k_1]^2} \quad (7.13)$$

$$Z_0(s) = \frac{[(m_1+m_{b1})s^2+c_1s+k_1]F_0(s)}{\{[m_0+m_0'(\omega)+m_{b1}]s^2+[c_v'+c_{zr}(\omega)+c_1]s+k_0+k_1\}[(m_1+m_{b1})s^2+c_1s+k_1]-[m_{b1}s^2+c_1s+k_1]^2} \quad (7.14)$$

It is convenient to define some dimensionless parameters in the analysis and design in order to make the mathematical expressions more universal. By introducing dimensionless parameters, Equations (7.13) and (7.14) can be expressed as follows:

$$Z_1(s) = \frac{A_1 \cdot A_2}{A_3 \cdot A_4 - {A_1}^2} \tag{7.15}$$

$$Z_0(s) = \frac{A_4 \cdot A_2}{A_3 \cdot A_4 - {A_1}^2} \tag{7.16}$$

where coefficients A_1, A_2, A_3, and A_4 are given by

$$A_1 = \mu\delta s^2 + 2\mu\gamma\xi\omega_s s + \mu\gamma^2\omega_s^2 \tag{7.17}$$

$$A_2 = \frac{F_0(s)}{m_0 + m_0'(\omega)} \tag{7.18}$$

$$A_3 = (1 + \mu\delta)s^2 + (2\omega_s\xi_v + 2\omega_s\xi_{zr} + 2\mu\gamma\xi\omega_s)s + \omega_s^2 + \mu\gamma^2\omega_s^2 \tag{7.19}$$

$$A_4 = (\mu + \mu\delta)s^2 + 2\mu\gamma\xi\omega_s s + \mu\gamma^2\omega_s^2 \tag{7.20}$$

where

$$\mu = \frac{m_1}{m_0 + m_0'(\omega)} \tag{7.21}$$

$$\delta = \frac{m_{b1}}{m_1} \tag{7.22}$$

$$\xi_v = \frac{c_v}{2[m_0 + m_0'(\omega)]\omega_s} \tag{7.23}$$

$$\xi_{zr} = \frac{c_{zr}(\omega)}{2[m_0 + m_0'(\omega)]\omega_s} \tag{7.24}$$

$$\xi = \frac{c_1}{2m_1\omega_1} \tag{7.25}$$

$$\gamma = \frac{\omega_1}{\omega_s} \tag{7.26}$$

$$q = \frac{\omega}{\omega_1} \tag{7.27}$$

in which μ is the mass ratio between the receiving and source bodies; δ is the inertance-to-mass ratio of IVIS; ξ_v and ξ_{zr} are the inherent viscous and radiation damping ratios, respectively; ξ is the damping ratio of IVIS; γ is the natural frequency ratio between the receiving and source bodies; q is the excitation frequency ratio. ω_1 and ω_s are the vibration frequencies of the receiving and source bodies, respectively, and they can be calculated by

$$\omega_1 = \sqrt{k_1/m_1} \tag{7.28}$$

$$\omega_s = \sqrt{k_0/(m_0 + m_0'(\omega))} \tag{7.29}$$

As mentioned above, the purpose of IVIS is to isolate the receiving body from the motions induced by the source body. To evaluate the isolating performance, the displacement transmissibility function $\mathcal{G}_z(s)$ of IVIS is generally calculated, and it can be expressed by the following equation:

$$\mathcal{G}_z(s) = \frac{|Z_1(s)|}{|Z_0(s)|} = \sqrt{\frac{(1-\delta q^2)^2 + (2q\xi)^2}{(1-(1+\delta)q^2)^2 + (2q\xi)^2}} \tag{7.30}$$

It is worth mentioning that $\mathcal{G}_z(s)$ is a function of δ, ξ, and q as shown in Equation (7.30), and it is independent of the mass ratio μ defined by Equation (7.21).

For floating platforms, the response amplitude operator (RAO) is a commonly utilized measure to evaluate the performance of the platform, and it can be calculated by the following equation:

$$RAO_n(\omega) = \frac{|Z_n(s)|}{\zeta_a} \tag{7.31}$$

in which Z_n is the complex motion amplitude of the receiving (n=1) or source (n=0) body; ζ_a is the wave amplitude, which is half of the wave height.

It is obvious that the heave response spectrum can be calculated as follows:

$$S_n(\omega) = S(\omega)[RAO_n(\omega)]^2 \tag{7.32}$$

when the spectrum of the incident wave acting on the platform $S(\omega)$ is known. In the present study, the JONSWAP spectrum is adopted, and it is expressed as:

$$S(\omega) = a^* H_s^2 \frac{\omega^{-5}}{\omega_0^{-4}} \exp\left[-1.25(\omega/\omega_0)^{-4}\right] \gamma_w^{\exp\left[-\frac{(\omega-\omega_0)^2}{2\tau^2\omega_0^2}\right]} \tag{7.33}$$

in which H_s is the significant wave height, ω_0 is the wave peak frequency, and

$$a^* = \frac{0.0624}{0.230 + 0.0336\gamma_w - 0.185(1.9+\gamma_w)^{-1}} \tag{7.34}$$

where γ_w is the peakedness factor with an average value of 3.3 [52]; τ is the shape parameter and equals to 0.07 when $\omega \leq \omega_0$ and 0.09 when $\omega > \omega_0$ [52].

To quantitatively assess the isolating performance of IVIS, the heave motion standard deviation is calculated as follows:

$$\sigma_n = \sqrt{\int_0^\infty S_n(\omega) d\omega} \; (n = 0,1) \tag{7.35}$$

7.3 Prototype and Validation

7.3.1 Prototype of SSP

In the present study, a classical HYSY981 platform is chosen as the prototype in the present study. Figure 7-2 shows the schematic drawings of the SSP, and detailed physical properties are tabulated in Table 7-1. As illustrated, the SSP consists of four rectangular columns, two pontoons and one deck. The total displacement tonnage (i.e. physical mass) of the SSP is 51700 tonnes, and the operating draft is 19 m. In the figure, G is the center of gravity of the platform. It is worth mentioning that the damping ratio of the chosen SSP has been identified in the previous free-decay tests [6], and it is equal to 4.48% in the heave direction. Moreover, a panel model of the SSP is established in the commercial software ANSYS AQWA (version: R17.2 academic) to calculate the frequency-dependent parameters (i.e. $m_0'(\omega)$ and $c_{zr}(\omega)$ in Equation (7.10)) and wave-excited force (i.e. f_0 in Equation (7.1)). The detailed processes of generating these parameters in the software can be found in Ref. [53].

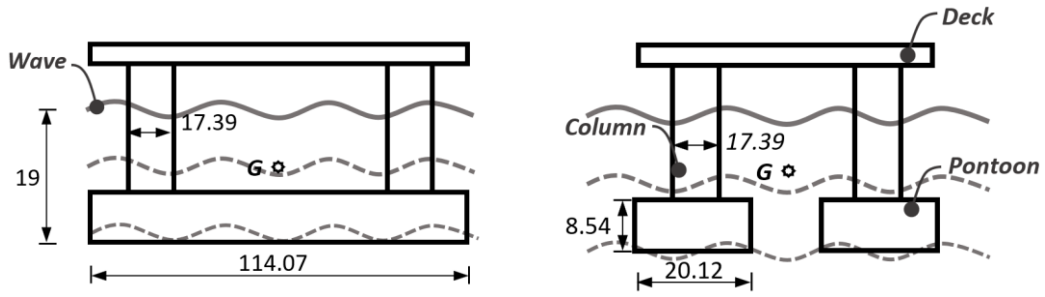

(a) Elevation view (b) Side view

Figure 7-2 Schematic drawings of the HYSY 981 platform (unit: m)

Table 7-1 Geometric properties of HYSY 981 platform

Properties	Value
Deck (m)	77.47×74.38×8.60
Column (m)	17.39×17.39×21.46
Pontoon (m)	114.07×20.12×8.54
Operating draft (m)	19
Displacement (tonnes)	51700

7.3.2 Validation of Analytical Model

In this subsection, the developed analytical model is validated by comparing the heave RAO in this research with the previous experimental and numerical results. As shown in Figure 7-3, a 1:70 scaled model of HYSY 981 platform was constructed by Liu and Ou [6], regular wave tests with the excitation frequency ranging from 0.3 rad/s to 1.2 rad/s were performed. Numerical simulations were also conducted in the study [6] to calculate the heave RAO. Figure

7-4 shows the heave RAOs of the original SSP (i.e. without any control) obtained in the present study and in the previous study [6]. As shown, the RAO curve in the present study (i.e. the black curve) coincides well with both the experimental (i.e. the blue diamond dots) and numerical results (i.e. the red circle dots) in the previous study. The analytical model of the SSP in the present study therefore yields good accurate predictions.

Figure 7-3 Scaled model of HYSY 981 platform in the previous study [6]

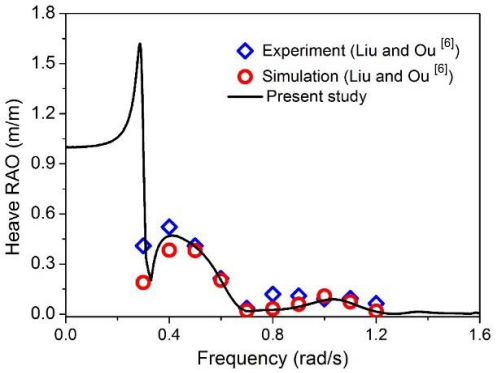

Figure 7-4 Heave RAO comparisons of SSP obtained in the present study and in the previous study [6]

7.4 Results and Discussions

Based on the validated analytical model, the isolating performance of the developed IVIS is investigated and compared with that of the conventional VIS in this section. The heave motion of the SSP without any control is also calculated as a benchmark. It is worth noting that the physical mass ratio between the receiving and source bodies (i.e. $m_1 : m_0$) is assumed as 3:7 in the present study based on the currently available information. This assumption may not be completely consistent with the realistic situation, but it does not affect the isolating performance of IVIS since the displacement transmissibility function $\mathcal{G}_z(s)$ (i.e. Equation (7.30)) is independent of the mass ratio as discussed in Section 7.2. In this section, optimization analyses are also performed to determine the optimal inertance-to-mass ratio of IVIS (see Section 7.4.3).

7.4.1 Displacement Transmissibility

Figure 7-5 shows the displacement transmissibility with respect to different damping ratios ξ when the inertance-to-mass ratio $\delta = 0.1$. To explicitly show the effectiveness, the transmissibility value of unity is also shown in the figure by the grey dotted line. As shown, all the curves pass through an invariant point which is independent of the damping ratio ξ. When the excitation frequency ratio q is less than the invariant value, the transmissibility magnitude is larger than 1.0 and decreases with the increase of ξ. On the contrary, when q exceeds the invariant point, the transmissibility magnitude is less than 1.0 and increases with

the increment of ξ. Obviously, the IVIS is valid only when q is larger than the invariant value, and the smaller the damping ratio is, the better is the control effectiveness. However, it should be noted that a zero or very low damping ratio is generally unacceptable in engineering practices since the possible resonant could lead to catastrophic results.

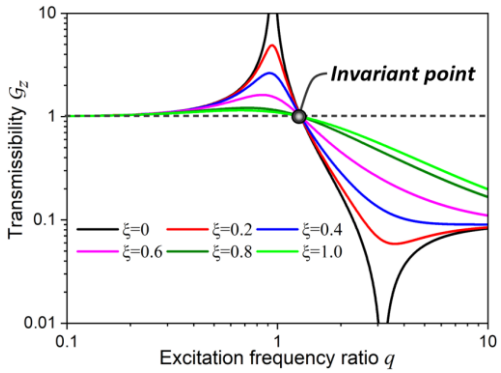

Figure 7-5 Influence of damping ratio on the displacement transmissibility of IVIS (δ=0.1)

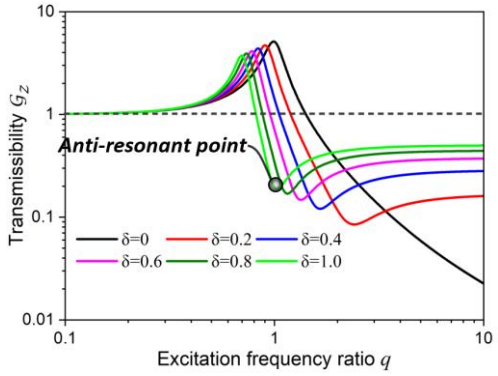

Figure 7-6 Influence of inertance-to-mass ratio on the displacement transmissibility of IVIS (ξ=0.1)

Through some straightforward derivations, the expression of the invariant point can be obtained as follows:

$$q_i = \sqrt{\frac{2}{1+2\delta}} \tag{7.36}$$

It is obvious that the invariant point $q_i = \sqrt{2}$ when $\delta = 0$, which is the same as the conventional VIS.

Figure 7-6 depicts the displacement transmissibility with respect to different inertance-to-mass ratios δ when the damping ratio $\xi = 0.1$. Similarly, the transmissibility value of 1.0 is also highlighted by the grey dotted line in the figure. As shown, all the curves move leftward gradually with the increase of δ. In other words, the inerter can lower the invariant point and increase the effective frequency range of the conventional VIS. This is more obvious based on Equation (7.36). Moreover, an anti-resonant point, i.e. the point with the minimum transmissibility magnitude, is introduced by the inerter. When the excitation frequency ratio q exceeds the anti-resonant frequency ratio (i.e. the particular excitation frequency ratio at the anti-resonant point), the transmissibility magnitude increases with the increase of q and gradually tends to a specific value. On the other hand, Figure 7-6 also shows that the control effectiveness actually becomes less evident with the increment of δ. This is because a larger δ makes the receiving and source bodies tend to be more rigidly connected with each other, which decreases the isolation performance.

The above results indicate that incorporating a parallel-connected inerter into the conventional VIS system has the following fundamental properties which are beneficial to

improve the performance of conventional VIS: (1) without changing the natural frequency of the receiving body, the inerter can lower the invariant point, and thus enhance the effective isolating frequency range; (2) the inerter introduces an anti-resonant point, at which the IVIS outperforms the conventional VIS (i.e. $\delta = 0$).

7.4.2 Response Amplitude Operator (RAO)

In this subsection, both the heave RAOs of the receiving and source bodies are calculated to comprehensively understand the isolating performance of the VIS and IVIS. The performance of the conventional VIS is firstly investigated by parametric studies (namely varying the frequency and damping ratios in the system), and the existing limitations of VIS are discussed. The isolating performance of the proposed IVIS is then investigated with an emphasis on addressing the limitations of the conventional VIS. As will be demonstrated in the following subsections, the IVIS is more effective in reducing the heave motion of the receiving body, and has a wider effective frequency range.

7.4.2.1 Vibration Isolation System (VIS)

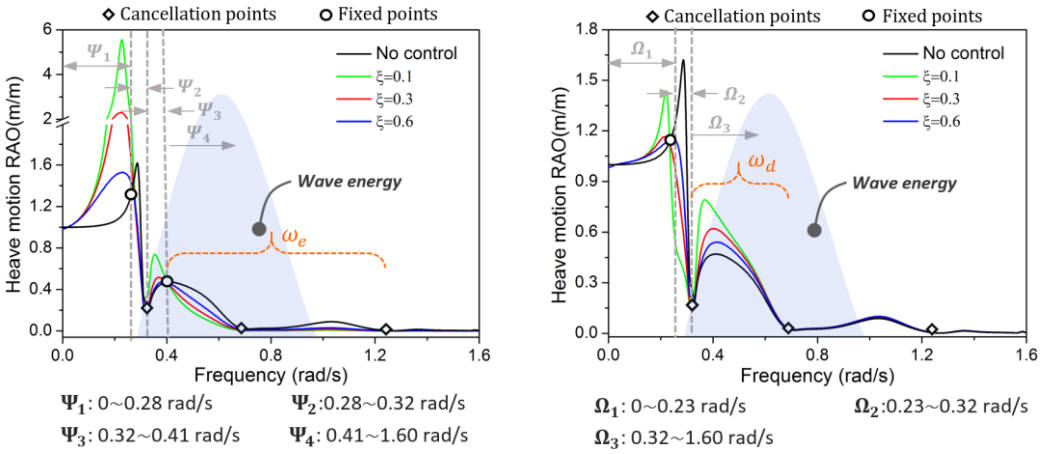

(a) Receiving body (b) Source body

Figure 7-7 RAO curves of the SSP controlled by the VIS with different damping ratios (γ=0.8)

Figure 7-7 shows the RAO curves of the SSP without control and controlled by the conventional VIS (i.e. without inerter) with different damping ratios. In this case, the frequency ratio γ of VIS is assumed as 0.8, and the damping ratio ξ is set to 0.1, 0.3 and 0.6, respectively. To facilitate a better understanding on the control performance, an approximate energy distribution of the sea wave (the blue shaded area) is illustrated in Figure 7-7 as well. This wave energy distribution is estimated according to the previous statistical data [49], in which the most probable dominant period (i.e. the period with the highest energy in the curve) of the sea wave is around 10s. As shown in Figure 7-7(a), the RAO curve of the uncontrolled SSP (the black curve in the figure) shows an obvious peak at 0.290 rad/s, which corresponds to the fundamental natural frequency of SSP in the heave direction. It is obvious that this

fundamental natural frequency almost falls outside the dominant frequency range of wave energy, which is consistent with the design principle of floating platforms, i.e. to avoid the possible resonance to the utmost extent. Figure 7-7(a) also shows that, around frequencies of 0.33, 0.71 and 1.26 rad/s, all the RAO curves show almost identical valleys (see the black diamond dots), namely the heave RAOs reach the minimum values within certain frequency ranges at these points. These minima points are called "cancellation points" which are caused by small wave forces at these frequencies [1]. As explained by Halkyard [1], the wave forces acting on the bottom of columns due to wave pressure can partly or completely cancel the inertial forces acting on the pontoons at these specific frequencies. In Figure 7-7(a), it is also found that all the RAO curves almost pass through two "fixed points", which is independent of the damping ratios of IVIS (see the black circle dots). This finding is similar to the fixed points observed in the displacement transfer curves of the ordinary structure-TMD system under white noise. On the other hand, different from the traditional TMD theory, each "fixed point" is not exactly overlapped for all the RAO curves in the present study. This is due to the fact that the fixed point theory was derived based on the assumption that the host structure is undamped or lightly damped. However, the SSP in the present study has a damping ratio of 4.48% in the heave direction, which can slightly influence the locations of fixed points.

To better understand the influence of damping ratio, the entire frequency band in Figure 7-7(a) is roughly divided into four ranges based on the two fixed points and the cancellation point at 0.33 rad/s. In the Ranges Ψ_1 (0-0.28 rad/s) and Ψ_3 (0.32-0.41 rad/s), increasing damping ratio leads to smaller RAO values. However, in Ranges Ψ_2 (0.28-0.32 rad/s) and Ψ_4 (0.41-1.60 rad/s), the influence of damping ratio is opposite. It is also found from Figure 7-7(a) that the VIS increases the RAO in Ranges Ψ_1 and Ψ_3, and decreases it in Ranges Ψ_2 and Ψ_4. The VIS are thus effective in the Ranges Ψ_2 and Ψ_4. However, the control effectiveness of the VIS in Range Ψ_2 is "illusory" since the corresponding displacement transmissibility is larger than 1.0 in this frequency range. The VIS is therefore only effective in reducing the RAO of the receiving body in Range Ψ_4. Moreover, as shown in Figure 7-7(a), the control effectiveness of VIS is not obvious when the frequency is larger than 1.26 rad/s (i.e. the third cancellation point). The effective frequency range of using VIS (i.e. ω_e in the figure) in suppressing the vibration of receiving body is thus between 0.4 rad/s (i.e. the second fixed point) and 1.26 rad/s (i.e. the third cancellation point). It is also found that the VISs with different damping ratios have the same effective frequency range, in which their performances increase with the decrease of damping ratio. In other words, the damping ratio does not influence the effective frequency range of VIS, and the VIS is more effective when its damping ratio is low. These findings are consistent with our common understanding on the base isolation system.

Figure 7-7(b) shows the RAO curves of the source body when the VIS is with different

damping ratios. Similarly, cancellation and fixed points are also observed in the RAO curves of the source body. However, only one obvious fixed point is observed in Figure 7-7(b), which is different from those in Figure 7-7(a). The entire frequency band is also divided into different ranges (i.e. the three ranges as shown) to indicate the influence of damping ratio. In Range Ω_2, the VIS reduces the RAO of the source body, which increases with the increase of damping ratio. However, in Ranges Ω_1 and Ω_3, the VIS increases the RAO of the source body, which decreases with the increase of damping ratio. Moreover, it is also found that the VISs with different damping ratios have the same detrimental frequency range (i.e. ω_d in the figure), which is defined as the frequency bandwidth where the heave motion of the source body is aggravated. It should be noted that slightly increasing the vibration of the source body is acceptable since most vibration-sensitive equipment and crew staff are normally on the receiving body as mentioned in the introduction.

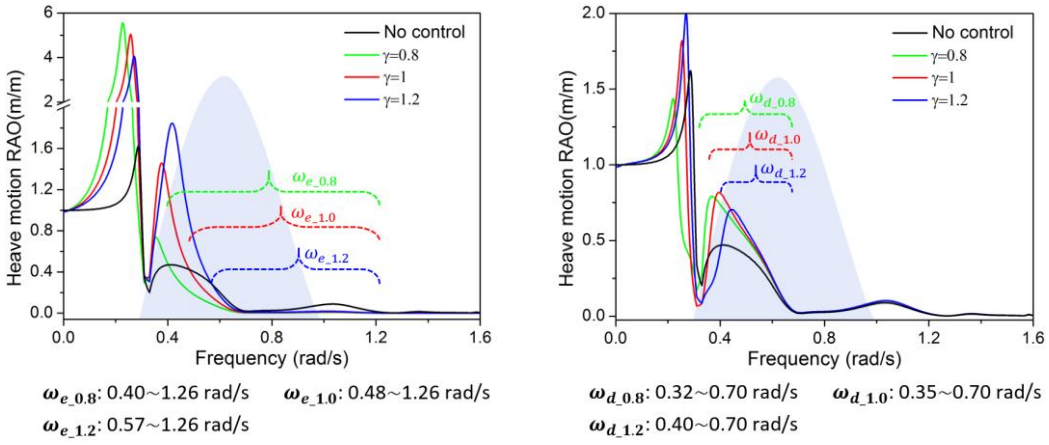

(a) Receiving body (b) Source body

Figure 7-8 RAO curves of the SSP controlled by the VIS with different frequency ratios (ξ=0.1)

Figure 7-8 shows the RAO curves of the SSP without control and controlled by the VIS with different frequency ratios. In this case, the frequency ratio γ of VIS is set to 0.8, 1.0 and 1.2, respectively, and the damping ratio ξ is kept as 0.1. Similarly, the wave energy distribution is also plotted in the figure. As shown in Figure 7-8(a), the RAO curve of the receiving body moves leftward with the decrease of frequency ratio, and the effective frequency range of VIS is thus broadened (see dashed brackets in the figure). It is also found that the isolating performance of VIS increases with the decrease of frequency ratio in the effective frequency range. In other words, the smaller the frequency ratio of VIS is, the larger is its effective frequency range of VIS, and thus the better is its isolating performance. To achieve a better control performance, the VIS should be designed with a low frequency ratio, which requires a soft suspension stiffness. On the other hand, it should be noted that the suspension stiffness cannot be too small in engineering practices since it is possible to result in instability issues of the entire system. Figure 7-8(b) shows the RAO curves of the source body when the VIS is

with different frequency ratios. Similarly, the RAO curve of the source body moves leftward with the decrease of frequency ratio, and the detrimental frequency range of VIS is thus widened (see dashed brackets in the figure). The smaller the frequency ratio of VIS is, the larger is the detrimental frequency range of VIS. In the detrimental frequency range, the RAO of the source body is aggravated by introducing VIS.

The above results reveal that the conventional VIS has the following characteristics: (1) the VIS can reduce the heave motion of the receiving body, but it in turn aggravates the heave motion of the source body; (2) the isolating performance of VIS increases with the decrease of damping ratio, and the VIS is more effective when the damping ratio is low; (3) both the effective frequency range and control effectiveness of VIS increase with the decrease of frequency ratio, and the VIS performs better when the frequency ratio is small. Because of these properties, the conventional VIS thus has the following inherent issues to be solved: (1) for a better isolating performance, low damping and frequency ratios are required for the conventional VIS. However, a low damping ratio may cause catastrophic resonance of the receiving body in some extreme cases while a small frequency ratio can result in instability as discussed; (2) more importantly, the suspension stiffness and damping coefficient of the conventional VIS are generally invariant since they are difficult to change once the spring and damper are fabricated. On the other hand, as a mobile floating platform, a SSP may work in various areas with different wave conditions (e.g. wave peak period, wave height, etc.) and the isolating performance of VIS may thus be degraded in some areas. As will be demonstrated in the following subsection, these limitations can be overcome by introducing an inerter element into the conventional VIS.

7.4.2.2 Inerter-Based Vibration Isolation System (IVIS)

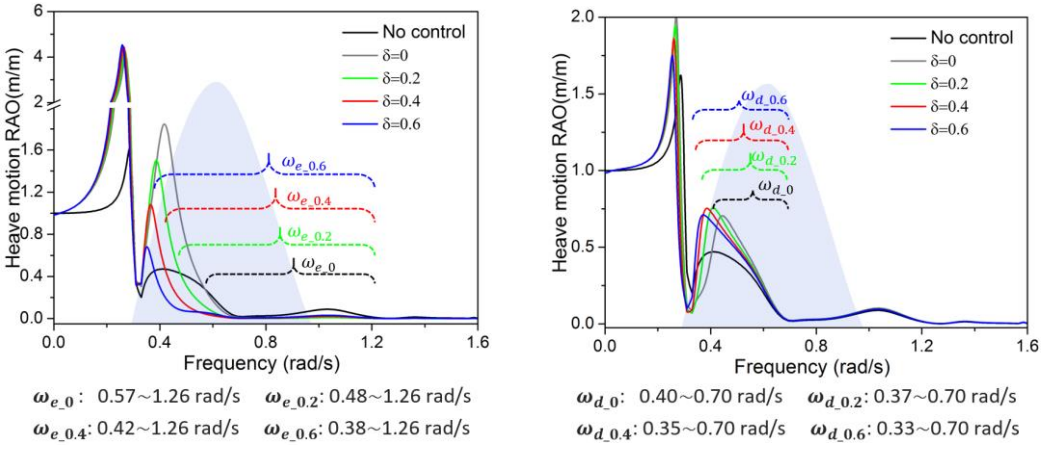

(a) Receiving body (b) Source body

Figure 7-9 RAO curves of the SSP controlled by the IVIS with different inertance-to-mass ratios (γ=1.2, ξ=0.1)

Figure 7-9 shows the RAO curves of the SSP without control and controlled by the IVIS with

different inertance-to-mass ratios. Four inertance-to-mass ratios (i.e. 0, 0.2, 0.4 and 0.6) are considered for the IVIS, and the frequency ratio γ and damping ratio ξ are assumed to be 1.2 and 0.1, respectively. In these figures, the same wave energy distribution as shown in Figure 7-7 and Figure 7-8 is plotted as well. As shown in Figure 7-9(a), the RAO curve of the receiving body gradually moves leftward with the increase of inertance-to-mass ratio. This effect can be attributed to the negative stiffness effect of inerter, i.e. the negative slope in the force-deformation relationship as observed in Refs. [54, 55]. Different from the positive stiffness provided by springs, the negative stiffness introduced by the parallel-connected inerter (see Figure 7-1) can decrease the global stiffness of IVIS, and a smaller global stiffness moves the curve leftward as shown in Figure 7-9(a). It is found that the conventional VIS, namely the IVIS with the inertance-to-mass of 0, has a narrow effective frequency range ω_{e_0} in the figure. Moreover, the VIS only slightly reduces the RAO curve of the receiving body in its narrow effective frequency range. In other words, the isolating performance of the conventional VIS is limited. By introducing an inerter element into the VIS (i.e. forming the IVIS), the effective frequency range is obviously widened, and it increases with the increment of inertance-to-mass ratio (see the dashed brackets in the figure). In other words, compared to the VIS, the IVIS is more effective in reducing the RAO of the receiving body, and the control effectiveness increases with the increment of inertance-to-mass ratio. The performance improvement can be attributed to the anti-resonant point introduced by the inerter as discussed in Section 7.4.1. Figure 7-9(b) shows the RAO curves of the source body when the IVIS is with different inertance-to-mass ratios. Similarly, the RAO curve of the source body moves leftward with the increase of the inertance-to-mass ratio, and the detrimental frequency range is thus increased (see the dashed brackets in the figure). Furthermore, it is also found that both the VIS and IVIS aggravate the heave RAO of the source body in the frequency range of wave energy.

The results in this section demonstrate that the proposed IVIS exhibits the following merits: (1) compared to the VIS, the IVIS has a wider effective frequency range and better isolating performance in reducing the heave motion of the receiving body; (2) as indicated in the literature review, developing an inerter with changeable inertance is technologically feasible, and has been developed in the previous studies [16, 17]. The IVIS is therefore capable of achieving the best isolating performance in different sea areas (i.e. with different wave conditions) by adjusting the inertance rather than changing the spring stiffness and damping coefficient in the system, which are not easy to change as discussed. This property makes the IVIS more practical and reliable in engineering practices. Considering these benefits, the proposed IVIS is believed to be an attractive alternative to the conventional VIS.

7.4.3 Optimal Design of IVIS

In this subsection, optimization analyses are performed to determine the optimal inertance-to-mass ratio of the IVIS with specific frequency and damping ratios. In the case of wave excitation, the H_2 optimization is more reasonable and practical than the H_∞ optimization since the H_2 optimization aims to minimize the total vibration energy rather than the maximum response at a specific frequency [56]. As mentioned above, this research aims to mitigate the heave motion of the receiving body, the heave motion standard deviation of the receiving body (i.e. σ_1) is therefore chosen as the optimization objective. The corresponding optimization problem can be formulated as follows:

$$\Delta = \text{argmin}\ (\sigma_1) \tag{7.37}$$

in which $0 \leq \delta \leq 1$, $8\text{s} \leq T_0 \leq 14\text{s}$, T_0 is the peak period of wave, and a range between 8s and 14s is considered in the optimal design. Apparently, an explicit mathematical expression for the optimal inertance-to-mass is very difficult, and the numerical search method is thus utilized to search the optimal inertance-to-mass ratio of IVIS in the present study. Figure 7-10 displays the contours of the heave motion standard deviation of the receiving body for the considered wave peak period and inertance-to-mass ratio ranges when the wave height is 6.0 m. As shown, for all the wave peak periods, the heave motion standard deviation of the receiving body initially decreases and then increases with the increment of inertance-to-mass ratio. In other words, there always exists an inertance-to-mass ratio (i.e. the optimal value) that leads to a minimum heave motion standard deviation for a specific wave peak period. The locus of all the optimal inertance-to-mass ratios for the given wave peak periods is represented by the black dashed lines in the figures. It can be observed that the optimal inertance-to-mass ratio of IVIS increases with the increment of the wave peak period. Moreover, the influences of the frequency and damping ratios on the optimal inertance-to-mass ratio are also investigated. Four scenarios with different frequency and damping ratios are considered in the optimization (Figure 7-10(a), (b), (c) and (d), respectively). The results demonstrate that the heave motion standard deviation of the receiving body increases with the increase of both the frequency and damping ratios. It is also found the locus of optimal inertance-to-mass ratio (i.e. the black dashed lines in the figure) moves rightward when a larger frequency/damping ratio is adopted. This fact suggests that the optimal inertance-to-mass ratio of IVIS increases with the increase of both the frequency and damping ratios.

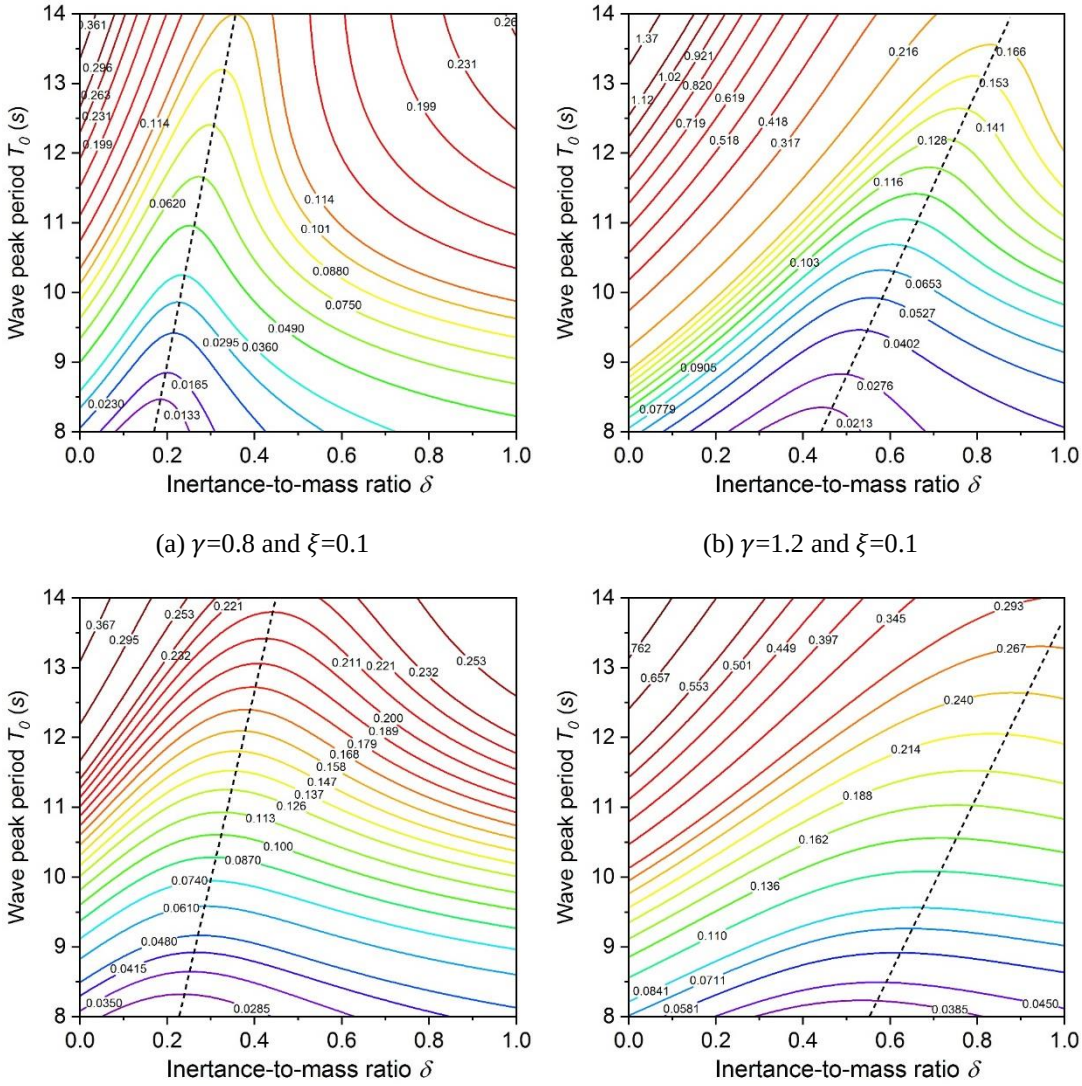

(a) γ=0.8 and ξ=0.1

(b) γ=1.2 and ξ=0.1

(c) γ=0.8 and ξ=0.3

(d) γ=1.2 and ξ=0.3

Figure 7-10 Contours of the heave motion standard deviation of the receiving body controlled by the IVIS with different frequency and damping ratios

7.5 Case Study

In this section, a case study is performed to further demonstrate the control effectiveness of IVIS in both the frequency and time domains. Without loss of generality, a classical sea wave, i.e. the working condition in the South China Sea (SCS) with the significant wave height H_s of 6 m and the peak period T_0 of 11.2s, is chosen for the case study. The frequency ratio γ and damping ratio ξ of both the VIS and IVIS are set to 0.8 and 0.3, respectively. Under the specified frequency and damping ratios, the inertance-to-mass ratio of IVIS is taken as 0.34 which is the optimum value as shown in Figure 7-10(c).

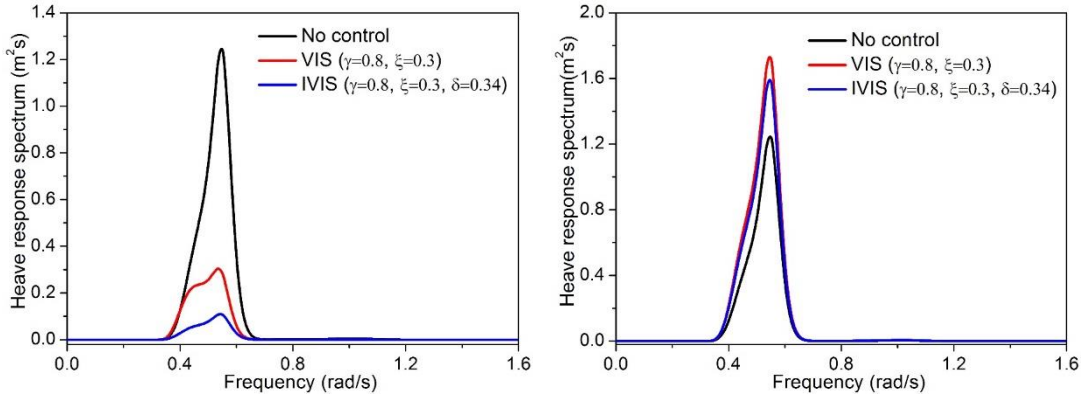

(a) Receiving body (b) Source body

Figure 7-11 Heave response spectra of the receiving and source bodies

Figure 7-11 shows the heave response spectra of the receiving and source bodies, respectively. For comparison, the heave response spectrum of the SSP without any control (i.e. the black solid line) is plotted as well. As shown in Figure 7-11(a), both the VIS and IVIS can reduce the heave response spectrum of the receiving body, but the IVIS is more effective. Additionally, one peak is observed around 0.56 rad/s in the heave response spectrum of the SSP without any control, which corresponds to the dominant frequency of the wave. This fact demonstrates that the heave motion of SSP mainly comes from the rigid-body motion induced by the wave rather than the resonance of the platform itself. In Figure 7-11(b), it is found that both the VIS and IVIS increase the heave motion of the source body, but the peak in the heave response spectrum of the SSP controlled by the IVIS (i.e. the blue curve) is lower than that of the VIS (i.e. the red curve). In other words, the IVIS slightly outperforms the VIS in terms of aggravating the heave motion of the source body.

The heave motion standard deviations are also calculated for both the VIS and IVIS based on Equation (7.35), and the results are tabulated in Table 7-2. To quantitatively show the control effectiveness, the reduction ratios are also calculated as follows:

$$\chi = \frac{\sigma_{nc} - \sigma_c}{\sigma_{nc}} \times 100\% \tag{7.38}$$

in which σ_{nc} is the heave motion standard deviation of the uncontrolled SSP; σ_c is the heave motion standard deviation of the receiving and source bodies controlled by the VIS or IVIS. It is worth noting that a positive reduction ratio represents the heave motion is suppressed while a negative value indicates that the heave motion is aggravated. As listed in Table 7-2, for the receiving body, the reduction ratios of the VIS and IVIS are 42.51% and 67.80%, respectively. As for the source body, the reduction ratios of the VIS and IVIS are -20.54% and -15.55%. By introducing an inerter into the VIS, the reduction ratios of the receiving and source bodies are further increased by 25.29% and 4.99%, respectively.

Table 7-2 Standard deviations of heave motion and the corresponding reduction ratios

Parts	Standard deviation (m)			Reduction ratio (%)		
	No control	VIS	IVIS	No control	VIS	IVIS
Receiving body	0.381	0.219	0.123	--	42.51	67.80
Source body	0.381	0.460	0.441	--	-20.54	-15.55

To more explicitly show the control effectiveness, the performance in the time domain is also investigated, and it is achieved by directly solving Equations (7.8) and (7.9) based on the Simulink models developed in the Appendix. It should be noted that the time histories of the wave force acting on the SSP are generated in ANSYS AQWA, and Figure 7-12 shows the simulated wave elevation and corresponding time histories of wave force.

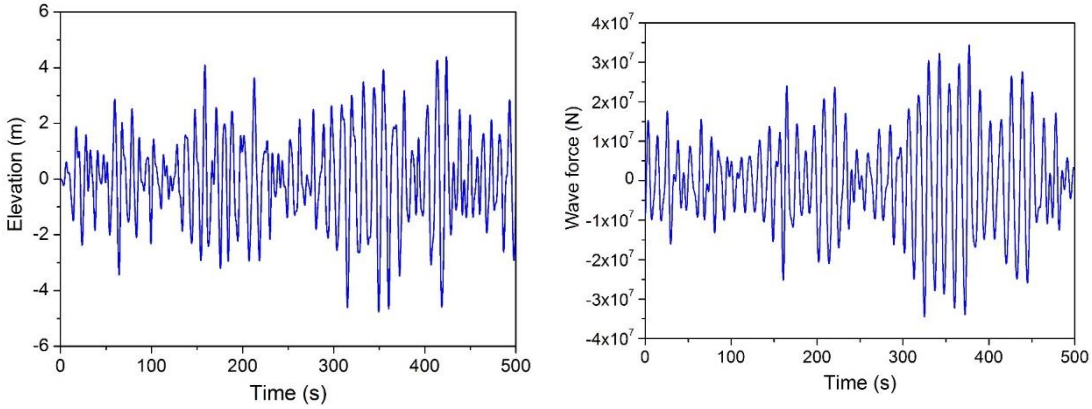

(a) Wave elevation (b) Wave force

Figure 7-12 Simulated wave elevation and time-histories of wave force

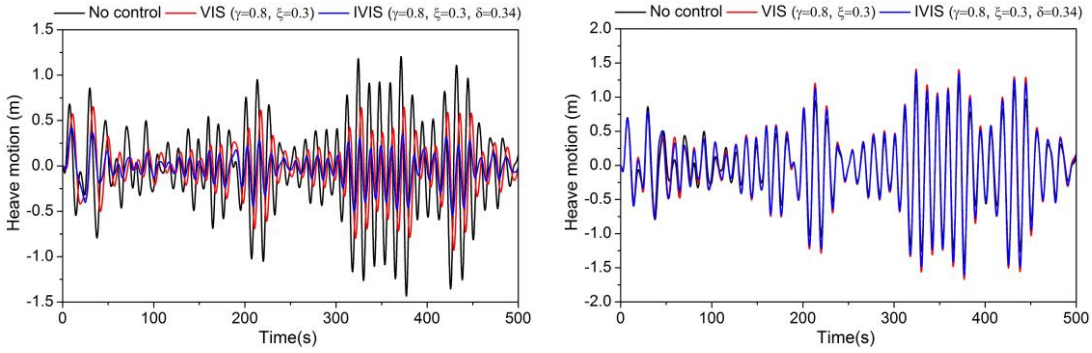

(a) Receiving body (b) Source body

Figure 7-13 Heave motion time histories of the receiving and source bodies

Figure 7-13(a) and (b) illustrate the heave motion time histories of the receiving and source bodies, respectively. Root mean squares (RMSs) and the corresponding reduction ratios are calculated to quantitatively evaluate the isolating performance of the VIS and IVIS, and they are tabulated in Table 7-3. It can be seen that, similar to the frequency-domain results, both the VIS and IVIS can suppress the heave motion of the receiving body while increase the

heave motion of the source body; compared to the VIS, the IVIS is more effective in reducing the heave motion of the receiving body; after incorporating an inerter into the VIS (i.e. constituting the IVIS), the RMS reduction ratios of the receiving and source bodies are further increased by 23.84% and 4.28%, respectively.

Table 7-3 Root mean squares (RMS) of heave motion and the corresponding reduction ratios

Parts	RMS (m)			Reduction ratio (%)		
	No control	VIS	IVIS	No control	VIS	IVIS
Receiving body	0.478	0.286	0.172	--	40.21	64.05
Source body	0.478	0.561	0.540	--	-17.43	-13.15

7.6 Conclusions

Inerter-based vibration isolation system (IVIS) is proposed to isolate the heave motion of SSP. The analytical model of the SSP controlled by the IVIS is established and validated based on the previous experimental and numerical results. Optimization analyses are performed to determine the optimal inertance-to-mass ratio of the IVIS with specific frequency and damping ratios. A case study is conducted to investigate the isolating performance of the proposed IVIS in both the frequency and time domains. The following conclusions can be drawn based on the analytical results:

(1) The conventional VIS can suppress the heave motion of the receiving body, but aggravates the heave motion of the source body. The isolating performance of VIS increases with the decrease of the damping ratio of the receiving body, and the VIS is more effective when the damping ratio is low. Both the effective frequency range and control effectiveness of VIS increase with the decrease of the frequency ratio between the receiving and source bodies, and the VIS performs better when the frequency ratio is small.

(2) The proposed IVIS can effectively suppress the heave motion of the receiving body, and slightly aggravates the heave motion of the source body. Moreover, the effective frequency range of IVIS increase with the increment of the inertance-to-mass ratio.

(3) Compared to the conventional VIS, the proposed IVIS is more effective in reducing the heave motion of the receiving body, and has a wider effective frequency band. For the SSP investigated in the present study, the reduction ratio of the receiving body can be further improved by more than 23%.

(4) The frequency and damping ratios have an obvious influence on the optimal inertance-to-mass ratio of IVIS. A larger optimal inertance-to-mass ratio is required when a larger frequency or damping ratio is adopted.

(5) The proposed IVIS is capable of achieving the best isolating performance by adjusting the inertance rather than changing the spring stiffness and damping coefficient in the system, which makes the proposed system more practical compared to the conventional VIS system.

7.7 Appendix: Simulink Model

A dynamic Simulink model is developed in MATLAB (R2017a) to investigate the time-domain control performance of the proposed IVIS by directly solving Equations (7.8) and (7.9). Figure 7-14 shows the developed Simulink model. As shown, on the left side of the Simulink model, the external forces including the wave-excited force and four feedback loops are input into the system. In particular, these feedback loops are the restoring force regarding to the displacement, the viscous force regarding to the velocity, the radiation damping force regarding to the velocity, and the control force from the IVIS. On the right side, the heave time histories of the receiving and source bodies are outputted, respectively. A variable-step solver is adopted during the analysis. It is worth noting that the symbol $\frac{1}{s}$ is an integrator block that outputs the value of the integral of its input signal with respect to time t. For convenience of constructing the Simulink model, a parameter is further defined as follows:

$$M_0 = m_0 + m_\infty \tag{7.39}$$

in which M_0 is the total mass of the source body, including the physical mass m_0 and infinite-frequency added mass m_∞.

Moreover, as indicated by Equation (7.7), the radiation force consists of two components: the added-mass force proportional to the acceleration, and the damping force proportional to the velocity (i.e. the fluid-memory effect). As shown in Equation (7.39), the first component (i.e. the infinite-frequency added mass) has been considered in the total mass M_0 of the source body. As for the second component (i.e. $\int_0^t K_0(t-t')\,\dot{z}_0(t')dt'$), it is time-consuming to be solved directly since it requires a discrete-time approximation of the convolution integral and enough past data to assess the convolution at each simulation step. To this end, an equivalent state-space model is utilized to calculate the damping force, and it can be expressed as follows:

$$\begin{cases} \dot{\boldsymbol{x}}(t) = \boldsymbol{A}\boldsymbol{x}(t) + \boldsymbol{B}\dot{z}_0(t) \\ y(t) = \boldsymbol{C}\boldsymbol{x}(t) \approx \int_0^t K_0(t-t')\,\dot{z}_0(t')dt' \end{cases} \tag{7.40}$$

in which $\boldsymbol{x}$ is the state vector; $\boldsymbol{A}$, $\boldsymbol{B}$, and $\boldsymbol{C}$ are the system matrices of the state-space model. $\dot{z}_0(t)$ is the input of the system at time t; $y(t)$ is the output, i.e. the damping force of radiation force as shown in Equation (7.7). In the present study, a toolbox developed by Perez and

Fossen [57] is utilized to identify the state-space model and infinite-frequency added mass m_∞. Furthermore, it is noteworthy that the other parameters in the Simulink model are the same as those in the frequency-domain analytical model.

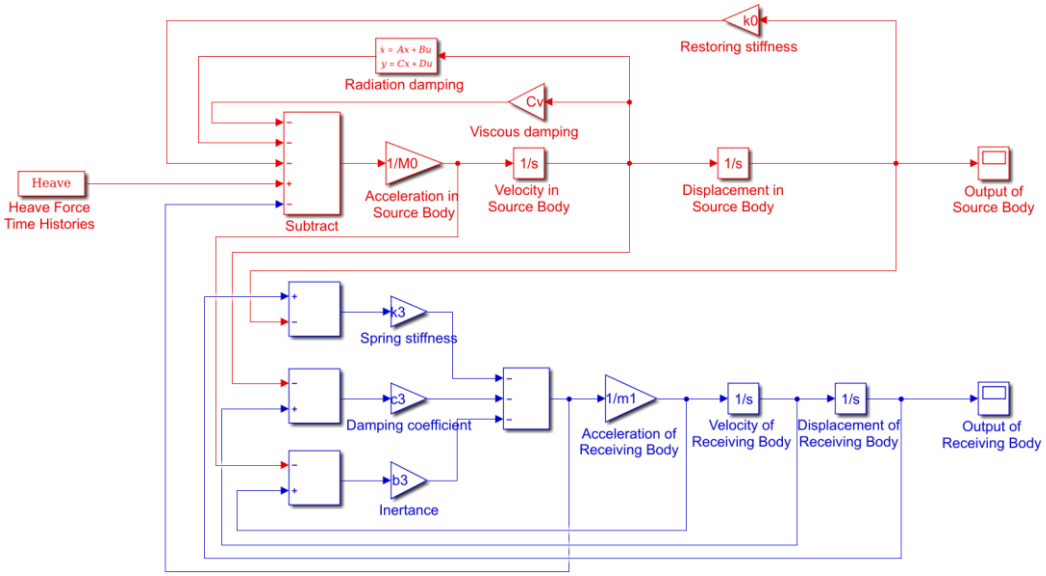

Figure 7-14 Simulink model of the SSP controlled by IVIS

7.8 References

[1] Halkyard J. Floating offshore platform design: Handbook of offshore engineering. Oxford: Elsevier Ltd; 2005.

[2] Kandasamy R, Cui F, Townsend N, Foo CC, Guo J, Shenoi A et al. A review of vibration control methods for marine offshore structures. Ocean Eng. 2016;127:279-97.

[3] Zhang BL, Han QL, Zhang X-M. Recent advances in vibration control of offshore platforms. Nonlinear Dynam. 2017;89:755-71.

[4] Tao L, Cai S. Heave motion suppression of a Spar with a heave plate. Ocean Eng. 2004;31:669-92.

[5] Li B, Huang Z, Low YM, Ou J. Experimental and numerical study of the effects of heave plate on the motion of a new deep draft multi-spar platform. J Mar Sci Tech. 2013;18:229-46.

[6] Liu K, Ou J. A novel tuned heave plate system for heave motion suppression and energy harvesting on semi-submersible platforms. Sci China Technol Sc. 2016;59:897-912.

[7] Bi K, Hao H. Using pipe-in-pipe systems for subsea pipeline vibration control. Eng Struct. 2016;109:75-84.

[8] Zuo H, Bi K, Hao H. Using multiple tuned mass dampers to control offshore wind turbine vibrations under multiple hazards. Eng Struct. 2017;141:303-15.

[9] Lackner MA, Rotea MA. Passive structural control of offshore wind turbines. Wind energy. 2011;14:373-88.

[10] Stewart GM, Lackner MA. The impact of passive tuned mass dampers and wind–wave misalignment on offshore wind turbine loads. Eng Struct. 2014;73:54-61.

[11] Liu K, Liang H, Ou J. Numerical investigation of a tuned heave plate energy-harvesting system of a semi-submersible platform. Energies. 2016;9:82.

[12] Ou J, Long X, Li Q, Xiao Y. Vibration control of steel jacket offshore platform structures with damping isolation systems. Eng Struct. 2007;29:1525-38.

[13] Wu B, Shi P, Wang Q, Guan X, Ou J. Performance of an offshore platform with MR dampers subjected to ice and earthquake. Struct Contorl Health Monit. 2011;18:682-97.

[14] Travanca J, Hao H. Control of wave-induced vibrations on floating production systems. Ocean Eng. 2017;141:35-52.

[15] Smith MC. Synthesis of mechanical networks: The inerter. IEEE T Automat Contr. 2002;47:1648-62.

[16] Brzeski P, Kapitaniak T, Perlikowski P. Novel type of tuned mass damper with inerter which enables changes of inertance. J Sound Vib. 2015;349:56-66.

[17] Xu T, Liang M, Li C, Yang S. Design and analysis of a shock absorber with variable moment of inertia for passive vehicle suspensions. J Sound Vib. 2015;355:66-85.

[18] Zhu H, Li Y, Shen W, Zhu S. Mechanical and energy-harvesting model for electromagnetic inertial mass dampers. Mech Syst Signal Pr. 2019;120:203-20.

[19] Marian L, Giaralis A. Optimal design of a novel tuned mass-damper–inerter (TMDI) passive vibration control configuration for stochastically support-excited structural systems. Probabilist Eng Mech. 2014;38:156-64.

[20] Pietrosanti D, De Angelis M, Basili M. Optimal design and performance evaluation of systems with Tuned Mass Damper Inerter (TMDI). Earthq Eng Struct Dyn. 2017;46:1367-88.

[21] Giaralis A, Taflanidis A. Optimal tuned mass-damper-inerter (TMDI) design for seismically excited MDOF structures with model uncertainties based on reliability criteria. Struct Contorl Health Monit. 2018;25:e2082.

[22] Marian L, Giaralis A. The tuned mass-damper-inerter for harmonic vibrations suppression, attached mass reduction, and energy harvesting. Smart Struct Syst. 2017;19:665-78.

[23] Lazar I, Neild S, Wagg D. Using an inerter-based device for structural vibration suppression. Earthq Eng Struct Dyn. 2014;43:1129-47.

[24] Lazar I, Neild S, Wagg D. Vibration suppression of cables using tuned inerter dampers. Eng Struct. 2016;122:62-71.

[25] Shen W, Niyitangamahoro A, Feng Z, Zhu H. Tuned inerter dampers for civil structures subjected to earthquake ground motions: optimum design and seismic performance. Eng Struct. 2019;198:109470.

[26] Cao L, Li C. Tuned tandem mass dampers-inerters with broadband high effectiveness for structures under white noise base excitations. Struct Contorl Health Monit. 2019:e2319.

[27] Giaralis A, Petrini F. Wind-induced vibration mitigation in tall buildings using the tuned mass-damper-inerter. J Struct Eng. 2017;143:04017127.

[28] Zhang R, Zhao Z, Pan C. Influence of mechanical layout of inerter systems on seismic mitigation of storage tanks. Soil Dyn Earthq Eng. 2018;114:639-49.

[29] Xu K, Bi K, Han Q, Li X, Du X. Using tuned mass damper inerter to mitigate vortex-induced vibration of long-span bridges: Analytical study. Eng Struct. 2019;182:101-11.

[30] Zhang R, Zhao Z, Dai K. Seismic response mitigation of a wind turbine tower using a tuned parallel inerter mass system. Eng Struct. 2019;180:29-39.

[31] Li Y, Shen W, Zhu H. Vibration mitigation of stay cables using electromagnetic inertial mass dampers: Full-scale experiment and analysis. Eng Struct. 2019;200:109693.

[32] Hu Y, Wang J, Chen MZQ, Li Z, Sun Y. Load mitigation for a barge-type floating offshore wind turbine via inerter-based passive structural control. Eng Struct. 2018;177:198-209.

[33] Ma R, Bi K, Hao H. Mitigation of heave response of semi-submersible platform (SSP) using tuned heave plate inerter (THPI). Eng Struct. 2018;177:357-73.

[34] Ma R, Bi K, Hao H. A novel rotational inertia damper for heave motion suppression of semisubmersible platform in the shallow sea. Struct Contorl Health Monit. 2019:e2368.

[35] Ma R, Bi K, Hao H. Using Inerter-Based Control Device to Mitigate Heave and Pitch Motions of Semi-Submersible Platform in the Shallow Sea. Eng Struct. 2020;207:110248.

[36] Hu Y, Chen MZQ, Shu Z. Passive vehicle suspensions employing inerters with multiple performance requirements. J Sound Vib. 2014;333:2212-25.

[37] Jiang JZ, Matamoros-Sanchez AZ, Goodall RM, Smith MC. Passive suspensions incorporating inerters for railway vehicles. Vehicle Syst Dyn. 2012;50:263-76.

[38] Smith MC, Wang FC. Performance benefits in passive vehicle suspensions employing inerters. Vehicle Syst Dyn. 2004;42:235-57.

[39] Wang FC, Hong MF, Chen CW. Building suspensions with inerters. P I Mech Eng C-J Mec. 2010;224:1605-16.

[40] De Domenico D, Ricciardi G. Improving the dynamic performance of base-isolated structures via tuned mass damper and inerter devices: A comparative study. Struct Contorl Health Monit. 2018:e2234.

[41] De Domenico D, Ricciardi G. An enhanced base isolation system equipped with optimal tuned mass damper inerter (TMDI). Earthq Eng Struct Dyn. 2018;47:1169-92.

[42] Zhao Z, Zhang R, Jiang Y, Pan C. Seismic response mitigation of structures with a friction pendulum inerter system. Eng Struct. 2019;193:110-20.

[43] Saitoh M. On the performance of gyro-mass devices for displacement mitigation in base isolation systems. Struct Contorl Health Monit. 2012;19:246-59.

[44] De Angelis M, Giaralis A, Petrini F, Pietrosanti D. Optimal tuning and assessment of inertial dampers with grounded inerter for vibration control of seismically excited base-isolated systems. Eng Struct. 2019;196:109250.

[45] Hu Y, Chen MZQ, Shu Z, Huang L. Analysis and optimisation for inerter-based isolators via fixed-point theory and algebraic solution. J Sound Vib. 2015;346:17-36.

[46] Alujević N, Čakmak D, Wolf H, Jokić M. Passive and active vibration isolation systems using inerter. J Sound Vib. 2018;418:163-83.

[47] Zhao Z, Chen Q, Zhang R, Pan C, Jiang Y. Optimal design of an inerter isolation system considering the soil condition. Eng Struct. 2019;196:109324.

[48] Sun H, Zuo L, Wang X, Peng J, Wang W. Exact H_2 optimal solutions to inerter-based isolation systems for building structures. Struct Contorl Health Monit. 2019;26:e2357.

[49] Faltinsen O. Sea loads on ships and offshore structures. New work: Cambridge University Press; 1993.

[50] Cummins W. The impulse response function and ship motions. Washington DC: David Taylor Model Basin; 1962.

[51] Newman JN, Landweber L. Marine hydrodynamics. American Society of Mechanical Engineers; 1978.

[52] Chakrabarti SK. Hydrodynamics of offshore structures. Southampton: WIT Press; 1987.

[53] ANSYS AQWA. AQWA user's manual release 17.0. Canonsburg: ANSYS Inc; 2016.

[54] Lu L, Duan YF, Spencer Jr BF, Lu X, Zhou Y. Inertial mass damper for mitigating cable vibration. Struct Contorl Health Monit. 2017;24:e1986.

[55] Shi X, Zhu S. Dynamic characteristics of stay cables with inerter dampers. J Sound Vib. 2018;423:287-305.

[56] Asami T, Nishihara O, Baz AM. Analytical solutions to H_∞ and H_2 optimization of dynamic vibration absorbers attached to damped linear systems. J Vib Acoust. 2002;124:284-95.

[57] Perez T, Fossen TI. A matlab toolbox for parametric identification of radiation-force models of ships and offshore structures. Model Ident Control. 2009;30:1-15.

CHAPTER 8 CONCLUSIONS AND RECOMMENDATIONS

Inerter-based vibration control technology is a very hotly debated topic in the recent five years. Inerter-based devices are widely used in the vibration control of onshore structures, their applications to the offshore structures are however very limited. This thesis proposes three novel inerter-based vibration control systems, namely the THPI, RID and IVIS systems, for offshore SSP vibration control. Comprehensive analytical studies are performed to examine the control effectiveness for all the three systems, and experimental studies are performed to further understand the mechanical behaviors and control performance of the RID system. The main findings of this thesis and the recommendations for future works are presented below.

8.1 Main Findings

This thesis performs comprehensive analytical and experimental studies to investigate the effectiveness of using inerter-based vibration control systems for offshore SSP vibration control. The major contributions and findings in this thesis are summarized below:

1. Chapter 1 provides a comprehensive state-of-the-art review on the research and development of inerter-based passive vibration control systems and their applications, which are categorized into three groups: inerter-based energy dissipator, inerter-based dynamic vibration absorber and inerter-based vibration isolator. The critical literature review reveals that: (1) Inerter can significantly improve the energy dissipation capacity of conventional energy dissipators due to its negative stiffness effect. However, the negative stiffness of inerter increases significantly with the increment of excitation frequencies and is thus possible to cause an excessive damping force at high frequencies; (2) Inerter can enrich the configuration of traditional DVA by placing it between the tuned mass and the host structure. However, the performance enhancement is normally not very evident in this scenario; (3) The secondary mass of traditional DVA can be significantly reduced when the inerter is connected between the tuned mass and ground. However, this scheme might not be easy to be implemented for some structures, e.g. high-rise buildings and bridges; (4) Inerter especially the parallel-connected inerter is effective in enhancing the isolation performance of automotive suspensions and vibration isolators. The lateral displacement demand of BIS can be effectively reduced by introducing inerter-based energy dissipators (e.g. IMD) or inerter-based dynamic vibration absorbers (e.g. TMDI/TID).

2. Chapter 2 proposes using the THPI to mitigate the heave motion of SSP and performed analytical studies to investigate its control effectiveness. The counterpart FHP and

THP systems are investigated for comparison and parametric studies are performed to investigate the influences of different plate sizes and depths on the control performance. Analytical results reveal that: (1) Compared to the conventional FHP and THP systems, the THPI can result in better control performance. In particular, the THPI can further reduce the heave motion up to about 19% compared to the THP; (2) The size of the heave plate can significantly influence the control effectiveness of the THPI. Increasing the size of the heave plate generally leads to better control performance, but the increase in the control performance of THPI is not monotonic with the heave plate size; (3) The depth of the heave plate obviously influences the control performance of THPI especially when the depth of the heave plate is small; (4) Although the proposed THPI is demonstrated more effective than the THP, the performance enhancement of THPI is not very significant in some cases.

3. To further improve the control performance, the RID is proposed in Chapter 3, and analytical studies are performed in Chapters 3 and 4 to investigate its effectiveness in reducing the heave motion and the simultaneous heave and pitch motions of SSP, respectively. For comparison, the motion responses of the SSP controlled by the FHP and THP systems are also calculated. Analytical results show that: (1) The RID can generate considerable inertial and damping forces to the SSP due to the amplification mechanism of the ball screw assembly; (2) The RID can provide almost the same or even better control performance in both the heave and pitch directions with a much smaller physical mass compared to the FHP and THP systems; (3) The spacing between the two control devices can significantly influence the performance of the FHP, THP, and RID systems in controlling the pitch response, and a larger spacing leads to better control of the pitch motion.

4. In Chapter 5, a RID prototype was manufactured and systematically tested by using a series of harmonic excitations with different frequencies and amplitudes. Additionally, a nonlinear mechanical model considering inerter nonlinearities is proposed to capture the behaviors of the RID prototype, and its parameters are identified by using a nonlinear least-squares method based on the experimental results. The theoretical results predicted by the proposed mechanical model are then compared with the experimental results. It is observed that: (1) The RID deployed in the air has the mass amplification and negative stiffness effects. A mass amplification factor of 108 is obtained for the RID prototype; (2) The RID can generate significant damping force by rotating turning plates in the water, and an equivalent viscous damping ratio of more than 0.4 is realized; (3) The proposed mechanical model is accurate to predict the behaviors of the RID. For most cases considered in this chapter, the differences

between the experimental and analytical results are less than 9.13% and 3.12% in terms of the peak force and dissipated energy, respectively; (4) The mechanical behaviors of RID are governed by the nonlinear damping force acting on the turning plates, and the inertial force acting on the turning plates is insignificant; (5) The drag coefficient c_d is highly dependent on KC number and tends to be constant with the increase of KC number. The influence of KC number should be incorporated into the performance evaluation of RID.

5. Large-scale wave flume tests were carried out in Chapter 6 to examine the feasibility and control effectiveness of using RID in reducing the heave motion of SSP. A 1:70 scaled SSP model was constructed, and the free vibration, regular wave and irregular wave tests were performed successively. The SSP model equipped with the conventional FHP was also tested for comparison. Experimental results demonstrate that: (1) The RID system is feasible and effective in reducing the heave motion of SSP by using a relatively small physical mass, which provides an attractive alternative for the vibration control of offshore platforms; (2) The conventional FHP system is effective in reducing the heave motion of SSP. For the regular waves, the heave RAOs in the normal wave excitation range is slightly reduced. As for the irregular waves, both the peak and standard deviation of the heave motion are mitigated, and the maximum reduction ratios of 14.45% for the maximum response and 11.74% for the standard deviation are realized; (3) Compared to the FHP system, the RID system is more effective in reducing the heave motion of the SSP. For the regular waves, the heave RAOs are obviously reduced especially when the excitation frequency is relatively small. For the irregular waves, both the peak and standard deviation of the heave motion are mitigated more effectively, and the maximum reduction ratios of 28.27% for the maximum response and 38.72% for the standard deviation are realized.

6. Besides the THPI and RID systems, Chapter 7 proposes an inerter-based vibration isolation system (IVIS) for the heave motion mitigation of SSP subjected to sea waves, and analytically investigates its control effectiveness. A case study is then conducted to illustrate the control performance of IVIS in both frequency and time domains. Analytical results demonstrate that: (1) The proposed IVIS can effectively suppress the heave motion of the receiving body, and slightly aggravates the heave motion of the source body. Moreover, the effective frequency range of IVIS increase with the increment of the inertance-to-mass ratio; (2) Compared to the conventional vibration isolator, the IVIS is more effective in reducing the heave motion of the receiving body, and has a wider effective frequency band. For the SSP investigated in the present study, the reduction ratio of the receiving body can be further improved by more than 23%;

(3) The IVIS is capable of achieving the best isolating performance by adjusting the inertance rather than changing the spring stiffness and damping coefficient in the system, which makes the proposed IVIS more practical compared to the conventional vibration isolator.

8.2 Recommendations for Future Works

Although this thesis has systematically demonstrated the promising performances of inerter-based control systems in the vibration control of offshore SSP, there still exist some attractive topics which deserve further attentions. The following future works are recommended along the lines of the current research.

(1) Analytical and experimental studies are performed in the thesis to investigate the performances of inerter-based control systems. High-fidelity numerical models that are validated by the experimental results can be developed in the future, and used to further investigate the performances of the proposed methods.

(2) This thesis carries out the wave flume tests only for the RID system. Experimental studies of the THPI and IVIS systems are also needed to validate the corresponding analytical results.

(3) The turning plates in the RID system are constructed with a rectangular shape in the thesis. It is well recognized that the damping effect can be significantly affected by the geometry of the plates. More comprehensive experimental studies and numerical simulations can be performed to obtain the optimal geometry of the turning plates.

(4) In this thesis, the effectiveness of inerter-based control systems is examined only under the wave load. However, floating platforms may be subject to multiple hazards during their service lives, including the wave, current and wind loads, etc. A comprehensive performance evaluation of the inerter-based control systems under multi-hazards is necessary.

(5) As indicated in many previous studies, the negative stiffness of inerter increases significantly with the increase of excitation frequencies and is thus possible to cause an excessive damping force at high frequencies. How to overcome this problem deserves further investigations.

(6) Not only SSP, the developed RID can also be applied to many other engineering structures. For example, the RID systems can be used as diagonal braces to control the vibrations of high-rise buildings and fixed offshore platforms.

(7) Combining the inerter device with active control systems (i.e. developing inerter-

based active control systems) is believed to be able to lead to better control performances compared to the conventional active control systems, which deserves further attentions.

APPENDIX I ATTRIBUTION OF AUTHORSHIP

To whom it may concern

I, Ruisheng Ma, contributed (performed analytical and experimental studies, analysed results and wrote the manuscript which was revised and edited by other co-authors) to the papers entitled below.

Ma R, Bi K, Hao H. Mitigation of heave response of semi-submersible platform (SSP) using tuned heave plate inerter (THPI). Eng Struct. 2018;177:357-73.

Ma R, Bi K, Hao H. A novel rotational inertia damper for heave motion suppression of semisubmersible platform in the shallow sea. Struct Control Health Monit. 2019;26:e2368.

Ma R, Bi K, Hao H. Using inerter-based control device to mitigate heave and pitch motions of semi-submersible platform in the shallow sea. Eng Struct. 2020;207:110248.

Ma R, Bi K, Hao H. A novel rotational inertia damper for amplifying fluid resistance: Experiment and mechanical model. Mech Syst Signal Process. 2021;149:107313.

Ma R, Bi K, Hao H. Heave motion mitigation of semi-submersible platform using inerter-based vibration isolation system (IVIS). Eng Struct. 2020;219:110833.

(……..)

I, as a co-author, endorse that this level of contribution by the candidate indicated above is appropriate.

(Dr. Kaiming Bi) (…..……..)

(Prof. Hong Hao) (…..……...)

APPENDIX Ⅱ COPYRIGHT CLEARANCE

The proof of the rights, granted by publishers for the publication that forms the chapters of this thesis, to reproduce the contribution in the thesis are attached below.

Ma R, Bi K, Hao H. Mitigation of heave response of semi-submersible platform (SSP) using tuned heave plate inerter (THPI). Eng Struct. 2018;177:357-73.

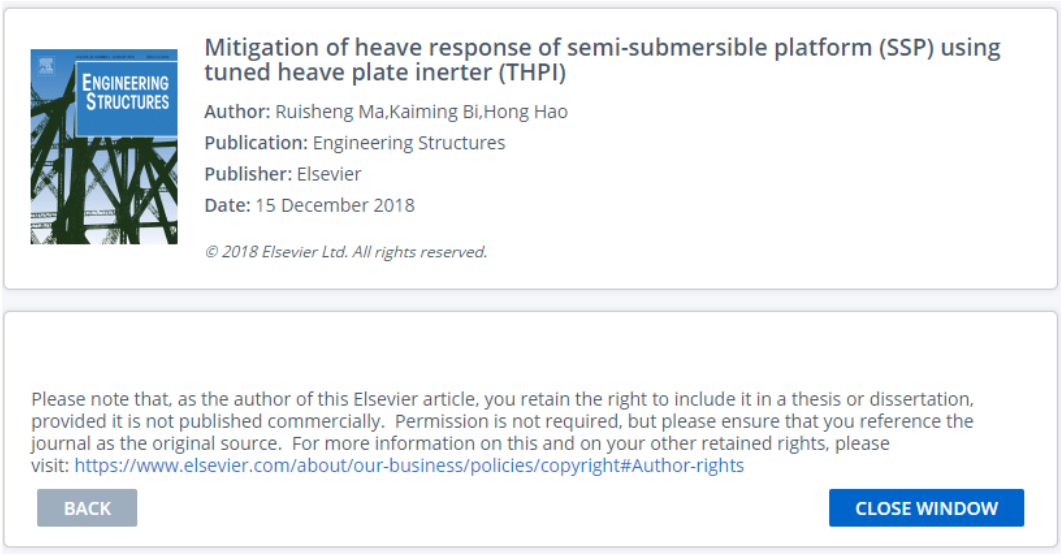

Mitigation of heave response of semi-submersible platform (SSP) using tuned heave plate inerter (THPI)

Author: Ruisheng Ma,Kaiming Bi,Hong Hao

Publication: Engineering Structures

Publisher: Elsevier

Date: 15 December 2018

© 2018 Elsevier Ltd. All rights reserved.

Please note that, as the author of this Elsevier article, you retain the right to include it in a thesis or dissertation, provided it is not published commercially. Permission is not required, but please ensure that you reference the journal as the original source. For more information on this and on your other retained rights, please visit: https://www.elsevier.com/about/our-business/policies/copyright#Author-rights

BACK CLOSE WINDOW

Ma R, Bi K, Hao H. A novel rotational inertia damper for heave motion suppression of semisubmersible platform in the shallow sea. Struct Control Health Monit. 2019;26:e2368.

Thank you for your order!

Dear Mr. Ruisheng Ma,

Thank you for placing your order through Copyright Clearance Center's RightsLink® service.

Order Summary

Licensee:	Curtin University
Order Date:	Nov 29, 2020
Order Number:	4958061226274
Publication:	Structural Control and Health Monitoring
Title:	A novel rotational inertia damper for heave motion suppression of semisubmersible platform in the shallow sea
Type of Use:	Dissertation/Thesis
Order Ref:	10
Order Total:	0.00 USD

View or print complete details of your order and the publisher's terms and conditions.

Sincerely,

Copyright Clearance Center

Tel: +1-855-239-3415 / +1-978-646-2777
customercare@copyright.com
https://myaccount.copyright.com

Copyright Clearance Center RightsLink®

Ma R, Bi K, Hao H. Using inerter-based control device to mitigate heave and pitch motions of semi-submersible platform in the shallow sea. Eng Struct. 2020;207:110248.

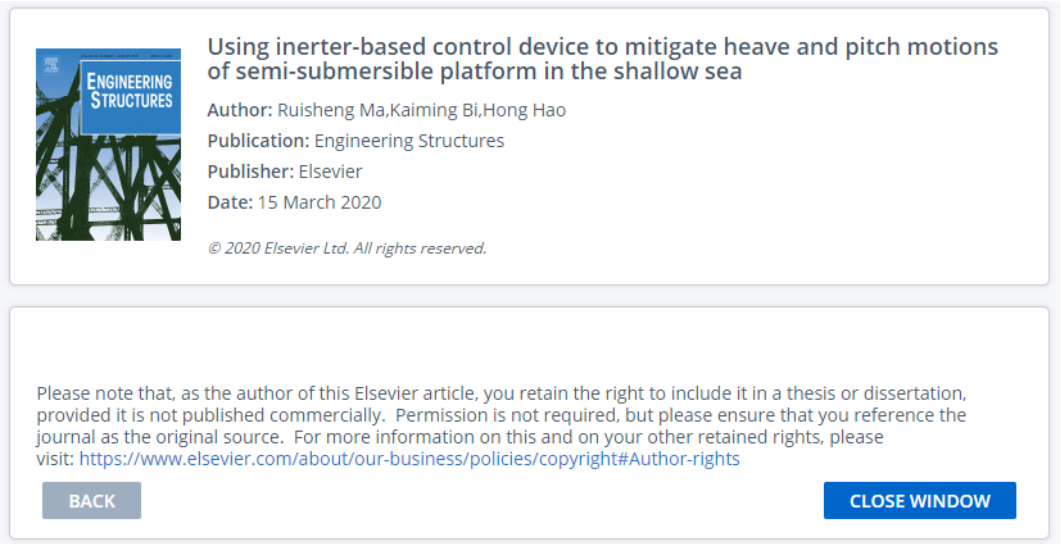

Ma R, Bi K, Hao H. A novel rotational inertia damper for amplifying fluid resistance: Experiment and mechanical model. Mech Syst Signal Process. 2021;149:107313.

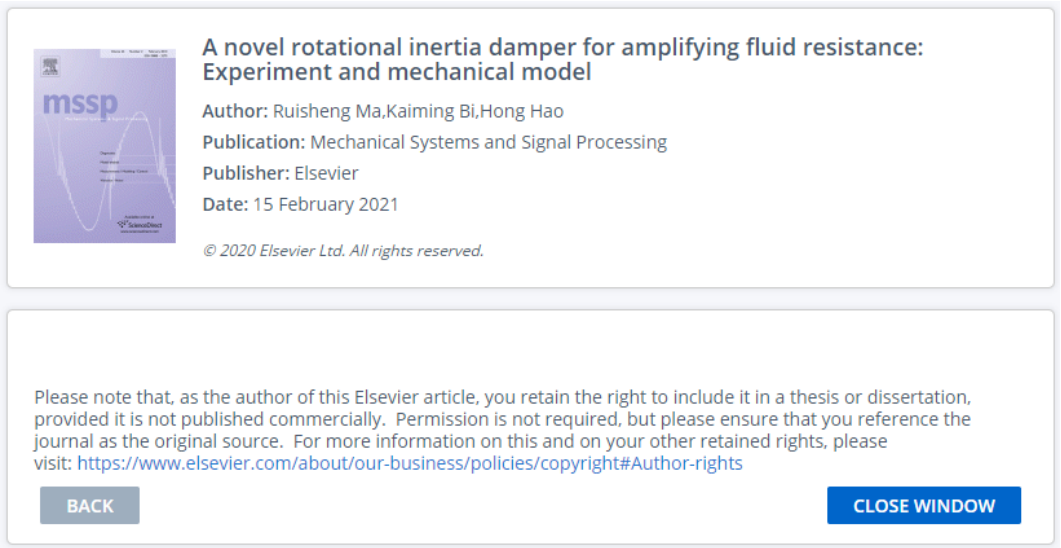

Ma R, Bi K, Hao H. Heave motion mitigation of semi-submersible platform using inerter-based vibration isolation system (IVIS). Eng Struct. 2020;219:110833.

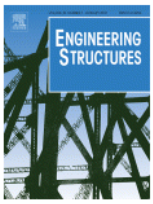

Heave motion mitigation of semi-submersible platform using inerter-based vibration isolation system (IVIS)

Author: Ruisheng Ma,Kaiming Bi,Hong Hao

Publication: Engineering Structures

Publisher: Elsevier

Date: 15 September 2020